University of California
Santa Barbara

Fundamental Studies on the Origin of the Support Effect in VO/TiO_2 (110) Model Catalysts

A dissertation submitted in partial satisfaction
of the requirements for the degree

Doctor of Philosophy
in
Chemistry

by

Jeremy C. Robins

Committee in charge:

Professor Steven K. Buratto, Chair
Professor Horia Metiu
Professor Mattanjah de Vries
Professor Mike Gordon

September 2019

The Dissertation of Jeremy C. Robins is approved.

Professor Horia Metiu

Professor Mattanjah de Vries

Professor Mike Gordon

Professor Steven K. Buratto, Committee Chair

July 2019

Fundamental Studies on the Origin of the Support Effect in VO/TiO_2 (110) Model Catalysts

by

Jeremy C. Robins

To my loving family!

Acknowledgements

First and foremost, I must thank Prof. Steve Buratto for taking me on in his group. Without his advisement none of this would be possible. Over the years, I have learned a lot from Steve about analyzing and presenting data, and having a clear narrative.

I am really thankful to have a former labmate like Dr. Hunter Neilson. Hunter's patience and clarity made him the leader we needed in the lab. Over the years, Hunter has become a good friend and mentor; I look forward to being labmates again at Intel. I am really grateful for former senior scientist, Dr. Xiao Tong, for none of this work would be possible without his tireless efforts collecting data. Some of the most beautiful microscopy images ever recorded in the surface science lab were taken by Xiao; some of these images include VO clusters interacting with methanol that are featured heavily in this dissertation- thank you!

I am also really grateful to have to had Dr. Josh Buffon as a former labmate. His resourcefulness had saved us all a lot of time, like modifying a LabView program for an experiment or finding a clever way to diagnose certain mechanical or electrical problems without breaking vacuum. I am also really thankful for Dr. Scott Price's willingness to help us in the lab and getting us started on how to etch and load STM tips and take a scan. Without Scott's institutional knowledge, the three of us: Hunter, Josh and I would surely turn the lab into shambles. I also really grateful to be part of friendly lab, full of smart, resourceful and caring people. I am thankful former labmates Dr. Jon Burk and Dr. Nick Economou welcomed me to the lab with our daily lunches. I am also really thankful to former labmate Dr. Max Giammona for our philosophical talks. I also have

to thank labmate Austin Barnes, whom has not only become a good friend but also an excellent resource for technical help and understanding physics.

My development as a problem solver in the lab could not have been with out the tremendous and tireless efforts of my father. He taught me how to read and diagnose circuit diagrams and solder properly. Without his incredible knowledge of all things in the material universe I would be lost trying to fix the countless electronic problems in the lab. For that matter, I and the rest of the Buratto lab are in-debted to him. I am really grateful for having a family that constantly provided me with the support and confidence I needed to endure graduate school.

I also give thanks to my committee members who were kind and helpful in providing me with much needed perspective on being a scientist. I also incredibly thankful they took the time to write me numerous letters of recommendations for the many post-doctoral fellowships I applied for.

I am also grateful for the many graduate students I have befriended on the fourth floor. My daily interactions with Jake, Faady, Marshall, and Sam for lunch or weekend hang outs over the years have been a beacon of warmth and laughter. I have to especially thank Jake for constantly reassuring me that I belonged in graduate school. I will also cherish the memories from my first year of at UCSB, taking graduate-level quantum chemistry and teaching general chemistry lab with my 4th floor comrades: Jake, Josh, Faady, Ryan, and Jose; I am not sure I would have made it past this grueling year without them in the trenches with me.

Curriculum Vitæ

Jeremy C. Robins

Education

2019	Ph.D. in Physical Chemistry, University of California, Santa Barbara
2011	B.S. in Chemistry, University of California, Santa Cruz

Publications

1. Robins, J. C., Tong, X., Price, S. P., Metiu, H., Bowers, M. T., Buratto, S. K. "Direct Visualization of Wet Electron States in Methanol on TiO_2 (110)-(1 x 1)" *Manuscript in Preparation*

2. Robins, J. C., Neilson, H. L., Tong, X., Buffon, J. W., Price, S. P., Metiu, H., Bowers, M. T., Buratto, S. K. "Origin of the Support Effect in VO/TiO_2 (110) Model Catalysts" *Manuscript in Preparation*

3. Robins, J. C., Neilson, H. L., Tong, X., Buffon, J. W., Price, S. P., Metiu, H., Bowers, M. T., Buratto, S. K. "On the Role of Ti Interstitials in Methanol Reactivity on TiO_2 (110) - (1 x 1)" *Manuscript in Preparation*

4. Buffon, J. W., Neilson, H. L., Robins, J. C., Kristofferson, H. H., Metiu, H., Bowers, M. T., Buratto, S. K. Methyl Formate Production by Size-Selected V_2O_6 Supported TiO_2 (110) - (1 x 1)" *Manuscript in Preparation*

5. Tong, X., Price, S. P., Robins, J. C., Buffon, J. W., Ridge, C., Kim, H. Y., Metiu, H., Bowers, M. T., Buratto, S. K. "VO-Stabilized H_2O Adsorption on a TiO_2 (110) Surface at Room Temperature." *Manuscript in Preparation*

4. Price, S. P., Tong, X., Ridge, C., Neilson, H. L., Buffon, J. W., Robins, J., Metiu, H., Bowers, M. T., Buratto, S. K. "Catalytic Oxidation of Methanol to Formaldehyde by Mass-Selected Vanadium Oxide Clusters Supported on a TiO_2 (110) Surface" The Journal of Physical Chemistry A 118.37 2014 8309-8313.

6. Fei, H., Onyango, Tedman M., Robins, J. C., Zavalij, P. Y., Oliver, S. R. J. "Synthesis and Magnetic Properties of a 3-D Nickel Hydroxide Capped by Succinate" Journal of Materials Chemistry C 2013 (1), 1099-1104.

7. Fei, H., Cari, H., Robins, J. C., Oliver, S. R. J. "A Cationic Metal-Organic Solid Solution based on Co(II) and Zn(II) for Chromate Trapping" Chemistry of Materials 2013 25 (5), 647-652.

Presentations

1. Jeremy Robins, Hunter L. Neilson, Xiao Tong, Josh Buffon and Steven K. Buratto. " Thermal Desorption Productions of Methanol TPD on TiO_2 (110) with Scanning Tunneling Microscopy at Room Temperature" CATL: 110 American Chemical Society, San Diego 2016

2. Jeremy Robins, Hunter L. Neilson, Josh W. Buffon, Horia Metiu, Mike T. Bowers and Steven K. Buratto. "Structure and Reactivity of V_XO_Y clusters supported on TiO_2 (110)" Gordon Research Conference: Clusters & Nanostructures, July 2017 Poster Presentation.

Fellowships & Awards

2014 - 2015 PIRE-ECCI NSF Fellowship

2011 Deans Award for Undergraduate Research (UCSC)

Abstract

Fundamental Studies on the Origin of the Support Effect in VO/TiO_2 (110) Model Catalysts

by

Jeremy C. Robins

Vanadia supported on TiO_2 belong to a class of mixed-metal oxides capable of catalyzing the oxidative dehydrogenation (ODH) of alkanes into high commodity olefins at lower temperatures than current commercial technology. As olefins are central to many important industrial processes, improving the reactivity of vanadia catalysts has become an active area of research. The unique reactivity in supported vanadia is attributed to the complex local bond-coordination present at the interface, therefore, understanding the role of each metal oxide at the interface is critical to designing better catalysts.

Previous investigations found the catalytic activity of vanadium oxide is inversely related to the support oxygen-vacancy formation energy. However, the nature in which support metal oxide defects contribute to this catalytic synergy is unknown. This is due to the fact that the metal oxide support is typically oxidized in the growth of the catalyst, and the resulting vanadium oxide active sites are stoichiometrically ill-defined. We circumvent these problems by soft-landing mass-selected cationic VO^+ clusters onto single-crystal rutile TiO_2 (110) - (1×1) surfaces to create well-defined model interfaces. By integrating temperature programmed desorption/reaction (TPD/R) studies with variable temperature scanning tunneling microscopy (VT-STM), we correlate ensemble surface reactivity with sub-nanometer VO clusters and electron-donating point

defects: sub-surface Ti interstitials and surface bridging-oxygen vacancies. Both defects are well known to react with oxygenates adsorbed on the reduced TiO_{2-x} (110) surface. Employing methanol ODH to formaldehyde and water as a probe reaction, we identify sub-surface Ti interstitial defects in TiO_{2-x} as the the active site in a new reaction whereby two stranded methoxide intermediates disproportionate into methane, formaldehyde and an oxygen adatom. Oxygen adatoms subsequently react with Ti interstitials to form titania islands of varying stoichiometry.

We find the inclusion of VO clusters on the surface perturbs the formation of titania islands and methanol dissociation at bridging oxygen vacancies. In-lieu of these defect-driven reactions, methoxides stabilize on under-coordinated Ti sites and on VO clusters in the form of VO-$(OCH_3)_n$ intermediates. These intermediates lead to an exothermic, VO-mediated disproportionation reaction to formaldehyde and methanol at high temperature. Kinetic studies by STM reveal VO-$(OCH_3)_n$ forms easily at room temperature. Our results indicate the classical Mar-van Krevelen mechanism, involving one methanol dehydrogenating into formaldehyde and water at a vanadium oxide site needs revising to account for multiple methanols dissociating into VO-$(OCH_3)_n$ intermediates. Given the favorable thermodynamic and kinetic barriers for this cluster-mediated reaction, we suggest this mechanism is of general consequence in all mixed-metal oxide catalysts and may be the origin of numerous side reactions observed in the literature. Furthermore, we propose VO clusters achieve this reactivity by scavenging electrons from Ti interstitials and bridging oxygen vacancy defects, resulting in an effectively oxidized surface. The VO/TiO_2 interface investigated here represents an interesting model towards understanding the synergistic effects of mixed-metal oxides catalysts.

Contents

Chapter 1

Introduction

1.1 The Case Against Current Technologies

Olefins such as ethylene and propylene are precursors to many different plastic and high commodity chemical products.[1] The production of olefins is therefore an important endeavor to the chemicals industry and projected to increase significantly in the near future. Presently, the main sources of olefins are steam cracking and fluid-catalytic-cracking of crude oil feedstocks under high temperatures. However, as ethylene is the preferred product in steam crackers and fluid crackers, other technologies will be needed to meet the growing market demand for propylene.[2] In addition to these issues, the high energy demands for these processes (760 - 850 ^{o}C), the low selectivity towards propylene and the rising prices of oil have spurred the energy sector to look elsewhere for a carbon feedstock.

The recent abundance of natural gas found in the United States has sparked industrial and academic interest. Several patented technologies developed to catalyze ethane and

propane dehydrogenation to alkenes on demand, have made natural gas an economically viable source of energy and added-value feedstock. As a result of the successful valorization of shale gas, the United States has become the lowest cost chemical producer outside of the Middle East, as evident by the 126 investment projects totaling 84 billion dollars in 2013.[3] Although these processes are widely used to date in industry, they have a few major disadvantages:

1. The two patented technologies currently in use employ unsustainable materials for catalysts: the Catofin process[4] uses rare Pt-based catalysts and the Oleflex process[5] uses environmentally harmful CrO_x-based catalysts.

2. Dehydrogenation is equilibrium-constrained and therefore the total conversion of alkane feedstock is severely limited.[6]

3. Overall, the dehydrogenation process is endothermic ($\Delta H^o > 0$), requiring temperatures typically above 500 ^{o}C. The high temperature demands lead to undesired side reactions and therefore coking of the active sites, resulting in rapid catalyst deactivation.[7]

Therefore, the need exists for new technologies devoted to the production of specific olefins, which have none of the disadvantages characterizing dehydrogenation.

1.2 The Case for ODH Catalysts

To circumvent problems associated with dehydrogenation, catalytic oxidative dehydrogenation (ODH) of paraffins have been proposed. ODH reactions are carried out by the addition of an oxidant to the alkane feedstock and can proceed in one of two ways:

(1) exothermic combustion of the alkane feedstock, followed by high temperature (typically above 700 ^{o}C) catalytic endothermic ($\Delta H^o > 0$) dehydrogenation or (2) a true ODH reaction via an exothermic ($\Delta H^o < 0$) reaction pathway on a redox-active catalyst at temperatures below 500 ^{o}C and not limited by reaction equilibrium. The lower energy requirements alone make ODH catalysis advantageous over the previously mentioned processes. Finding a cheap, robust material capable of true ODH catalysis would therefore greatly benefit the energy and chemical industry and is the subject of intense research.

The most promising ODH catalysts are a class of mixed-metal oxides catalysts (MMOC) consisting of relatively cheap transition metal oxides MO_x clusters (M = W, Mo, V), supported on top of a second oxide (MgO, Al_2O_3, SiO_2, TiO_2 and CeO_2).[6, 8, 9] In addition to ODH reactions, MMOCs are capable of catalyzing the selective hydrogenation and isomerization of olefins, oxidation of alkanes and carbon monoxide, SO_x decomposition, NO_x reduction, photolysis of water, water-gas shift reaction and CO_2 reduction.[9] Due to their unique reactivity and affordability, MMOCs contribute to nearly one-third of the catalyst materials used in the private sector.[10] Thus, much of the catalysis community is devoted to understanding and improving the reactivity of MMOCs.

1.3 Supported Vanadia Catalysts

Supported vanadia in particular, is used extensively as a catalyst in the industrial sector. In the 1960's, titania supported V_2O_5 was initially discovered as an efficient catalyst for the oxidation of o-xylene to phthalic anhydride.[11] Since then, vanadia catalysts can be found in many industrially relevant reactions, including the reduction of NO_x to NH_3[12], and the oxidation of SO_2 to SO_3.[13] Oil shortages in the 1970's sparked

new research into the partial oxidation of methanol to formaldehyde[14] and the ODH of butane to butadiene[15] over supported vanadia catalysts. The former process is the now successfully commercialized Formox^{TM} process, licensed by Johnson Matthey Inc. The selectivity of methanol oxidation to formaldehyde on vanadia is still an active area of research, as many other useful oxygenates like dimethyl ether and methyl formate are synthesized in the process.[14, 16]

Since the 1990's, researchers have demonstrated supported vanadia is capable of catalyzing the ODH of light alkanes (C_1 - C_4) into olefins (see all references there-in).[6, 8, 9, 17] Success has been shown for both ethane and propane ODH at temperatures as low as $\sim 300^o$ C.[8] However, in order for vanadia to be commercialized for ODH reactors, there are two major obstacles that need to be addressed: (1) the catalyst cannot be fully regenerated after initial cycling of the feedstock and (2) the yield for many ODH processes is too low.[6, 8] In order to overcome these problems, a fundamental understanding of the laws governing the reactivity of supported vanadia catalysts is needed. Approximately forty years of research has been devoted to understanding the catalytic properties of metal oxide supported vanadia catalysts; I will highlight some of these major findings that led to the work discussed in the Buratto lab.

1.3.1 Sub-monolayer Powder Catalysts

Initial reactor studies demonstrated the sensitivity of vanadia coverage on the oxide support to methanol partial oxidation and ammoxidation reactivity.[14, 18, 19, 20] The higher reactivity and selectivity observed at sub-monolayer to monolayer coverages

were attributed to the growth of isolated VO_x and 2D poly-vanadate structures not observed among their bulk polycrystalline V_2O_5 and V_2O_3 counterparts. To contrast, the ODH of propane to propene increases monotonically with vanadia loadings ranging from poly-vanadate structures to polycrystalline V_2O_5 thin films.[21] To reconcile these discrepancies, various kinetic and isotope labelling experiments on the partial oxidation of methanol[16] and ODH reactions of ethane and propane[22, 23] were conducted as a function of vanadia coverage and found that the rate-limiting methyl-dehydrogenation step to be independent of the O_2 feedstock concentration. Interestingly, these studies concluded that both reactions proceeded by the Mar-van Krevelen mechanism, whereby lattice-oxygen oxidizes the reactant followed by replenishing oxygen-vacancies with gas phase O_2.[24]

1.3.2 V-O-V Bond

After establishing that lattice-oxygen bonds directly participate in vanadia reactivity, the question arises: which vanadium oxide bond contributes most to catalytic activity? This is difficult to answer as the structure of mono and poly-VO_x consists of a number of different terminal bonds (V=O, V-O-V, V-O-O, V-O-Support).[17] At sub-monolayer coverages, the structure is widely believed to be the tetrahedral VO_4 sub-unit, consisting of a vandayl (V=O) bond and three V-O-Support bonds.[9, 17] These sub-units form poly-vanadates that are linked by a V-O-V bond. For clarity, the monomer and polymeric structure are illustrated in Fig 1.1 as a function of coverage.

Wachs and co-workers employed UV-Vis spectroscopy on powder samples of supported poly-vanadate structures to correlate the number of V-O-V bonds measured with propane

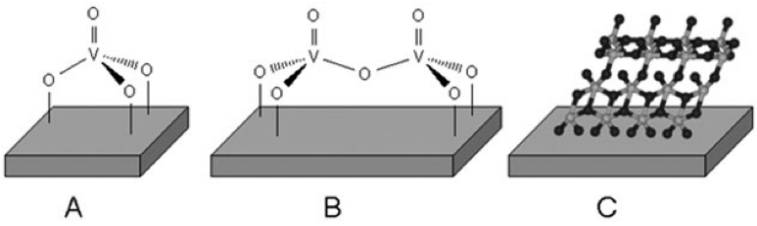

Figure 1.1: The three different forms of VO_x species as a function of the degree of isolation. Reproduced with permission from Physical Chemistry Chemical Physics, Vol. 11, 2009, p. 2827.

ODH reactivity.[25] These authors found that ODH reactivity declined linearly with number of V-O-V moieties. Instead, the reactivity was found to vary by more than order of magnitude with more reducible supports, suggesting the V-O-Support bond is more reactive. Similar results were found for methanol partial oxidation on alumina supported vanadia.[26] A recent ^{51}V solid state NMR report confirmed that the active species for methanol partial oxidation were monomer and dimers of VO_x clusters, indicating that V-O-V bond is not active.[27] The results of these previous studies suggest monomeric VO_x is the active species.

1.3.3 V=O Bond

Given that VO_x monomers are evidently the active species, the reactivity of the terminal V=O bond and V-O-Support bond need to be considered. The V=O bond was first suggested by Mars and van Krevelen in 1954 as the active bond, given at the time, the scientific community thought the surface and bulk structures of metal oxides were equivalent.[24] However, Routray et al.[28] have shown in a study, that these previous authors did not normalize for the surface area nor the actives sites available for adsorption. In this same report, using quantitative methods of flow reactors, methanol TPD/R and Raman spectroscopy, Routray and co-workers found the V=O bond to be

in-active.[28]

More conclusive results by Freund and co-workers employed DFT to compare spectroscopic results from reactor studies with UHV surface science results (STM, FTIR and TPD) on model VO_x/Al_2O_3 and VO_x/SiO_2. These authors concluded that the Raman and FTIR spectroscopic bands commonly used in the literature to indicate V=O functionality is incorrect, and suggested the vibrational modes describe the coupling of the V-O-Support bond.[29] Despite this work, there are DFT studies by Sauer and Metiu that suggests V=O cannot be discounted in the ODH of propane and partial oxidation of methanol.[30, 31] Clearly, more research is needed to reach a consensus on the activity of the terminal V=O bond.

1.3.4 V-O-Support Bond

After discussing V-O-V and V=O functionalities, we can address the activity of the V-O-Support bond. Indeed, there is overwhelming experimental and computational evidence that the V-O-Support bond is responsible for the catalytic properties. Review articles detailing the role of the V-O-Support bond can be found in the references cited here.[6, 8, 13, 16, 17] The importance of the V-O-Support bond was first reported by Roozeboom et al.[14], who had demonstrated the superior oxidation reactivity and selectivity of supported-vanadia powder catalysts over their pure metal oxide counterparts. Compelling evidence by Deo et al.[18], showed that the TOF for the partial oxidation of methanol on monolayer V_2O_5 varied by three orders of magnitude when measured as a function of the support composition. This same trend was also observed in supported monomeric VO_x species, as illustrated in Fig 1.2.[13]. The monotonic increase

in methanol TOF with the composition of the oxide support: $CeO_2 > ZrO_2 > TiO_2 > Al_2O_3 > SiO_2$, strongly indicates the importance of the V-O-Support bond. This trend correlates inversely with the electronegativity of the metal cation composition in the oxide support. In addition, the trend is independent of the temperature, the percent of O_2 in the feedstock and reactant (methanol, ethanol and propane).[32]

1.3.5 Reactivity Correlates Inversely to Support Oxide Electronegativity

Interestingly, the inverse correlation between the electronegativity of a support oxide and catalytic reactivity implies the presence of a static electric charge on the interfacial bond. Physically, this requires the V-O-Support bond to gain electron density and a nearby support metal cation to lose electron density, effectively becoming electropositive.[33] To date however, there are no direct measurements of the interfacial bond electron density reported. Nonetheless, the implications of this inverse relation is contrary to decades of research on supported vanadia catalysts. Vibrational and electronic structure characterization by in-situ Raman, UV-Vis spectroscopy, XANES and EXAFS at low vanadia loadings on various supports (ZrO_2, Al_2O_3, SiO_2), indicate reactants are oxidized via the reduction of $V^{+5} \rightarrow V^{+4}$ and V^{+3} active site.[34, 35, 36, 37]

The issue with this characterization arises from the assumption that surface-bound vanadia will have electronic structures (e.g. oxidation state, formal charge) comparable to bulk reference samples like $NaVO_4$ and V_2O_5. This assumption that transition metal semiconductors and insulators can be treated ionically is false. Chemists know this! DFT calculations by Metiu and co-workers found that VO_x monomers (x = 1 - 4) on rutile phase titania exhibit a Bader charge of approximately +2, regardless of the number of

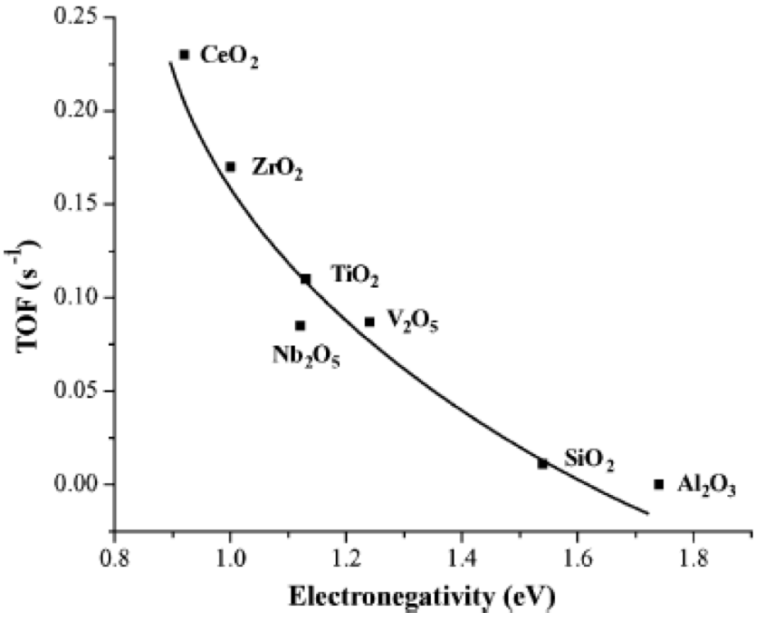

Figure 1.2: The catalytic activity for methanol ODH to formaldehyde per surface VO_4 site varies inversely with support cation electronegativity. Reproduced with permission from Catalysis Today, Vol. 100, 2005, p. 80.

oxygen bound to vanadium.[38] These findings oppose the typical assignment of the terminal V=O bond to V^{+5} and their reduction to V^{+4} or V^{+3} following methanol ODH to formaldehyde. As a result, the interpretation of XPS and XANES results should be re-evaluated on the degree of covalency, not charge. The lack of correlation between oxidation state and static electron charge among transition metal compounds was explained more generally a year later by Raebiger et al.[39], who proposed a charge self-regulation mechanism rather than charge transfer as the appropriate model. Besides vanadium oxide, the hybridization of electrons was employed successfully to account for the observed localization of excess electrons on surface five-coordinated Ti atoms in defective rutile TiO_2 (110) by accounting for electron-donating Ti interstitials in the bulk.[40] These concepts on the electronic structure of rutile TiO_2 (110) are important to the overall understanding of our findings and thus merit a more in-depth discussion in chapter 4.

1.3.6 Reactivity Inversely Relates to Support Oxygen Vacancy Formation Energy

Theorists from the Metiu group[41], Bell group [42] and Sauer group[43] found the discrepancy described above could be explained by the inclusion of oxygen vacancy defects near the vanadia active site. These authors reasoned that the reduced states of vanadium oxide can be stabilized by the accommodation of excess electrons at nearby metal oxide support sites (i.e. Ti^{3+} and Ce^{3+} sites), thus allowing the vanadium atom to remain in a high-valent oxidation state. Oxygen vacancy defects are expected to diffuse to the surface in the presence of background oxygen gas. Sum frequency generation IR and classic surface science experiments have shown this to be the case for anatase TiO_2.[44, 45] Recently, it has been proposed that surface oxygen vacancy defects are generated in the reoxidation of the active vanadium oxide site following one cycle of ethanol ODH.[46] Thus the inverse relation between the support oxide composition and vanadia reactivity can be modeled by a new descriptor: the enthalpy energy of oxygen vacancy formation. Calculations performed by Goodrow and Bell on various support oxides are illustrated in Fig 1.3. It should be noted, the calculations by Goodrow correspond to the anatase phase of titania, and the calculations by Metiu and co-workers modeled rutile phase titania in the presence of a vanadium metal substituted into the surface lattice. Furthermore, the models proposed by Sauer may not be accurate as the authors assume the CeO_2 thin films grown on a single crystal Rh substrate an UHV is equivalent to powder ceria catalysts.

Despite the experimental and theoretical work demonstrating a dependency between oxygen vacancy formation enthalpy in the support oxide and catalytic activity, no consensus has been reached as to which oxygen in the vanadia monomer is directly involved

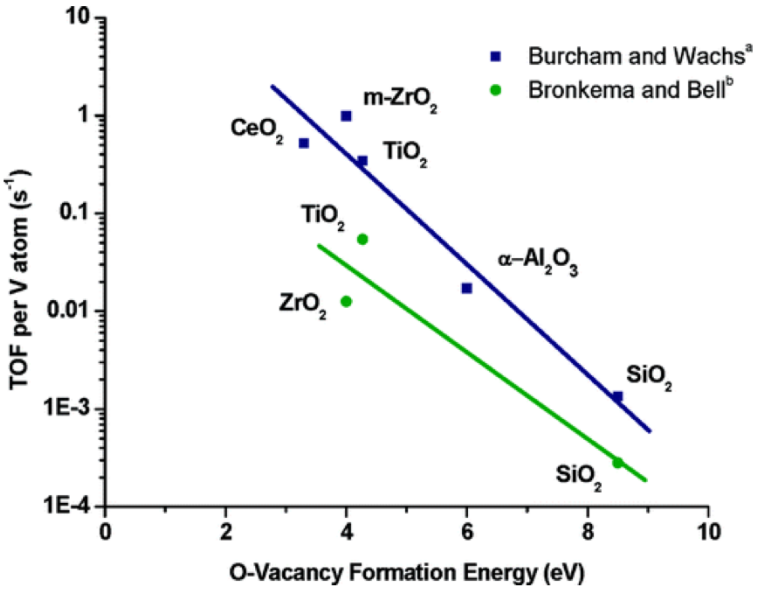

Figure 1.3: TOF per V atom for methanol oxidation versus the O-vacancy formation energy. Reproduced with permission from Journal of Physical Chemistry C., Vol. 112, 2008, p. 13212.

in the Mars-van Krevelen mechanism. For example, the Freund and Sauer group probed the methanol reactivity of monomeric vanadia supported on a thin film of ceria under ultra high vacuum conditions (UHV). These authors attributed the low temperature (370 K) formaldehyde production to methanol dissociation over the V-O-Ce bond to yield a V-OCH_3 + Ce-OH; the methoxide subsequently undergoes dehydrogenation to formaldehyde and the hydrogen atom combines with the adjacent Ce-OH to form water, leaving behind an oxygen vacancy.[43, 47, 48] In the case of anatase powder samples, the Bell group proposed the methanol reactivity of monomeric vanadia to the dissociation of the vanadyl bond with methanol to form V-OCH_3 + V-OH. The dehydrogenation to formaldehyde follows a hydrogen atom transfer to the V-OH to form water and depletion of V=O bond.[42, 49]

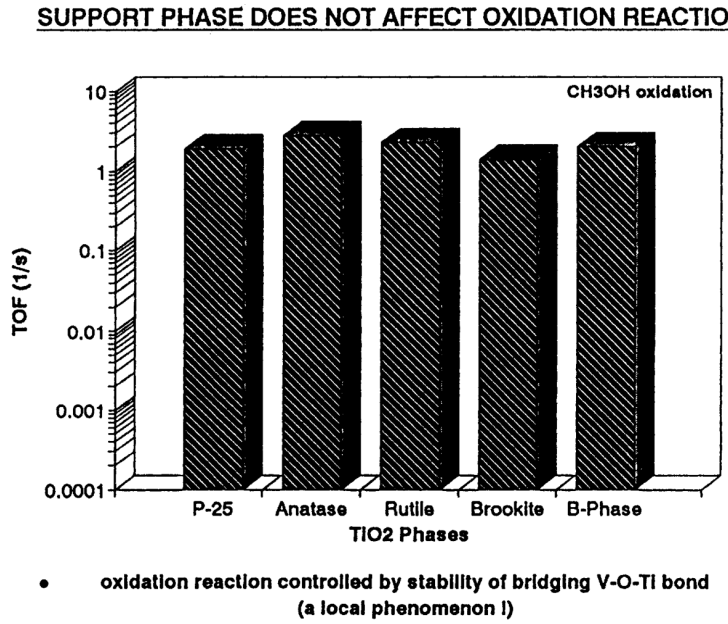

Figure 1.4: Reproduced with permission from Applied Catalysis A: General, Vol. 91, Issue 1, 1992, p. 27.

1.4 UHV Studies on Model VO_x/TiO_2 (110)

It is clear that the deviations in these reports arise from a lack of fully understanding the surface structure and defects in the support, the structure and adsorption site of the vanadia monomer, as well as the reactant binding site. To resolve these fundamental aspects, surface science techniques need to be employed on well-studied single crystal substrates under UHV conditions. The majority of fundamental studies involve the preparation of vanadium oxide on rutile phase TiO_2 (110) surfaces. The choice of rutile over the more catalytically relevant anatase polymorph is due to a couple reasons: (i) pure single crystals of rutile are much easier to grow (ii) the cleaved (110) plane is the most thermodynamically stable surface.[50] As a result, rutile TiO_2 is the most studied transition metal oxide semiconductor. Lastly, the catalytic oxidation of methanol to formaldehyde on vanadia supported on the two different polymorphs of titania are nearly

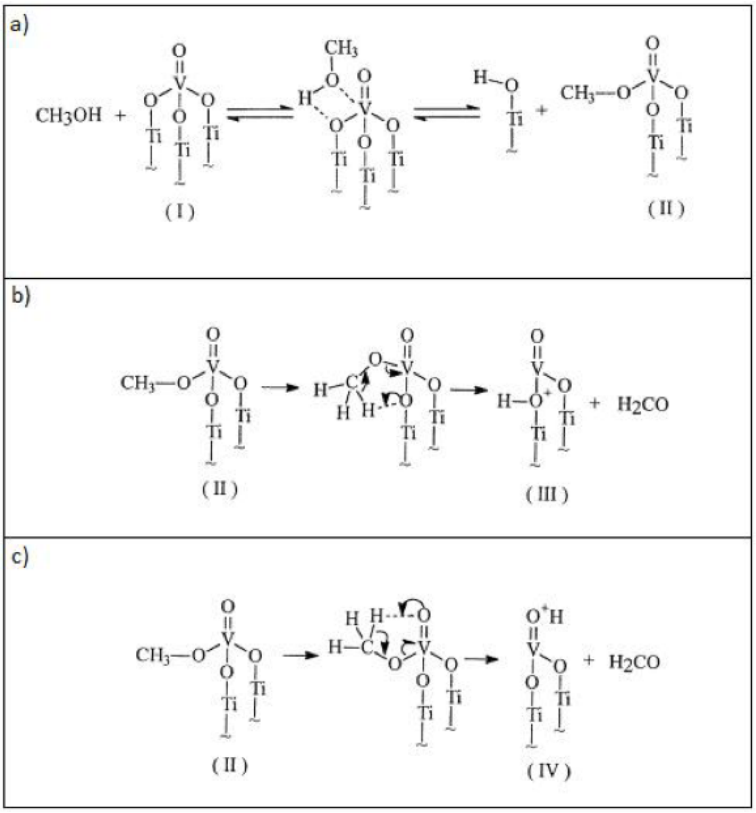

Figure 1.5: Reproduced with permission from Surface Science, Vol. 496, 2002, p. 61.

the same, as illustrated by the TOF rates in Fig 1.4, suggesting the local properties of the catalyst are similar.[51] The use of rutile TiO_2 (110) as a support oxide is therefore justified in the preparation of model vanadia catalysts.

Much of the foundational work on rutile TiO_2 was done by the Vohs group[52, 53, 54], Madix group[55, 56, 57], and the Grannozi group[58, 59]. Initial studies by Wong and Vohs established the validity of monolayer vanadia on rutile TiO_2 as a model catalyst for methanol oxidation to formaldehyde. Monolayer vanadia on TiO_2 (110) prepared by vapor deposition of vanadium in O_2 were found to be the most reactive while mutli-layer and bare TiO_2 were inactive.[53] Activity of the monolayer catalyst was also found to

vary with vanadium oxidation state. For a monolayer containing predominantly V^{+5}, formaldehyde production at 485 K, while a monolayer containing mostly V^{+3} produced formaldehyde at 613 K. The structure of the monolayer catalyst was on the pentavalent oxidation state, these authors ascribed the monolayer catalyst to V_2O_5. Similar trends were also published by Wang and Madix, although vanadia was prepared by deposition of a $VOCl_3$ precursor followed by hydrolysis to V_2O_5.[55] These authors concluded that V_{5+} is the active oxidation state and suggested V-O-Ti is active for the oxidation of the methoxide to formaldehyde and water.[56] Wang and Madix's proposed mechanisms as illustrated in Fig 1.5, indeed satisfy the well-known Mars-van Krevelen mechanism discussed earlier on powder samples under reactor conditions. However, there are a couple issues with this proposed mechanism: i) the structure put forth in Fig 1.5 is the VO_4 monomer despite the fact these authors claim the active catalyst is monolayer V_2O_5, ii) secondly, the authors never observed water desorption in their reaction studies.

A more recent studies by the Grannozi group raises questions about the active oxidation state of vanadium and what is the active structure of vanadia. The report by Artiglia and Grannozi, used similar a similar recipe to the Vohs group to generate low coverage vanadia on TiO_2 (110). Unlike the Vohs group, these authors report a V_4O_6 monomer structure with vanadium in a V^{+3} oxidation state.[58] Cryogenic deuterated methanol (CH_3OD) exposure on the V_4O_6 decorated surface produced formaldehyde (CH_2O), methanol and water at room temperature; the lowest ever reported temperature methanol oxidation. However, this claim of room temperature methanol partial oxidation is questionable give that a non-trivial amount of formaldehyde is produced on the bare TiO_2 (110) surface (see supporting information)[58] at the same temperatures

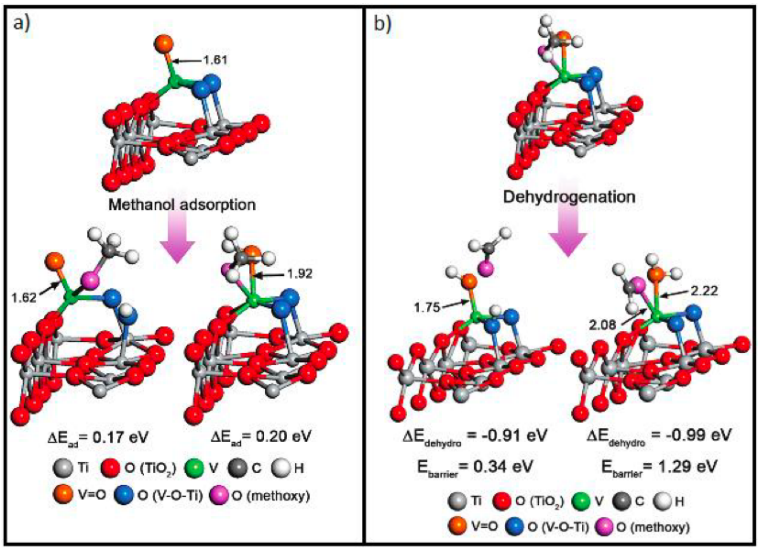

Figure 1.6: (a) Dissociative adsorption energy of methanol where the initial H abstraction step is carried out by the V-O-Ti atom (left) and the vandadyl O atom (right); (b) formaldehyde formation energy as well as the energy barrier to the methoxy deprotonation step where deprotonation is carried out by the V-O-Ti bridging O (left) and the V-OH O (formaldehyde and vanadyl oxygen). Reproduced with permission from Journal of Physical Chemistry C, Vol. 114, 2010, p. 13736.

as the vanadia decorated surface. Secondly, CH_3OH was observed concomitantly with CH_2O, suggesting a possible disproportionation reaction between two methoxides. It is also possible that formaldehyde production could be due to the oxidation of methanol by oxygen adatoms given the similar temperature range reported by Henderson at Pacific Northwest National Laboratory.[60] The large differences in results between the three groups mentioned thus far, may be a result of the growth methods for generating active vanadia monomers. Clearly, a more systematic study is needed to resolve the active structure of vanadia monomers and the mechanism for partial oxidation.

Recent work from our group prepared model catalysts by soft-landing cationic mass-selected V^+, $V_2{}^+$, VO^+, and $VO_2{}^+$ clusters onto vacuum-reduced TiO_2 (110). All four clusters were found to be inactive for methanol partial oxidation to formaldehyde. Post-oxidation in a background of O_2 showed that V^+, $V_2{}^+$, and $VO_2{}^+$ were minimally active for formaldehyde at around 617 K, while post-oxidized VO^+ however, exhibited strong activity for formaldehyde production.[61] DFT calculations by the Metiu group, reasoned that post-oxidized VO generates an octahedrally coordinated VO_3 monomer consisting of V=O bond and several V-O-Ti bonds.[38] It is also worth noting that the same authors assign the central vanadium atom in the VO_3 monomer to Bader charge of +2 and is independent of the V 2p core-level shifts, as discussed earlier. More importantly, the mechanism for the partial oxidation of methanol to formaldehyde, as depicted in Fig 1.6, was found to be energetically equivalent along both the V=O bond and V-O-Ti bond.[31]

The importance of the VO_3 stoichiometry and the effect of the support were most recently addressed in our group (see Hunter's dissertation[62]). The structure and reactivity of mass-selected $V_2O_5{}^+$, $V_2O_6{}^+$, $V_2O_7{}^+$ and $V_3O_9{}^+$ clusters were probed as a

function of the oxidation state of TiO_2 support. It was found that $V_2O_6^+$ soft-landed on highly defective TiO_2 (110) produced formaldehyde at 482 K, while clusters soft-landed on mildy defect surfaces produced formaldehyde at 437 K and methyl-formate at 540 K. Soft-landing $V_2O_6^+$ on TiO_2 pre-decorated with oxygen adatoms produced exclusively methyl-formate and water at 437 K. Furthermore, $V_3O_9^+$ on reduced TiO_2 catalyzed methanol into methyl-formate near room temperature; this the lowest temperature ODH reaction recorded in our experiments. Interestingly, soft-landed $V_2O_5^+$ on mildly reduced TiO_2 was inactive for methanol ODH and V_2O_7 on midly reduced TiO_2 was only slightly active for formaldehyde production at 455 K. These results show that the reactivity is extremely sensitive to the stoichiometry of the cluster: all clusters that are active have VO_3 stoichiometry in the gas phase. More importantly, the role of the V-O-Ti clearly appears to contribute the most to the reactivity of vanadia. The fact that the selectivity in methanol oxidation depends on the substrate reduction state demonstrates the importance of the V-O-Ti bond. Besides the importance of the stoichiometry and reduction state of the support, the structure of the cluster on the surface is important as demonstrated by the stark difference in methanol ODH reactivity between V_2O_6 plus an oxygen adatom and V_2O_7. V_2O_6 plus an oxygen adatom produces methyl formate and V_2O_7 is nearly inactive. The addition of one oxygen adatom at the active site highlights importance in stoichiometry, structure and nature of the V-O-Ti bond.

Indeed, the effects of the support reduction state on the electronic structure of vanadia and their subsequent reactivity has been studied. Several groups have shown that strong interactions between vanadium and defect-free rutile TiO_2 (110) led to drastic changes in the electronic structure, resulting in the reduction of Ti^{+4} to Ti^{+n} and the concomitant

oxidation of vanadium atoms to V^{+2}/V^{+3} [63, 57] These authors attributed the change in oxidation states to a *charge transfer*; as discussed earlier, there is no relation between oxidation state and charge.[39] Investigations by Goodman and co-workers showed that the monotonic increase in the dehydration of ethanol with V deposition coverage correlated with increasing reduction of Ti^{+4} to Ti^{+3} and the appearance of a V d-band near the Fermi level.[64] However, the identity of the reduced Ti^{+3} site and the nature of the active site were not discussed. Unpublished DFT calculations from the Metiu group found that cationic V_2O_6 clusters scavenges electrons from the defective TiO_2 substrate in order to stabilize the formal charge on the two vanadium atoms from +6 to +5. As a result, the substrate Ti^{+3} defects are oxidized to Ti^{+4}. This is reasonable given the cationic charge on these vanadium oxide clusters, although this trend departs from what was found on previous reactor studies on powder catalysts and UHV model catalysts: whereby Ti^{+4} is reduced to Ti^{+3} and vanadium is oxidized to V^{+5} after the catalyst is prepared in a background of O_2 gas.

Given that the selectivity of the V-O-Ti bond is modified by the reduction state of the support, we are now driven to understand the nature of these interactions. This endeavor is central to the research covered in this dissertation. Here-in we will employ variable-temperature STM and temperature programmed desorption/reaction to study the interactions responsible for methanol reactivity on the clean TiO_2 (110) support and how the inclusion of VO^+ clusters modifies this reactivity. We will show that the nature of these interactions are driven by a number of different support defects. In addition, we will uncover the adsorption sites and elementary reaction mechanisms involved in the partial oxidation of methanol on both the bare support and in the presence of VO clusters.

Our ability to prepare model catalysts without modifying the support puts us in a unique position to understand the synergistic effects between the support reduction state and vanadia and the fundamental laws governing methanol oxidation to formaldehyde.

Chapter 2

Principles & Techniques

2.1 The Necessity for Vacuum

In order to resolve many of the complex chemical and physical processes at the catalyst interface, it is imperative that surfaces be free of contaminants, and remain atomically pristine for several hours in-order to carry out experiments. This endeavor to maintain absolute cleanliness will become extremely important for surfaces of interest like TiO_2 when non-chemically specific techniques like scanning tunneling microscopy (STM) are employed. In order to ensure cleanliness pressures around the surface of interest must be kept below 10^{-9} torr, in the ultra high vacuum (UHV) regime, otherwise, surfaces at atmospheric pressure will become contaminated with water and carbonacous species in a matter of nanoseconds.

A quantitative treatment of pressure and surface cleanliness can be understood by invoking the kinetic theory of gases, where the flux (F) of a gas striking the surface is

proportional to

$$F = \frac{n\nu_{avg}}{4}, \tag{2.1}$$

where n is the number density of particles in a gas and ν_{avg} is the average velocity of the gas in the form

$$\nu_{avg} = \frac{8kT}{m\pi}, \tag{2.2}$$

as obtained from the Maxwell-Boltzmann distribution.[65] The variable m is the mass and typically given in SI units. The flux of impinging particles on the surface can be related to the pressure of the particles in the gas phase by relating n to the ideal gas law by

$$n = \frac{N}{V} = \frac{P}{kT}, \tag{2.3}$$

where N is the number of particles, V is volume, P is pressure, k is Boltzmann's constant, and T is temperature, to obtain the Hertz-Knudsen form of the flux equation for a gas,

$$F = \frac{P}{\sqrt{2\pi mkT}}. \tag{2.4}$$

For nitrogen gas ($m = 4.68\times10^{-26}$ Kg) at atmospheric pressure (101,325 Pa) and room temperature ($\sim$ 300K), the flux is equal to 1.19×10^{23} collisions cm^{-2} s^{-1}. For nitrogen gas incident on a typical face-centered cubic metal surface with an atom density of $\sim10^{15}$ atoms/cm^2, and an area of $\sim$1 cm^2, total contamination will be achieved in a matter of 10^{-9} seconds! At typical UHV pressures of $\sim1\times10^{-10}$ torr, a typical metal surface will be completely contaminated in 10^4 seconds or 3 hours. Maintaining UHV thus, is critical to ensuring control over surface related experiments. It should be noted these calculations assume that each N_2 molecule sticks to one metal atom at the surface upon

incidence, though in practice this is not the case with nitrogen at room temperature. This definition of a gas molecule "sticking" is defined by a sticking coefficient s

$$\Theta = 1 - \frac{\sigma}{\sigma_0}, \tag{2.5}$$

between 0 and 1 is dependent on the surface coverage Θ. Surface coverage Θ is defined by the ratio of the number of atoms occupied by adsorbates σ over the number of atoms unoccupied on the surface of the substrate σ_0. From the Hertz-Knudsen equation of flux, a useful definition for gas exposure is given in Langmuirs (L)

$$L = 10^{-6} torr \cdot seconds. \tag{2.6}$$

Langmuir units are used often in the surface science literature and therefore should be committed to memory for convention sake.

2.2 Smalley type Cluster Source

2.2.1 Principles of Laser Ablation

The generation of metal ions by laser vaporization (also known as ablation), is a technique principally based on thermionic emission, whereby a metal target is irradiated with a high powered laser to generate the requisite heat to ionize the interface into a hot plasma of electrons and metal ions. The production of metal ions from laser vaporization therefore is a thermal process that can be modeled by the Richardson-Dushman equation

in the Arrhenius form

$$J_+ = A_P T^2 e^{\frac{-\Phi}{kT}}, \tag{2.7}$$

where J_+ for is the emission current density for positive ions, A_P is an Arrhenius constant, Φ is the work function of the specified metal target, T is temperature, and k is Boltzmann's constant.[66] Generally the material parameter A_P, can be expressed in the form

$$A_P = \lambda A_0, \tag{2.8}$$

where λ is a material specific correction factor is typically ~ 0.5 and A_0 is,

$$A_0 = \frac{4\pi m K^2 e}{h^3}. \tag{2.9}$$

Variables m and e are the mass and charge of the electron, and h is Planck's constant. From the expression above, it is clear that laser vaporization must be equivalent or greater than the bulk Φ of the metal target. In addition the wavelength of light employed for vaporization must be optimized for optical absorption over reflection and depends on the properties of the metal target.

2.2.2 Principles of Nanocluster Formation

Synthesis of well-defined clusters in the gas-phase is typically carried out by sympathetic cooling methods that include a combination of collisional cooling and adiabatic expansion. Collisional cooling is achieved by inelastic collisions exchanged between excited ions and inert gaseous atoms to achieve clustering of various sizes and charges. Physically, this process is described by the transfer of translational (T) and vibrational

(V) energy from the hot ion to the cold, inert gaseous atoms in so-called, T-T and V-T collisions.[67] In the limit cooling is time independent, T-T and V-T energy transfer will increase with the mass of the inert gas. Experiments by Duncan and co-workers showed that collisional cooling with Ne gas created clusters with internal energies colder than with He or Ar as the carrier gas.[68] However, in the limit that collisional cooling is time dependent, as is the case with pulse-delay experiments on the order of tens of μsecs, collisional frequency between hot ions with the inert gas is the critical factor.[68] The speed of the cooling process can be quantified by how efficient heat is conducted from the hot ions to the cold inert gas to the walls of the chamber; also known as heat conductivity. The heat conductivity of common inert gases ranges by an order of magnitude and in the following order: He (156.7 mW/mK)> Ne (49.8 mW/mK) > N_2 (26.0 mW/mK) > Ar (17.9 mW/mK). In addition to collisional cooling, adiabatic expansion (supersonic jet cooling) is employed to further cool clusters to cyrogenic temperatures. When a high pressure gas expands into a vacuum on the order of several decades or more pressure, energy in the gas is lost to work done by the system, resulting in a gas with lower internal energy; this process is called isentropic (dS = 0) gas expansion.

In a typical Smalley-type cluster source seen in Fig 3.4, a pulse of inert gas (msec to μsec typically) entrains the metal rod, followed by a delayed nanosecond pulsed laser (10 - 20 mJ/pulse typically) impinged at a focal point on the rod. At the moment of vaporization, the pressure inside the source body is 1 - 2 atm, and electron temperatures of 10^4 K.[69] Inside the source body, also known as the waiting room, the high density of inert gas (Ar is used in our lab) is sufficient to ensure collisional cooling of the metal plasma. Once metal ions have cooled enough to recombine with other metal ions to form dimers,

trimers and larger clusters, both positive, negative and neutral clusters are present in the source body. Carrier gases can be seeded with small amounts of O_2 or N_2 to obtain metal oxide and metal nitride clusters. It should be noted that supersonic jet cooling of clusters to cryogenic temperatures is fundamental limited by the exothermic nature of condensation. For example, the enthalpic cost of forming V-V bonds (2.75 eV)[70] and V-O bonds (5.68 eV)[71, 72, 73] upon condensation in the gas phase, increases the internal energy of the cluster by their respective bond energies.

2.3 Mass Selection by Magnetic Sector

The filtration of gas phase ions by mass to charge ratio m/z is a rich field among the physics and chemistry community. There are several kinds of mass spectrometers based on very different fundamental principles of dispersion. For example, quadrupole mass spectrometers filter ions by the application of dc and rf-fields to achieve optimal ion trajectories with constant momentum but varying kinetic energy. Conversely, magnetic-sector spectrometers filter ions with uniform kinetic energy but varying momentum by dispersion through a radial flight path. Similarly, time-of-flight mass spectrometers operate with uniform kinetic energy requirements and varying momentum as magnetic sectors, except ions are dispersed over arrival time distributions, as the name suggests. Each type of mass filter has their own advantages and disadvantages that are defined by signal sensitivity, ion transmission, duty cycle, m/z range, mass resolving power and mass accuracy.

For deposition of mass-selected clusters onto surfaces, we require an additional figure of merit; the kinetic energy distribution of the cluster beam. Since experiments are

carried out at the surface/vacuum interface, avoiding fragmentation upon landing the cluster is imperative. Due to the uniform high kinetic energy requirements for magnetic sectors, their kinetic distribution energies are often around (0.5 eV - 2 eV), as well as high mass resolution ($m/\Delta m \sim 1000$ - 3000) as determined by the FWHM of a typical mass spectrum. Magnetic sectors are thus an optimal design for cluster mass-selection and deposition.

The principles of dispersion in the magnetic sector are simple: ions of a mass m_{ion} and charge z are accelerated by an external potential V to a uniform kinetic energy T

$$T_{ion} = zV = \frac{1}{2} m_{ion} v^2, \tag{2.10}$$

and filtered by their momentum. Ions accelerated into the magnetic sector are subjected to a centripetal force F imparted by deflection through the magnetic field B. The relation between centripetal F and the magnetic field B follows,

$$F_{magnet} = z(v \times B) = m\frac{v^2}{r}, \tag{2.11}$$

and is known as the Lorentz force law.[74] In the case where the direction of the cluster ion beam is orthogonal to the magnetic field, the equation now becomes,

$$F_{magnet} = evB = m\frac{v^2}{r}. \tag{2.12}$$

Rearranging eq. 2.12 into the following

$$v = \frac{Bzr}{m}. \tag{2.13}$$

Substituting eq. 2.13 back into eq. 2.10 and rearranging the terms allows for the following,

$$\frac{m}{z} = \frac{r^2 B^2}{2V}. \tag{2.14}$$

We now have a direct relation between the m/z of a desired ion and parameters B *and* V used in the laboratory. For practical purposes the radial flight path r is fixed, as illustrated by the schematic of a typical magnetic sector in Fig 2.1. Thus for the desired ion species to traverse the fixed radial flight path r unimpeded, the ratio of B/V must be nominal.

A mass spectrum of m/z can be obtained with a constant acceleration potential at a fixed path r while sweeping the magnet linearly. The inverse relationship between acceleration potential and m/z, reveals how the transmission of mass-selected clusters depends inversely on the maximum working voltage. In addition, deviations to the acceleration voltage due to ineffective low band pass filters in the power supply will result in deviations to the desired mass and appear in the mass spectrum with larger FWHMs. The mass resolution of the magnetic-sector is ultimately defined by the adjustable slit width of the allowed ion flight path Δr before ions enter the electromagnet.

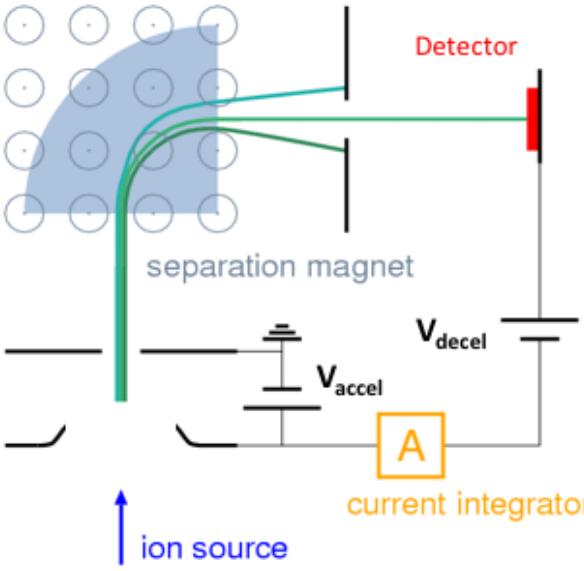

Figure 2.1: Magnetic Sector Schematic: Ions are accelerated to a uniform kinetic energy by a high voltage potential, typically 1 kV - 10 kV before entering the magnetic sector. Ions are subsequently filtered by their momentum and charge by traversing a specified flight path r. Ions exiting the magnetic sector are decelerated to achieve a uniform kinetic energy distribution prior to deposition onto a sample.

2.4 Temperature Programmed Desorption/Reaction

The approach to measuring surface kinetics at surfaces follow the same procedures typically used in solution-phase chemistry; that is to measure the rate of consumption of a gas-phase reactant and the production of gas-phase products as a function of time. Kinetic experiments can extract information on reaction activation barriers, turn-over-frequency (TOF), and reaction mechanisms. However, unlike traditional kinetic experiments, elucidating surface kinetics are obfuscated by the anisotropy of surfaces, as determined by different binding sites, defects, surface reconstructions, and the complexities associated with adsorption (non-dissociative versus dissociative adsorption). Therefore to accurately model surface kinetics, experiments must be carefully designed to take into account the local configuration of the adsorbates and knowledge of their respective occupation of a specified surface site.

The rate of chemical processes can be described by the Polanyi-Wigner equation. In the interest of studying surface reactivity, we will apply the rate equation to the rate of desorption r_{des} for chemical reactants and products. In the most general form, the Polanyi-Wigner equation can be written in the form

$$r_{des} = -\frac{\partial\theta}{\partial t} = \nu_n \theta^n exp(-\frac{E_{des}}{RT_s}), \tag{2.15}$$

where ν_n is the pre-exponential factor for the observed chemical process of order n, E_{des} is the desorption energy needed to eject the chemical species into the gas-phase, T_s is the surface temperature, and R is the ideal gas constant. The term θ is the number of surface atoms, but can substituted by an absolute coverage $\sigma = \sigma_0\theta$, if the absolute

coverage is known from other quantitative measurements. For the case of a monoatomic gas or physisorbed molecules, the absolute rate of desorption can be rewritten in terms of absolute coverage and the rate constant, k_{des} in the form,

$$r_{des} = \sigma_0 \theta k_{des}. \tag{2.16}$$

for which the rate constant is first-order and can be written in the Arrenhius form:

$$k_{des} = Aexp(-\frac{E_{des}}{RT_s}), \tag{2.17}$$

where A is the pre-exponential factor.

The rate constant for first-order desorption however is only valid for surfaces with homogenous binding energies, and assumes no adsorbate-lateral interactions. Furthermore first-order desorption rates do not take into account strong adsorbate interactions with the substrate, such as dissociation or precursor-dissociation, nor adsorbate-induced changes to the substrate surface structure. For rate constants larger than order $n > 1$, such desorption parameters A and E_{des} change as a function of adsorbate coverage (θ) in the form,

$$k_{des} = A(\theta)exp(-\frac{E_{des}(\theta)}{RT_s}). \tag{2.18}$$

Often, A and E_{des} vary in concert monotonically with adsorbate coverage and surface structure. Reports from Cardillo and Tully attributed this so called- *compensation effect* in A and E_{des}, to the equilibration of surface and gas-phase chemical potentials in the phase transition from a monolayer adsorbate to the gas phase.[75] The *compensation effect* can be easily observed by the intrinsic design of TPD experiments discussed below.

Temperature programmed desorption (TPD) utilizes variable heating and a quadrupole mass spectrometer (QMS) to obtain a desorption spectrum of adsorbate m/e ratios to extract kinetic parameters such as r_{des}, A and E_{des}. This surface-sensitive technique relies on the pressure and pumping speed of the vacuum pumps S, employed during the experiments to be sufficiently fast that the rate of desorption r_{des} *(t)* for a gas from the surface is proportional to the change in partial pressure of the gas $\Delta\ p$

$$\Delta p = p - p_{ss}, \tag{2.19}$$

where p_{ss} is the steady-state pressure in the chamber. This is *important* to note that the signal representing the partial pressure for the analyte of interest is detected by the cracking fragments from the QMS as the different between a baseline signal at that particular base pressure in the chamber and the desorbed gas pressure. A relationship between pressure changes for each mass and the rate of desorption can be written as a differential equation in the form,

$$V\frac{d\Delta p}{dt} + S\Delta p = kT_g A_s r_{des}(t), \tag{2.20}$$

where constants A_s is the area of the substrate, T_g is the gas temperature and k is the desorption rate constant. At high pumping speeds, the first term in the pressure differential equation is negligible, thus $\Delta\ p$ is directly proportional to r_{des} *(t)*. Since the substrate temperature T_s is ramped linearly with a specified heating rate β, in the form

$$T_s = T_0 + \beta t, \tag{2.21}$$

where T_0 is the substrate temperature at t = 0, integrating over a desorption spectrum for one mass over all time (t) will yield

$$A_p \propto \frac{S}{A_s k T_g} \int_0^\infty \Delta p dt = \int_0^\infty r_{des} dt = \sigma \tag{2.22}$$

where the peak area A_p or a sum of many peak areas in a TPD spectrum is proportional to the adsorbate coverage. Thus the coverage for a particular peak for anytime between t = 0 and t= i within a spectrum can be determined. Absolute coverages can be found for TPD signals if the initial coverage is known from a quantitative technique such as STM and XPS.

Surface kinetic parameters can be extracted from a TPD spectrum by substituting the linear temperature ramp equation into the Polyani-Wigner equation for desorption to yield,

$$\frac{E_{des}}{RT_p^2} = \frac{n\nu^n}{\beta}\theta_p^{n-1} exp(-\frac{E_{des}}{RT_p}). \tag{2.23}$$

where the reaction order is generalized by $n = 1$ for first-order and 2 for second-order. From transition-state theory, the pre-exponential factor ν, represents the entropic contributions to the total free energy of the adsorbate of interest, and usually ranges between $10^{11\text{-}13}$ and $10^{7\text{-}10}$ for first-order and second-order reaction. In practice, ν is either assumed, or experimentally determined by varying the heating rate β and holding the adsorbate coverage fixed for multiple TPD runs. Accurate determination of the E_{des} and reaction order can be found by taking multiple TPD spectrums as a function of initial coverage and surface temperature and fitting the data to a linear slope proportional $-E_{des}/R$. However these experiments are tedious and extremely difficult to obtain when

the sample requires long depositions of mass-selected clusters. Instead, Redhead showed an approximation for E_{des} can be found if the pre-exponential factor is known or assumed. Implicit in Redhead's equation is the assumption that the reaction is first-order and in the form,

$$E_{des} = RT_p[ln(-\frac{AT_p}{\beta}) - 3.46]. \tag{2.24}$$

Redhead's equation is often used as a rule of thumb, with deviations between 10 - 20 % from more accurate analysis.

2.5 X-ray Photoelectron Spectroscopy

X-ray photoelectron spectroscopy (XPS) is a common, yet powerful analytical technique that is widely used in the semiconductor and catalysis industry. The technique relies on the fundamental principles of the photoelectric effect to obtain information about the chemical oxidation state and energy distribution of electrons in a material. Since each element in a material has a unique energy distribution associated with their electronic structure, XPS is elemental-specific. In addition, with careful experimentation and knowledge of the analyte of interest at the surface, XPS can obtain chemical-specific information pertaining to the surface analyte's charge, bonding environment and size. The skin-depth penetration of X-rays and their subsequent photo-ejection of electrons is roughly 100 Åor less, making XPS an extremely surface-sensitive technique. It should be noted that other excitation sources can be used to generate photoelectron emissions from a material, including ultra-violet photons and highly mono-energetic electron beams.

Generally, the photoelectron effect begins with excitation of core-level electrons in a sample by X-ray irradiation ($h\nu$), followed by emission of electrons (see Fig 2.2) with discrete energy levels proportional to the sample's electronic structure, also known as binding energies (E_b). In theory, the sample binding energies are determined by the sample's workfunction Φ_{sample}, defined as the difference between the sample vacuum level (${E_V}^{\text{sample}}$) and the Fermi level (E_F). The sample E_b is determined by measuring the momentum of photo-ejected electrons (photoelectrons) and calculating the sample (${E_K}^{\text{sample}}$). In practice ${E_K}^{\text{sample}}$ is measured by the kinetic energy of the photoelectrons with respect to the frame of the spectrometer (${E_K}^{\text{spec}}$). Like the sample, ${E_K}^{\text{spec}}$ is determined by the spectrometer workfunction (Φ_{spec}), and vacuum energy (${E_V}^{\text{spec}}$). Since both the sample and spectrometer workfunctions are required to determine the kinetic energy of the photoelectron by the relation,

$$ {E_K}^{\text{spec}} = {E_K}^{\text{sample}} - (\Phi_{spec} - \Phi_{sample}), \tag{2.25} $$

the E_F must be the same. Typically, the sample on the manipulator is floating respect to the chamber ground and therefore does not share the same E_F as the spectrometer. Since the spectrometer is electrically connected to chamber ground, the sample on the manipulator must be electrically grounded by connecting the manipulator sample pins to the chamber chassis via alligator clips. Once ${E_K}^{\text{spec}}$ is measured, the E_b can be determined with a known x-ray radiation source and calibrated Φ_{spec} by the relation,

$$ h\nu = {E_K}^{\text{spec}} + E_B + \Phi_{spec}. \tag{2.26} $$

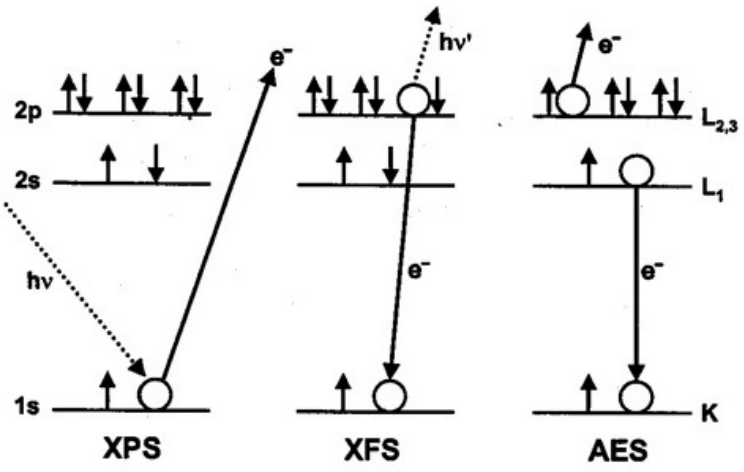

Figure 2.2: Depiction of the various photoelectron processes that occur after excitation by x-ray absorption or highly energetic electron collision.

Calibration of Φ_{spec} is typically performed by measuring a large range of binding energies (1000 eV) between small peaks of Au or Pt foil (or clean and sputtered single crystals is better) near the Fermi energy and large binding energies from Cu samples. A well calibrated Φ_{spec} will yield a precision of $\pm 5\%$ typically in XPS, with a detectable limit of 0.1 % ML, and therefore is an excellent method for both qualitative and quantitative analysis. While XPS can detect the elements as small as light as Lithium at the limit for large analyte coverages, the sensitivity of XPS for analyte coverages at the small coverage limit is highly dependent on the element photoionization cross section. For elements smaller than $Z \leq 25$, the sensitivity decreases and therefore careful choice of the analyte coverage must be considered before an experiment with XPS is performed. In addition, secondary electron relaxation processes from outer electron shells result in emission of X-ray fluorescence and Auger electrons, which are the subject of other elemental surface science techniques. All of these electron processes occur with varying degree of probability upon x-ray absorption.

2.6 Auger Electron Spectroscopy

Auger electron spectroscopy (AES) is another method of surface elemental analysis, and often used complementarily with XPS. AES relies on a secondary-electron relaxation process called the Auger effect (see Fig 2.2);where-by a core-shell electron is excited and ionized. An unstable vacancy in the core-shell orbital allows for the favorable transition of an outer-shell electron to fill the core-shell vacancy. The energy emitted by the electronic transition excites secondary outer-shell electron with an energy greater or equal to the ionization energy of the outer shell. With a mean free-path between 4 Å- 40 Å, in solids, Auger electrons are typically ejected with kinetic energies of 10 eV - 1000 eV. Determination of Auger electron kinetic energies are carried out the same way described in the previous XPS section. In practice, the ejection of excited core level electrons is done via a highly monoenergetic, collimated electron beam (typically 2 - 3 kV). Auger relaxation is inherently a low probability method that decreases with drastically for elements of atomic number $Z = 30$ and greater.

2.7 Scanning Tunneling Microscopy

Unlike the ensemble-based techniques described above, the scanning tunneling microscope (STM) is capable of obtaining local real-space images with sub-atomic resolution. The technology required for the STM was invented in 1982, for which Binning and Rohrer shared two-thirds of the 1986 Nobel prize in physics. The essence of the instrument is simple; a single atomically sharp metal electrode tip is brought within a distance of $\leq$ 10Å from the plane of a conducting sample, whereby an applied voltage between the tip junction results in a current. The electrode tip is raster scanned across the sample to

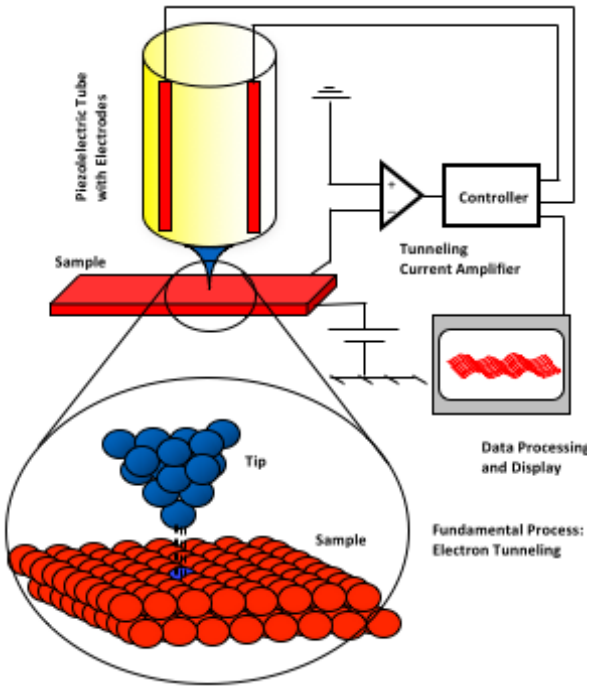

Figure 2.3: Schematic diagram of the STM electrode tip attached to a piezo-electric scan tube held at a floating ground. The metal contacts on the scan tube are electrically connected to the output of the control unit. Current at the tip-sample junction is amplified by an I-V converter and instrument amplifier, and subsequently read at the ADC input of the controller unit.

obtain current as a function of (x,y,z) locale and voltage V. A schematic of the STM is illustrated in Fig 2.3.

Spatial control at the atomic level is achieved by fitting the electrode tip to the inside of a lead zirconium titanate piezo-electric scan tube. Lead zirconium titanate is particularly used in STM designs due to it's high piezo-electric response and high poling efficiency. Height $\pm$ z control is achieved via a single metal contact fitted inside the piezo-electric scan tube and electrically isolated from the metal tip. In addition, metal contacts attached to the outer piezo tube and divided into four quadrants are employed for lateral $\pm$ x,y motion.

When the distance (z) between the tip and sample approaches the scale of $\leq$ 10Å, sub-Ångstrom sensitivity to sample topography becomes possible. This exponential sensitivity between current I and height z is the result of electrons quantum tunneling through vacuum between the metal tip and sample. Quantum tunneling in STM involves the transmission of the electron from the tip (sample) through a potential energy barrier to the sample (tip). The potential barrier in this case, is the vacuum junction between the tip and sample. By treating the potential barrier as a square, the probability of transmission of the electron through the potential barrier can be modeled with the assumption that the electron wavefunction exponentially decays to zero. Solving the Schrödinger equation in 1D and calculating the transmission probability T through the potential barrier yields the familiar functional form $T \sim exp(-2ks)$ where s is the barrier width and k is the decay constant in inverse Å^{-1} units.

To calculate total tunneling current, a rigorous definition of the sample and tip relative energies and their respective electronic structures are required. The most common derivation is based on Bardeen's seminal paper[76], with modifications by Tersoff and Hamann[77, 78], provides a thorough foundation for modeling tunneling current and interpreting scanning tunneling micrographs. For the case of a metal tip in close proximity to the sample ($\leq$ 10Å), the electron chemical potential, or Fermi level E_F of the system is in thermal equilibrium, resulting in negligible electron tunneling across the vacuum gap. To tunnel electrons from the tip to the sample, the process must be thermodynamically favorable, whereby the E_F of the tip is greater than the sample E_F. A diagram of the system in Fig2.4 illustrates the relative energy levels of the tip and sample.

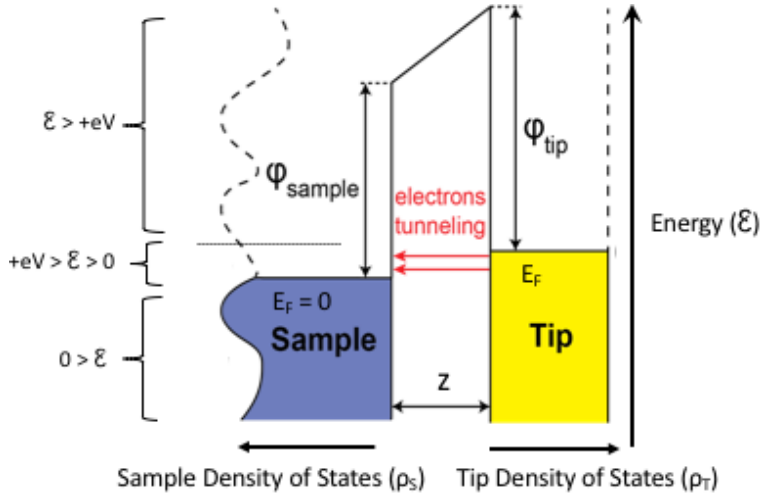

Figure 2.4: Energy diagram of the tunnel junction as a function of tip and sample density of states. Although the tip is virtual ground, the sample Fermi level is typically zero for reference

The tip to sample tunneling current $I_{\mathrm{T}\to\mathrm{S}}$ is derived from time-dependent perturbation theory to yield the familiar expression for Fermi's Golden Rule,

$$I_{T\to S} = -2e \cdot \frac{2\pi}{\hbar}|M|^2 \rho_T(\varepsilon - eV) f(\varepsilon - eV) \rho_S(\varepsilon)[1 - f(\varepsilon)]. \tag{2.27}$$

The sample E_F is set to zero for reference. It should be noted that the current is multiplied by a factor of 2 to account for the two spin states of the electron. At high temperatures, fluctuations in the energy results in some electrons tunneling from the sample to the tip $I_{\mathrm{S}\to\mathrm{T}}$ to yield

$$I_{S\to T} = -2e \cdot \frac{2\pi}{\hbar}|M|^2 \rho_T(\varepsilon - eV) \rho_S(\varepsilon) f(\varepsilon) \rho_T(\varepsilon - eV)[1 - f(\varepsilon - eV)]. \tag{2.28}$$

where $|M|^2$ is the tunneling matrix $|\langle f|H'|i\rangle|^2$. For the case of a positive bias, the system favors tunneling from the initial occupied state $|i\rangle$ of the tip to the unoccupied final state $\langle f|$ state of the sample. The density of states for the sample are denoted by ρ_{S} and ρ_{T}.

The Fermi distribution,

$$f(\varepsilon) = \frac{1}{1 + exp(\varepsilon/k_B T)}, \tag{2.29}$$

of the tip and sample are represented by *f(ε)* for occupied states and *f(1-ε)* for unoccupied states. Only occupied states of the tip in the energy range between ε and eV will contribute to the tunneling current, as denoted by the corresponding tip Fermi function and ρ_{T}. The total current I_{total} thus can be found by summing and integrating the two components of the current to yield,

$$I_{total} = \frac{-4e\pi}{\hbar} \int_{-\infty}^{\infty} |M|^2 \rho_S(\varepsilon) \rho_T(\varepsilon - eV)[f(\varepsilon - eV)(1 - f(\varepsilon)) - f(\varepsilon)(1 - f(\varepsilon - eV))]d\varepsilon. \tag{2.30}$$

The expression for I_{total} can be simplified by considering the conditions for our STM experiments were recorded at $T = 298$ K ($K_B = 0.026$ eV), the Fermi distribution will to have sharp cut-off energies compared to the band gap (3 eV) for n-doped rutile TiO_2 (110). Therefore the Fermi distribution can be treated as a step function over three distinct domains:

1. For the case $\varepsilon >$ eV, f(ε - eV) and f(ε) ~ 0. Therefore the Fermi energy expression for the total current I_{total} will be, f(ε - eV)[1 - f(ε)] - f(ε)[1 - f(ε - eV)] = 0

2. For the case eV $> \varepsilon > 0$, f(ε - eV) ~ 1 and f(ε) ~ 0. Therefore the Fermi energy expression for the total current I_{total} will be, f(ε - eV)[1 - f(ε)] - f(ε)[1 - f(ε - eV)] = 1

3. For the case $\varepsilon < 0$, f(ε - eV) and f(ε) ~ 0. Therefore the Fermi energy expression for the total current I_{total} will be, f(ε - eV)[1 - f(ε)] - f(ε)[1 - f(ε - eV)] = 0.

Since the total tunneling current is only valid in the energy range, eV $> \varepsilon >$ 0 for positive bias bias polarity, the expression I_{total} can be reduced to

$$I_{total} = \frac{-4e\pi}{\hbar} \int_0^{eV} |M|^2 \rho_S(\varepsilon) \rho_T(\varepsilon - eV) d\varepsilon. \tag{2.31}$$

Similarly, if a negative bias was used in our STM experiments, the I_{total} would only be valid for 0 $> \varepsilon >$ -eV.

For scan probes comprised of Tungsten or PtIr, the ρ_{T} is conveniently flat within the scan parameters used for this thesis (Hoffman Thesis). The ρ_{T} can be checked by scanning tunneling spectroscopy on an inert substrate, such as Au (111), over the relevant scanning parameters that are to be used in topography experiments. The use of a tip that is featureless of the relevant scan parameters drastically simplifies the interpretation of the features imaged by STM. By treating ρ_{T} independently from the energy of the system, the expression for total current becomes

$$I_{total} = \frac{-4e\pi}{\hbar} \rho_T(0) \int_0^{eV} |M|^2 \rho_S(\varepsilon) d\varepsilon. \tag{2.32}$$

In his theory of tunneling, Bardeen showed that under realistic conditions, $|M|^2$ is independent of the total system energy, based on the assumption that ρ_{T} and ρ_{S} are independent, and that the tip and sample wavefunctions exponentially decay to zero in the tunnel barrier.[76] Furthermore, for large enough tunnel barriers, the overlap density of the tip and sample wavefunctions will be negligible. The I_{total} can be expressed as

strictly an integral over of the sample density of states,

$$I_{total} = \frac{-4e\pi}{\hbar}|M|^2\rho_T(0)\int_0^{eV}\rho_S(\varepsilon)d\varepsilon, \tag{2.33}$$

where the other terms are evaluated as constants.

The term $|M|^2$ is evaluated by assuming the tunnel barrier is a square potential, and using the WKB approximation where $|M|^2 = \mathrm{e}^{-2\gamma}$. In potential barrier will have a sloped shape proportional to the applied voltage bias and the work function of the tip and sample (see Fig 2.4. The advantage of the WKB approximation is the variable dependence on $|M|^2$ on the tunnel barrier width z, expressed as an integral,

$$\gamma = \int_0^z \sqrt{\frac{2m\varphi}{\hbar^2}}dz = \frac{z}{\hbar}\sqrt{2m\varphi}, \tag{2.34}$$

where φ is typically treated as the average work function of the tip and sample. The average work function can be found experimentally from the familiar exponential decay expression,

$$I \propto e^{-2z\sqrt{2m\varphi}}, \tag{2.35}$$

by varying the tunnel gap z periodically, $z = z_0 + Acos(2\pi ft)$, and measuring the resulting changes to $ln(I)$ via a lock-in amplifier. The average work function measured by *I-Z* spectroscopy however, is influenced by the relative applied voltage. Thus, an apparent work function φ_{ap} is measured, where the sample and tip work functions are related by the expression,

$$\varphi_{ap} = \frac{1}{2}(\varphi_S + \varphi_T - |eV|). \tag{2.36}$$

One limitation in the measurement for φ_{ap} assumes the periodic change in the tunnel gap ds, is constant over one cycle, which today remains a point of contention among the STM community.(refs) Substituting $|M|^2$ for the WKB approximation, the expression for I_{total} becomes

$$I_{total} = \frac{-4e\pi}{\hbar} e^{-2z\sqrt{2m\varphi_{ap}}/\hbar} \rho_T(0) \int_0^{eV} \rho_S(\varepsilon) d\varepsilon, \tag{2.37}$$

for empty-state tunneling. The limits of integration are reversed for filled-state tunneling.

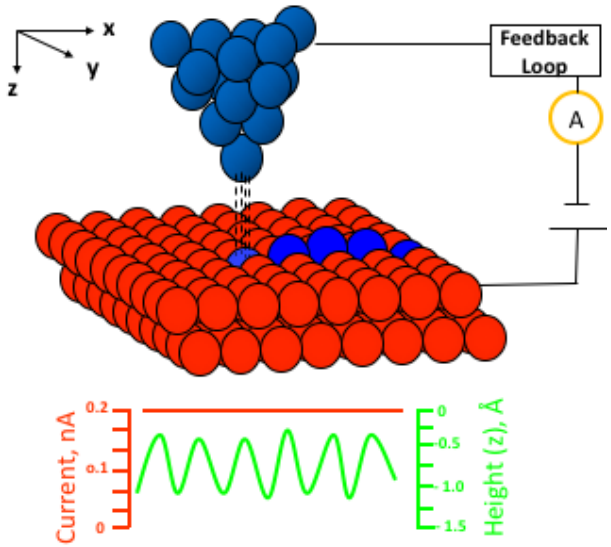

Figure 2.5: The total current is set to I = 0.2 nA (red), and is kept constant in the feedback loop via adjustments to the piezo scan tube. The voltage required to adjust the piezo scan tube in the (z) direction (green) is mapped as topography.

Topographic information from scanning tunneling micrographs can be extracted, however, not without careful consideration of the sample composition. Since the I_{total} signal at a given voltage, depends on both the tunnel gap distance z and ρ_{S}, obtaining and interpreting the topography of a conducting surface is non-trivial. In other words, how

does a microscopist distinguish between features due to changes in sample height and features due to changes in the ρ_S?In order to decouple electronic effects from topographic effects, a feedback loop in the I-V amplifier is employed to maintain a set constant current via adjustments to the piezo scan tube in the (z) direction.[79] The voltage signals required to maintain the piezo scan tube is recorded and mapped as the topography, while the total current signal remains nearly constant, see Fig 2.5. One major caveat to constant-current STM is that the micrographs strictly represent the apparent surface topography for a given contour of the $\rho_S(\varepsilon)$, where $\varepsilon = E_F + eV$. Thus, topography images are subject to change, depending on the applied bias. Interpretation of the topography is particularly problematic for non-monatomic semiconductors, where the ρ_S is highly localized in both the energy domain and real-space domain. Understanding topography images are inexorably linked to the sample ρ_S will become pertinent for the interpretation of TiO_2 surfaces discussed in Chapter 4.

Chapter 3

Surface Science Apparatus

3.1 Overview of Apparatus

The apparatus is a home-built instrument designed to interrogate the intricacies of supported heterogeneous catalysts at the atomic level. We are motivated by the fact that most of the supported catalysts have ill-defined composition of metal and metal-oxide particles and many different types of local bonding and geometries. As a result, elucidating a structure-function relationship of supported catalysts is difficult in other groups. To resolve the nature of supported catalysts, the apparatus is uniquely equipped with a Smalley-type ion-cluster source in combination with a suite of surface science techniques to probe the reactivity and structure of catalysts with atomically-precise composition and well-defined surface structure.

The apparatus can be organized into three separate sections with distinctive functions, given in order of descending vacuum pressure: (i) the Smalley-type cluster source, (ii) the ion acceleration and magnetic filter section, and (iii) two UHV chambers for cluster depo-

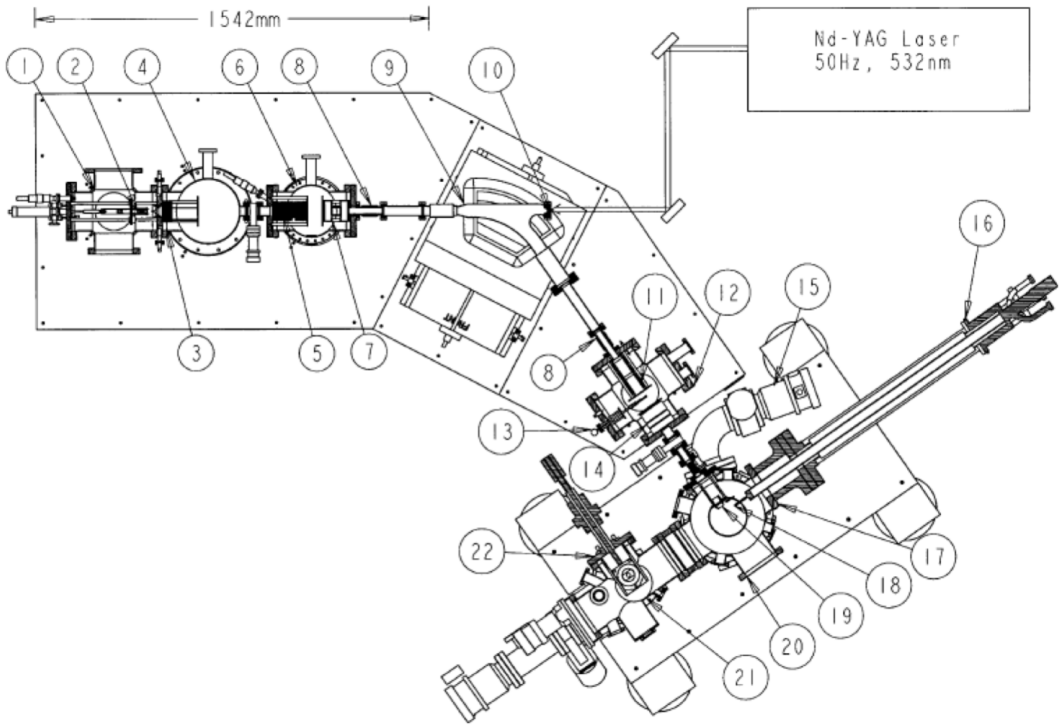

Figure 3.1: Overall view of instrument (drawn to scale). The absolute dimension of the laser vaporization source and associated pumping/expansion region is indicated: (1) source chamber; (2) cluster source (see Fig. 2); (3) first einzel steering lens; (4) diffusion pump chamber; (5) second einzel/steering lens; (6) acceleration chamber; (7) acceleration/focus lens (see Fig. 3); (8) ceramic break; (9) magnet flight tube; (10) laser entrance window; (11) deceleration/y focus lens; (12) deceleration/collector chamber; (13) moveable detector; (14) z focus/steering lens; (15) turbo pump; (16) cryo-manipulator; (17) deposition chamber; (18) sample holder stage; (19) final focus lens; (20) Auger; (21) microscope chamber; (22) microscope. Reproduced with permission from International Journal of Mass Spectrometry, Vol. 254, 2006, p. 204.

sition, sample preparation and characterization purposes. A diagram of the apparatus is illustrated in Fig 3.1, and labeled in descending order of pressure from the cluster source to the UHV-STM chamber. From the cluster source down to the deposition chamber, nearly nine decades of pressure differential is present during deposition conditions. Maintaining vacuum in the *molecular flow regime* is critical to the conductance of ions from the cluster source to the UHV chambers, and ensures the integrity of the cluster from contamination and collision-induced dissociation. To be in the *molecular flow regime*, the mean free path λ of a particle must be larger than the dimensions of the apparatus. Using the expression for the mean free path at T = 298 K,

$$\lambda = \frac{k_B T}{\sigma P \sqrt{2}}, \tag{3.1}$$

a quick calculation for Ar, with a collisional cross-section σ=0.36 nm, under deposition conditions ($P_{\text{cluster source}} = 1\times10^{-6}$ Torr and $P_{\text{collection chamber}} = 5\times10^{-9}$ Torr) will have a λ between $\sim$ 55 m-10.8 km. Since the mean free path of Ar is much greater than the path length from the cluster source to the UHV deposition chamber, roughly $\sim$2.5 m, the vacuum pressure is considered to be in the *molecular flow regime*.

Each chamber in the apparatus maintains a specified base vacuum pressure by a suite of pumps listed in Fig 3.2). It is important to understand that each pump in the apparatus was chosen for a specific utility in the pump down and maintenance of vacuum in the molecular flow regime. Moreover, pumping speed and compression ratios for each pump were carefully considered for the needs and applications in each chamber. For example, the helical grooved turbomolecular pump, due to its capability in maintaining optimal constant pumping speed in pressures up to 10^{-2} Torr, and inlet compression up to several

Chamber	Pump Type	Backing Pump	Base Pressure (Torr)
Source	Osaka TS440 440 L/s helical grooved turbomolecular pump	Edwards E2M40 44 m3/hr rotary pump	2×10^{-7}
First Differential Pumping	Edwards 250 M diffusion pump	Edwards E2M40 44 m3/hr rotary pump	4×10^{-9}
Acceleration	Osaka TG1133M 1100 L/s turbomolecular pump	Edwards E2M28 36 m3/hr rotary pump	1×10^{-9}
Intermediate Collection	Osaka TG413M 430 L/s turbomolecular pump	Edwards E2M28 36 m3/hr rotary pump	1×10^{-9}
Deposition & Characterization	Osaka TH261M 235 L/s turbomolecular pump; Varian Vaclon 300 L/s Ion pump	Edwards GVSP30 36 m3/hr scroll pump; none	3×10^{-10}
STM	Osaka TH261M 235 L/s turbomolecular pump; Varian Vaclon 300 L/s Ion pump	Edwards GVSP30 36 m3/hr scroll pump; none	5×10^{-11}
Gas Manifold	Osaka TG56 50 L/s turbo pump	Edwards XDS5 5m3/hr scroll pump	5×10^{-6}

Figure 3.2: List of Pumps and their respective function for each chamber. The base pressure is under optimal conditions and not while under laser ablation conditions.

Torr, was employed to handle high gas loads in the cluster source chamber. Another example, is the use of a momentum-transfer pump, such as the diffusion pump housed in the first differential pump section of the apparatus. Pump action by momentum transfer between collisions of oil jet-streams with gases in the chamber makes the diffusion pump optimal for compressing lighter gases such as Ne and He. In fact, the lighter the mass of the contaminants, the greater the pump speed will be. The advantage of a diffusion pump over a turbo pump is most acutely observed in our lab during a deposition of clusters seeded with He gas, where we find the $P_{\text{differential chamber}}$ is two orders of magnitude lower than $P_{\text{collection chamber}}$. A third example is the dry scroll pump, such as the Edwards GVSP30, that is employed in the foreline for both UHV chambers, to avoid back-streaming and contamination of oil pump vapor typically seen in rotary vein oil pumps.

3.2 Smalley-type Cluster Source

The Smalley-type cluster source is named after the inventor, Professor Richard E. Smalley, and was designed with the purpose of investigating the formation and stability of carbon allotropes in interstellar environments. His discovery of a new allotrope of carbon- the so-called fullerene (C_{60}) would later yield Richard Smalley the Nobel Prize. It should be noted that the ion-cluster source is among several different types of sources reported in the literature for the *facile* production of clusters. Modern methods for producing clusters rely on either high voltage pulsed arc expansion, highly energetic sputtering (30 kV) with heavy gases (Kr^+), or magnetron plasma sputtering to produce continuous cluster beams[]. The Smalley-type cluster source takes advantage of high-powered pulsed lasers to vaporize metal sources with even the most refractory properties at room temperature, to produce cluster beams with tight energy distributions (1 eV - 10 eV). The plasma from laser ablation produces both neutral, positive and negative ions, allowing for either charged ion to be conveniently extracted. For this lab, only positive ions are extracted. It should be noted that the choice for a cluster source depends on the desired experiment; for surface science experiments, deposition of intact clusters requires the kinetic energy distribution be less than or equal to the energy of the interatomic bonds (on the order of several eV or less per cluster). The kinetic energy distribution for magnetron sputtering and pulsed arc expansion are less than desirable due to their kinetic energy spread having $\geq$ 10 eV spread (refs).

The cluster source is housed in a 5-way cross shaped chamber with a tube diameter of 6". The entire cluster assembly is stabilized on several rods mounted to an ISO 160 flange for easy removal from the chamber. The cluster source plugs into four stainless steel rods

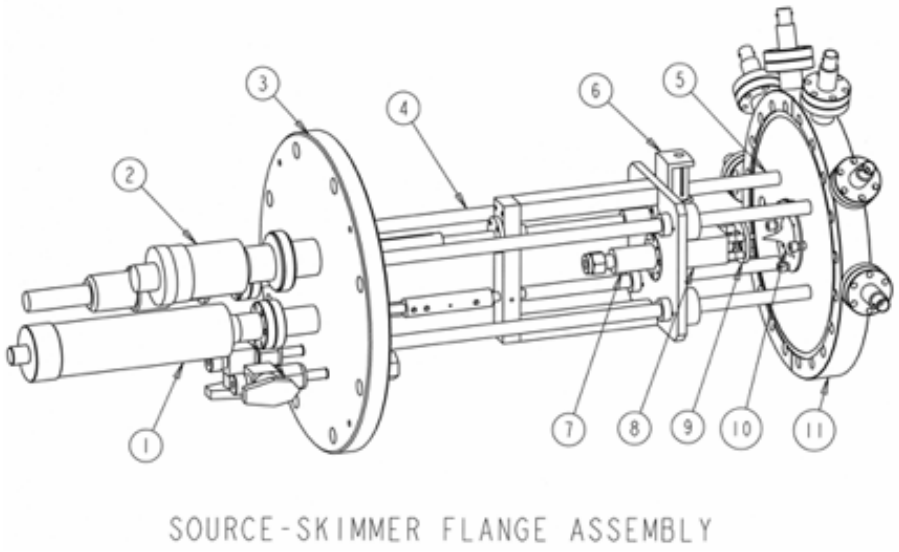

Figure 3.3: Cluster Source Assembly Diagram: (1) Sample rotary drive motion feed through; (2) source linear position feed through: (3) ISO 160 source mounting flange (all source conncections are made here): (4) source linear position guide rods: (5) Source locating posts (on skimmer flange): (6) rotation/translation mechanism; (7) pulsed valve: (8) source body ($\sim$ 1 cm^3): (9) focusing lens: (10) skimmer: (11) skimmer flange. Reproduced with permission from International Journal of Mass Spectrometry, Vol. 254, 2006, p. 204.

on the skimmer flange for easy alignment with the path of the laser. An overview of the cluster source assembly can be found in Fig 3.3. The source rod rotates and translates vertically by a rotary-drive motion feedthrough to ensure maximum surface area exposure to laser ablation. During depositions, the source rod can last typically 8-10 hours and can be easily replaced and pumped back down in under 2 hours. To achieve clustering of metal ions in the source, a magnetically driven solenoid pulse valve (General Valve, Series 9) introduces seed gas (typically Ar or He) into the source body to entrain the metal source rod. The backing pressure of the seed gas has been found to have no effect on cluster formation. The advantage of the source body is greater thermalization of the hot metal plasma by confining the plasma to a small volume (~ 1 cm^3) that ensures greater collisional frequency of the plasma with the carrier gas and the source body walls.

Laser ablation is achieved with the green (532 nm) light of a Nd:YAG laser (Spectra Physics, Lab Pro 290; 500 mJ/pulse at 50 $\pm$ 5 Hz). The power output of the laser, in Q-Switch mode, is more than enough for our experiments. A 1500 mm focal length plano-convex single lens is employed to focus the green light down the entrance window of the magnetic sector, through the exit nozzle and onto the metal rod with a typical spot size of ~ 0.5 mm. To optimize ion-current, a delay schema is employed (see Fig 3.4) between the onset of the pulsed gas and the delay of a laser pulse. The delay schema is executed by a function generator (SRS Model DS335) to initially trigger a home-built pulse-valve driver, operating with a square-wave (4 V amplitude) input at 55 Hz, and as a reference in the laser pulse delay (max 1 ms delay). The laser pulse delay is adjustable by a delay generator (System Donner 101 Pulse Generator), and is singularly, the most critical parameter to optimizing ion-current. In addition, ion current can be optimized

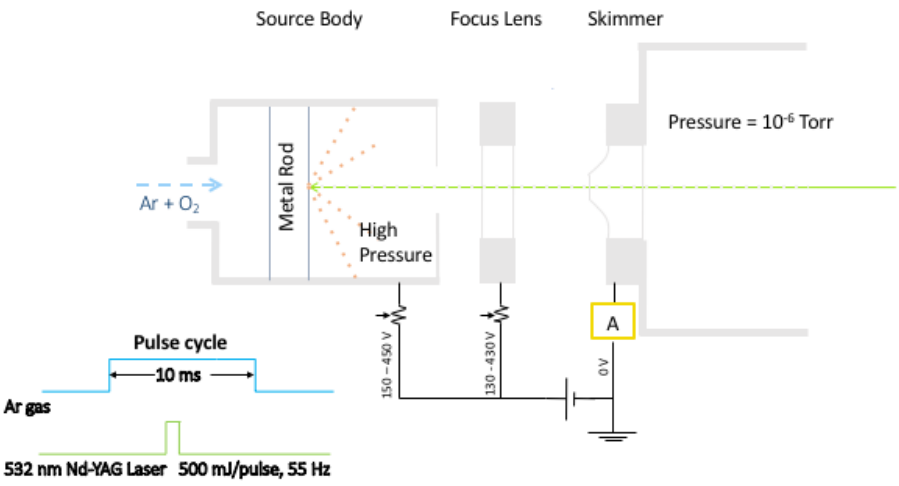

Figure 3.4: Cluster Source Schematic:

by adjusting the pulsed gas width with a 10-Turn potentiostat on the pulse-valve driver; this parameter is critical in the sense that if the pulse width is too narrow, ion current will be negligible, and if the pulse width is too wide, the pulse-valve will flood the cluster source above the *molecular flow regime*.

Ion optics in the cluster source (see Fig 3.3) attenuate turbulence and ensure extraction and collimation of well-defined cluster beams. The source body is biased with a positive potential with respect to the skimmer, held at ground virtual ground (0 V), to extract positively charged clusters; this DC potential will be referred to as the extraction voltage. Ions are collimated into a beam by a focus lens (ring-shaped electrode), biased at -10 to -20 V below the set extraction voltage. The ions extracted between the biased source body and the skimmer can be thought of as a closed circuit, allowing the skimmer to act as ammeter in addition to skimming ions into a well-defined ion beam. A circuit diagram of the ion optics in the cluster source is illustrated in Fig 3.4. The extent of larger cluster formation can also be optimized by extending the distance between the exiting nozzle and

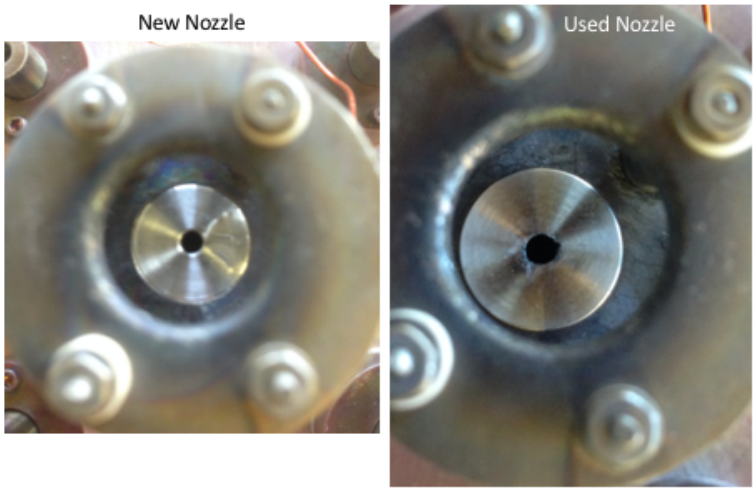

Figure 3.5: Picture of a brand new nozzle installed (left) versus a nozzle used over many depositions (right). The damaged nozzle has a couple notches visible on the edges of the bore. The damage to the bore of the nozzle is likely due to slight misalignment of the Nd:YAG laser during depositions.

the metal rod, allowing for more collisional cooling and condensation between metal ions and the carrier gas. The copper wire connection between the focus lens and the waiting room is also electrically isolated from ground and should be checked with a multimeter for isolation between periods of swapping out the source rod. The source body also consists of a replaceable exit beam nozzle of fixed bore (0.5983" diameter) and length (0.4"). The exit beam nozzle is critical for achieving narrow supersonic beam velocity distributions, as well as jet-cooling the clusters via adiabatic expansion. Damage to the nozzle bore will result in wider velocity distributions and ultimately wider mass spectra as the kinetic energy of the clusters will be wider prior to dispersion in the magnetic sector. The degree of damage to a nozzle are illustrated in Fig 3.5.

Following the skimmer, the first set of einzel/steering lens are employed to guide the cluster ion beam into the first differently pump chamber. This chamber consists of a

12" diameter chamber and is differentially-pumped by a rotary vein pump and diffusion pump to achieve near-UHV base pressures. During depositions, the pressure rises to 10^{-5} to 10^{-7} torr, depending on the pulse width of the pulse-valve driver. The chamber also contains a 1.5" manual gate valve for isolating the cluster source and first-differently pump chamber from the rest of the instrument for venting and swapping metal rods. Additionally, a 6 mm copper gasket is used in the gate valve to ensure contaminants are not leaked into the rest of the instrument when vented.

3.3 Acceleration Chamber and Magnetic Sector

Next, clusters enter the 8" acceleration chamber, where the working deposition pressure is typically $\sim 10^{-8}$ torr. The chamber contains the second series of einzel lenses and steering lenses, as well as acceleration slit/optics for the magnetic sector. Up until the acceleration chamber, the ion optics maintain cylindrical symmetry along the direction of the ion beam (x coordinate); however, because of the different focusing properties of the magnetic sector in the y-z plane, separate einzel and steering lenses in the y and z direction must be employed to account for the divergence. The flight tube and magnetic sector are not separately pumped like the rest of the apparatus, but instead maintain vacuum by the two turbo molecular pumps adjacent to the magnet. Due to the geometry of the flight tube (8.5 mm $\times$ 50 mm), the conductance is low around the magnetic sector, and therefore functions as a differentially pumped orifice.

As discussed in chapter 2, ions must be uniformly accelerated to high energy prior to the magnetic sector to achieve dispersion of heavier masses. To avoid burdening the cluster source optics and eventually the sample substrate with high voltages, the

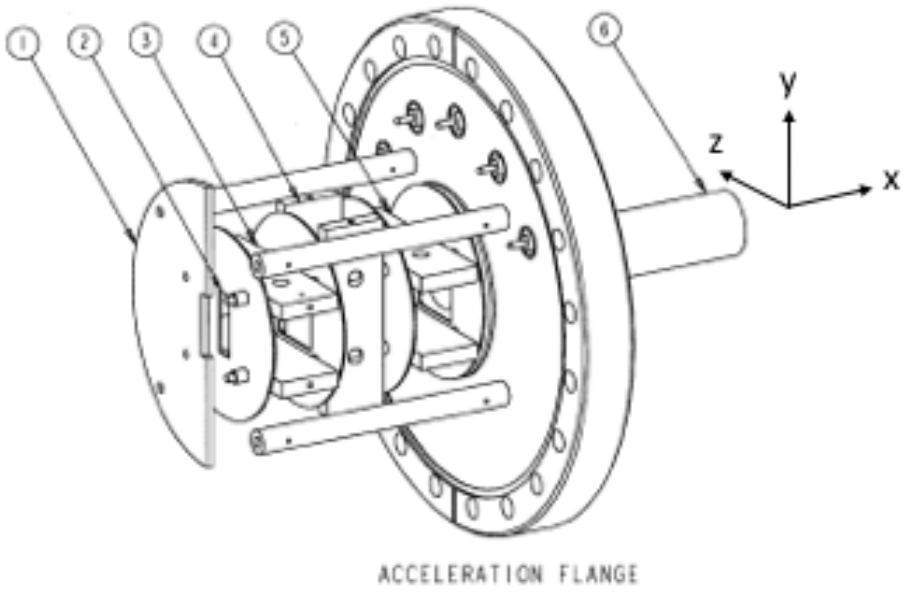

Figure 3.6: Acceleration slit optics: (1) initial orifice (0 V, cut away to show acceleration slit); (2) accerleration slit; (3) z steering plates; (4) y focus plates; (5) z focus plates; (6) high voltage shield. The ion beam travels along the x coordinate. Reproduced with permission from International Journal of Mass Spectrometry, Vol. 254, 2006, p. 204.

flight tube is biased (-800 to -1000 V). The flight tube is electrically isolated (from the chamber) by ceramic breakers to allow for application of a high DC voltage. A Keithly 6517A electrometer, in the floating ground configuration, is used to supply the necessary voltage. The decision to bias the flight tube is critical in avoiding problematic leakage current that can build up in the wiring of the sampler holder (see below). Too large of a leakage current will result in too much noise over the ion-beam signal during deposition experiments on the sample. Furthermore, with a size of 3 mm $\times$ 10 mm, the acceleration slit is also optimized for the transmission of ions rather than mass resolution.

Ions entering the magnetic sector are filtered by their momentum along the flight path r. Since the path curves at an angle of 55° with a radius of $r = 298.5\ mm$, all neutral clusters in the beam will be removed by collisions with the walls. Clusters with the proper momentum exit the magnetic sector and are immediately decelerated by an equal but opposite polarity of the acceleration voltage from the Kiethley electrometer. The symmetry in reimaging the acceleration potential in the deceleration slit of the flight tube allows for ease in tuning and re-focusing the transmission of ions through the magnetic sector. It should noted that the magnetic sector must be electrically isolated from ground to operate with the additional acceleration potential. Sheets of wax paper placed between the magnet and the flight tube ensure electrical isolation.

3.4 Intermediate Collection Chamber

Clusters exit the magnetic sector and pass through a deceleration slit (3 mm $\times$ 10 mm) in the flight tube. Subsequently, the cluster beam enters the intermediate collection chamber, consisting of a 5 way cross in a 6" (dimension) tube. The ion beam is refocused

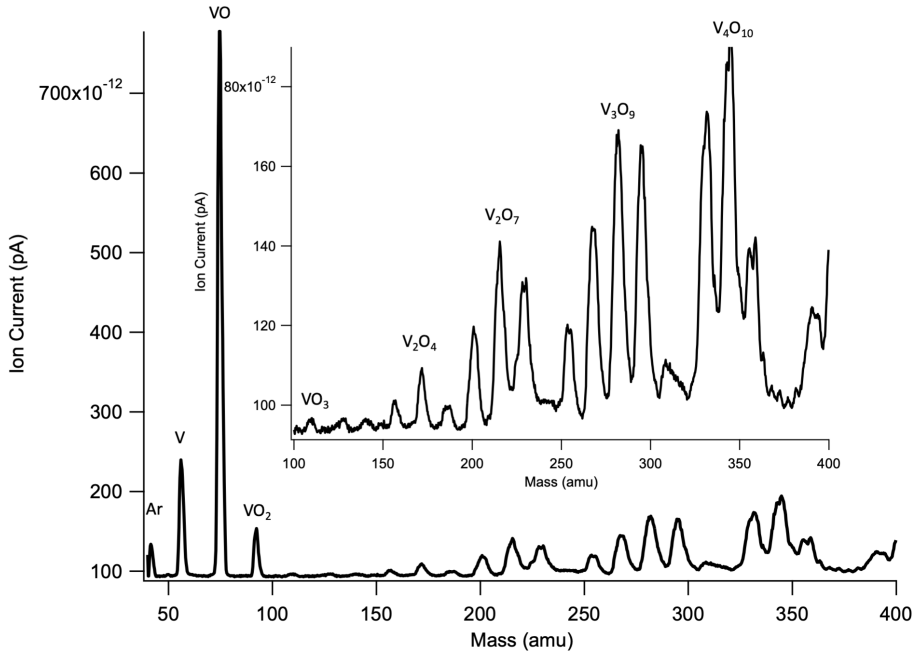

Figure 3.7: Mass Scan of vanadium oxide clusters seeded in 80 % Ar and 20 % O_2. Heavier vanadium oxide clusters are magnified for detail in the inset.

by a series of einzel and steering lenses in the y and z direction onto a removable disk that is electrically connected to the Keithly 6517A electrometer for reading current. A mass spectrum of the clusters in the ion beam is conducted by reading the ion current intensity as a function of magnetic field strength. Since the magnetic field strength is related quadratically to the mass of the cluster (see chapter 2), we can readily plot the ion current signal as a function of mass (amu), see Fig 3.7. The distribution of vanadia clusters observed in Fig 3.7 agrees well with the high-resolution mass scans reported by Bell et al.[80] and Kooi et al[81] Although the intensities for the mono-vanadium clusters are much lower than the dimer and trimer clusters in Bell et al., the high current intensities we observe may be attributed to differences in the seed gas and geometry of the cluster source.

During deposition experiments, the working pressure in the intermediate collection chamber is nearly the same as the base pressure $\sim 10^{-9}$ torr. The chamber ends with a manual 1.5" gate valve for the purpose of isolation and maintaining UHV pressure in the surface science chamber when no deposition experiments are underway. In addition, a welded bellows/differentially pumped rotary coupling assembly connects the collection chamber to the surface chamber. The flexibility of the welded bellows is necessary to account for the rock and pitch of the surface science chamber on the air table.

Once a cluster of a specified mass and charge is isolated in their corresponding magnetic field, the ion current intensity can be optimized by tuning the pulse-delay and ion-optics for deposition. In order to ensure mass-selected clusters do not dissociate upon deposition, a positive voltage proportional to the kinetic energy of the cluster is interposed on the removable disk or sample substrate. In theory, the voltage required to decelerate clusters to 0 V for "soft landing" is proportional to the cluster source extraction voltage (since the acceleration potential is reimaged in the collection chamber), however in practice, the average kinetic energy $\langle KE \rangle$ of the clusters is less than the extraction voltage. This is due to a fraction of clusters in the beam that gain translation kinetic energy from adiabatic expansion, and a fraction of clusters that lose energy by gas-phase collisions with the seeded gas in the acceleration region. These collisions are governed by a Poisson distribution (0 to several collisions), and is responsible for the lower average kinetic energy $\langle KE \rangle$ of the cluster beam. The interposing voltage therefore, is always less than the cluster source extraction voltage, and must be proportional to the average kinetic energy $\langle KE \rangle$ of the clusters in the ion beam. The gaussian distribution profile of the ion beam kinetic energy can be readily observed by recording the ion current intensity as a

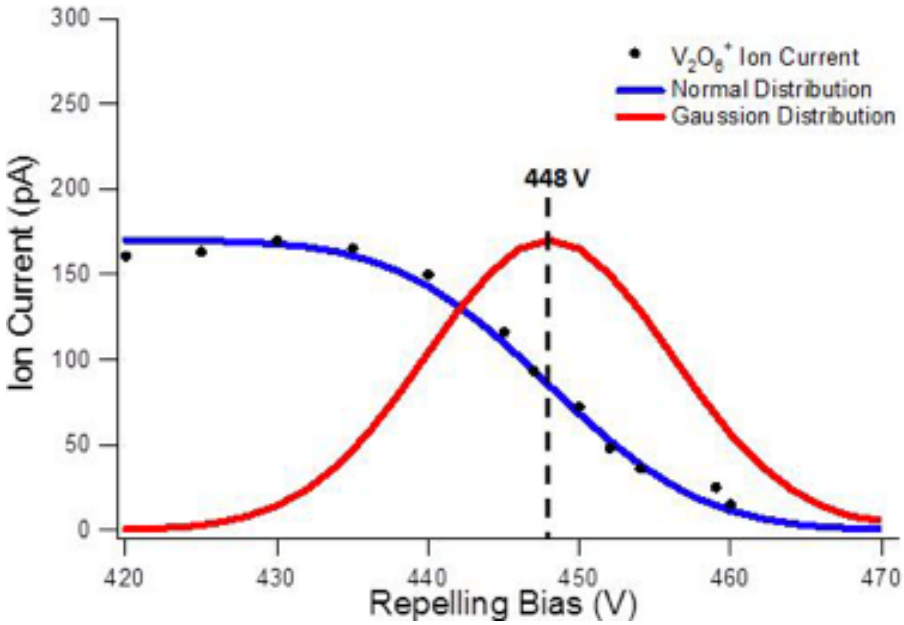

Figure 3.8: Kinetic Distribution graph of V_2O_6 seeded in 80 % Ar and 20 % O_2 with an extraction voltage of 450 V. Ion current is recorded in black dots and fitted to a normal distribution. The derivative to the normal distribution is the gaussian distribution is used to extract statistical parameters such as the average kinetic energy and standard deviation.

function of interposing voltage. For example in Fig 3.8, the recorded ion current (black dots) for V_2O_6 is fitted to a cumulative distribution (blue curve), and differentiated to yield a gaussian distribution (red curve).

From the gaussian distribution, we can obtain statistical information about the kinetic energy distribution of mass-selected clusters in order to interpose a suitable repelling voltage for deposition. The peak of the gaussian curve is the $\langle KE \rangle$ of the cluster; for the case of V_2O_6 clusters, $\langle KE \rangle = 448$ V. Applying a repelling voltage of 448 V will result in half of the clusters with kinetic energies ≥ 0 V will be soft-landed onto the substrate, and the other half of the clusters with kinetic energies less than $\langle KE \rangle$ will be repelled back into vacuum. The *impact kinetic energy* per atom ($\langle KE \rangle$/atom) can be calculated

by

$$\frac{\langle KE \rangle}{atom} = \frac{\sigma}{N\sqrt{\pi/2}}, \tag{3.2}$$

where σ is the standard deviation and N is the number of atoms in the cluster. For V_2O_6 clusters, the distribution of kinetic energies above the 448 V is uniform (σ = 8 eV) and will result in $\langle KE \rangle$/atom = 0.8 eV/atom. Compared to the dissociation energy of a V-O bond (6.48 eV), the $\langle KE \rangle$/atom is suitable for ensuring the structural integrity of the cluster upon landing on a substrate.[71, 72, 73] Since the $\langle KE \rangle$/atom is determined by the narrowness of the high side of the kinetic energy distribution ($\sim$12 eV), maintaining uniformity in the ion beam during adiabatic expansion and acceleration is critical. Factors such as AC noise in the einzel lenses, and degradation to the nozzle orifice will often result in turbulence and widening of the ion beam kinetic energy distribution.

3.5 Surface Science Chamber

The surface science chamber linked to the STM chamber via a 6" manual gate valve, constitute the UHV portion of the apparatus, and rest entirely on a steel table that float atop four vibration-isolation legs (Newport I2000). The table and legs rest on a home-built sandpit for additional isolation from building vibrations. The surface science chamber has a 12" cylindrical dimension, and attaches to the cluster side of the apparatus (not floating) by a flexible rotary-couple, noted in the last section. The chamber is purposed with three experiment tiers: (1) deposition of clusters onto the substrate (typically TiO_2), (2) sample preparation (Ar sputtering and annealing) and (3) sample characterization (XPS/AES/TPD).

3.5.1 Manipulator

The surface science chamber is fitted with a long-reach, 4-axis (x,y,z,θ) cryogenic manipulator (VG Helitran 1000) for moving samples from the surface science chamber to the STM chamber and positioning samples for XPS/AES/TPD experiments. In addition, the manipulator is equipped with a set of insulated wires for cluster deposition and heating experiments (see Fig 3.9). For heating the sample, the fork is *electrically* grounded via a connection to the manipulator, opposite of the heating wire clip. For deposition experiments, the thermocouple wires are attached to clips on the fork and are *electrically* isolated from the manipulator by two ceramic spacers as shown in Fig 3.9. Damage to the ceramic spacers will not permit the sample and fork to be biased for 'soft-land' depositions; instead a load is created, and a large leakage current is observed. It should be noted that the manipulator is electrically floating, and therefore must be grounded (via an alligator clip) to the chamber during XPS/AES experiments to ensure the sample and the detector workfunctions reference a shared Fermi level, and if detecting the current from impinging ions directly on the fork is desired.

3.5.2 Cryogen Set-Up

The manipulator can be cooled to cryogenic temperatures ($\sim$10 - 20 K) by flowing liquid He or N_2 from a dewar (see Fig 3.10). Liquid nitrogen or helium flows from a transfer line attached to a bayonet tube placed inside the dewar via a thermal exchanger built into aefrigerator unit located at the end of the manipulator. Thermal insulation in the transfer line is maintained by evacuation of the Control of flow is initially regulated by a needle valve located at the tip of the bayonet and further regulated by stream by a block knob located on the transfer line. Once the needle valve is set; typically maximum

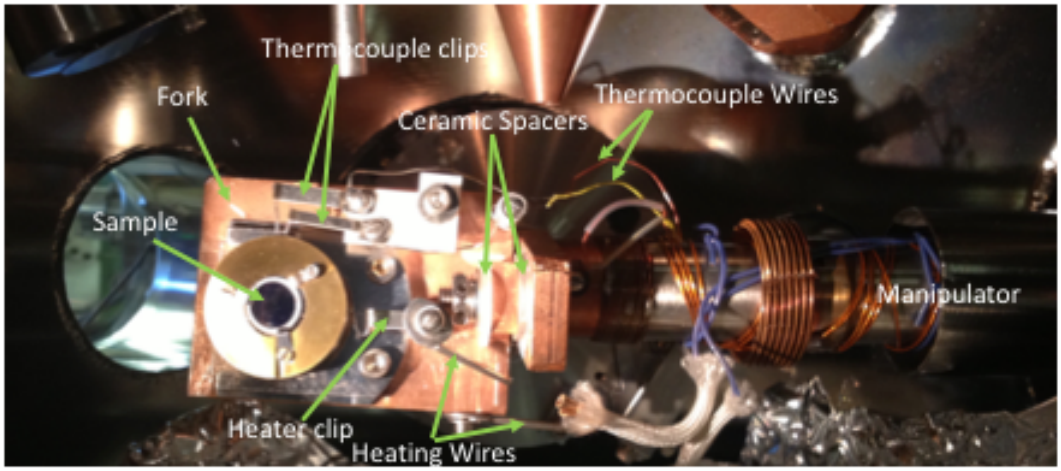

Figure 3.9: The fork that holds the sample is electrically isolated from the manipulator by ceramic spacers. Cracks in the spacers may lead to

cryogen flow is desired by completely opening the needle valve, the bayonet can be placed inside the dewar. Pressure inside the dewar should typically be ∼9 psi for nitrogen, and is regulated by an external gas tank of the same cryogenic element. Although the fork and sample are electrically isolated, they are indeed in thermal contact with the manipulator via ceramic washers for cooling. Cooling the sample is desired for TPD studies of physisorbed species (10 meV $\leq$ 100 meV) or deposition experiments on films of Ar of Kr. With the needle valve and regulator fully opened, the sample can be cooled by liquid N_2 to $\sim$ 90 K in approximately 60 min.

3.5.3 Gas Manifold

Sample preparation (Ar bombardment) and TPD experiments carried out in the surface science chamber require easy access to an array of gases and liquids to be used anytime. A manifold (see Fig 3.11) made up of valves and 1/4" stainless steal gas lines, connected by standard Swagelok fittings rests separately from the surface science

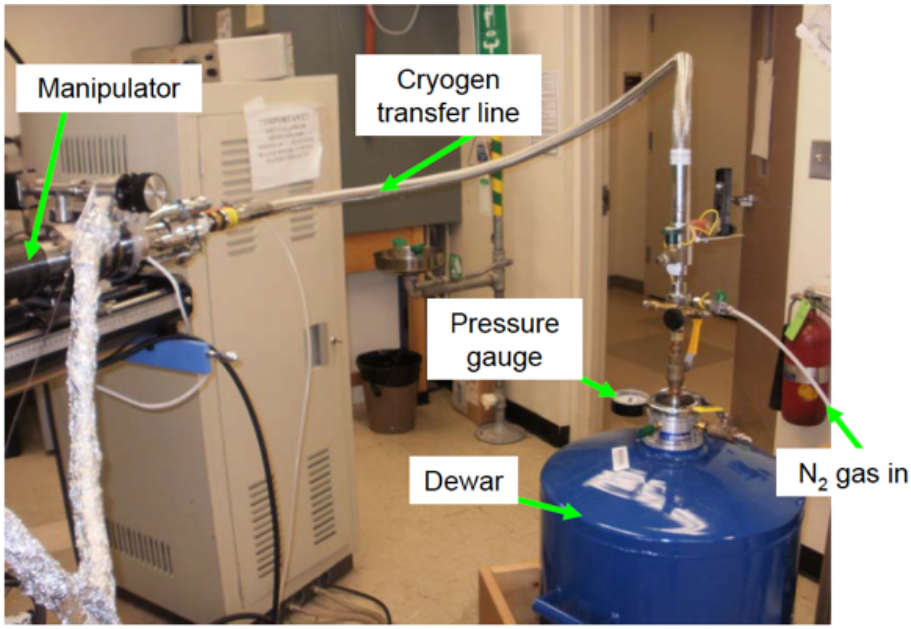

Figure 3.10: Cryogen manipulator set up.

chamber on the floating table. The manifold provides standard female fittings for 4 different sources. For substances that are gases at room temperature and 1 atm, a gas cylinder and pressure regulator can be connected directly to the manifold input. For substances that remain a liquid at room temperature and 1 atm, a specially home-built glass container fused to a standard Swagelok male fitting is used for mating with the manifold. The pressure in the manifold ($\sim 5{\times}10^{-6}$ torr) is measured by a Pirani gauge and and pumped by a compound molecular turbo pump backed by a scroll pump (see pump table). The gas manifold also provides a gas line to the STM chamber for studying adsorbates on catalyst model systems. For residual condensable substances in the manifold the ballast in the scroll pump must be fully opened as to avoid inefficient evacuation of the contaminant. Additionally, the manifold can be baked for cleanliness with heating tapes.

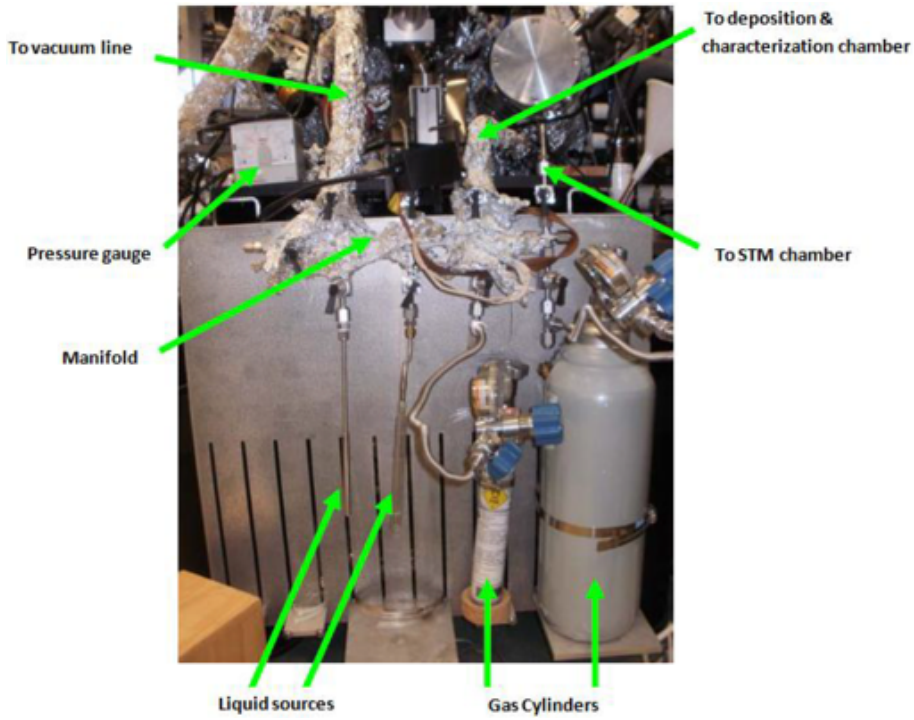

Figure 3.11: Set up of the gas manifold.

The pressure in the manifold is also sufficient for degassing liquids of gaseous contaminants, which is critical to maintaining purity and avoiding adsorption of contaminants onto the substrate of interest. This becomes important as monolayer coverages on the TiO_2 substrate are on the order of 10^{14} atoms/cm^{-2} and many features observed by TPD and STM are usually less than 10% of a monolayer. Degassing is typically done by the freeze-pump-thaw method, where by the liquid substance is frozen by partial submersion in liquid nitrogen, followed by pumping out contaminant vapors present in the glass container holding the liquid for 10 to 15 min. The liquid nitrogen is removed, and the valve between to the turbo pump is closed, allowing the liquid in the glass container to thaw back to a liquid. This procedures assumes the contaminants have a lower freezing point than the substance of interest, like methanol.

3.5.4 Sampler Holder

The sample (typically TiO_2) with rectangular dimensions 2 $\times$ 10 $\times$ 0.5 mm^3 is mounted on a universal OHFC copper sample holder supplied by RHK Technologies Inc. The sample holder depicted in Fig 3.12, is purposed for STM experiments and heating for sample preparation- hence the name *STM sample*. In the STM sample configuration, the sample sits below a sapphire washer (RHK Technologies) with dimensions OD: 10.5 mm and ID: 5.5 mm and 0.3 mm thick, and held in place by three retainer clips. Below the sample, sits an n-type silicon wafer ($\sigma \sim$ 0.10 - 0.15 Ω cm) supplied from Silicon Inc. with dimensions 2 $\times$ 10 $\times$ 0.4 mm^3, that is resistively heated to anneal the sample. A molybdenum wire (Alfa Aesar 0.5 mm thick) spot welded to a tantalum flap provides metallic contact to the silicon wafer. The wire is also insulated from any contact with the sample holder by ceramic feedthroughs (RHK technologies) to ensure only electrical contact is made with the silicon wafer. A second sapphire insulator washer with dimensions 2 $\times$ 10 $\times$ 0.4 mm^3 sits below the silicon wafer for further insulation. A second tantalum flap opposite of the molybdenum wire, wraps around the second sapphire washer below to provide electrical contact to the sample to the fork body. Electrical contact between the wafer, tantalum flap and fork closes the circuit and provides a ground for the voltage supplied to the heating wire; this circuit provides the basis for reading current during STM experiments. Typically 1A is sufficient to heat the silicon wafer to 870 K. In addition, the built-in heating circuit allows the fork body to be used as a detector for ion-current impinging on the entire fork body.

For the *TPD sample*, a larger sample with dimensions 10 mm dia. and 0.5 mm thick is used to provide greater area for gas adsorption/desorption that contribute to the TPD

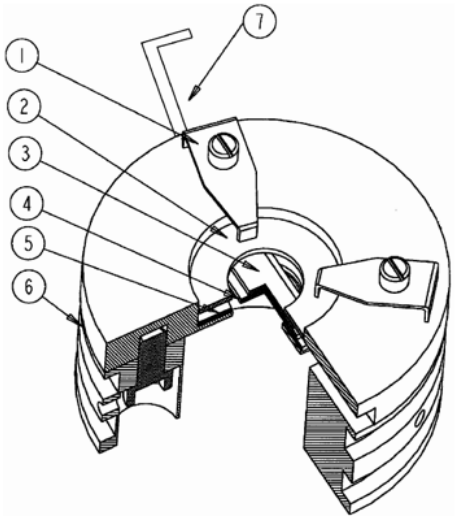

Figure 3.12: STM sample holder configuration consists of: (1)Retainer clips; (2)Sapphire washer (RHK Technologies); (3) Sample; (4) Silicon heater (Silicon Inc.); (5)Sapphire disk (Mindrum Precision Inc.); (6) OHFC copper sample holder; (7) Molybdenum heating wire (Alfa Aesar 0.5 mm thick).

signal. Additionally, a thermocouple circuit is installed to read temperatures directly on the sample. For clarity, a cross-section of the TPD sample is depicted in Fig 3.13. A sapphire disk with dimensions 10 mm dia. and 0.5 mm thick (Mindrum Precision) rests on top of the silicon wafer for electrical insulation followed by a K-type thermocouple (Omega) with a butt-welded junction. The thermocouple junction wires are too flimsy for maintaining sturdy connection to the thermocouple clips; instead thicker alumel and chromel wires are spot welded to their respective places on the ends of the junction and installed into the sample holder. The alumel and chromel wires extend out to the thermocouple clips, and are electrically insulated from the sample holder and fork by ceramic feedthroughs. Once the thermocouple wires are in place and are tested for electrical isolation, the TPD sample is placed directly in contact. Thermal conduction through the sapphire disk installed between the thermocouple and silicon wafer is poor, resulting in a lag time between temperature read out on the sample and the actual

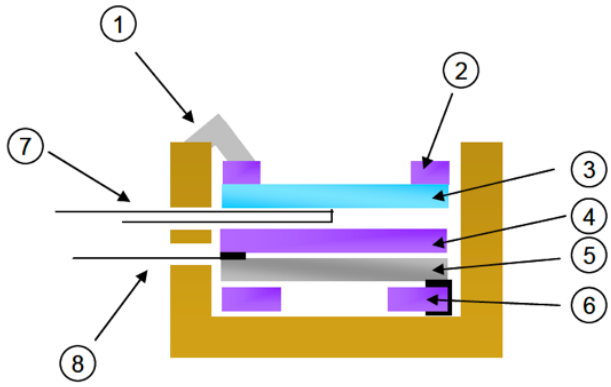

Figure 3.13: TPD sample holder. (1) Retainer clips; (2) sapphire washer; (3) sample (4) sapphire disk (Mindrum Precision); (5) silicon wafer (Silicon Inc.) (6) sapphire washer; (7) thermocouple wires (8) molybdenum heating wire.

temperature of the silicon wafer. In addition, the insulation between the heater and the sample limits the heating to lower final temperatures.

3.5.5 Cluster Deposition

For depositions, the sample on the manipulator is placed orthogonally with respect to the incoming path of the ion beam, and the gate valve between the collection chamber and surface science chamber is opened. Optimization to the ion beam is made with a focusing element located between the sample and the entry orifice of the surface science chamber. Cluster ions impinging on a conductive surface generate current proportional to the flux of the ion beam. Deposition coverage θ_{ML} of clusters on the sample can quantified by measuring integrating the ion beam flux I_D over a measurable time t_D and known area A. Deposition coverage is calculated from,

$$\theta_{ML} = \frac{I_D t_D N}{A \cdot s \cdot q}, \tag{3.3}$$

where N is the number of cluster metal atoms, A is the area of the sample (cm^2), s is the density of binding sites given in unit cell density, and q is the charge per cluster ion (1.16×10^{-19} coulombs). The equation assumes that the sticking probability of cluster ions on the surface is unity. In the case of rutile TiO_2 (110) - (1×1), s will be $5.2\times10^{14}/cm^2$, where one cluster binds to one unit cell. For depositions onto the TPD sample, ion current is directly measured on the sample by contact with the thermocouple wires. Therefore A is proportional to the exposed area of the sample (0.82 cm dia.). Calculation of deposition coverage on the STM sample is less straight forward since the ion current is read on the fork with the heating wire. In this case, the ion current is proportional to the sum of clusters striking the fork, sample holder and the sample. Instead, a profile of the ion beam flux must be measured for calculating θ_{ML} on the STM sample. With the TPD sample, variations in the current can be measured as a function of distance in the *y,z* plane to yield a gaussian distribution of the ion beam flux shown in Fig 3.14. The FWHM of the ion beam is roughly 1 cm and therefore sufficiently large enough to assume both TPD and STM samples are evenly decorated with clusters during depositions.

For TPD experiments, coverages of at least 0.05 ML are necessary to ensure enough desorption signal from cluster-related activity is present above the background. Calculations of θ_{ML} for V_2O_5 and V_2O_7 with typical deposition currents of 40 pA and 200 pA observed in our lab, will show that depositions can range between 7.5 hours and 1.5 hours. Our estimates also assume deposition currents remain the same over the long periods of time. In reality, deposition currents decrease with decomposition of the source metal rod. In addition, periodic adjustments to the laser second harmonic generator to increase power, may misalign the beam enough to vaporize orifice of the source nozzle.

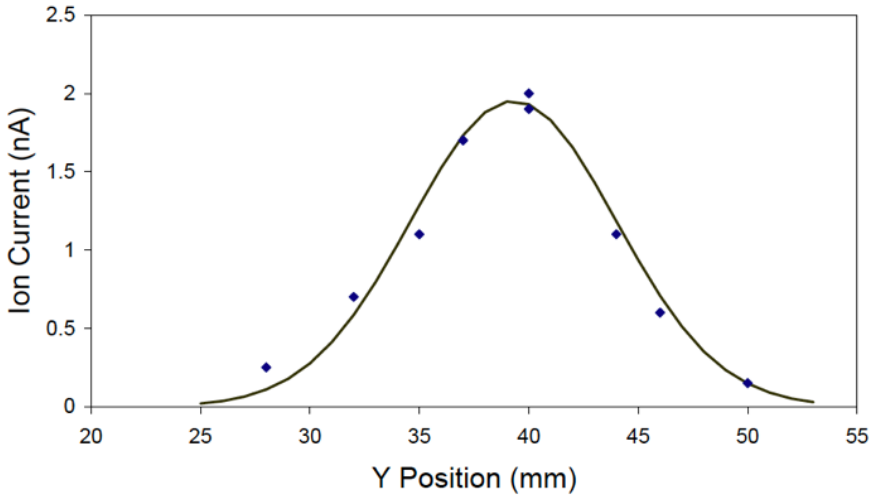

Figure 3.14: Profile of the ion beam intensity recorded on the TPD sample as a function of Y on the manipulator. The FWHM profile of the beam is roughly 1 cm.

Enlargement of the nozzle orifice leads to less ion collisions with the seeded gas, caused by the smaller pressure differential between the waiting room and chamber pressure, and ultimately results in less formation of clusters. Therefore it is critical to measure the ion current during depositions every 30 mins or integrate the ion current on the home-made *Cluster Deposition* program on LabView. In practice, V_2O_5 depositions were typically around 12 hours, including the time spent on swapping vanadium rods. For STM experiments, a 0.01 to 0.03 ML coverages are acceptable. It should be noted that before every deposition, the titania substrate must be flashed to sufficient temperatures ($\sim$ 550 K) to desorb all contaminants like hydroxyls, molecular water and molecular nitrogen.

To measure the magnitude of the ion current, we record the difference between the ion current and the baseline current. First, we record average ion currents (10 - 15 data points) on the sample via the electrometer (Keithly 6517 A) and then subsequently, block the ion beam path with the removable detector to measure the average baseline current.

During depositions we monitor the ion current on a home-made LabView program by connecting the electrometer output to the external ADC of the lab computer. To soft-land *positive* ions on the sample, two external batteries (250 V) with variable output outputs the negative pole to the floating ground input of the electrometer, and the positive pole is connected directly to the sample via electrical connections to thermocouple wires on the manipulator. As explained in the manipulator subsection, high VDC biases in the thermocouple wires of the manipulator result in leakage currents and must be subtracted out to accurately quantify the ion current. Large leakage currents, greater than 500 pA may be due to poor isolation in the fork and manipulator. For soft-landing depositions, a record of the baseline current with the bias voltage left on, will quantify the amount of leakage current read on the sample. This leakage current does not contribute to the deposition of clusters on the sample, and must be accounted for when determining cluster θ_{ML}.

3.5.6 Temperature Programmed Desorption

Once enough clusters are deposited on the surface, the system can be probed chemically by exposure to a gas and then studied by temperature programmed desorption and reaction (TPD/R). A schematic diagram of the TPD set-up is shown in Fig 3.15. Experiments are carried out by exposing the substrate of interest (typically TiO_2) on the fork of the manipulator, to a gas though an MDC-100 ultra-precision leak-valve. The leak-valve is modified with a welded stainless steel tube doser to *directly* expose the substrate positioned $\sim$ 1 cm below the orifice, to high gas pressure while maintaining low UHV pressures through out the rest of the chamber. Direct exposures of gases expedite monolayer coverages in reasonable time, and can be quantified roughly by finding the

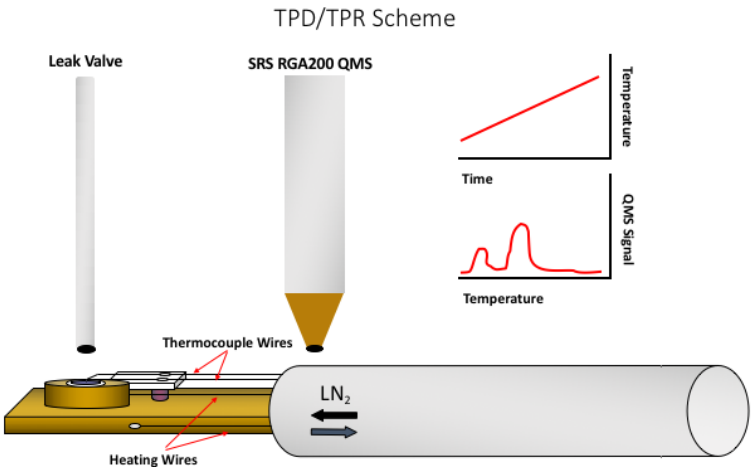

Figure 3.15: Temperature programmed desorption setup housed in the surface science chamber. Key elements of the setup are labeled and an example heating curve and TPD spectrum is provided.

enhancement factor. The nominal sample dosage is calculated using a LabView program which integrates the pressure rise in the chamber over time.

To convert the nominal sample dosage to an actual sample dosage, it is necessary to first calculate the dosing enhancement factor. The dosing enhancement factor is determined by varying the sample dose over several TPD runs, where at least one run shows saturation of the monolayer peak for a well known gas, such as water. The monolayer signature for H_2O monolayer ($\sim$ 270 K) is well known in the literature.(refs) Integrating the area under the TPD peaks and comparing them to the area under the saturated monolayer peak allows for calculation of the actual coverage. The actual coverages are then divided by the nominal coverages measured using the LabView program to find the enhancement factor. With the set-up used for these experiments, the enhancement factor is $\sim$ 14 when dosing chemicals that are gases at STP and $\sim$ 100 when dosing chemicals that are liquids at STP. The enhancement factor is significantly greater for substances

that are liquids at STP because the stronger intermolecular interactions between these gas molecules cause the gas to remain highly collimated. In a real TPD experiment, this calibration factor is multiplied by the nominal exposure to determine the actual exposure.

For TPD, all experiments are executed by interfacing custom build LabView programs that interface with our quadrupole mass spectrometer (Stanford Research Systems RGA200) through an external control unit (ECU). The ECU is connected to a BNC feedthrough on top of the surface science chamber. Following exposure, the ionizer built into the quadrupole mass spectrometer is turned on via SRS RGA software. Typically, the pressure spikes briefly due to the ionizer degassing from heating up. After waiting 15 - 20 min for the ionizer, the sample is moved to $\sim$ 1 mm below the orifice of the copper cone for TPD. The copper cone and steel cylindrical tube encases the entire ionizer and quadrupole mass spectrometer for protection from contaminants in the chamber. Before TPD, up to a maximum of 10 mass fragment signals m/z are programmed, which are recorded simultaneously as a function of time (sec) on our custom designed LabView program "RGA1." An external power supply provides power to the heating element of the TPD sample by connections made to the heating pins marked 2 and 1 on the manipulator.

While the "RGA1" program is recording the first 500 to 1000 data points for background subtraction, the TPD sample is kept near 300 K. Once enough background points have bee collected, the sample is heated linearly by a preprogrammed heating rate β as a function of time (sec) and range (typically 300 K - 800 K) in our LabView program, "HeatDaniel." Near the end of the TPD experiment, just before the terminal temperature ($\sim$ 790 K) is reached on the sample, the "RGA1" program is stopped and all data

is saved as a text file. Afterwards, "HeatDaniel" is stopped and the sample is brought away from the nose cone to avoid residual heating from the ionizer. The ionizer is shut off, while power to the RGA ECU is left on (The ECU should be on at all times during regular operations unless STM/XPS/AES experiments are performed). The ECU power must be turned on at least 1 hour before TPD experiments are to be done.

After saving the data, it is necessary to calibrate the recorded temperatures. Calibration is necessary because the thermocouple measures the temperature below the sample, which, due to inefficient heat transfer, is hotter than the temperature at the top face of the sample. Since the desorbing species come from the top face of the sample, it is necessary to have an accurate measurement of the temperature here. Calibration is done by performing thermal desorption from a bare TiO_2 surface using a well studied adsorbate (typically water). Desorption peak temperatures reported in the literature are plotted versus the corresponding peak temperatures recorded from our TPD run, and a calibration equation is generated from linear least-squares fitting to the data. This equation is then applied to the recorded temperatures in future TPD runs. The raw TPD data is graphed in Igor Pro software and smoothed to around 155 points before additional background subtraction and flattening is performed in Excel.

3.5.7 XPS/AES

Our lab is equipped with a spectacular 1978 Perkin-Elmer double-pass cylindrical-mirror energy analyzer (CMA) model: PHI 15-255G, and electron-gun (0.5 kV to 3 kV) for XPS and AES capability. The apparatus is equipped with a Perkin-Elmer non-monochromatic X-Ray source (PHI 04-548) housed with two filament sources: Mg and

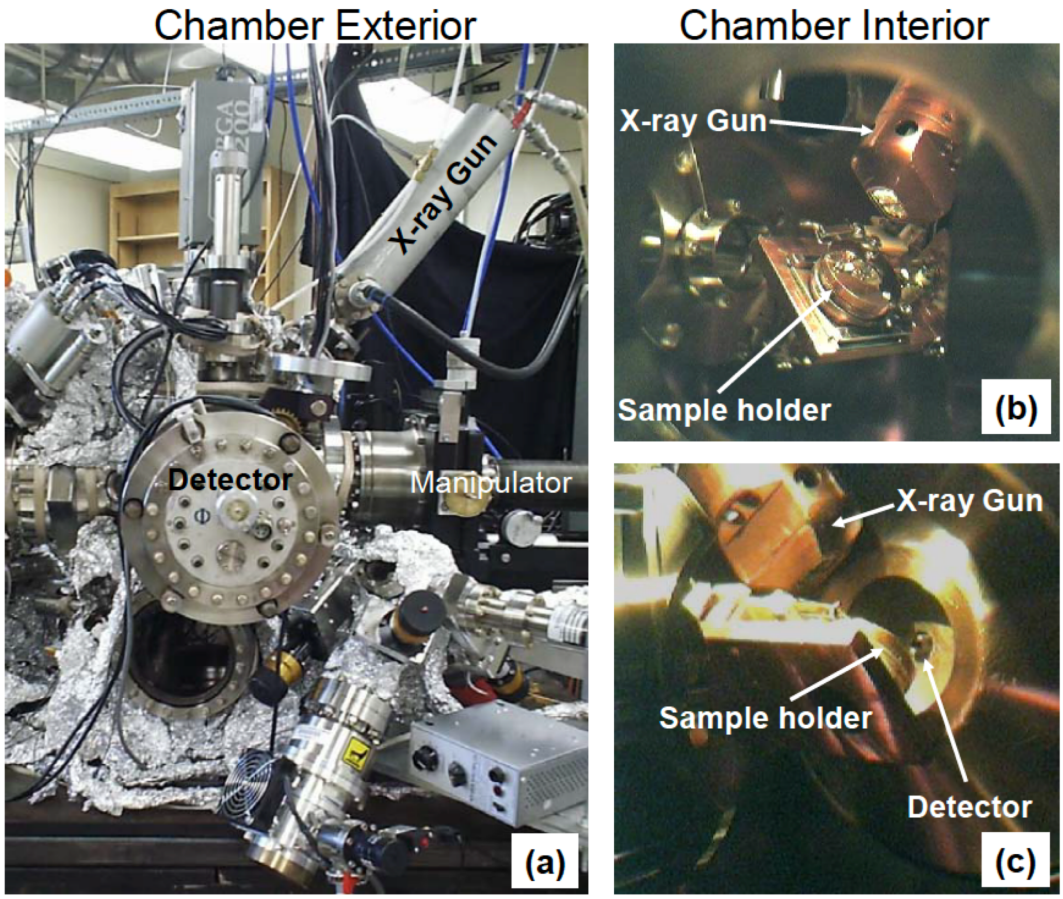

Figure 3.16: Set-up of the XPS/AES instrumentation in our lab: (a) Exterior picture of the XPS/AES detector mounted onto the surface science chamber, (b) Interior picture of the sample and manipulator positioned for XPS/AES experiments by rotating the angle. (c) Another interior picture of the sample from the back of the surface science chamber.

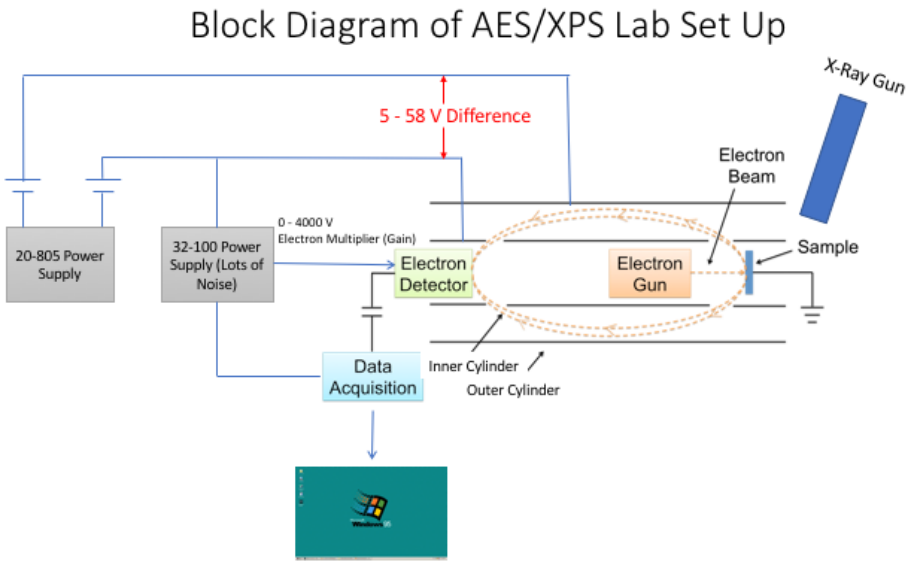

Figure 3.17: Diagram of XPS/AES Lab set up.

Al (The Mg source is burned out) for XPS experiments. The entire set up is pictured in Fig 3.16 and labeled accordingly. The double-pass cylindrical-mirror energy analyzer detects electrons by a channel electron multiplier (replaced in 2016). The channel electron multiplier gain can be optimized by the 32-100 power supply for increased signal to noise, by supplying higher voltages (0 - 4000 V) across the multiplier electrodes. The integrated voltage signal is then converted to a frequency modulation in a V/F converter pre-amp, located above the apparatus and connected via BNC cables. The V/F converter then sends the modulated frequency signal to an A/D converter followed by a digital signal to the computer. A diagram of power supplies and their functions in the XPS/AES set up are shown in the Fig 3.17.

The Perkin-Elmer double-pass CMA consists of an inner and an outer cylindrical mirror electrode and a hemispherical retarding grid analyzer in series, to determine the velocity of charged particles with an energy up to several KeV. In AES mode, the velocity of a

charged particle is determined solely by measuring the extent of deflection in a static potential between two cylindrical mirror analyzers. The photoelectron is emitted from the sample at a polar angle and passes through the annular slot in the inner electrode. Photoelectrons with energy E are deflected so that they pass through an exit slot in the same inner electrode, and are focused to an image point (detector) on the long axis (see Fig 3.17). The advantage of the double-pass focus in the CMA configuration, is that any azimuthal take-off angle for a photoelectron from the sample normal can be collected. Although the optimum performance for collection and transmission of photoelectrons is to position the take-off angle at 42.3°. The extent of deflection for a particle path is a function of the particle energy per unit charge or momentum per unit charge. The electron flight path in the CMA and electrical schematic diagrams that control the potentials between the cylindrical mirrors are depicted in Fig 3.17. In AES mode, the sample and inner electrode are grounded to the apparatus, and only the 32-100 power supply provides voltage of

$$V_{outer} = 0.763(E/q)ln\frac{R_2}{R_1} \tag{3.4}$$

to the outer electrode. Radii for the inner and outer electrodes are denoted as R_1 and R_2.

In AES mode, the energy resolution (ΔE/E) for the CMA is generally constrained by the energy *passband* ΔE, defined as the full width-half max (FWHM), centered about the peak of energy E of a charged particle. The peak of a particle with energy E, typically resembles a Gaussian profile and therefore, lends the energy spectrum to statistical analysis. To first order, the energy *passband* is determined by the geometry and aperture

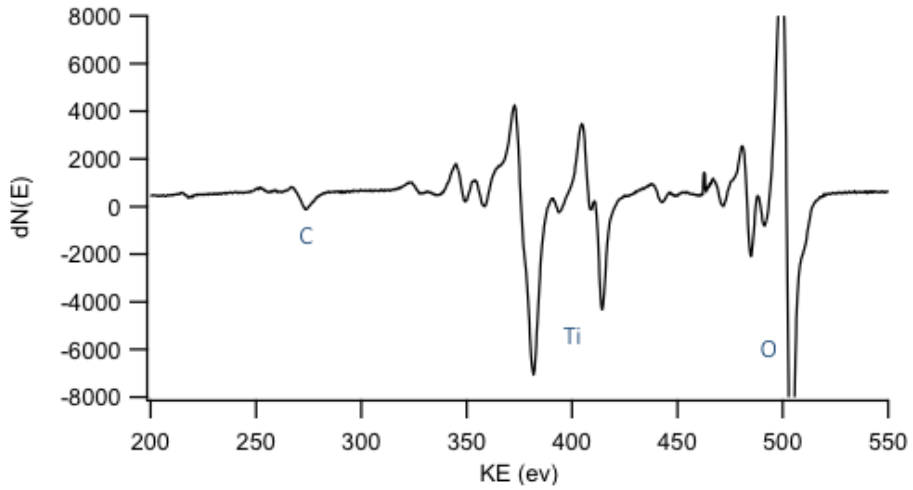

Figure 3.18: Typical Auger electron spectrum of TiO_2 (110) surface after 1 KV Ar^+ bombardment and several cycles of annealing in UHVat 850 K for 10 min.

diameter typically specified in the CMA. For the CMA, the geometry is defined by the axial length L, as the length from the source (sample) to the detector, and the aperture diameter *dia* for both entrance and exit holes. The axial-focusing of the CMA gives an energy resolution,

$$\frac{\Delta E}{E} = 1.09(\frac{dia}{L}), \tag{3.5}$$

for a source of axial length or extent L and the energy resolving aperture of diameter $w' = w{\cdot}sin(\alpha)$ perpendicular to L. The energy resolution for the Perkin-Elmer double-pass cylindrical-mirror energy analyzer (CMA) model: PHI 15-255G is listed by two aperture sizes and an axial length, L = 40.7 cm. An official document for our CMA was uploaded to the surface science lab drop box. A typical Auger electron spectrum of a clean, reduced TiO_2 after sample preparation is shown in Fig 3.18. Even after sputtering and annealing, some carbon contaminants are still present. AES is an excellent tool to checking the cleanliness of the sample before and after depositions and sample preparation.

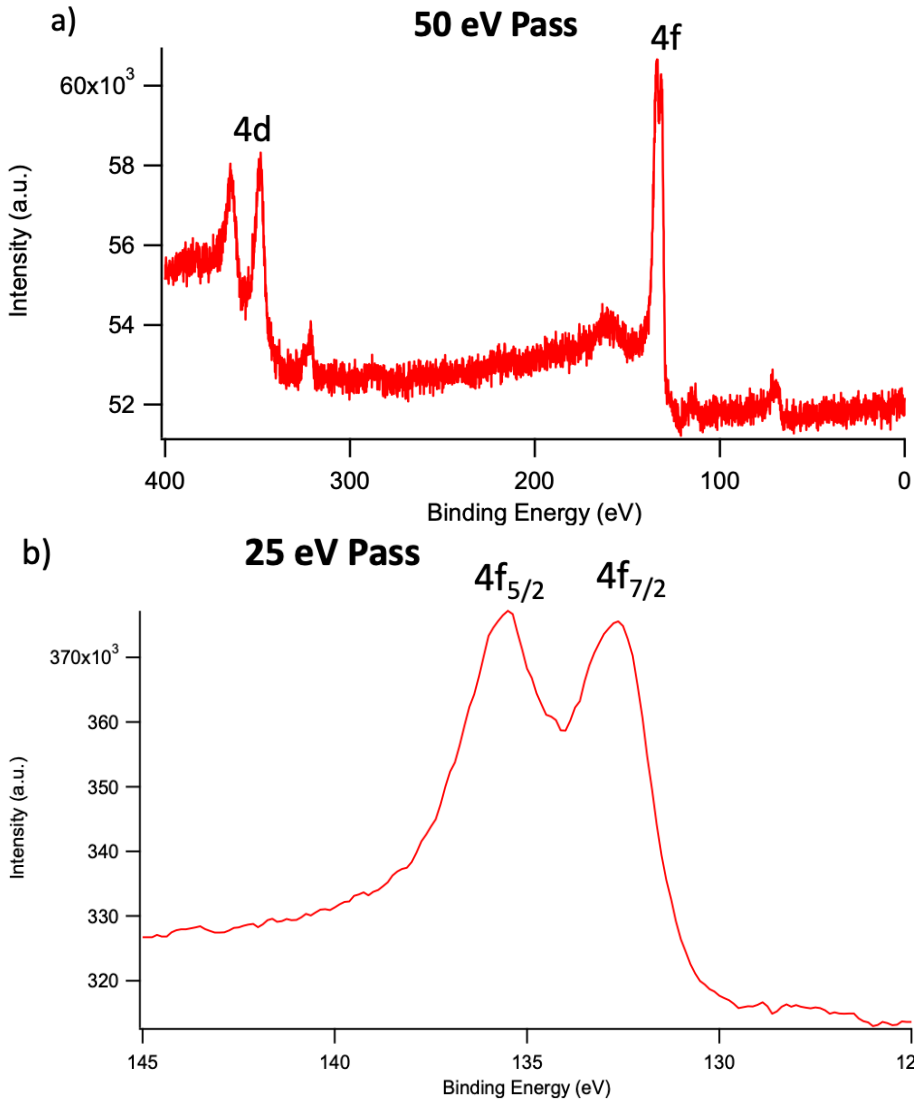

Figure 3.19: Typical X-ray photoelectron spectrum of Pt (111) surface after Ar^+ bombardment and several cyclese of annealing in O_2 for 10 min followed by UHV anneal at 950 K for 5 min. (a) Low resolution wide energy spectrum taken with a pass energy of 50 eV; (b) High resolution spectrum taken with a pass energy of 25 eV. Both spin states in the 4f peak are resolved.

In XPS mode, an additional retarding potential grid is utilized in series with both cylindrical mirror electrodes to extract kinetic energy information from velocity distributions of incoming photoelectrons. The retarding potential grid perturbs all incoming photoelectrons to within a specified window or range of *pass energy* allowed by the user. The current density of the incoming photoelectron signal is measured and integrated as function of opposing voltage, allowing for a map of photoelectron intensities to be mapped as a function of kinetic energy and subsequently, as a function of the sample binding energies (see Fig 3.19). The ΔE/E in XPS mode is dependent on the specified pass energy in addition to the size of the aperture; for a pass energy of 10 eV in conjunction with the smallest aperture typically used in AES mode, ΔE/E will be around 1 eV. This resolution is difficult to achieve in practice for adsorbates that are in small concentrations $\leq$ 0.05 ML or have a small photoionization cross section (elements for z $\leq$ 25).[82]

3.6 STM Chamber

The STM chamber is the second UHV chamber of the apparatus, and consists of the STM and entrance to the load-lock chamber by a manual valve. The load-lock is differentially pumped by the same turbo pump and scroll pump used in the STM chamber. It should be noted that the chamber *did* have an argon sputter gun, but as of 2015, has since moved into the Surface Science chamber. This allows the chamber to maintain UHV pressure typically around 1×10^{-10} torr and lower.

The STM chamber houses an RHK designed STM stage, outfitted for variable temperature experiments and current acquisition on the sample-holders (discussed earlier)

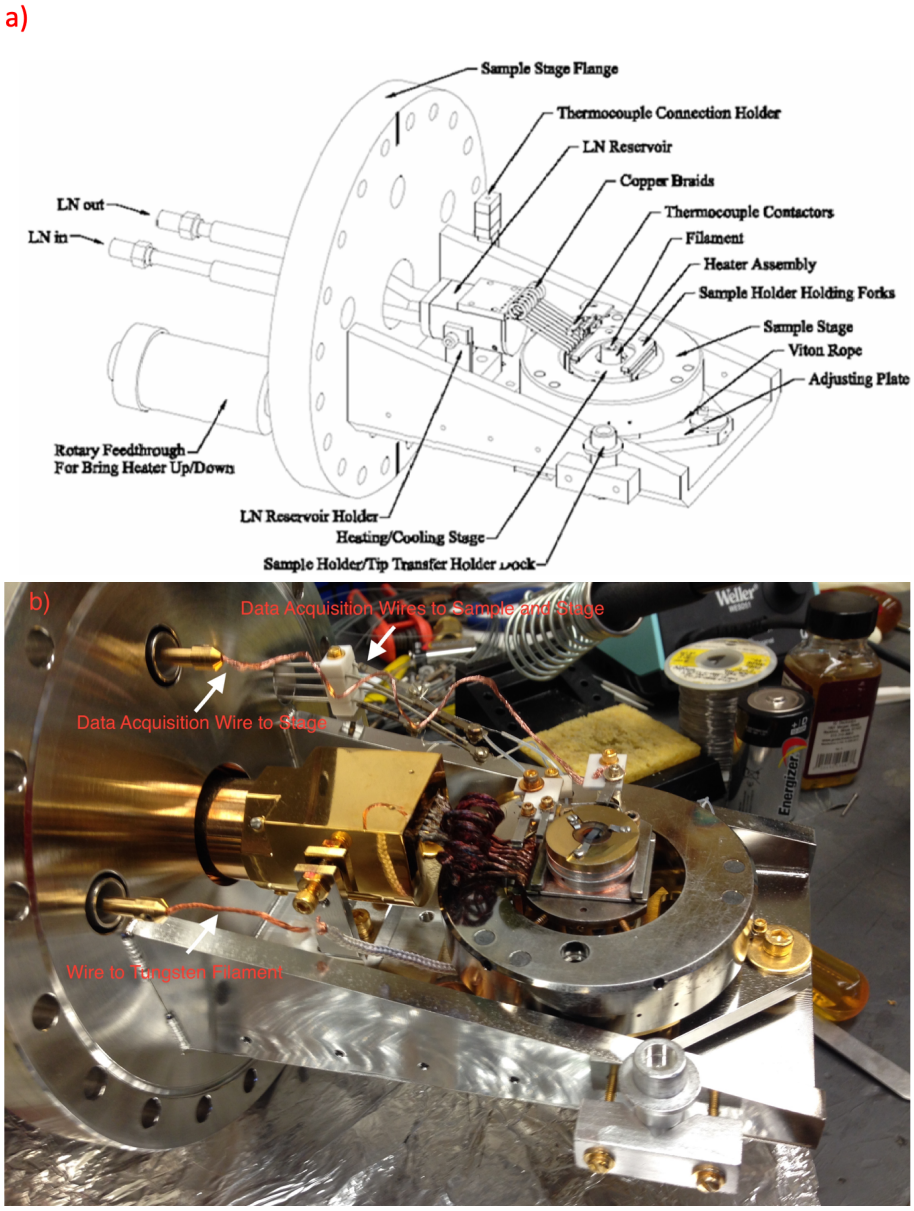

Figure 3.20: RHK STM scan stage. (a) Drawing depicting the various parts of the stage. (b) Picture of the stage showing the three BNC ports available and wires for signal acquisition and heating the sample. A fourth port below the stage (not visible) provides the electrical connection to W filament for electron bombardment of STM tips.

via thermal couple and heating wire clips, see Fig 3.20 for details. When cryogenic temperatures are desired, a cryostat can be connected to the flange, in thermal contact with the copper braids. For liquid nitrogen, stage temperatures can reach 150 K. It should be noted that the cryostat rests directly on the floor, resulting in the introduction of undesired vibrations into the STM stage. The stage is vibrationally isolated from the chamber by resting on three black viton rings, held in place by gold plated hex screws.

Samples can be heated resistively through the heating wire to $\sim$ 900 K, if a silicon element was installed. Alternatively, samples can be heated resistively to $\sim$ 600 K by providing 20 W to a built-in tungsten filament (0.25 mm dia.) located directly underneath the stage. The tungsten filament is designed to be extended *maximally* by a rotary motion feedthrough (MDC Vacuum Products) when heating the sample by filament is desired. Samples can be electron bombarded under appropriate voltages and currents to achieve $\sim$ 1300 K if desired. The advantage of heating samples via the tungsten filament, over the silicon heater method, is the ability to simultaneously acquire STM images with out providing additional electrical noise from a high current power supply. In addition, the tungsten filament is used to electron bombarding freshly etched STM tips. To accomplish this, the filament is brought within $\sim$ 1 mm of the tip, which is biased at +500 V. The filament is then energized with 5-6 A, and the current of electrons bombarding the tip can be measured on an electrometer. A current of 200 mA for $\sim$ 5 seconds is sufficient to remove any oxide from the tip without melting the tip. Extreme caution must be taken to not melt or crash the tip during the electron bombardment process. The entire stage assembly is built on a single 12 inch flange to allow for *not-so-easy* removal.

3.6.1 STM

The microscope (RHK STM100/AFM100) is a beetle-head design, consisting of three piezo-electric legs soldered to the scan head for course sample approach, and a stack of piezo-electric elements for the scanner. The RHK design is depicted in Fig 3.21 for clarity. The scan head also features a planar photodiode detector for measuring cantilever displacements in AFM mode. In STM mode, the metal tip is electrically floating, allowing the sample to be biased across both polarities. The beetle scan head utilizes a number of DAC outputs from the SPM1000 scan unit and PPO 100 control unit that supplies sawtooth signals to the three piezo legs and a as a function of x,y directions for course approach. Between each step of the course approach, a feed back loop is used to extend the scan tube in the z direction and detect current between the tip and the sample; the scan head continues the descent until a current is detected. Once the tip reaches the sample, the scan head can be manually adjusted on the SPM 1000 scan unit for constant height mode or constant current mode.

In constant current mode, the current is typically set between 0.1 nA for large scans and 1 nA for achieving atomic resolution. The set current range is limited by the I-V preamplifier (RHK IVP-200) which can range between 5 pA and 100 nA when the gain is 1. The IVP-200 preamp converts current to voltage (0.01 V to 10 V) with manually adjustable (jumper pins) gain pre-settings of 1 or 10, before the signal is converted from voltages to bits in the ADC located in the SPM 1000 unit. Our lab typically operates the IVP-200 with the gain = 1, meaning 1 nA = -100 mV, up to a maximum of 100 nA = -10 V. The bandwidth of the IVP-200 preamp is 50 KHz, with a minimum tunneling current of 5 pA, allowing for microsecond line scans in constant height mode. However,

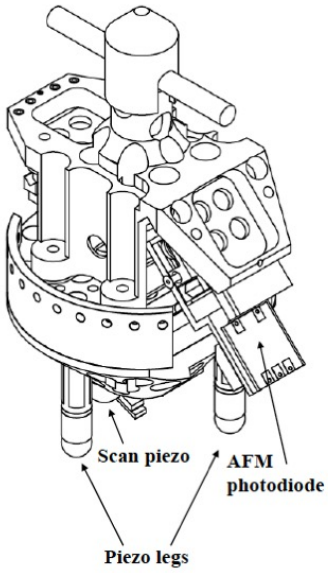

Figure 3.21: RHK STM100/AFM100 scan head. The head is a beetle-scanner design with a photodiode for detecting beam deflection as a function of cantilever height.

in constant current mode, the scanner is limited by the bandwidth of the feedback loop ∼1 KHz.

3.6.2 Noise Considerations

The resolution of our measurements are inexorably limited by both the *true resolution* of the scan controller unit and thermal and external vibration and electrical noise associated with the scan head environment. When obtaining and subsequently analyzing STM data, the resolution of both the scan unit, preamp and thermal noise must be considered. The RHK SPM1000 scan unit utilizes a 12 bit DAC with a scan range of ± 130 VDC, which corresponds to 1.3 Å/bit for a 500 × 500 nm^2 image, with a A/D increment gain = 1. Unfortunately, this bit range is not good enough to atomically resolve heights and proximities of individual atoms. However, by adjusting the A/D gain from anywhere

between 32 to 128, the resolution improves to 0.04 Å/bit and 0.01 Å/bit. We have found for 30 × 30 nm^2 size images, that having the A/D = 32 or 64 is sufficient for achieving near-atomic resolution. Still, thermal noise of the preamp must be considered.

Thermal noise can be quantified by the one-sided voltage spectral density (voltage variance) with the Johnson-Nyquist equation,

$$\sqrt{\langle v^2 \rangle} = \frac{0.13\sqrt{R(\Omega)} \cdot nV}{\sqrt{Hz}}. \tag{3.6}$$

For the IVP-200 preamp, the gain = 10^8, corresponding to R = 0.1 GΩ. For constant height images, each scan is summed up over a 50 KHz bandwidth, resulting in an rms voltage $\sqrt{\langle v^2 \rangle}$ of 0.150 mV, or 1.5 pA in the IVP-200 preamp. In constant current mode, we are limited by the bandwidth of the feedback loop of 1 msec scan per line (1 KHz), yielding an rms $\sqrt{\langle v^2 \rangle}$ of 0.128 mV, or 1.28 pA. Translating the rms current to peak-to-peak current ($1.4 \cdot I_{rms}$) and dividing by 2 yields ΔI = ± 0.9 pA. Typically, ΔI is too small to affect constant current images, as I_{set} is three orders of magnitude larger. In addition, the minimum threshold current signal for the IVP-200 is 5 pA. To be thorough, we can approximate the uncertainty in height (Δ z) due to thermal noise ΔI in the current by

$$\Delta z = \frac{-1}{2\kappa} ln \frac{\Delta I}{I_{set}}, \tag{3.7}$$

where κ is the tunneling decay constant (1.095 $Å^{-1}$), to yield Δz = ± 0.100 pm. It is clear that under the conditions (i.e. T = 298 K and $I_{set} \geq 0.1$ nA) we perform constant current STM, both Johnson noise in IVP-200 and the scan resolution of the DAC in the RHK SPM 1000 scan unit is more than adequate to resolve atomic features reserved for

point defects, molecules and metal oxide clusters shown through out this dissertation.

Other sources of noise from building vibrations, and external electrical noise can also affect the capabilities of the STM. Since the entire apparatus is located on the fourth floor, building vibrations of typically 5 - 45 Hz can become problematic if care is not taken to ensure the steel table and vibration isolation legs are properly pressurized by the building air system and balanced. The isolation legs typically use between 25 - 35 psi air pressure. In addition, the isolation legs should be not in direct contact with the ion pumps, as this will lead to major vibration coupling. For best results, we turn off all mechanical and turbo pumps before imaging. When building vibrations are not suppressed properly, low frequency streaks across the trace and retrace (in opposite directions based on scan direction) can be readily seen. Vibration noise will also increase with scan speed. Another way to investigate vibrational noise is to take a power spectrum of the noise density before a scan to quantify the frequency and intensity.

Residual electrical noise in the STM can arise from capacitive coupling to external electrical fields like light fixtures, pressure gauges and even computers. The power spectral density for electrical noise is typically most intense around 60 Hz followed by less intense harmonics at 120 Hz and 180 Hz. Like vibrational noise, electrical noise appears as scan streaks in opposite directions in the trace and retrace, but will remain independent of the scan speed. Ideally, we could eliminate electrical noise perfectly by placing the entire scan head into a Faraday cage, but since that is not possible, we cover electrical contacts like BNC connectors and multi-pin PGA connectors in foil! In addition, we turn off all the lights, TPD computer, and electrical gauges and their controllers before scanning.

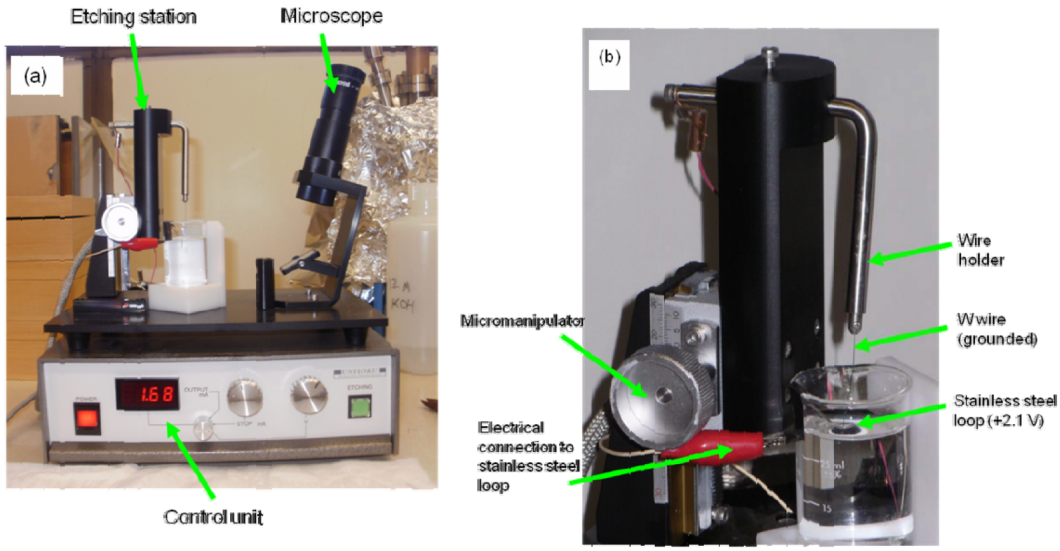

Figure 3.22: Images of a Unisoku tip etching station: (a) is a front view of the station; (b) is

3.6.3 STM Tip Preparation

All of the STM experiments reported here used home-made tungsten tips which were prepared by electrochemically etching a tungsten wire. A 0.2-mm diameter tungsten wire is purchased from Alfa Aesar and cut into 80-mm long pieces. The pieces of wire are sanded in order to remove the thin layer of tungsten oxide on the surface of the wire. Following this step, the wires are sonicated in acetone for five minutes and then methanol for an additional five minutes to remove any organic contamination on the surface of the wire. The wires are then loaded onto a tip-etching apparatus (Unisoku), which is shown in Fig 3.22 (a).

Fig 3.22 (b) shows a close-up of the electrochemical etching part of the tip-etching station. A beaker is filled with just enough 1.2 M KOH to bring the meniscus of the solution to the same level as a stainless steel wire loop. Tungsten wires are then carefully positioned in the center of the platinum wire loop (a stainless steel electrode loop can

be used in lieu of Pt) at an entry angle normal to the meniscus of the KOH solution. Approximately 10 mm of the length of the tungsten wire is submerged below the meniscus for the initial etching step, during which a DC voltage of 7 V is applied between the stainless-steel wire loop (cathode) and the tungsten wire (anode). This step is taken to remove several outer layers of the tungsten metal, ensuring a smooth surface. Using a micromanipulator, the tungsten wire is partially moved out of the solution, leaving only 5 mm of the wire submerged. At this time, the second etching step takes place. In this step, a voltage of 2.1 V is applied across the cell, and electrochemical etching of the tip occurs according to the following chemical equations:[83]

$$Cathode: 6H_2O(l) + 6e^- \xrightarrow{\text{SRP = -2.45 V}} 3H_2(g) + 6OH^-(aq) \tag{3.8}$$

$$Anode: 6W(s) + 8e^- \xrightarrow{\text{SOP = 1.05 V}} 6WO_4^{2-}(aq) + 6H_2O(l) + 6e^- \tag{3.9}$$

$$Total: 6W(s) + 2OH^- + 2H_2O \xrightarrow{\text{E = -1.40 V}} 6WO_4^{2-}(aq) + 3H_2(g) \tag{3.10}$$

In the above reactions, E_0 is the standard cell potential calculated by summing the standard reduction potential (SRP) for water and the standard oxidation potential (SOP) for tungsten to tungstate. These oxidation and reduction potentials are reported relative to the standard hydrogen electrode. During etching, metallic tungsten is anodically dissolved as a result of during oxidation of the metal to water-soluble tungstate anions. At the cathode, water is reduced to form hydrogen gas and hydroxyl ions. Application of a voltage of +2.1 V between the cathode and anode provides an over-potential of 0.7 V, allowing the reactions to readily proceed.

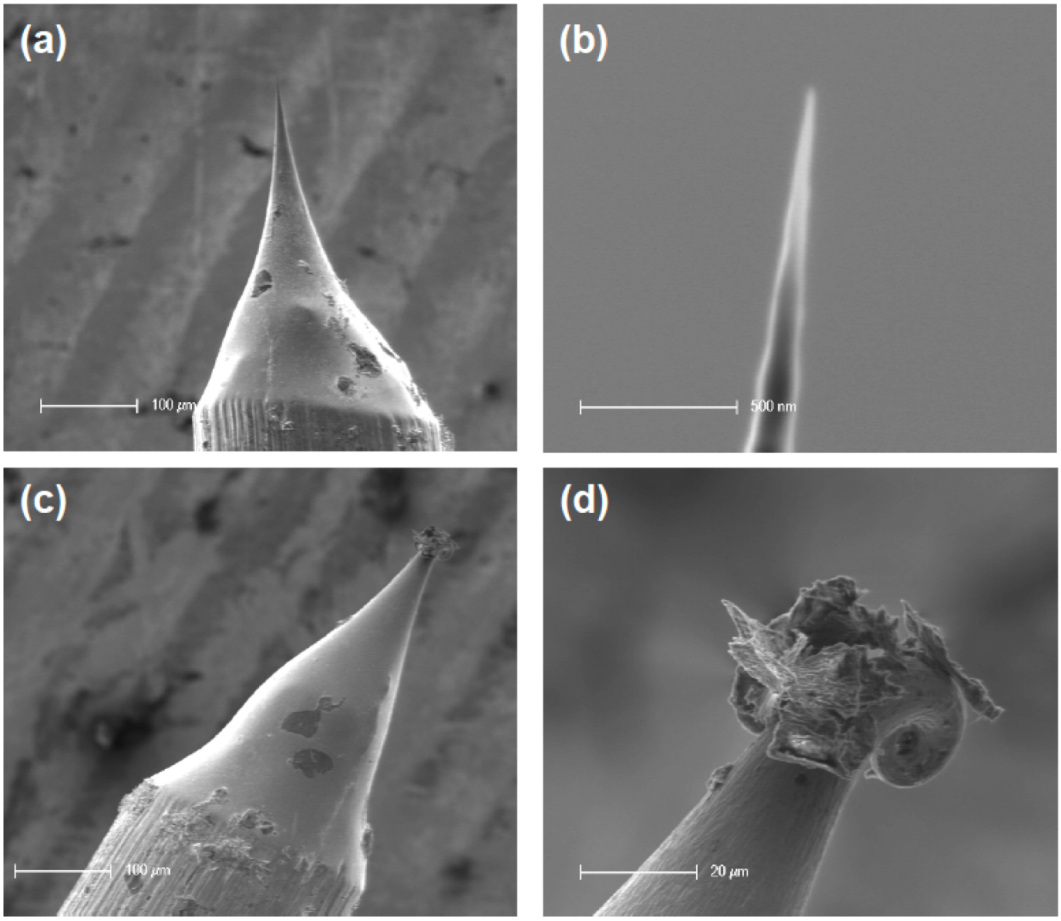

Figure 3.23: Representative scanning electron micrographs of etched, tungsten STM tips. (a) An ideal STM tip. (b) High-resolution zoom-n image on the end of the ideal tip. (c) A crashed STM tip. High-resolution zoom-in on the crashed tip.

Although the entire portion of the tungsten wire below the meniscus would be expected to etch at the same rate, the region of the tip at the meniscus of the solution actually etches much more quickly than the region below the meniscus. As the reaction proceeds, the concentration of [OH-] decreases and the density of the solution increases in the area around the wire (due to the formation of tungstate ions). This results in a region of solution with low [OH] concentration that continuously flows down the tungsten wire, protecting it from etching.

As the reaction proceeds, the current density is inversely proportional to the surface area of the tungsten wire and directly proportional to the concentration and activity of the OH- ions in solution. Therefore, the portion of the wire at the meniscus etches faster than the submerged region; once the tungsten at the meniscus is etched sufficiently thin, the weight of the submerged part will cause the wire to break at the meniscus, resulting in a decrease in etching current and the formation of an atomically sharp tip. The etching apparatus contains a feedback loop which cuts off the applied voltage within 500 ns of the drop in current when the tip is formed. A quick response time is essential in ensuring that the tip remains sharp. With increasing cut-off time, the radius of curvature and cone angle of the tips increases, causing the tip to be less ideal for achieving atomic resolution.[84] After the etching step, the tips are then carefully rinsed with methanol and examined with an optical microscope to ensure that they have not crashed. An ideal tip has a pencil-shaped tip, whereas crashed tips have a variety of irregular shapes that are easily noticeable under the microscope. Representative scanning electron micrographs of a *good* tip is shown in Fig 3.23(a - b).

At this point, tips are very carefully loaded into a tip holder by pulling the tungsten wire through a 0.2-mm inner diameter barrel on the holder. As the wire is pulled through the barrel, it is periodically bent at $\sim 30^{\circ}$ angles to ensure that the tip is seated snugly in the holder. Be careful to not pull the tip through the tip holder barrel as you may risk *crashing* the tip as shown in Fig 3.23(c - d). After cutting the tip to appropriate length, it is examined under the optical microscope once again to make sure that the tip did not crash. The tip holder is then loaded into the tip exchanger and introduced into the UHV STM chamber via the load lock. Once introduced into the STM chamber, it

is necessary to electron bombard the tips to remove any undissolved tungsten oxide that formed during etching. Refer to the STM section for more information on the electron bombardment process.

Chapter 4

Surface Properties of TiO_2 (110)

To elucidate the catalytic synergy of supported VO we must first understand the physical and chemical properties of the rutile phase titania support. Although the chemical and physical properties of the different phases of titania are rich and complex, I devote only one chapter to explaining these concepts in the context of just the rutile phase TiO_2, as a primer to understanding the results of our investigations into methanol reactivity and interactions with VO clusters. Moreover, I will discuss these properties only in the context of single crystals on the (110) facet, as it is the most stable and the most studied. Much of the first three decades of research on TiO_2 can be summed up in Ulrike Diebold's habilitation thesis[50], and should be referred to for more detail. More recent reviews on the surface science and chemistry TiO_2 can be found in work by Thornton[85] and Dohnálek and company.[86]

Ever since Fujishima and Honda published their seminal 1972 paper on the electrochemical photolysis of water on n-doped TiO_2 anodes, research on fundamental understanding the nature of TiO_2 materials have exploded.[87] Much of the research on

TiO_2 also focuses on improving their photoelectrochemical properties for the photo-oxidation of organics like methanol and ethanol into aldehydes and ethers as a direct fuel source.[88, 89, 90, 91] The photoelectrochemical properties of TiO_2 has also been extended to waste water treatment, whereby E. Coli undergoes photo-decomposition at the anode surface.[92]

TiO_2 has also found tremendous use among surface scientists as a model support for heterogeneous catalysts, due to their high thermal stability, availability of single-crystals, and extensive characterization in the literature. Additionally, much to our advantage, perturbations to the stoichiometry (i.e. TiO_{2-x}) introduces band gap states, making rutile conductive enough for STM experiments. Many studies into model TiO_2 supported catalysts by surface science techniques, have resulted in unprecedented insight into the atomistic mechanisms of surface structure and reactivity.

4.1 Bulk Structure

Since many interesting physical and chemical properties at the surface result from bulk defects, it is necessary to discuss the bulk properties of rutile titania. Single crystal rutile TiO_2 consists of single titanium atoms bound to six oxygen atoms with distorted octahedral symmetry and crystallizes into a body-centered tetragonal unit cell, defined by three crystallographic parameters where a = b = 4.584 Åand c = 2.953 Å. A ball and stick model of bulk rutile is depicted in Fig 4.1. Oxygen atoms in the bulk are three-fold coordinated to adjacent titanium atoms. Each octahedral titanium atom in a unit cell will have an oxidation state of +4 and each oxygen atom have an oxidation state of -2. The bulk rutile structure consists of unit cells stacked along the distorted axis (O-Ti-O

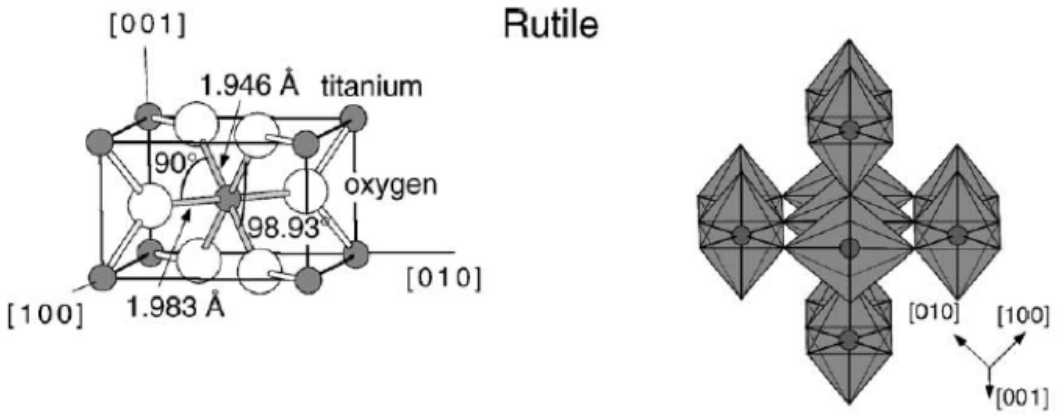

Figure 4.1: Ball and Stick model of bulk rutile (a) Body-centered tetragonal unit cell of rutile TiO_2 with a = b = 4.584 Åand c = 2.953 Å; (b) Stacking arrangement in rutile TiO_2. Reproduced with permission from Surface Science Reports, Vol. 48, 2003, p. 67

), in a corner sharing configuration along the ⟨110⟩ crystallographic axis (see Fig 4.1).

4.1.1 Bulk Defects

The ratio of O/Ti in rutile titania is tunable, with large reductions leading to many stable phases as reported by Samsonov et al.[93] For small reductions in the oxygen content, the structure of TiO_{2-x}, becomes complex, with the formation of point defects like doubly charged oxygen vacancies, Ti^{3+} and Ti^{4+} interstitials, and extended 2-D defects like crystal shear planes (CSP). Electron paramagnetic resonance (EPR) and bulk conductivities studies reveal oxygen deficiencies in the range $TiO_{1.9996}$ to $TiO_{1.9999}$ (3.7×10^{18} to 1.3×10^{19} missing O atoms), result in a majority of Ti interstitial point defects in the bulk, while greater reductions of around $TiO_{1.9965}$ tend to produce extended crystal shear plane (CSP) defects.[94]

Figure 4.2: Rutile TiO_2 (110) single crystals subjected to increasing cycles of Ar bombardment UHV annealing (900 K) where the change in color is attributed to increasing Ti^{3+} bulk defects.

Investigations in the electronic structure of TiO_{2-x} by EPR and bulk conductivities by Li et al.[95] reveal point defects are negatively charged and are highly correlated with color changes to the substrate. Increasing oxygen reduction to the rutile lattice leads to more color centers and darker shades of blue. This optical effect is typically observed over the life time of the rutile substrate when subjected to numerous cycles of high energy Ar^+ sputtering or electron bombardment and high temperature annealing in UHV, as seen in Fig 4.2.

Bulk Ti interstitials defects are also important in the reoxidation and growth of rutile substrates under UHV conditions. Annealing of the substrate in a background of oxygen between 400 K to 900 K, oxidizes the bulk substrate and a noticeable color change from dark blue to light blue is observed. The mechanism for bulk-reoxidation was studied extensively with ensemble measurements by Henderson[96, 97], who showed that indeed low-valent Ti interstitials diffuse from the bulk to the surface and subsequently react with oxygen to form new terraces. Further studies by STM into the growth mechanism have shown Ti interstitials as the primary active site in the formation of face-sharing rows that lead to new (1×1) surfaces.[98] Additionally, studies on bulk defects reveal that Ti interstitials retain a octahedral symmetry and diffuse much faster than bulk oxygen

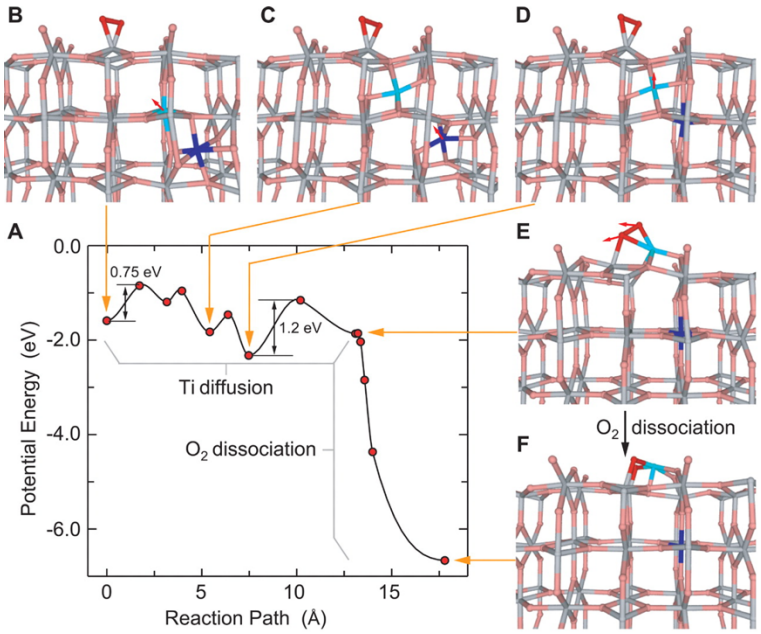

Figure 4.3: (A) Potential-energy profile for the reaction of an adsorbed O_2 molecule and a Ti interstitial on TiO_2 (110). The energy zero corresponds to O_2 in the gas phase and the Ti interstitial at the octahedral position between the second and third TiO_2 trilayer. (B) Adsorbed O_2 molecule (red). (C) Ti interstitial (dark blue) moved to tetrahedral position and lattice Ti (light blue) to tetrahedral position between the first and second TiO_2 trilayer. (D) Original Ti interstitial (dark blue) now at lattice position. (E) Exchanged Ti interstitial (light blue) appearing at the surface. (F) Adsorbed O_2 dissociated and a surface TiO_2 island formed at the terrace. Orange arrows indicate position on the potential-energy profile that correspond to the configurations shown in (B) to (F). Reproduced with permission from Science, Vol. 320, Issue 5884, 2008, pp. 1755-1759.

vacancies.[99] This mechanism occurs along the [001] direction.[100] DFT calculations by Besenbacher and co-workers also show that the diffusion and reaction of an Ti interstitial with adsorbed O_2 is energetically downhill.[101] The result of these calculations are illustrated in Fig 4.3. It is clear that Ti interstitial defects are the major contributors to the physical and chemical properties of bulk rutile. We will see later Ti interstitials play a major role in the chemical properties of the surface.

Like many other metal oxides, electrostatic forces must be considered in understand-

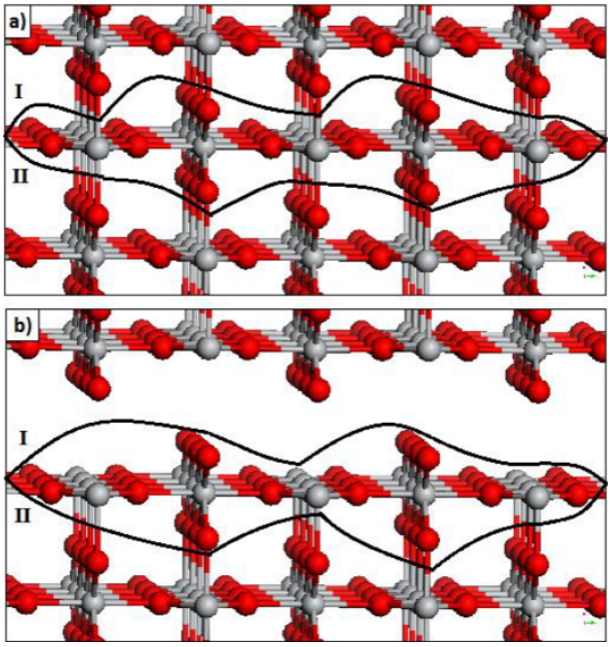

Figure 4.4: (a) Ball and stick model representing the structure of rutile TiO_2 where Ti atoms are represented by silver balls and O atoms by red balls. The two lines enclose a repeating charge neutral unit. Cleaving along line (1) leads to the (110) surface shown in (b).

ing the thermodynamic stability of the corrugated (110) surface that is observed on cleaved rutile single crystals. Ideally, when treated ionically, the overall net charge between layers in a metal oxide will be neutral, however due to the distorted octahedral unit cell in bulk rutile TiO_2 (see Fig 4.4(a)), charge accumulates between the different oxygen and titanium (110) planes.[102] For the (110) surface to be neutral; the surface must cleave along the black line (1) to yield the surface depicted in Fig 4.4(b); resulting in the well-known corrugated surface. Further treatment by LaFemina[103] rationalized that the surface is stabilized by an additional *autocompensation effect*- whereby excess charge redistributes from cationic Ti^{4+} states to anionic O^{2-} dangling bonds to achieve a partial *covalent* character. Density functional theory calculations confirm the electronic structure of rutile TiO_2 depicted in Fig 4.5; zero energy (eV) marks the Fermi level. In Fig 4.5, the total density of states (DOS) (black) is a hybridization of filled states that correlate with oxygen DOS (red) and the unfilled states correlate with titanium DOS (green).[104] Taking into account electrostatic forces and autocompensation together, correctly predicts a (1 × 1) reconstruction of the (110) facet.

4.2 (1 × 1) Surface Structure

The (1 × 1) reconstruction consists of periodic troughs of five-coordinated Ti (Ti_{5c}) atoms bound together by three-coordinated in-plane oxygens, and two-coordinated bridging oxygen rows (O_{br}). The Ti density per (1 × 1) unit cell is one or 5.2×10^{14} cm^{-2}; this will be important for calculating coverages of vanadia clusters and methanol on the surface. A model of the (1 × 1) reconstruction surface and comparison with empty-state constant-current STM images is shown in Fig 4.6. The contrast in the topographic STM

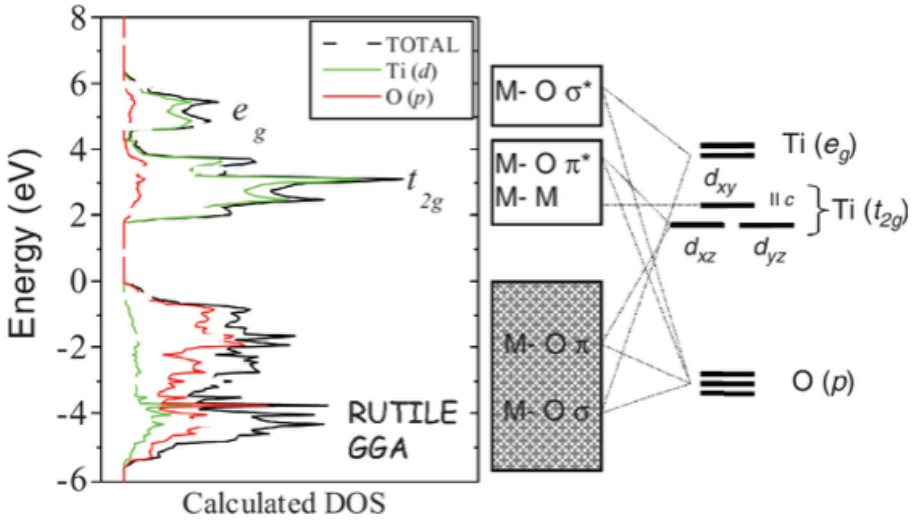

Figure 4.5: Calculated density of states (DOS) of rutile-TiO_2 within the conventional GGA DFT method. The black lines denote the total DOS; the partial DOS of titanium and oxygen are represented in green and red lines, respectively. The Fermi level has been arbitrarily chosen as the origin of the energy. The right panel is a schematic representation of rutile-TiO_2 band. Reproduced with permission from The Journal of Chemical Physics, Vol. 135, 2011 p. 6

images (Fig 4.6 b and d) are dominated by the previously discussed *autocompensation effect*, whereby Ti_{5c} troughs appear bright due to the greater density of states in the *d orbitals* available above the Fermi level, while O_{br} appear dark due to filled 2p valence states.

Under UHV conditions, surfaces prepared by standard Ar^+ sputtering (500 to 1000 V) and annealing to $\sim$ 850 K in an O_2 background for 30 to 40 min, typically yield large pristine terraces of the (1 $\times$ 1) reconstructed surfaces. Fig 4.7(a) and (b) is a typical large scale image of the pristine surface after carefully sputtering annealing the substrate for several cycles. Terraces are characterized by a typical height of 3.2 Å, as observed in Fig 4.7(c). Measuring the heights of terraces can also be used to calibrate the STM piezo response, as well as assess the reduction level of the substrate. For example, heavily

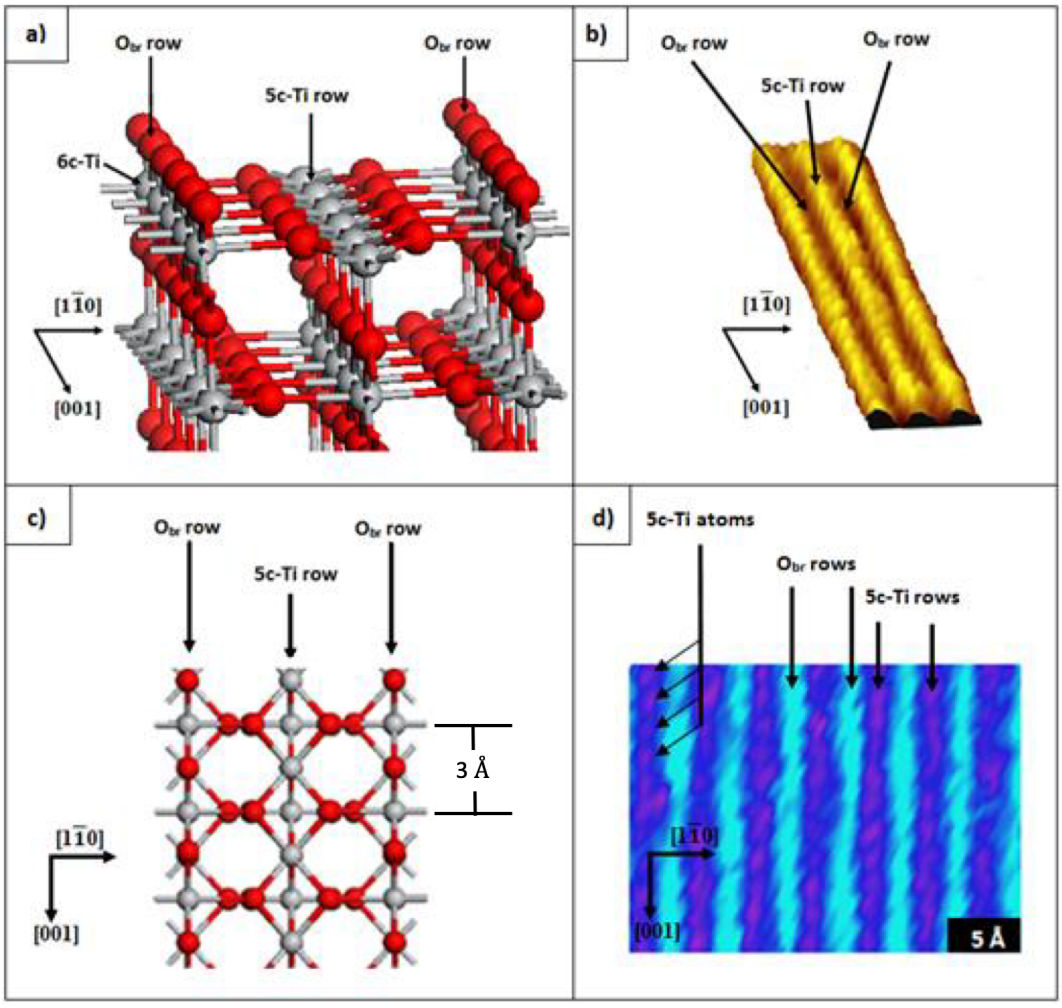

Figure 4.6: The (1 × 1) reconstructed surface of TiO_2 (110) as depicted by a ball and stick models in (a) and (c) and selected atomically resolved empty-state STM images in (b) and (d).

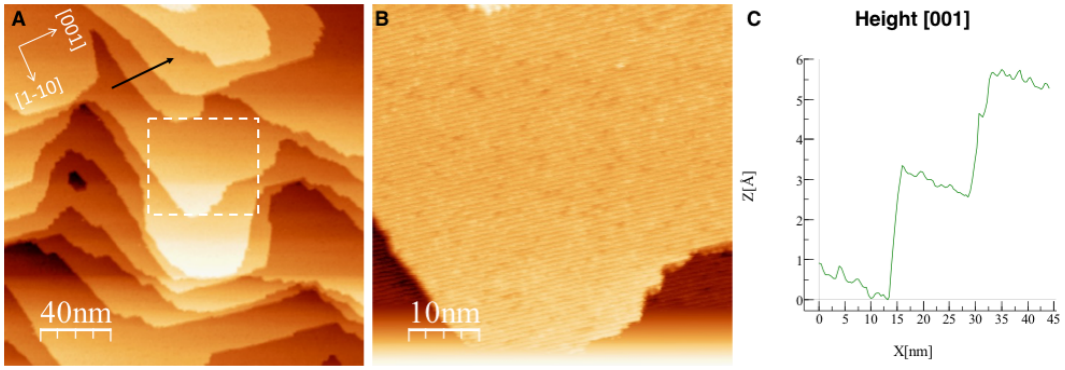

Figure 4.7: Image (a) 200 × 200 nm^2 reveals pristine, atomically flat terraces of the TiO_2 (110) surface. Image (b) is close up of the surface in (a), marked by a dashed-white lines, revealing the (1 × 1) reconstruction. A cross-section of the surface height in (c) was taken along the [001] direction, marked by a black arrow from image (a).

reduced rutile ($\geq TiO_{1.9965}$) exhibit terrace heights of ∼1.6 Å, due to the presence of extended CSP defects.[105]

4.3 Sub-Stoichiometric Surface Structure

Sub-stoichiometric or reduced substrates (TiO_{2-x}), denoted as r-TiO_2, are considered n-type semiconductors, due to the range of negatively-charged intrinsic point defects including, surface bridging oxygen vacancies (O_{vac}) and sub-surface Ti interstitials, as well as extended 1-D reconstructed defects that form in UHV. These charged defects are widely regarded as the source of reactivity in rutile titania, and therefore the subject of intense research in the surface science community. Moreover, a fundamental understanding of these n-type defects is important for understanding methanol reactivity and novel support-interactions with deposited mass-selected VO clusters that will be discussed in later chapters.

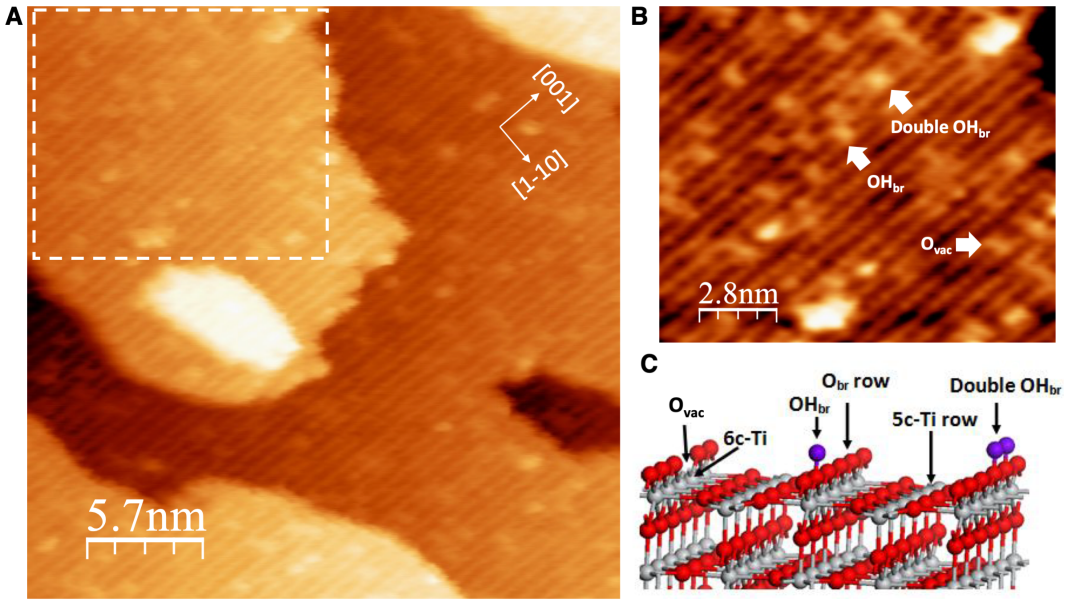

Figure 4.8: STM images of a reduced rutile TiO_2 (110) surface after numerous cycles of Ar^+ bombardment UHV annealing (900 K). (a) Is a large scale STM image of the surface. Vacancies (O_{vac}) appear as bright spots over the O_{br} rows.

For lightly to moderately reduced crystals ($TiO_{1.9996}$ to $TiO_{1.9999}$), the most abundant defect at the *surface* is a bridging oxygen vacancy defect site (O_{vac}). The vacancies are present at typical densities between 0.03 to 0.10 ML (1 ML is (1×1) surface density $= 5.2 \times 10^{14}$ cm^{-2}), depending on the surface preparation conditions (i.e. number of sputter and anneal cycles). Surface vacancies appear as bright features over O_{br} rows in STM images labeled in Fig 4.8, consistent with the literature.[50] First principles calculations rationalize the dim features observed by STM to available d-states in coordinatively-unsaturated Ti atoms located below the O_{vac} site.[50] Assignment of bright features to O_{vac} sites is also justified by the observed dissociation of H_2O into two hydroxyls (OH_{br}).

Double OH_{br}s are considered negatively charged extrinsic point defects, that appear as very bright features over O_{br} rows in STM images, as is seen in the magnified area in

Fig 4.8(b).[106] The source of double hydroxides typically come from background water in UHV conditions after several hours of exposure, depending on the quality of vacuum in the chamber and whether a cryo-pump is being utilized to getter water. Features that appear with a brightness in between double OH_{br} and O_{vac} are assigned to single OH_{br} (see Fig 4.8(b)).

Single OH_{br} sites form from water-mediated diffusion of double OH_{br} sites.[107] At room temperature, the diffusion of trace molecular water on Ti_{5c} rows is too fast to be observed by STM, but can be inferred by hopping rates of OH_{br} sites and DFT. When the surface is cooled to 270 K or below, molecular water on Ti_{5c} sites form a 1 ML coverage of hydrogen-bonded chains along the [001] direction.[108, 109, 110] Water TPD in Fig 4.9, provides ensemble-based evidence for the desorption of molecular water: the large integrated peak corresponds to 1 ML, and desorption peaks observed above 270 K correspond to hydroxyl recombination, in agreement with the literature.[108, 111]

Surface O_{vac} are also reactive sites for the facile dissociation of O_2, typically found as a contaminant in our UHV chambers if a small leak is present. Otherwise, O_2 should not be present in a UHV system.[65] Gas phase O_2 typically dissociate at O_{vac}s to regenerate O_{br} sites and an oxygen adatom (O_{ad}), located atop a nearby Ti_{5c} site. Surfaces oxidized by this way are denoted o-TiO_2, and are typically characterized by an O_{ad} density nearly commensurate with the original O_{vac} density on the surface. The O_ad species is readily observed in a large scale STM image in Fig 4.10(a), prepared by 156 L of O_2 *directly exposed* to the reduced surface at 300 K. Heights for the bright features on the Ti_{5c} observed in the magnified image Fig 4.10(b) reveal a range of heights between 25 - 40 Å, consistent with O_{ad}.[50] Typically, we prepare o-TiO_2 surfaces at RT, as O_2 dissociation

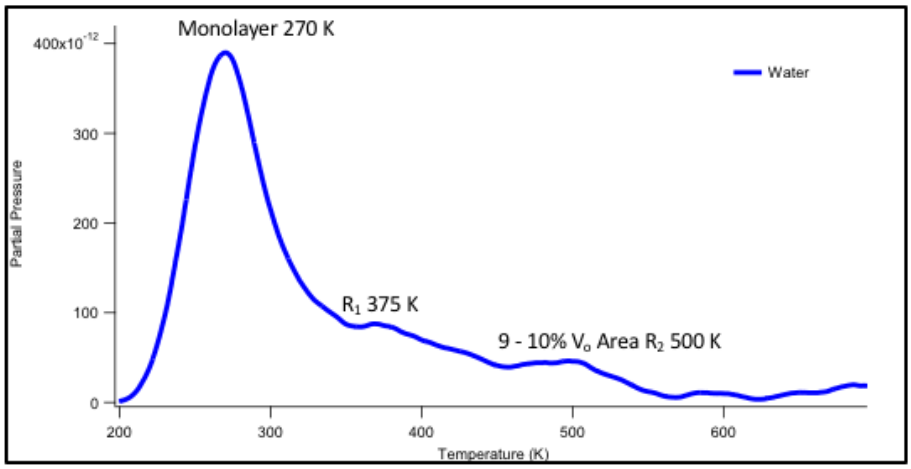

Figure 4.9: Quantitative water TPD on a reduced TiO_2 (110) sample purchased from Princeton. All peaks are calibrated to literature values. The major desorption peaks are listed by monolayer, recombination 1 (R_1) and recombination (R_2). The peak R_2, corresponds to hydroxyl recombination at O_{vac} sites. The manipulator and sample were cooled cryogenically with liquid N_2. The sample was flashed to 600 K for 10 sec to desorb hydroxyl contaminants before water exposure. Water was degassed with several freeze-pump-thaw cycles describe in the gas manifold section

at a O_{vac} site is thermally activated down to temperatures between 150 K to 180 K.[112, 113, 114] Although O_{ad} are extrinsic point defects, they are relatively stable, as indicated by their high diffusion barrier ($\sim$ 1.1 eV).[115] The stability of single O_{ad} on Ti_{5c} is at this point in time remains unclear. Interestingly, these O_{ad} are not inert, as they can facilitate various Bronsted acid/base reactions with oxygenates, like H_2O and CH_3OH.[116, 117, 118]

A second brighter feature, enlongated along the Ti troughs in Fig 4.10(b), is consistent with the closely- spaced O_{ad} pair, first reported by Wendt et al.[101] It should be noted that O_{ad} pairs appear as singular features in the magnified image in Fig 4.10(b), due to the large scale scan parameters and low D/A gain settings when the image was taken. Pairs of O_{ad} have been shown by several groups to be indicative of a second dissociation

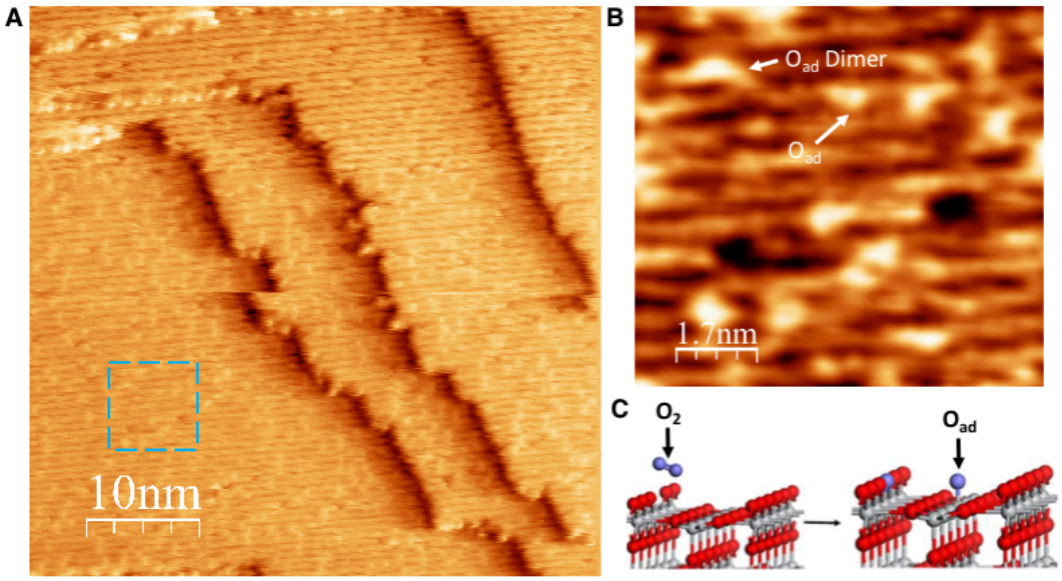

Figure 4.10: Reduced TiO_2 (110) surface after exposure to 156 L of O_2 at 300 K. The oxidized surface is denoted o-TiO_2. (a) Typical large scale STM image of o-TiO_2 and a magnified image in (b) of an area, marked by a blue-dashed box. (c) Ball and stick model of dissociative adsorption of O_2 to fill an O_{vac} site and form an O_{ad}.

channel at Ti_{5c} sites, and not statistically correlated with O_{vac} sites.[101, 119] However, density functional calculations by several groups indicate that O_2 dissociation at a Ti_{5c} site is not favorable on stoichiometric surfaces (denoted s-TiO_2), as no excess electrons are available for the reaction.[120, 121] Wendt et al.[101] employed STM and photoelectron spectroscopy to show that the second dissociation channel is mediated by sub-surface Ti interstitial sites, as deduced by the formation of TiO_x islands upon annealing the O_{ad} decorated surface to 393 K (see Fig 4.11(a - c)). DFT results from the same report rationalized that dissociation over a Ti_{5c} site is exothermically downhill by 4 eV when sub-surface Ti^{3+} interstitials donate 0.9 electrons to adsorbed O_2. The barrier for Ti^{3+} interstitial to diffuse to the surface of an o-TiO_2 surface was found to be $\sim$ 1 eV with an onset of diffusion around 390 K. Understanding the stability and diffusion barrier Ti^{3+} interstitials will be important in understanding the reactive sites for methanol in

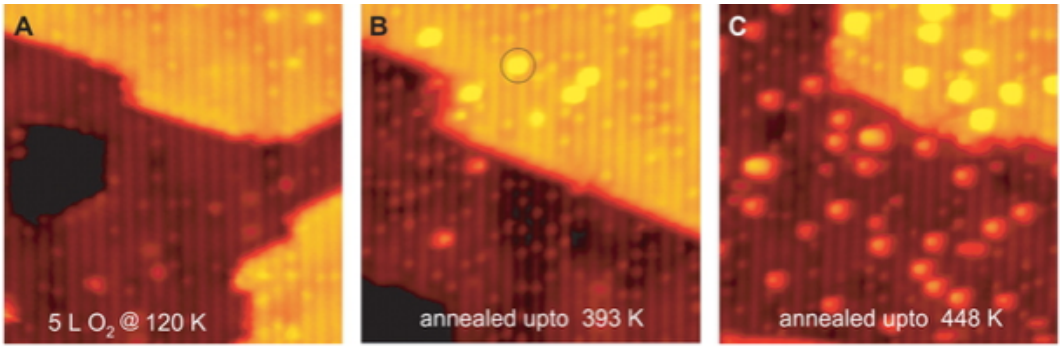

Figure 4.11: STM images (150 Å× 150 Å) of a reduced TiO_2 (110) crystal characterized by an O_{vac} density of $\sim$ 4.5% MLs, (A) exposed to 5-L O_2 at 120 K, (B) subsequently annealed up to 393 K, and (C) further annealed up to 448 K. The circle in (B) indicates one of the newly formed TiO_x islands on the terraces with an STM height of $\sim$ 2.2 Å. Reproduced with permission from Science, Vol. 320, Issue 5884, 2008, pp. 1755-1759.

chapter 6. In addition, a fundamental understanding of both channels of O_2 dissociation in preparation of o-TiO_2 surfaces is important for the deconvolution of reactivity from the different types of point defects.

4.4 Origin of Excess Electrons

Now that the different types of point defects in r-TiO_2 have been discussed qualitatively, we can discuss their electronic structure and their contribution to the excess electrons present at the surface. Understanding the nature of excess electrons and their origins at a fundamental level is absolutely necessary for unraveling the complexities and disparities found by many groups concerning the adsorption and reactivity of H_2O and oxygenates. More importantly, the models discussed below will be useful for elucidating the adsorption and reactivity of methanol, and support effects on VO clusters discussed in the proceeding chapters.

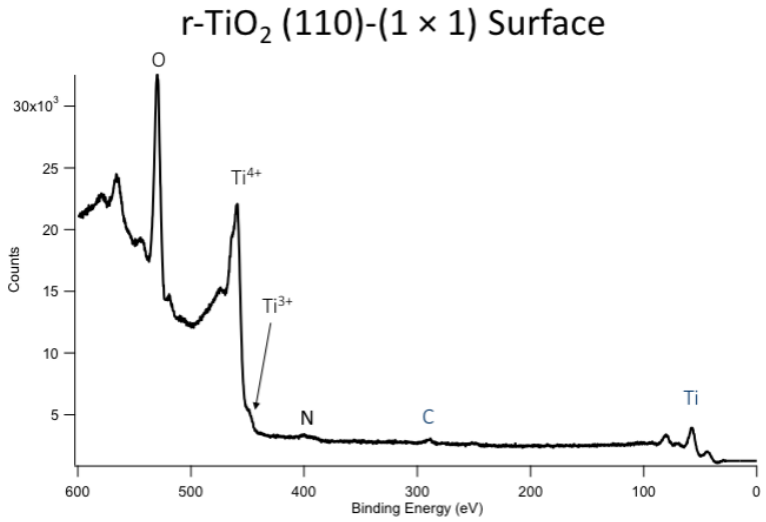

Figure 4.12: XPS survey scan of reduced TiO_2 (110) surface after several cycles of sputtering and annealing to 880 K. The source of the X-rays is a non-monochromatic Al filament. The electron detector captures electrons at an escape angle of 45^o with respect to the surface and the pass energy set to 50 V. These settings account for the low energy resolution spectrum.

As discussed earlier, cleaning rutile substrates by standard surface science methods under UHV conditions gives rise to negatively charged intrinsic (Ti interstitials, O_{vac}) and extrinsic (OH_{br}, O_{ad}) point defects. Spectroscopically, oxygen-deficient substrates are characterized by the appearance of an occupied $3d^1$ band-gap state, typically located $\sim$ 0.8 eV below the Fermi Level.[50] In XPS, the $3d^1$ state in r-TiO_2 is assigned to the Ti^{3+} binding energy state, seen in Fig 4.12. Thus, there is a strong correlation between the Ti^{3+} band-gap state and n-type point defects observed in r-TiO_2 substrates. However, questions that naturally arise are: which defect contributes the most to the occupied $3d^1$ band-gap state and what is the physical and chemical nature of these excess electrons? Solutions to these questions remain contentious, with several disparate views expressed among the theorists and experimentalists in the surface science literature.

Henrich et al.[122] pioneered the first efforts to spectroscopically observe Ti^{3+} on a defective surface, and ascribed the process to the formation of O_{vac} sites and 2 electrons. Thus, O_{vac} sites contribute two electrons to the dissociation of O_2, in the reaction,

$$O_2^0 + O_{\text{vac}} + 2Ti^{3+} \xrightarrow{\text{T} \geq 150 \text{ K}} O_{br}^{2-} + O_{ad}^0 + 2Ti^{4+}. \tag{4.1}$$

In addition, the dissociation of water at O_{vac} sites can be written as,

$$H_2O^0 + O_{\text{vac}} + 2Ti^{3+} \xrightarrow{\text{T} \geq 187 \text{ K}} 2OH_{br}^- + 2Ti^{4+}, \tag{4.2}$$

where each OH_{br} site now is assigned a formal charge of -1. The O_{vac} model for excess electrons holds up when hydroxylated-rutile (h-TiO_2) is exposed to low amounts of O_2, in which the overall reaction,

$$4OH_{br}^- + O_2 \xrightarrow{\text{T} \geq 190 \text{ K}} 2O_{br}^{2-} + 2H_2O^0, \tag{4.3}$$

proceeds by several reaction intermediates.[123, 124, 125] The model breaks down, however, when h-TiO_2 surfaces exposed to larger amounts of O_2 ($\geq$ 90 L) does not react stoichiometrically to produce the commensurate number of O_{ad} products. This is in direct contradiction with the reaction,

$$2OH_{br}^- + 2Ti^{3+} + O_2 \xrightarrow{\text{T} \geq 240 \text{ K}} 2O_{br}^{2-} + 2Ti^{4+} + H_2O^0 + O_{ad}^0, \tag{4.4}$$

first proposed by Henderson et al.[126] Instead, Selloni and co-workers found that H_2O_2 is the most stable product in their DFT calculations.[127] In an effort to resolve the

contradiction, Thornton and co-workers employed both STM and DFT to show that sub-surface Ti interstitials must donate electrons in the proton-mediated reduction of O_2, which results in a charge-withdrawing O_{ad} product.[40] Most recently, Hansen et al.[128], attributed the formation of excess O_{ad} features to O_2 dissociation over Ti_{5c} sites, once all the OH_{br} reactants are depleted. These findings are also consistent with attributing O_2 dissociation at Ti_{5c} sites to electron donating Ti interstitials, as discussed previously.

Furthermore, STM experiments by Lira et al.[113] quantified the number of O_{vac} sites before and after O_2 TPD from o-TiO_2 surfaces, and concluded that Ti interstitials accounted for approx. 90% of the excess electrons in O_2 dissociation. The extensive reactivity between Ti interstitials and O_2 is consistent with previous literature that modeled the growth of new rutile (1×1) terraces to the diffusion of Ti interstitials to the surface.[129, 98] In addition to being active in O_2 and H_2O dissociation, r-TiO_2 surfaces have also been shown to be active in the dissociation of benzaldehyde and phenylmethanol. This reactivity has been largely attributed to Ti interstitials.[130, 131, 132] It is clear Ti interstitials are major reactive sites in the surface chemistry of TiO_2, but it is not clear how this defect relates to the $3d^1$ band-gap state.

From the previous discussion on reactivity, one might be justified in assigning the $3d^1$ band-gap state to sub-surface Ti^{3+} interstitials, however, there is evidence that suggests O_{vac}'s are responsible. Additional evidence indicates the source of the excess electrons is inconsequential and only dependent on the nature of the rutile structure. The ambiguity in these views may lie in the fundamental differences in techniques employed and the quality of vacuum maintained in the experiment. Nonetheless, understanding the

complexities in the electronic structure of defective rutile will help our understanding of methanol reactivity. As discussed earlier in the context of oxygen dissociation, Wendt et al.[101], utilized valence band photoelectron spectroscopy with STM and DFT and found surprisingly, that titration of O_{vac}s by O_2 and H_2O did not affect the $3d^1$ band-gap state. Only when TiO_x islands formed by the diffusion and reaction of Ti^{3+} interstitials with adsorbed O_2, did they observe complete attenuation of the $3d^1$ band-gap state.[101] Contrary to Wendt's findings, Kimmel and co-workers investigated O_2 chemisorption on variously prepared surfaces, including electron-radiated surfaces by molecular beams, TPD, and ESD found O_{vac} defects were the largest contributors to O_2 dissociation.[123] However, the conclusions reached by in this same report are based on the following major assumptions: (i) electron-radiated surfaces have more surface O_{vac}s than Ti interstitials, (ii) electron-radiation of r-TiO_2 substrates does not change the (1×1) structure, and (iii) the O_2 sticking probability at 25 K is unity for differently prepared surfaces. Based on these same assumptions, Yim et al.[133], employing UPS, found a linear relation between the $3d^1$ band-gap state and O_{vac} densities in electron-radiated surfaces and therefore concluded that only O_{vac} sites are the origins of the band-gap state.

Photoelectron diffraction (PhD) experiments by Krüger et al.[134], indicate that excess electrons localize at Ti^{6c} sites in the second and third layers of r-TiO_2, as opposed to Ti interstitial sites. In addition, Krüger and co-workers[135] investigated initially oxidized surfaces that are then chemically reduced by Na deposition, and found no spectroscopic differences between r-TiO_2 and Na-TiO_2 surfaces. Krüger and co-workers concluded Ti interstitials do no contribute to the $3d^1$ band-gap state, in agreement with the classical O_{vac} origin model. However, these findings assume excess charge must localize specifically

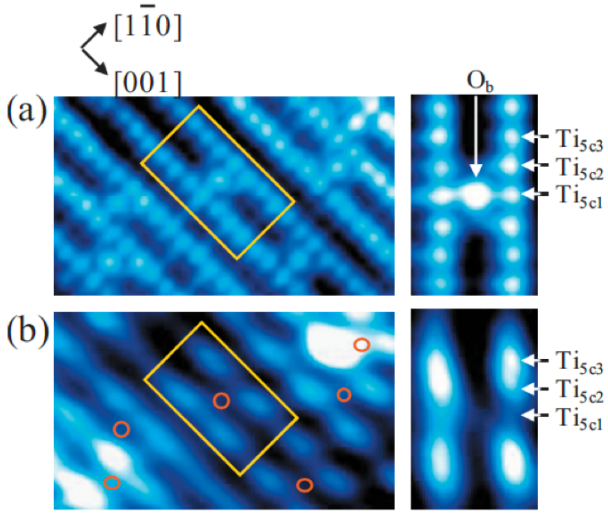

Figure 4.13: Constant current 3.4 × 5.8 nm STM images of the TiO_2 (110) at 78 K. (a) Unoccupied state image (V = +0.6 V; I = 0.6 nA) is ovbserved in forward scanning, and (b) occupied state (V = -1.1 V; I = 0.1 nA) in reverse scanning. The expanded images (2.1 × 1.3 nm) around an O_{vac} (yellow rectangles) of (a) and (b) are also shown. Red open circles indicate the positions of O_{vac}'s. Reproduced with permission from Journal of Chemical Physics, Vol. 130, Issue 134502, 2009.

at Ti interstitials (and only in second and third layers), which Papageorgiou et al.,[40] has indicated with O_2 reactivity and STS studies, is not the case. Nonetheless, Krüger and co-workers make an interesting point: despite the origins of the excess electrons, the electrostatic interactions of the rutile lattice confine the $3d^1$ charge to an array of surface and near-surface Ti atoms- so called *polarons*. This finding also concurs with recent *filled-state* STM experiments by several groups that observed localization of $3d^1$ surface states on Ti_{5c} sites located near-by O_{vac} sites.[136, 137] Fig 4.13 illustrates the presence of lattice polarons in the filled states images on the defective rutile TiO_2 (110) surface. From a chemical view, the reactivity of O_2 with h-TiO_2, as well as the favored adsorption of CO at Ti_{5c} sites has been alluded to surface polaronic states.[40, 138] While the exact origins for the $3d^1$ band-gap state remain uncertain, Ti interstitials without doubt are involved. It is the opinion of this author that Ti interstitials are at least sufficient but

not necessary in modeling the electronic structure and chemical properties of the rutile (110) defective surface.

Chapter 5

Visualizing Wet Electron States in Methanol on TiO_2 (110)

5.1 Introduction

Understanding the behavior of electron solvation and localization in a 2D dielectric medium on a semiconductor surface is foundational to advancing sustainable energy technologies, such as water splitting on titania.[87] Alcohols on titania are also a subject of interest, as methanol can be used as a sacrificial agent for improving the oxidation of water[88], as well as a source for hydrogen[89], and as a model for photooxidation studies[90, 91].

Initial studies into methanol wet electron states have addressed their chemical and dynamic nature. Petek and co-workers discovered that photoexcitation of electrons from the substrate $3d^1$ defect band, results in the population of a resonant surface-state over a broad range of energies (2.1 - 2.5 eV).[139] The same report also showed that wet electron

state is highly sensitive to the surface coverage and localizes over adjacent substrate bridging oxygen rows. A model of methanol's electronic structure on the rutile TiO_2 (110) surface is illustrated in Fig 5.1. The model shows a clear spatial difference in the unoccupied orbitals associated with the ground state and wet electron state. Isotopic (CH_3OD) labeling experiments reveal wet electron states relax back to the conduction band through a manifold of adiabatic and non-adiabatic decay pathways; the latter of which is assigned to a concerted proton coupled electron transfer.[140] Calculations show that the response of methanol to the injection of the excess electrons is stabilized by dangling electropositive hydrogen atoms, created from the scission of interfacial hydrogen bonds.[141, 142]

Efforts to understand the spatial distribution of methanol wet electron states however, are lacking. This is partly due to the ambiguity of the methanol adsorption state at saturated coverages. Experimentalists have reported conflicting results, with some groups claiming the saturated layer consists of both intact and dissociated methanol[60, 143], and others reporting only an intact species.[144, 145] Despite these disparate reports, theoretical results from Zhao *et al*,[141] generally becomes more stable with more intact methanol. In agreement with Zhao and co-workers, DFT calculations by Migani *et al*[146] showed that by accounting for the dielectric properties of the surface, only the intact methanol configurations lead to an accurate energy for the observed wet electron state. Moreover, Migani and co-workers predict methanol wet electron states will be spatially heterogeneous, as result of electrostatic screening with the dielectric medium of rutile TiO_2 (110) and electron-electron correlation effects.[147] Indeed, a better understanding of the wet electron state would benefit from a microscopic picture.

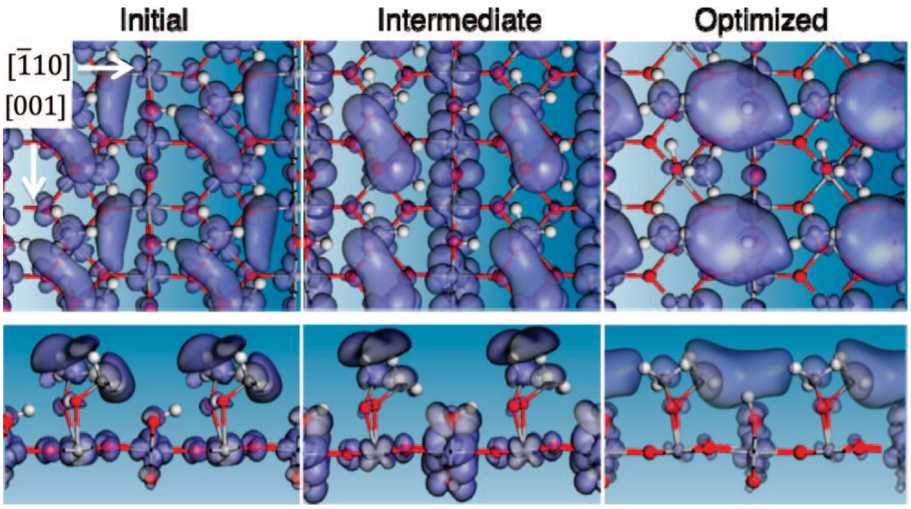

Figure 5.1: Top and side views of wet electron orbital distributions for the HD4 structure at different stages during Δ-SCF excited state optimization (see methods for more details). At the start of the optimization, electron is added to the wet electron orbital (translucent orb) in the ground state molecular geometry. During the optimization, the charge density flows initially from orbitals mainly localized on H atoms of CH_3 groups, to the O_{br} row. An increase in charge density near OH_{br} on O_{br} causes OH_{br} to break its hydrogen bond to the O atom of methoxy and rotate to nearly vertical configuration, where it stabilizes the wet electron on top of a surface OH_{br} in a pocket formed by neighboring methanol and methoxy CH_3 groups. Reproduced with permission from Chemical Reviews, Vol. 110, No. 12, 2010 p. 7094.

Here-in we employed constant current STM to directly map the spatial distribution of electronic surface states in a saturated layer of methanol on rutile TiO_2 as a function of applied bias and adsorbate coverage. The wet electron state is identified by comparing the spatial distribution of local unoccupied states with previously reported DFT calculations. We also assume the density of states for tungsten tips is independent at the biases used here in, and will have no effect on our results. Our assumption is based on a previous report.[148]

5.2 Experimental

All UHV-STM experiments were carried out at base pressure of 1×10^{-10} torr in a surface science apparatus discussed in detail elsewhere.[149] STM experiments were performed on a TiO_2 (110) substrate (Princeton Scientific), polished on one side ($10 \times 2 \times 0.5$ mm^3) and mounted in a sample holder with a silicon slab for resistive heating. The STM substrate was prepared by Ar^+ bombardment and annealing to $\sim$ 880 K to yield a O_{vac} density of approx. 4.4% ML (1 ML = 5.2×10^{14} cm^{-2} Ti atom density) as determined by direct counting over areas greater than 2000 nm^2. All STM experiments were performed in a separate STM chamber of the apparatus (base pressure $\leq 1 \times 10^{-10}$ torr), on an RHK STM100/AFM100 combination scan head, see elsewhere for more details see.[149] All micrographs were obtained with electrochemically etched W tips and cleaned by several cycles of electron-bombardment. Empty-state constant-current images were obtained at RT with biases between +1.0 V to +2.2 V, and processed with WSxM 5.0 (Nanotech) software.[150]

5.3 Results and Discussion

Large scale micrographs in FIG 5.2A-B, indicate that the (1 × 1) reconstructed surface, consisting of alternating five-fold coordinated Ti (Ti_{5c}) troughs (bright rows), and geometrically protruding bridging oxygen (O_{br}) rows (dark rows), strongly templates the adsorption of methanol at room temperature. The bright features in FIG 5.2A and FIG 5.2C, correspond to bridging oxygen vacancies (O_{vac}) and bridging hydroxyl (OH_{br}) contaminants present on the bare surface, and are typical of a substrate prepared *in vacuo*. Measurements below 2.00 V, reveal the integrated DOS localize on Ti_{5c} troughs (black dotted lines) in FIG 5.2(D), resulting in the appearance of 1D structures along the [001] crystallographic direction.

Previous DFT calculations by Zhao *et al.*[141] ascribe the localization to unoccupied CH_3 molecular orbitals of several isoenergetic ground state adsorption structures, whereby all methanol adsorbates either remain intact, or half undergo dissociation of the O-H bond. In these calculations, the dominance of unoccupied CH_3 molecular orbitals in the ground state arises from the occupation of both intermolecular and interfacial hydrogen bond states. Similar trends in the ground state electronic structure for dilute coverages of methanol were also reported by STM and DFT experiments.[151] Furthermore, similar charge density contours of these ordered 1D structures were observed between 1.0 V to 2.0 V (not shown), providing further evidence methanol is stable and in its ground state at room temperature. Recognizing that these 1D structures are due to filled hydrogen bond states, is critical for the later discernment of wet electron states, which arise from the scission and reorientation of these hydrogen bond states to stabilize the injection of energetic excess electrons.

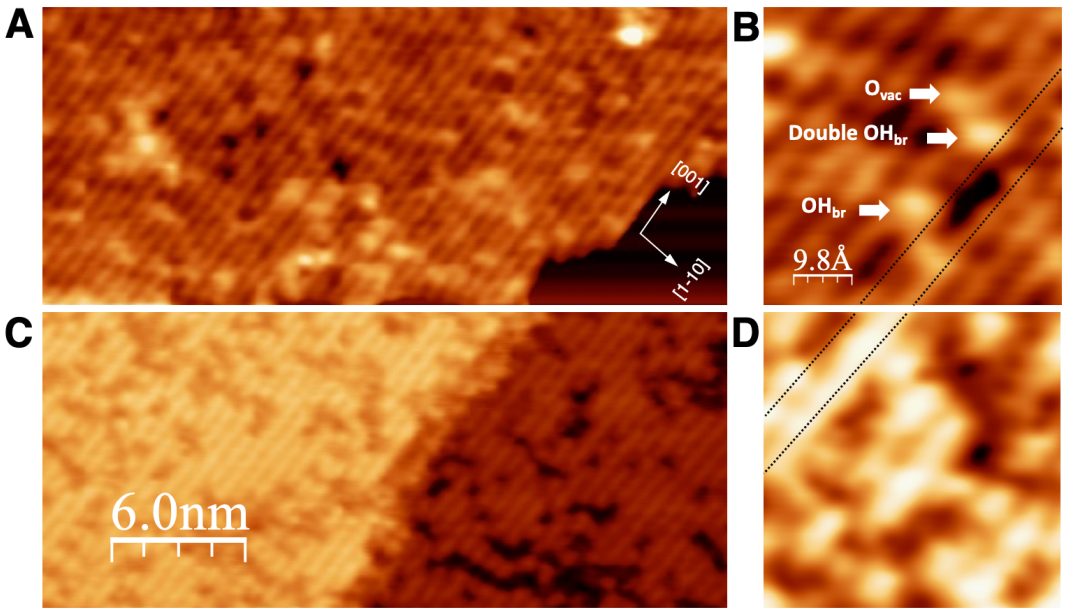

Figure 5.2: Selected room temperature images (150 × 300 Å^2) of the reduced TiO_2 (110) surface before (a) and after exposure to 100 L (1 L = 10^{-6} torr·sec) of methanol at room temperature (b). Images were taken with a 1.87 V bias. High resolution images (50 × 50 Å^2) indicate methanol preferentially adsorbs over Ti troughs, indicated by black-dotted lines.

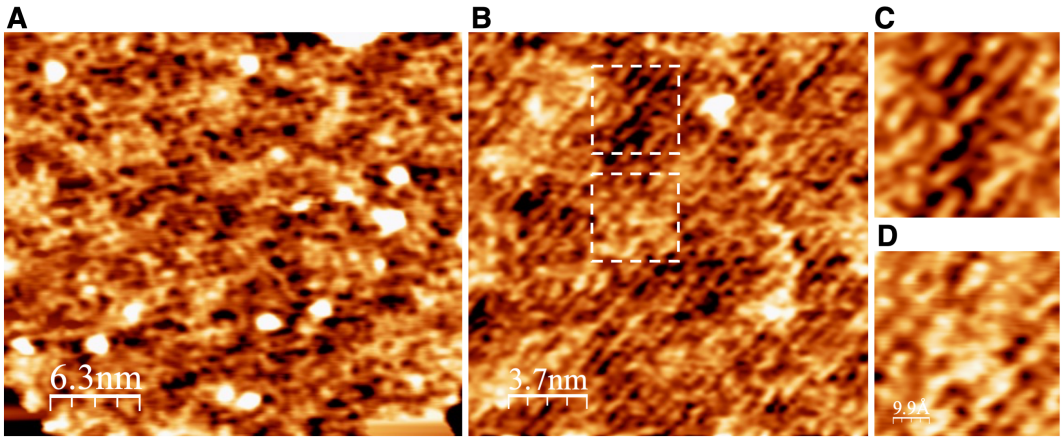

Figure 5.3: Selected large scale STM image (300 × 325 Å^2) at bias = 2.04 V of TiO_2 (110) surface exposed to 100 L of CH_3OH in (A) and a high resolution image (185 × 185 Å^2) at bias = 2.12 V in (B). White dotted lines in (B) indicate the magnified areas of the disordered clusters in (C) and and the ordered lattice states in (D).

Increasing the bias parameter into the wet electron regime resulted in drastic changes to the spatial distribution of surface states, depicted in the large scale micrograph in FIG 5.3A. Bright clusters corresponding to higher integrated local DOS, appear disordered, while darker clusters corresponding to lower integrated local DOS appear ordered. A high-resolution micrograph of the surface in FIG 5.3B reveals the stark structural differences between the bright and dark domains. These disordered clusters exhibit delocalization across the [1-10] crystallographic direction, resulting in attenuation to the underlying (1 × 1) surface order. A typical cluster, outlined by white-dashed lines in FIG 5.3(B) and magnified in FIG 5.3C, illustrates the degree of delocalization and disorder. The geometry of the delocalized states resemble several methanol wet electron state configurations predicted in the literature, suggesting the disordered clusters are indeed, wet electron states.[140, 141, 146]

Contrary to the bright clusters, the dark clusters in FIG 5.3D exhibit a high degree of order, resembling the underlying (1 × 1) surface structure. A typical dark domain, outlined by white dotted lines in Fig 5.3B and magnified in FIG 5.3C, illustrates the similarity to the underlying substrate order in the unoccupied states. The average distance between the rows in FIG 5.3D is ∼6.7 Å, is nearly identical to the typical dimensions of the (1 × 1) unit cell: 6.5 Å× 3.0 Å.[50] These dark, higher ordered domains may reflect a configuration of methanol that does not have a wet electron state, as recent DFT calculations by Migani *et al.*[146], found only intact methanol adsorbates to have the requisite interfacial hydrogen bonds to stabilize wet electron states. Although, since methanol does not occupy all Ti sites at room temperature, these dark domains may also represent the absence of methanol. These new surface states appear to be robust at room temperature, as a cross-correlation analysis of both the trace and retrace indicate nearly identical features (see supporting information). In addition, we observed no variations to these features when imaged with similar parameters (±100 mV and ±100 pA) from those reported here. Clearly, the features observed with biases above 2.00 V can be ascribed to electronic effects from the surface.

To determine if the electronic effects are attributed to methanol adsorption, the substrate was annealed to ∼640 K and imaged with similar parameters, shown in FIG 5.4. According to previous temperature programmed desorption studies by Henderson *et al.*[60], and recent STM investigations by Robins *et al.*[152], annealing to 640 K will result in the desorption of a majority of methanol and methoxides from Ti_{5c} and O_{vac} defect sites. The micrograph in FIG 5.4A, imaged at 2.00 V, indeed indicates the majority of methanol and methoxides desorbed. Cross sections of the bright sym-

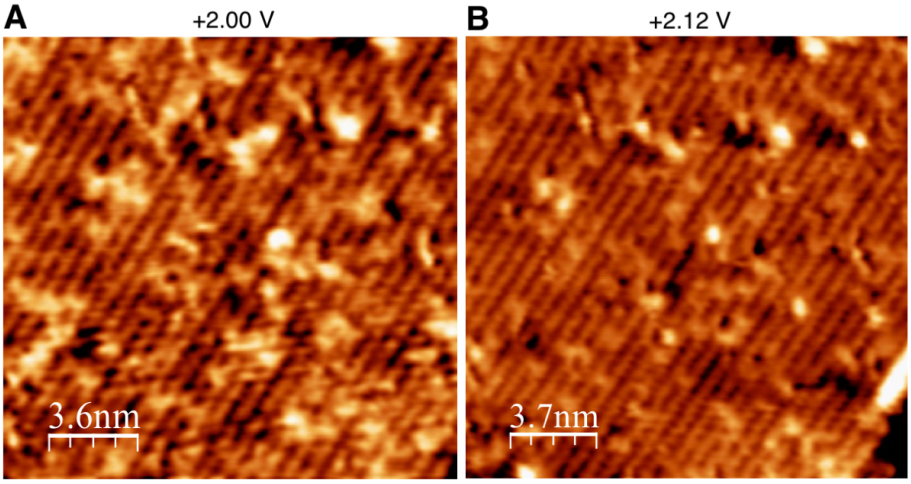

Figure 5.4: Selected micrographs (185 × 185 Å^2) of the methanol decorated surface TiO_2 (110) surface after annealing to 640 K: (a) +2.00 V (b) +2.12 V

metrical (see supporting information) features adsorbed on Ti_{5c} and O_{vac} defect sites indicate heights (∼0.75 Å) characteristic of dissociated methoxides, in agreement with the literature.[152, 151, 153]. Additionally, the defective (1 × 1) reconstructed surface was recovered. When the same surface was imaged in the wet electron regime, see Fig 5.4B, no delocalization of the methoxide unoccupied states were observed and no delocalization of the underlying (1 × 1) surface was observed. Furthermore, no disorder of the substrate was observed. The lack of electronic effects in Fig 5.4B confirms: (1) the disordered electronic state is not strictly a substrate effect, and (2) the wet electron states are absent for dilute methanol coverages, in agreement with 2PPE studies by Onda *et al.*[139] Thus the electronic effects observed in the wet electron regime can be attributed to methanol at saturated coverages.

Further evidence the delocalized 2D states are electronic in origin lie in the recovery of the localized 1D chain states. An abrupt change from the delocalized 2D state (bias = +2.17 V) in FIG 5.5A to a localized state in FIG 5.5B was immediately observed

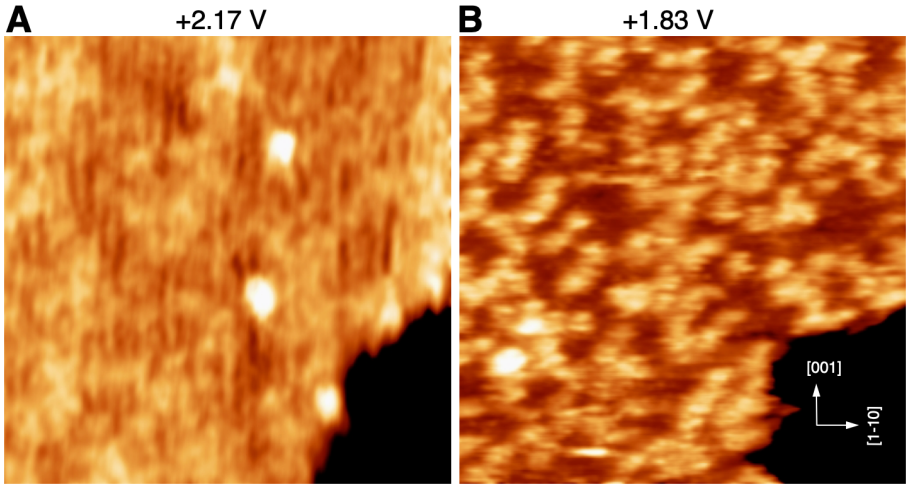

Figure 5.5: Selected micrographs (200 × 100 Å^2) of CH_3OH/TiO_2 (110) of the same area after switching the bias from: (A) +2.17 V to (B) +1.83 V.

in the same area of the substrate when the voltage bias was lowered (bias = +1.83 V). The chemical nature of the methanol species and the presence of OH_{br} could not be distinguished however, the localized 1D chain features along the [001] direction are stable after an additional 12 hours of scanning. The similarity between these 1D chains and the methanol 1D chains observed in FIG 5.2B, suggests the 1D chain features in FIG 5.5B are likely the same methanol species. The retraces (not shown) of the area in the other scan direction had no apparent changes, again suggesting these 2D LUMO states are electronic and reversible in origin.

The drastic changes in the spatial distribution of methanol LUMO states from a localized 1D state to a delocalized 2D state and their absence at dilute adsorbate coverages at 2.05 V above the Fermi level is consistent with the resonant wet electron state previously observed by 2PPE experiments.[139] We therefore ascribe our results to a direct visualization of the wet electron state. Interestingly, the apparent delocalized 2D LUMO states

are interspersed among ordered 1D states throughout the substrate (see Fig5.3A-D). We attribute the ordered 1D states to a configuration of methanol that is not conducive to the 2D wet electron state. Our proposed assignment of these 1D ordered states in Fig5.3B and D are supported by recent DFT calculations that concluded only intact methanol adsorbates have the requisite interfacial hydrogen bonds to stabilize the 2D wet electron state; as opposed to methoxide states which were found to have only 1D LUMO states.[146] Thermal programmed desorption studies by Henderson *et al*[60] also support a mix of intact and dissociated configurations of methanol adsorbates at room temperature. Another driving force for the spatial heterogeneity of the delocalized 2D LUMO state may arise from dielectric screening of interfacial adsorbate dipoles formed from strong methanol-substrate binding as suggested by calculations.[147] Similar to our results, a previous STM investigation into saturated coverages of water on Si (100) - (2 $\times$ 1) revealed a sudden onset of delocalized 2D LUMO states at 2.6 V above the Fermi level, and were associated with electron states stabilized by dangling hydrogen bonds from nearby hydroxyl adsorbates.[154] Also similar to our results, the STM images reported from Chander et al. revealed the trapped electron state were interspersed heterogeneously throughout the surface.

5.4 Conclusion

We have shown with constant-current STM that wet electron states can be directly visualized by changes in the spatial distribution of the integrated local density of states in methanol. Our assignment of methanol wet electron states are justified by the similar energy parameters with those reported in the literature. The recovery of localized

states from the wet electron state suggests that the change in the spatial distribution of methanol states are electronic in origin. Our results also indicate that the wet electron state can be accessed without the the creation of substrate photo-induced electron hole pairs. Surprisingly, methanol wet electron states appear heterogeneously throughout the surface, suggesting that dielectric properties of the substrate interface may affect the solvation of excess electrons in methanol. A full understanding of wet electron states on a semiconductor substrate may therefore require more than a quantum mechanical treatment but also consideration of their thermodynamic properties. These results are likely to be a general property of the protic solvent monolayer, like water.

Chapter 6

Methanol Reactivity on Pristine TiO_2 (110)

6.1 Introduction

Investigations into the reactivity of methanol on TiO_2 surfaces are largely motivated by emerging sustainable energy and industrial chemical technologies. Considerable research efforts have focused on understanding the photochemistry of methanol for environmental remediation[155, 156, 157] and reforming reactions.[158, 159, 160] Fundamental reactivity studies use single crystal rutile TiO_2 (110) as the model substrate of choice, due in part to its high thermal stability and its well-characterized physical and chemical properties.[50, 85, 86, 161] Despite the extensive characterization of TiO_2 (110) surfaces, little is known about the sites responsible for methanol reactivity.

Correlating atomic-scale details of methanol adsorption with surface reactivity is difficult due, in part, to the reducibility of rutile TiO_2. Upon sputtering and vacuum-

annealing the substrate (as is standard practice in surface science), oxygen atoms are displaced from the surface into vacuum, resulting in *excess* unpaired electrons in the Ti$3d^1$ band gap state, and a rich variety of point defects including surface bridging oxygen vacancies (O_{vac}), bulk oxygen vacancies (f-centers), sub-surface Ti interstitials, and extended reconstructions such as the (1 × 2) and (2 × 1).[50, 85]. Historically, O_{vac} defects have been classified as the primary electron donor and the source of reactivity.[50] Recent evidence of a Ti interstitial pathway in the reoxidation of defective TiO_2, however has challenged this notion.[129, 97, 98, 101] Ti interstitials have been implicated as stabilizing sites for benzaldehyde and phenyl-methanol.[130, 132]

Methanol reactivity on TiO_2 (110) has been studied studied extensively in the surface science community. The production of formaldehyde, ethylene, and methane has been shown to vary with varying levels of reduction to the titania substrate. For example, some groups observed methanol disproportionation to formaldehyde from an oxidized surface, but not from a reduced surface.[60, 52, 53, 61] Conversely, some groups have observed disproportionation to formaldehyde from reduced surfaces.[162, 117, 118] In addition to formaldehyde, Madix and co-workers observed methane simultaneously on a lightly reduced surface, and only ethylene from a heavily reduced surface.[162] Despite these disparate observations, many groups have adopted the view of Henderson *et al.*[60], that methoxides disproportionate into formaldehyde and methanol on Ti_{5c} sites. However, the stability of these methoxides at high temperatures is not well known; nor is the selectivity of methanol towards methane and ethylene well understood.

Here-in we report methanol TPD/R experiments performed over various levels of reduction to TiO_2 (110) - (1 × 1), to show that formaldehyde and methane are produced

by a second disproportionation reaction. Our TPD/R results indicate that in addition to dissociative adsorption at vacancy sites, methanol oxidizes the reduced surface and this reaction is intimately linked to sub-surface Ti interstitials defects. We confirmed the contribution of Ti interstitial defects to methanol reactivity by employing UHV-STM to image methanol adsorbates along the temperature programmed reaction pathway.

6.2 Experimental

TPD/R experiments were carried out on a single crystal TiO_2 (110) (Princeton Scientific), polished on one side (10 mm^2 dia. $\times$ 1 mm thick), mounted in a (OHFC copper) sample holder and equipped with an isolated silicon slab for resistive heating, and K-Type thermocouple wires for temperature readout. The substrate was prepared by several cycles of Ar sputtering (1 kV, 2μA for 20 minutes) and alternating anneal cycles in UHV and O_2 at 900 K for 10 minutes until a blue crystal with a O_{vac} density of approximately 5.2% was prepared. The O_{vac} density was determined by integrating the second methanol recombination desorption peak with respect to the saturated single monolayer (1 ML = 3.2 $\times$ 10^{14} cm^{-2} Ti atom density) covered sample (TPD spectrum not shown). Substrate cleanliness was checked by auger electron spectroscopy (AES). TPD experiments were carried out with a residual gas analyzer, quadrupole mass-spectrometer (Stanford Research Systems RGA 200 QMS), mounted in the surface-science chamber of our apparatus, see elsewhere for more details.[149] Typical base pressure in the surface-science chamber was maintained at approximately 5 $\times$ 10^{-10} Torr. Methanol (Fisher Scientific, 99.9 %) was purified by several freeze-pump-thaw cycles before usage. All TPD/R experiments were performed with a heating rate of 1 K/sec. Methodology for formaldehyde

TPR analysis and mass-fragment cracking ratio details can be found in Price et al.[61] Briefly, the formaldehyde signal is the excess signal between m/z = 29 contributions from methanol and formaldehyde as well as the cracking ratio of methanol to m/z = 29:31 = 1.02. The equation for the overall formaldehyde signal is

$$I_{\mathrm{Form}} = I_{29} - (1.02 \times I_{31}). \tag{6.1}$$

To calculate methane, the cracking ratio m/z = 15:31 was found in our system to be 0.63. Excess signal calculated as

$$I_{\mathrm{Meth}} = I_{15} - (0.63 \times I_{31}) \tag{6.2}$$

can then be assigned to methane desorption.

All UHV-STM experiments were carried out on a second TiO_2 (110) substrate (Princeton Scientific), polished on one side ($10 \times 2 \times 0.5$ mm^3) and mounted in a sample holder with a silicon slab for resistive heating. The STM substrate was prepared by the same procedure used for the TPD substrate and yielded a O_{vac} density of approximately 4.4% ML (1 ML = 5.2×10^{14} cm^{-2} Ti atom density) as determined by direct counting over areas greater than 2000 nm^2. All STM experiments were performed in a separate STM chamber of the apparatus (base pressure below 2×10^{-10} torr), on an RHK STM100/AFM100 combination scan head, see elsewhere for more details see.[149] All micrographs were obtained with electrochemically etched W tips and cleaned by several cycles of electron-bombardment. Empty-state images were obtained at RT with biases between +1.4 V - 2.0 V, in constant current mode and processed with WSxM 5.0 (Nanotech) software.[150]

The substrate was transferred to the surface-science chamber for direct methanol exposure and imaged immediately afterward.

6.3 Results and Discussion

Fig 6.1(a) is a typical TPD/R spectrum of the reduced TiO_2 (110) (r-TiO_2) surface, exposed to 100 L (1 L = 1×10^{-6} torr sec) of methanol at room temperature. Methanol desorption peaks R_1 and R_2 (black trace), denote recombination between adjacent bridging hydroxyls (OH_{br}) and methoxides bound to undercoordinated Ti sites (Ti_{5c}-OCH_3) and bridging oxygen vacancies (O_{vac}-OCH_3). Both R_1 and R_2 peaks are consistent with assignments from Henderson and co-workers.[60] Concomitant desorption of formaldehyde (red trace) and methanol above 550 K, can be attributed to a disproportionation reaction between stranded Ti_{5c}-OCH_3, also consistent with the literature.[60, 162, 117, 118, 163] Stranded OH_{br} that did not contribute to methanol recombination (R_1 and R_2), were consumed by recombinative desorption of water at 500 K (see Fig6.2(a)), in agreement with the literature.[111, 108, 60] Methane (purple trace) also appears to have desorbed concomitantly with formaldehyde and methanol, possibly suggesting a disproportionation-like reaction mechanism involving stranded methoxides. If two stranded methoxides are indeed disproportionating into formaldehyde and methane, then the titania substrate should be oxidized by the production of an oxygen adatom (O_{ad}).

To confirm whether the proposed second disproportionation reaction oxidizes the surface via O_{ad}, five consecutive TPD/R cycles were performed without sputtering and annealing the sample between cycles. The fifth methanol TPD/R spectrum in Fig 6.1(b), reveals the R_2 peak, the disproportionation reaction to methanol (black trace) and

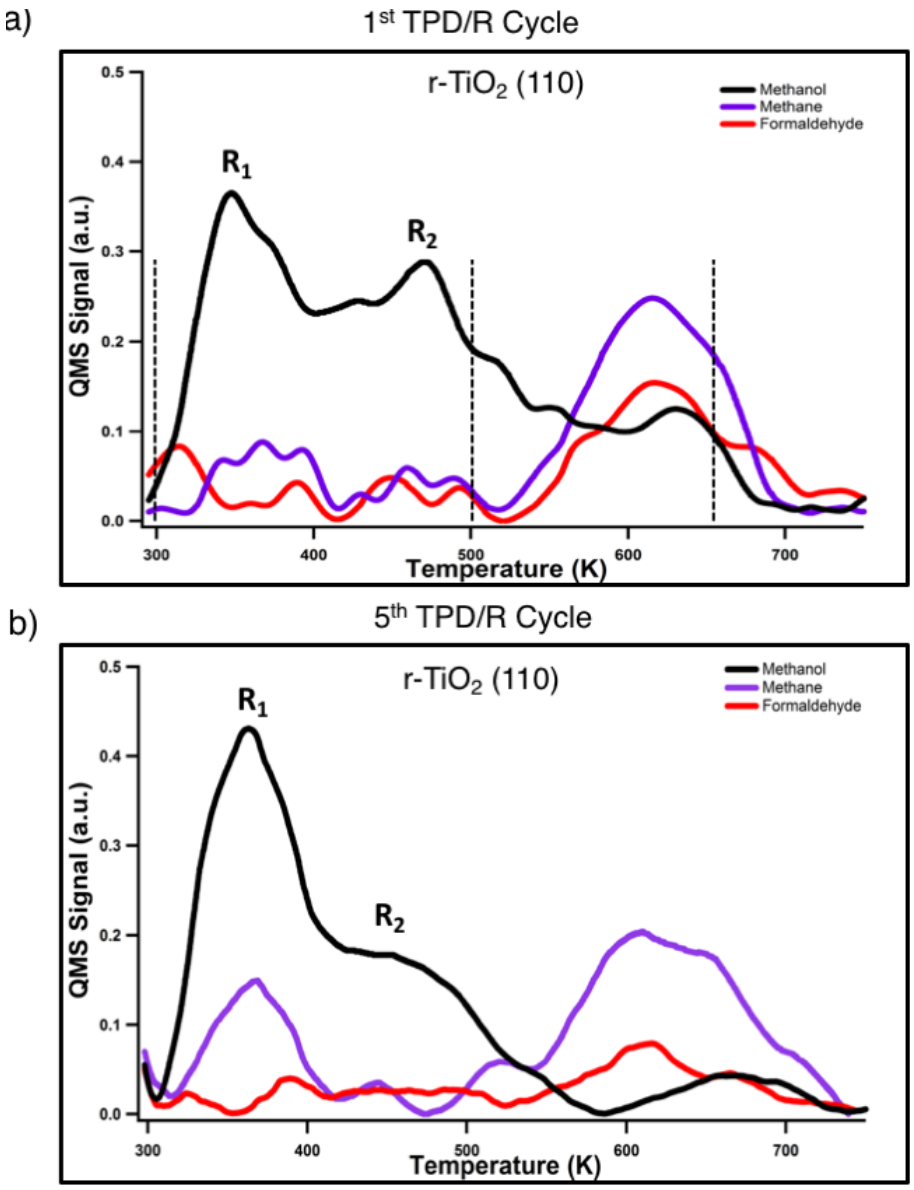

Figure 6.1: TPD/R spectrum of reduced TiO_2 (110) (r-TiO_2) prepared by exposure to 100 L (1 L = 1×10^{-6} torr sec) of methanol at room temperature (a). TPD/R spectrum on r-TiO_2 after five consecutive TPD/R cycles. The sample was not sputtered or annealed between TPD/R cycles

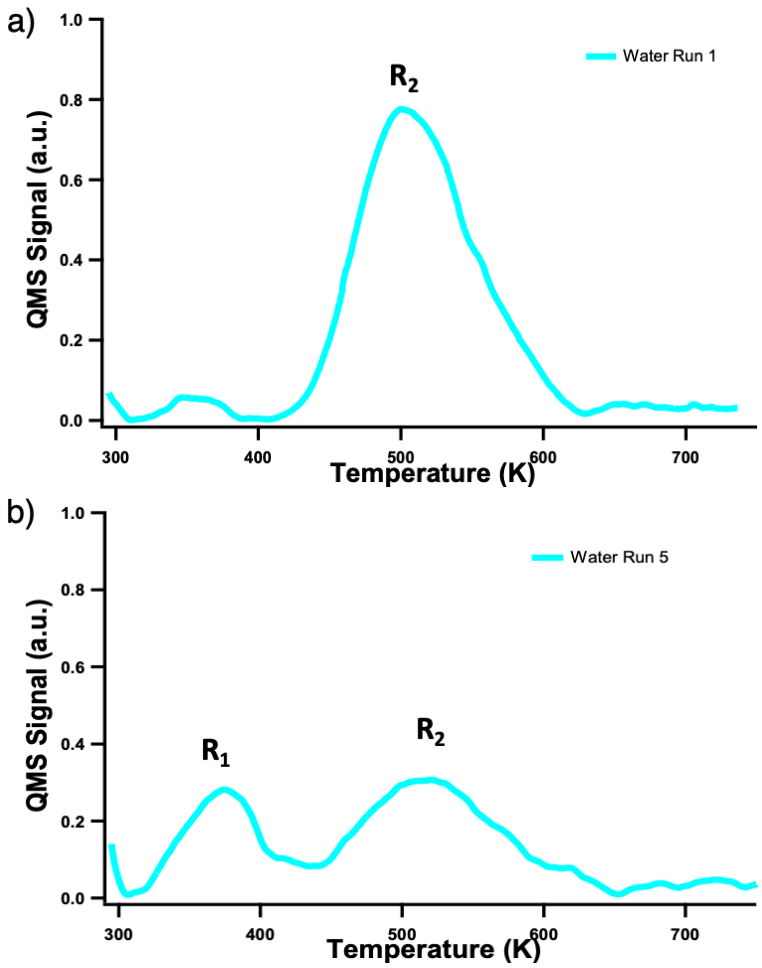

Figure 6.2: Comparative TPD water signal following 100 L methanol exposure. (top) is a spectrum of the 1st methanol TPD/R experiment denoted 1st run on r-TiO_2. (bottom) is the methanol TPD/R spectrum after the 5th consecutive run on the r-TiO_2. The surface was not sputtered or annealed between each TPD/R experiment.

formaldehyde (red trace), as well as the proposed disproportionation reaction to methane (purple trace) and formaldehyde had a substantial decrease in signal. In addition, the water desorption signal at 500 K (see Fig**??**(b)) was markedly lower. Interestingly, a new methane desorption peak below 400 K was observed. This low temperature methane peak is likely due to recombination between hydrogen adatoms (H_{ad}) and stranded CH_3. Since the sum of the R_2 and water desorption peak at 500 K is proportional to the density of O_{vac} sites, the attenuation of these desorption peaks after five consecutive TPD/R cycles indicates the surface has been oxidized. Oxidation to the surface can be accomplished by filling O_{vac} defect sites or by oxidizing sub-surface Ti interstitial defects, depending on the adsorption site of the stranded methoxide. More interestingly, the attenuation of both disproportionation reactions above 550 K, suggests at least in part that methanol reactivity depends on charge donating defects. To investigate how O_{vac} and Ti interstitial defects contribute to methanol reactivity, methanol TPD/R was performed over TiO_2 surfaces with varying degrees of oxidation.

The contribution of Ti interstitial defects to methanol reactivity can be probed by selectively oxidizing O_{vac} defects, via direct exposure to low amounts of O_2 between 180 K to 300 K. At RT, molecular oxygen dissociates at a O_{vac} site, generating a O_{br} site and neighboring O_{ad} defect on Ti_{5c}.[101, 119, 113] For O_2 exposures of approx. 10 L, this procedure typically oxidizes a majority of O_{vac}, while leaving the remainder of the sub-surface Ti interstitials unoxidized.[101, 119] Surfaces prepared this way are denoted o-TiO_2. Exposing the o-TiO_2 surface to 100 L of methanol at room temperature results in the TPD/R spectrum depicted in Fig 6.3(a). The methanol trace (black trace) has an absent R_2 peak, indicating that 10 L of O_2 sufficiently healed most O_{vac} defects.

Methanol reacts dissociatively with O_{ad} defects to produce Ti_{5c}-OCH_3 and terminal Ti_{5c} bound OHs. These surface bound OHs subsequently undergo recombinative water desorption (R_1) from Ti_{5c} sites near room temperature.[60, 117] Water desorption from methanol TPR on the o-TiO_2 surface is shown in Fig 6.4. A small amount of hydroxyls also recombine from the R_2 site, indicating that not all the O_{vac} sites were titrated with O_2. The increased density of Ti_{5c}-OCH_3 results in significant enhancement to the R_1 peak (black trace) as well as the reaction products, methane (purple trace) and formaldehyde (red trace) in Fig 6.3(a), when compared to the TPD/R spectra for r-TiO_2 in Fig 6.1(a). The increased production of methane and formaldehyde, also indicates the proposed new disproportionation reaction likely does not involve O_{vac}-OCH_3. Interestingly, the methanol peak corresponding to the classical disproportionation, remained unchanged from the methanol TPD/R spectrum for r-TiO_2 in Fig 6.1(a). Therefore, Ti_{5c}-OCH_3 likely prefers to disproportionate to methane, formaldehyde and O_{ad}, rather than to disproportionate to methanol and formaldehyde. This preference towards one disproportionation reaction pathway over the other disproportionation reaction may be explained by thermodynamics; there is a strong driving force to oxidize nearby sub-surface Ti interstitials.[101] In addition, the new disproportionation reaction is entropically favorable.

To confirm Ti interstitials contribute to methanol disproportionation, methanol TPD/R depicted in Fig 6.3(b) was carried out on freshly grown (1 × 1) stoichiometric surfaces, denoted s-TiO_2. The growth of new (1 × 1) terraces involves the diffusion and subsequent oxidation of Ti interstitials in an oxidizing background under high temperatures (see figure notes for generating a s-TiO_2 surface), and results in surfaces that are nearly

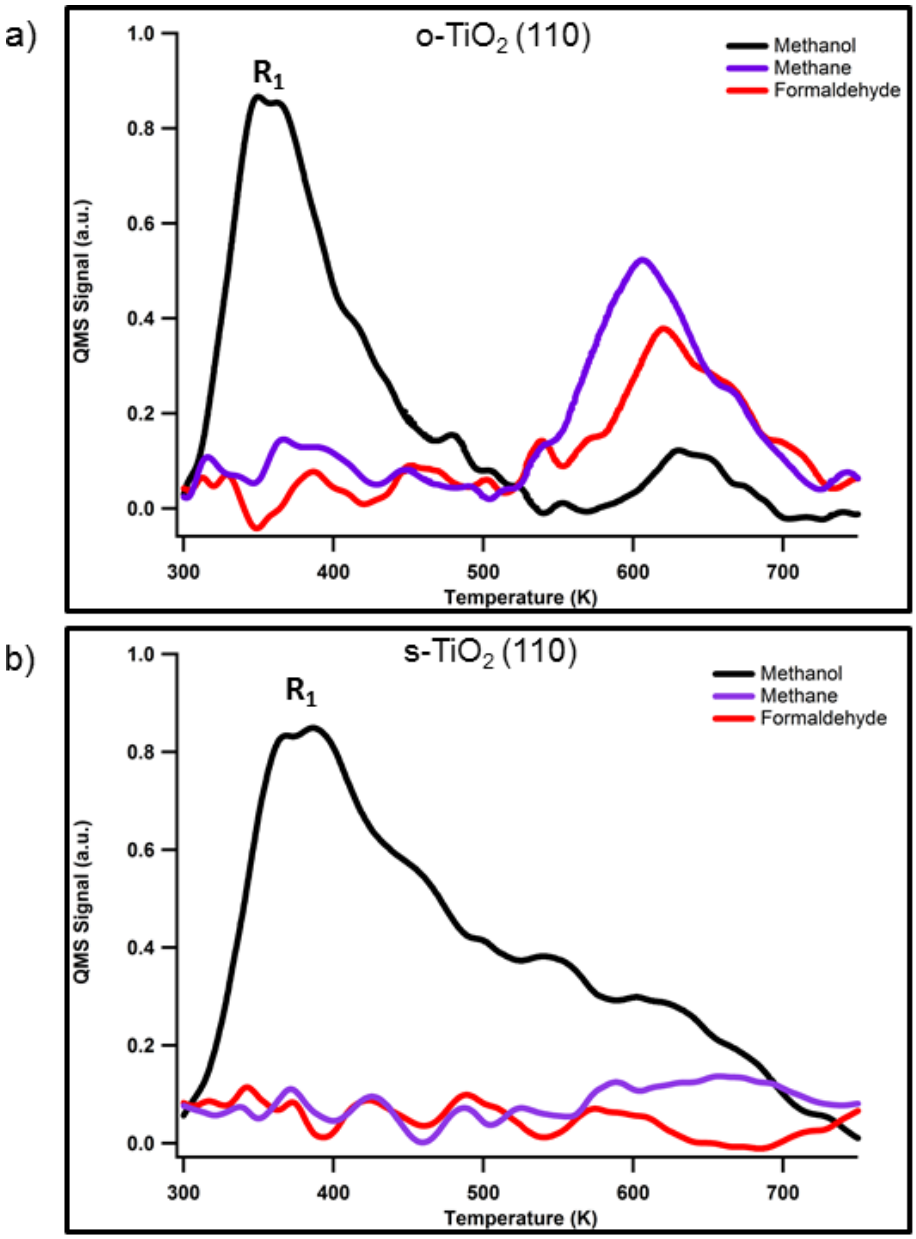

Figure 6.3: TPD/R spectrum from a reduced surface pre-exposed to 10 L of O_2 at room temperature, denoted as o-TiO_2 (a). TPD/R on a stoichiometric surface denoted as s-TiO_2 (b). Stoichiometric surfaces were prepared by sputtering in vacuum, followed by annealing the substrate in 2×10^{-6} Torr of O_2 at 840 K for 30 minutes.

depleted of O_{vac} and Ti interstitial defects.[101, 164, 129, 98] As seen in Fig 6.3(b), both methane (purple trace) and formaldehyde (red trace) desorption peaks were completely attenuated, indicating methanol reactivity from the s-TiO_2 surfaces was nearly absent. The majority of methanol (black trace) desorbing from the s-TiO_2 surface desorbs from Ti_{5c} sites (R_1 peak). The large peak broadening in methanol desorption is attributed to methoxide diffusion events associated with surfaces roughened from the growth of new (1×1) terraces, in agreement with the literature.[165, 166] Water desorption in the methanol TPR on the s-TiO_2 surface, shown in Fig 6.4 also confirms depletion of O_{vac} sites and a small R_1 peak around 400 K, we attribute to left over O_{ad}.

Comparing the TPD/R spectra observed from the o-TiO_2 and s-TiO_2 surfaces, we attribute a major driving force of methanol reactivity to be the sub-surface Ti interstitials. Furthermore, we observe oxidation of the r-TiO_2 surface after just five consecutive methanol TPD/R cycles (see Fig 6.1(b)). This result coupled with the enhancement in the methane production over the o-TiO_2 surface strongly suggests that stranded Ti_{5c}-OCH_3 are the major reactants in methanol disproportionation. Finally, methanol oxidation of the surface must involve the diffusion of Ti interstitial defects to the surface, binding to adsorbed Ti-OCH_3 and subsequent oxidation of the surface, resulting in the formation of TiO_x from O_{ad} left behind CH_4 desorption.

To confirm whether methanol oxidizes the reduced substrate by a Ti interstitial pathway, UHV-STM was employed to directly image the reactants along their temperature programmed desorption trajectory, denoted by the dashed lines in Fig 6.1(a). When r-TiO_2 was exposed to methanol at room temperature, brightly ordered 1D structures, templated along the [001] crystallographic direction were observed in the micrograph in

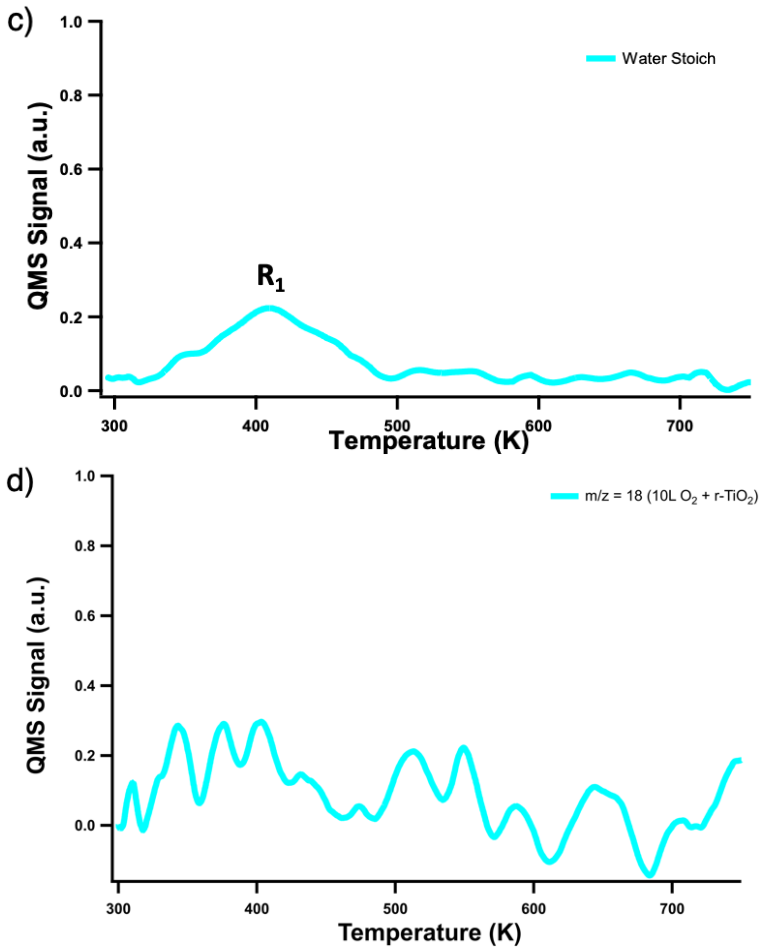

Figure 6.4: Comparative TPD water signal following 100 L methanol exposure. (top) is a spectrum of the 1st methanol TPD/R experiment denoted 1st run on r-TiO_2. (bottom) is the methanol TPD/R spectrum after the 5th consecutive run on the r-TiO_2. The surface was not sputtered or annealed between each TPD/R experiment.

Fig 6.5(a). The coverage was approximated to ∼0.80 monolayer (ML), by calculating ratio of the area of the methanol 1D structures to the area of the image. Our results are in good agreement with the compressed coverage (0.77 ML) of methanol reported previously with temperature programmed desorption (TPD) and quartz microbalance experiments.[167] The 1D structures also appear featureless, making it difficult to discern between bound Ti_{5c}-OCH_3 and Ti_{5c}-$HOCH_3$ in our STM images. Methanol likely exists in both molecular and dissociated forms as methanol recombination peak (R_1) was observed in our methanol TPD, and is consistent with previous investigations.[60, 143] In addition, previous DFT calculations show the adsorption energies of molecular and partially dissociated methanol at saturated coverages are degenerate.[141, 144]

In order to isolate the precursors involved in methanol disproportionation, the sample was subsequently flashed to ∼500 K and imaged at room temperature. As expected in the micrograph in Fig 6.5(b), the majority of the surface is dominated by electronic effects of the titania (1×1) reconstruction, whereby geometrically protruding O_{br} rows appear dark, and Ti_{5c} troughs bound by in-plane oxygen, appear bright.[50, 85] Dim features observed over O_{br} rows were discernible by height (see supplemental SI 2) and assigned to O_{vac} (black rectangle) and stranded OH_{br} (black oval), with densities of 2.0 ±0.35 % ML and 2.5 ±0.20 % ML. The appearance of both O_{vac} and OH_{br} defects is consistent with the surface flashed past the methanol recombinative desorption (R_2) peak. Evidence of stranded Ti_{5c}-OCH_3 (blue dot) precursors required for both disproportionation reactions, appear as bright features over Ti_{5c} troughs with apparent heights of ∼0.75 Å(see supplemental S2). Stranded O_{vac}-OCH_3 (purple dot) were also visible in O_{br} rows, with similar apparent heights to Ti_{5c}-OCH_3. Heights for both species of methoxide are

consistent with the literature.[153, 168, 169]

Interestingly, the Ti_{5c}-OCH_3 adsorbate appears to be more stable than O_{vac}-OCH_3, as reflected in their densities, 2.1 ±0.65 % ML and 0.74 ±0.12 % ML respectively. DFT calculations suggest Ti_{5c}-OCH_3 is less stable than O_{vac}-OCH_3, with reported adsorption energies of 0.9 eV and 1.51 eV.[144, 170] The apparent stability of the Ti_{5c}-OCH_3 may be accounted for by the donation of electrons from sub-surface Ti interstitial defects. Previous ultraviolet photoelectron spectroscopy showed the Ti$3d^1$ band gap state in defective TiO_2 was attenuated upon methanol adsorption at room temperature.[171] Bound Ti_{5c}-OCH_3 is highly electrophilic, and the transfer of an electron from the TI interstitial to bound Ti_{5c}-OCH_3 is enough to stabilize this specific surface interaction. In order to understand which substrate defects contribute to surface oxidation, room temperature STM images of the surface were taken after the surface was subsequently flashed to ∼640 K, as indicated by the dashed line in Fig 6.1.

The micrograph in Fig 6.5(c) reveals most of the Ti_{5c}-OCH_3 (blue dot) and O_{vac}-OCH_3 (purple dot) desorbed from the surface (∼0.2 % ML). The density of OH_{br} were also attenuated (∼0.1 % ML), presumably due to recombinative desorption of water, as observed in our water TPD spectra (see SI 1). New features (black open circle) appeared on the surface with apparent heights between 2.2 - 3.2 Å tall and two to three Ti_{5c} rows wide. The new features are assigned to TiO_x islands, based on the similarity to TiO_x islands reported by Besenbacher and co-workers.[101] The density of TiO_x islands, were 1.1 ±0.2 % ML per 900 nm^2 area, as calculated from a combined area of 22,500 nm^2. Similar concentrations of TiO_x islands were observed in different areas on the substrate, seen in Fig 6.5(d). Up until the surface was flashed to 640 K, the density of TiO_x islands

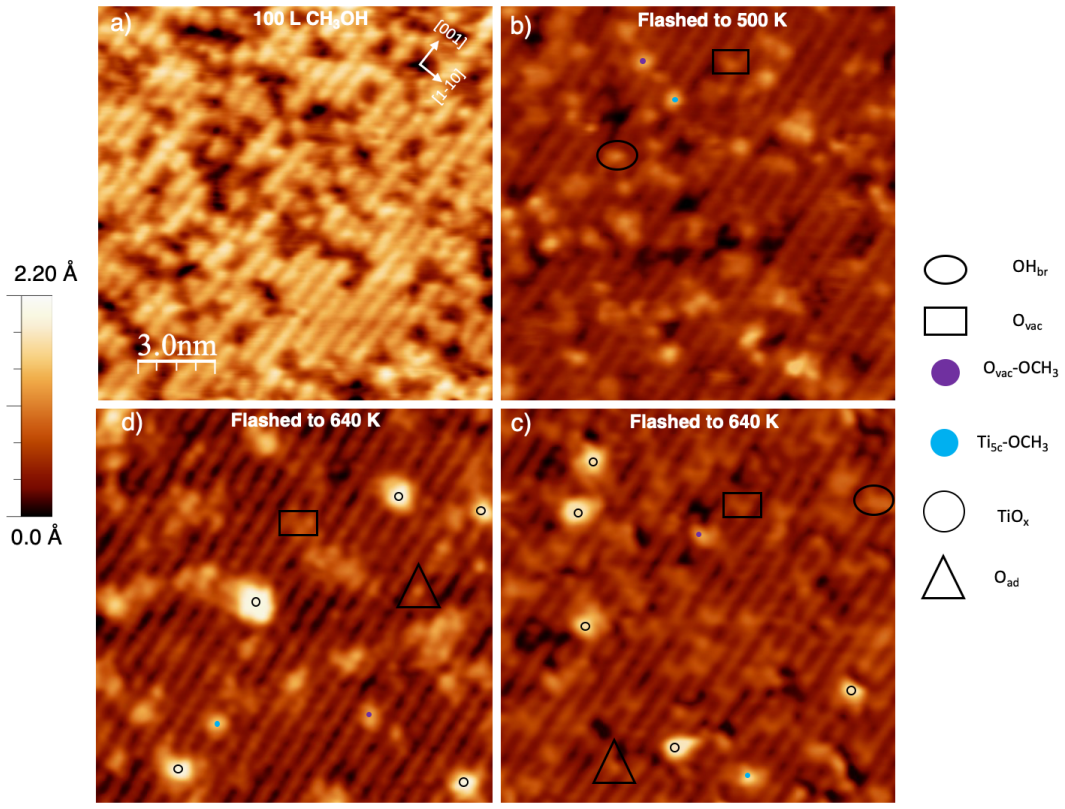

Figure 6.5: Selected room temperature STM images (150 Å×150 Å) of r-TiO_2 exposed to 100 L of methanol at room temperature (a) followed by a subsequent flash to 500 K (b) and to 640 K (c) and (d). Purple and blue dots indicate O_{vac}-OCH_3 and Ti_{5c}-OCH_3. Black rectangles indicate O_{vac} and black ovals indicate OH_{br}. Black circles indicate TiO_x islands and black triangles indicate O_{ad}.

remained ∼0.1 % per 900 nm^2 as illustrated in Fig 6.6. Moreover, the freshly sputtered and annealed (pristine) surface displayed similar concentrations of ∼0.1 % per 900 nm^2 area, counted over 25,000 nm^2 by STM. Large scale micrographs in Fig 6.7 illustrate the stark contrast between the pristine surface and the surface following methanol exposure a flash to 640 K.

The onset of TiO_x islands observed only after the substrate was flashed to 640 K, indicates stranded methoxides oxidized the surface via a Ti interstitial pathway. The source of oxygen therefore likely comes from O_{ad} left behind from the scission of the C-O bond in stranded Ti_{5c}-OCH_3. Our results are consistent, considering the diffusion barrier for a Ti interstitial (E_{diff} ∼1.0 eV)[172] is substantially lower than the desorption barrier for methane (E_{des} ∼1.7 eV) observed in our TPR spectrum (Fig 6.1(a)), when desorption is treated as first-order.[173] We propose that Ti interstitials diffuse to the surface at high temperatures to stabilize and nucleate Ti_{5c}-OCH_3 in the high temperature disproportionation reaction:

$$2Ti_{5c} - OCH_3 \xrightarrow{620\ K} CH_2O(g) + CH_4(g) + O_{ad}. \tag{6.3}$$

These Ti interstitials are consumed in the reaction with O_{ad} to form TiO_x islands of varying stoichiometry. The formation of TiO_x islands are likely dependent on methoxide kinetics, as not all O_{ad} (black triangle) observed in Fig 6.5(c-d) did not form TiO_x islands.

The O_{vac} density in Fig 6.5(c), (∼2.0 % ML) and Fig 6.5(d) (∼3.8 % ML), are noticably different, and reflects the heterogeneity of the r-TiO_2 substrate. Nonetheless, the average O_{vac} density ∼ 3.1 % ML is lower with respect to the pristine reduced sub-

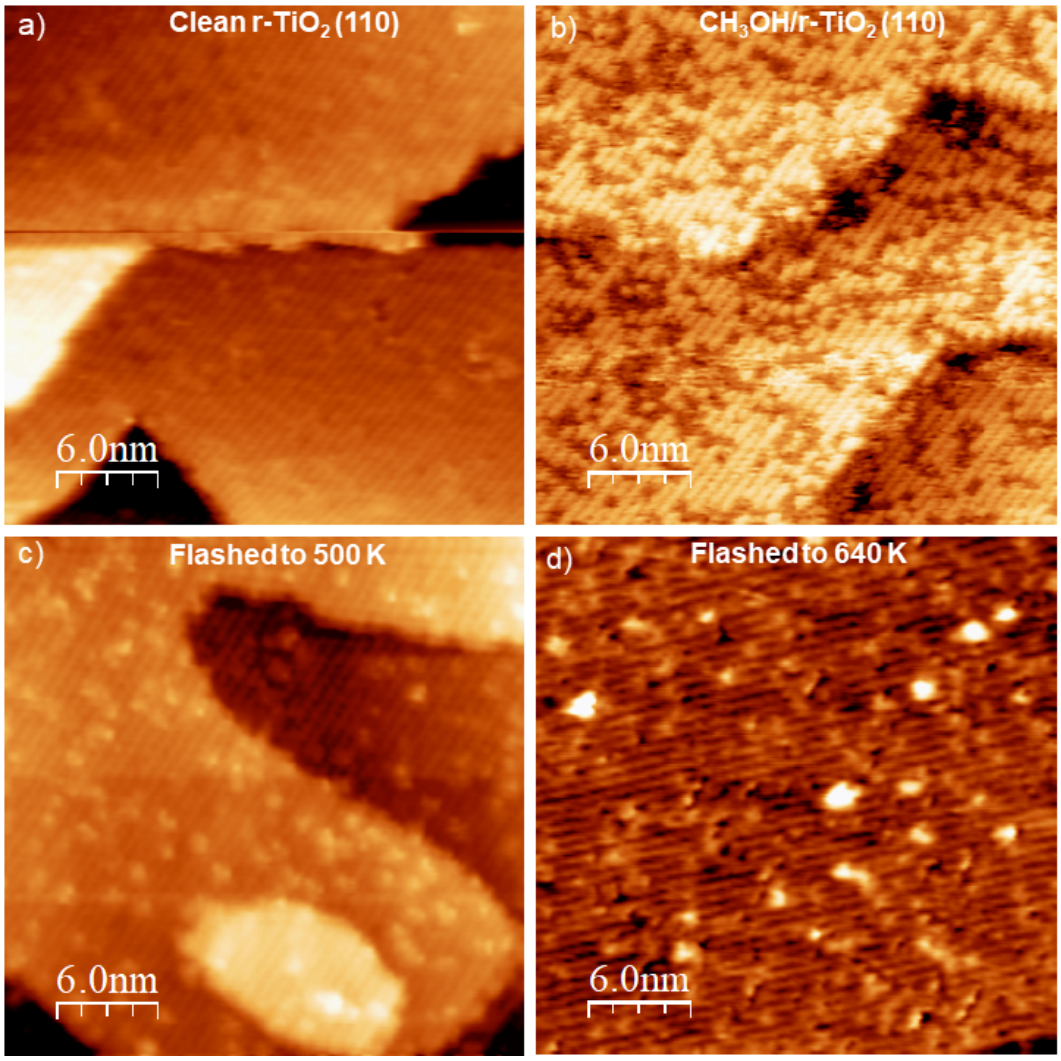

Figure 6.6: Selected room temperature STM images (30 nm×30 nm) of different areas of the surface following methanol exposure and flashing to variable temperatures. (a) is the bare r-TiO_2 surface. (b) following exposure to 100 L of methanol at room temperature. (c) is following a flash to ∼500 K. (d) is the surface following a subsequent flash to ∼640 K.

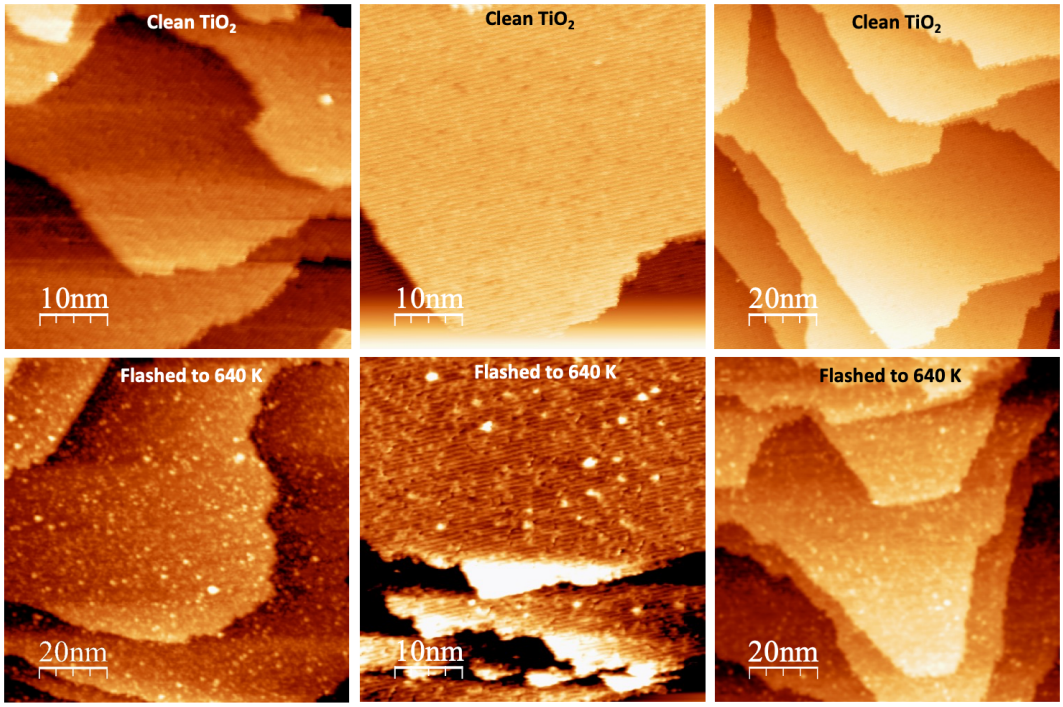

Figure 6.7: Various selected room temperature STM images of different areas of the pristine surface (top row) and following 100L methanol exposure and flashed to ∼640 K (bottom row).

strate, indicative of an oxidized surface. The decreased O_{vac} density is also consistent with the observed decrease in the R_2 methanol desorption peak after five TPD/R cycles (see Fig 6.1(b)). We argue that the O_{vac} sites were likely filled by O_{ad} left behind in the formation of CH_4 and this surface oxygen leads to the growth of TiO_x islands. We propose that the new disproportionation reaction occurs simultaneously with the classical disproportionation reaction to methanol and formaldehyde. Our findings agree with quantitative methanol TPD/R studies by Crampton *et al.*[174] who concluded the desorption of methane, methanol and formaldehyde were linked by a common methoxide precursor, but did not discuss the identity of the binding sites, nor the formation of TiO_x islands.

6.4 Conclusion

By performing a combination of methanol TPD/R on various reduction states of TiO_2, coupled with atomic-scale investigations by UHV-STM, we identify a new disproportionation reaction that results in the oxidation of sub-surface Ti interstitial defects. Methanol oxidation to the defective surface reduces the reactivity of the surface. Complete oxidation of the surface by annealing in a background of molecular oxygen attenuates methanol reactivity nearly completely. Our results add to the growing body of evidence that Ti interstitials contribute to the reactivity of rutile titania. Interestingly, our results demonstrate that methanol adsorption and reactivity is adversely different from longer aliphatic alcohols, known to dehydrate into alkenes at O_{vac} sites.[175, 176] Additionally, the adsorption properties between ethanol and methanol appear to be very different; ethoxides bound to Ti sites desorb below 380 K, but remain stable in O_{vac}

sites, above 500 K.[177, 165] Clearly, changes to the adsorption properties and reactivity of alcohol, by the addition of just one methyl group is not well understood, and warrants more atomic-scale investigations.

Chapter 7

Methanol Reactivity on VO/TiO_2 (110)

7.1 Introduction

In the previous chapter we observed with TPD, the chemistry of methanol on different modalities of bare TiO_2 and with STM, deciphered the relevant reaction sites and precursors associated with methanol reactivity. We learned that defects drive methanol chemistry, and sub-surface Ti interstitials in particular, are active sites for the high temperature methoxide disproportionation to methane and formaldehyde. Now we will investigate how this system is perturbed by the deposition of cationic mass-selected VO^+ clusters on the reduced surface. By carrying out similar TPD and STM experiments, we can observe how methanol chemistry is affected by the addition of VO clusters and gain atomistic insight into the role of Ti interstitials in supported vanadia catalysts. While many groups have focused on structure-reactivity relationships, other pertinent questions

that still remain largely unanswered are: (1) what is the role of the reducible support on the vanadia catalyst? and (2) what are the elementary reaction mechanisms involved in the oxidative dehydrogenation of methanol?

The two questions to be addressed in this chapter are largely motivated by previous work in our group on larger vanadia clusters. Hunter and co-workers had demonstrated that the degree of reduction in the support determines the selectivity of methanol ODH for multi-vanadium oxide systems.[62] For example, the selectivity of mass-selected $V_2O_6^+$ clusters towards methanol ODH correlated with the density of O_{vac}s: highly reduced supports produced formaldehyde at 482 K, and lightly reduced support produced formaldehyde at 437 K and methyl formate at 540 K. Catalysts prepared by deposition of $V_2O_6^+$ onto a reduced surface pre-adsorbed with oxygen adatoms produced exclusively methyl formate and water at 437 K. While our methanol TPD/R correlates with support O_{vac} density, our STM results found a statistically insignificant number of vanadia clusters dissociated at O_{vac} sites. On the contrary, $V_2O_6^+$ on the reduced surface mainly decomposed into doubled-lobed structures over two Ti troughs. Utilizing DFT calculations, Hunter and co-workers reasoned that the peroxo moiety on the $V_2O_6^+$ cluster is reduced to a pair vanadyl groups upon soft landing. Although the identification of defects responsible for electron donation to the cluster was not addressed. As discussed in chapter 4 of this dissertation, a consensus on the source of the excess electrons in rutile titania has been not reached. Thus, the motivation of this dissertation is to obtain a fundamental understanding on how electron-donating defects in the rutile support interact with V-O-Ti bond and the reactivity associated with the vanadia clusters.

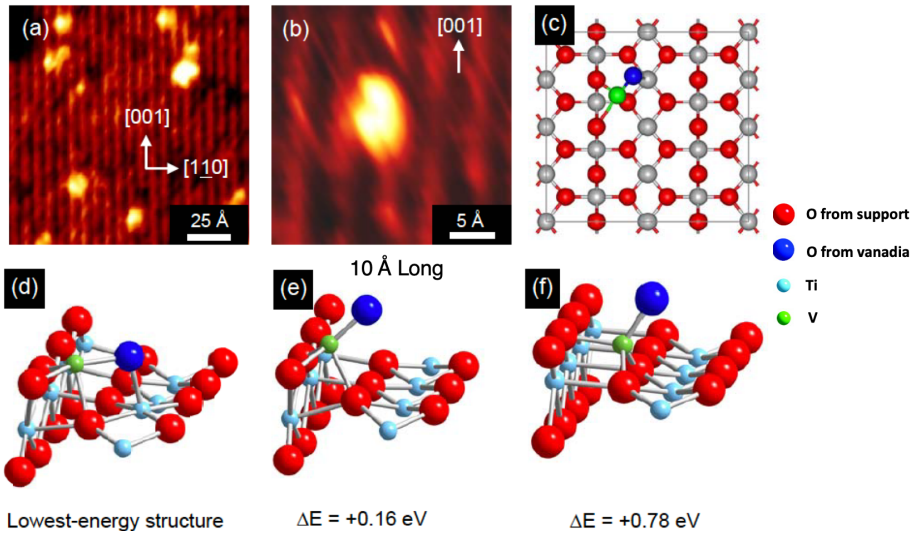

Figure 7.1: (a) Large-area and (b) high-resolution STM images of VO clusters supported on TiO_2 (110). (c) Top-view and (d) side-view models showing the binding site of the VO cluster on the titania surface. Side view-models showing the (e) Second-lowest and (f) third-lowest energy binding sites for VO clusters on the titania surface. The silver and light blue spheres correspond to titanium atoms, red spheres are oxygen atoms, the green sphere is a vanadium atom, and the dark blue sphere is the oxygen atom in the VO cluster. The model shown in (c) and (d) is also identical to the lowest-energy DFT structure for VO on TiO_2 from Shapovalov et al.[38]

In addition to questions about the role of defects in the support, I seek to address our second question about the reaction mechanisms proposed to explain methanol ODH on V_2O_6 system in this study. Motivation for this study stems from the observation that the lowest temperature desorption peaks associated with formaldehyde and methyl formate production were accompanied by methanol and or methane desorption.[62] Given the persistence of these signals through out all of our experiments, it would stand to reason that methanol ODH may proceed by methoxide disproportionation as opposed to a single methanol decomposing into water and formaldehyde via a vanadyl bond. In addition, our work on methanol reactivity from the bare surface (see chapter 6) highly suggests a methoxide disproportionation reaction mechanism. One concern is the requirement of multiple methoxides in close proximity around a single vanadia cluster: this would seem unlikely given the reduction in configurational entropy. It is possible that the simultaneous desorption of different species is merely coincidence. In order to answer this mechanistic question and questions about the role of the point defects in the support, we used STM to probe the interactions between methanol and supported VO clusters.

The choice to use VO clusters as a probe for investigating reaction mechanisms was based on the abundance of previous work done in the Buratto group. Also from a practical standpoint, VO^+ is the most abundant species in our ion beam as seen in the our mass scan spectrum in Fig 3.7. This is not to say VO clusters are not special. In fact, we have found VO in particular stabilizes water at room temperature (unpublished manuscript)[178] and facilitates the growth of the VO_3 cluster, responsible for ODH of methanol into formaldehyde and water.[61] The wealth of knowledge accumulated from these previous experiments will be a tremendous advantage in elucidating fundamental

laws that govern methanol reactivity as well as deconvoluting the role of the support from VO.

Before discussing our results with methanol, we need to understand the structure of VO and their unique effects. Previous UHV-STM experiments show VO clusters adsorb asymmetrically between the Ti troughs and O_{br} row. VO also has a coffee bean shape and appears enlongated along the [001] direction with an average length and height of 10 Åand 1.6 Å. STM images of the VO cluster on the bare reduced surface is shown in Fig 7.1(a - b). DFT calculations by Shapovalov et al.[38] indicate VO preferentially adsorbs in the upper-three fold hollow site. The three most energetically stable configurations are shown in Fig 7.1(c - f). The same authors also calculated a Bader charge of +1.95 on the V atom. This oxidation state of nearly 2+ is reasonable considering gas-phase IR spectroscopy and DFT calculations have found VO^+ clusters are mainly ionic in character.[72]

Given the ubiquity of water in ODH catalysts, UVH-STM and TPD studies were employed in our group to study their interactions with mass-selected vanadia clusters: V^+, V_2^+, VO^+, and VO_2^+ soft-landed on reduced TiO_2 (110). Fig 7.2(a - d) shows a series of STM images following multiple cycles of water exposure and heating to 600 K. The results of these STM images demonstrate that VO clusters pre-adsorbed on the reduced surface serve as anchor points for the reversible adsorption of molecular water at room temperature. Time-lapsed images not shown here, reveal a water monomer binds to an anchor point, resulting in a VO-H_2O complex that facilitates further the formation of string-beads, consisting of water dimers along the [001] direction. TPD experiments shown in Fig 7.3, reveal two new states, corresponding to desorption of the water in the

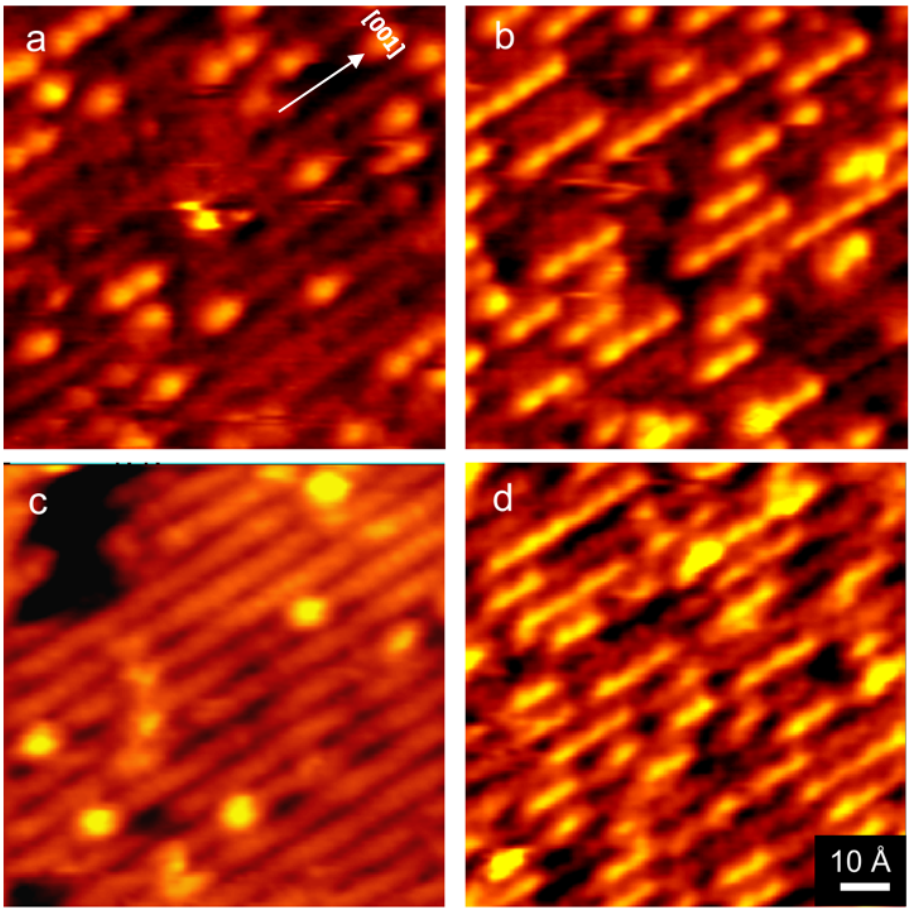

Figure 7.2: Room-temperature STM images of the VO-decorated TiO_2 surface (a) 12 hours after deposition, (b) after exposing the surface from (a) to an additional 2.5 L water, (c) 2 hours after annealing the surface from (b) to 600K for 30 seconds, (d) after exposing the surface from (c) to 2.5 L water. STM images were taken from Xiao et al.[178]

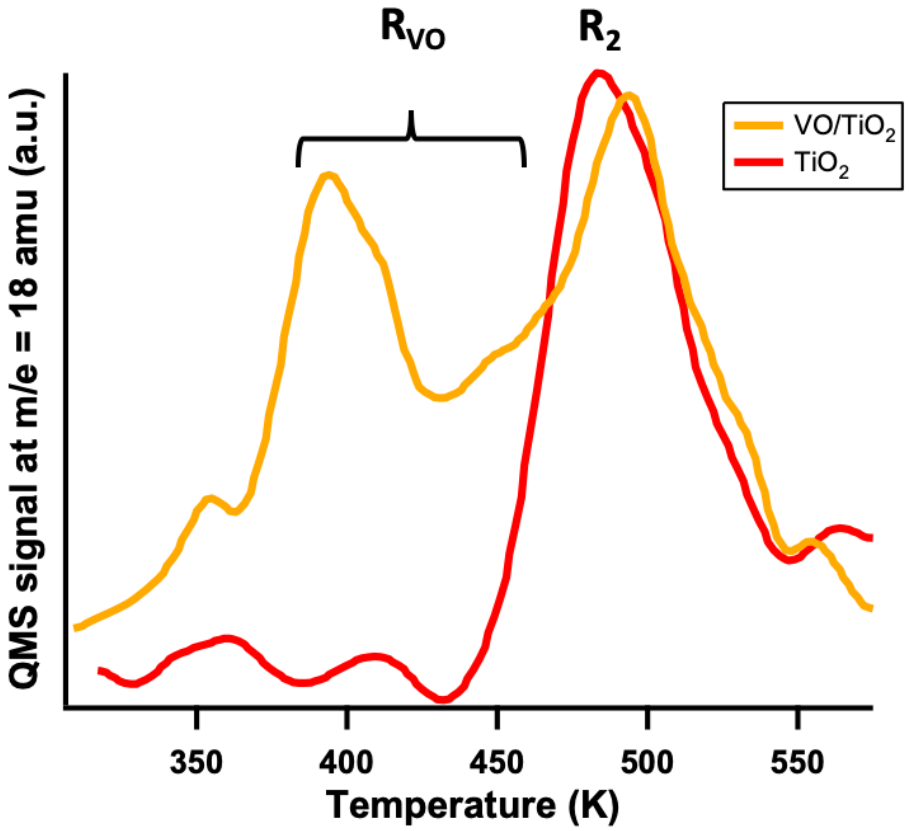

Figure 7.3: Water TPD spectra from the bare (red line) and 2% ML VO-decorated (yellow line) reduced TiO_2 (110) surface following exposure to 2.5 L H_2O at room temperature. TPD spectrum was taken from Tong et al.[178]

string-bead and water from the VO-H_2O complex, for the VO-decorated TiO_2 surface. These interactions were not observed on the bare reduced TiO_2 (110) surface and are also highly dependent on the composition of the pre-adsorbed cluster: surfaces decorated with V, V_2, or VO_2 did not exhibit this behavior. Comparison of STM and TPD results with DFT calculations suggests water forms a hydrogen bond with the oxygen atom of the VO cluster surface. For more information see the results there-in the unpublished manuscript by Tong et al.[178]

Here-in we employ UHV-STM and TPD/R to study the interactions of methanol with mass-selected VO^+ soft-landed on the reduced TiO_2 (110) surface. Our methanol TPD/R results indicate that VO oxidizes the electron-donating point defects associated with the reduced surface. A VO-mediated methoxide disproportionation reaction to methanol and formaldehyde was also observed at high temperature. UHV-STM results after flashing the VO-decored surface to various temperatures along the methanol desorption pathway confirm the formation of a precursor VO-$(OCH_3)_n$. Kinetic experiments with room temperature STM reveal the formation mechanism and structure of the VO-$(OCH_3)_n$.

7.2 Experimental

VO^+ clusters were synthesized via a home-built mass-selected cluster source described in detail elsewhere.[149] Vanadium oxide clusters are created by laser ablation of a vanadium metal target in an argon expansion gas seeded with 20 % O_2.[179, 61] Positive ions are extracted, accelerated, and focused using several steering lenses before being size-selected by a magnetic-field analyzer. The size-selected VO^+ ion beam has a flux of $\sim$1 nA/cm^2. This beam is directed into a UHV chamber containing the TiO_2(110)-(1$\times$

1) substrate which is held at +190V to decelerate the VO^+ ions. Biasing the titania sample allows VO^+ ions to be soft-landed onto the surface with incident kinetic energy less than 2.0 eV per atom. The base pressure of deposition chamber is less than 4×10^{-10} torr during deposition. Exposure times of 90 minutes at RT result in a surface coverage of approx. 0.02 ML as determined from the STM images. Monolayer coverage is defined as one VO cluster or one water molecule per TiO_2 unit cell (5.2×10^{14} cm^{-2}).

After deposition, the VO-decorated surface is transferred to the STM chamber and imaged using a RHK UHV350 SPM at a base pressure of 1×10^{-10} torr. Empty state STM images of the surface are acquired at 300 K in constant-current mode with a sample bias of +0.8 V to +1.9 V and a tunneling current of 0.1-0.2 nA. Analytical CH_3OH was purified by several freeze-pump-thaw cycles and introduced into the UHV STM chamber through a calibrated leak valve. Methanol TPD was carried out by moving the sample into position about 1 mm in front of a 3-mm wide skimmer cone aperture of a mass spectrometer (RGA200, Stanford Research Systems) and heating from RT to 800K at a rate of 1K/s.

TPD/R experiments were carried out on a single crystal TiO_2 (110) (Princeton Scientific), polished on one side (10 mm^2 dia. $\times$ 1 mm thick), mounted in a (OHFC copper) sample holder and equipped with an isolated silicon slab for resistive heating, and K-Type thermocouple wires for temperature readout. The substrate was prepared by several cycles of Ar sputtering (1 kV, 2μA for 20 minutes) and alternating anneal cycles in UHV and O_2 at 900 K for 10 minutes until a blue crystal with a O_{vac} density of approximately ∼5.0% was prepared. The O_{vac} density was determined by integrating the second methanol recombination desorption peak with respect to the saturated single

monolayer (1 ML = 3.2×10^{14} cm^{-2} Ti atom density) covered sample (TPD spectrum not shown). Substrate cleanliness was checked by auger electron spectroscopy (AES). TPD experiments were carried out with a residual gas analyzer, quadrupole mass-spectrometer (Stanford Research Systems RGA 200 QMS), mounted in the surface-science chamber of our apparatus, see elsewhere for more details.[149] Typical base pressure in the surface-science chamber was maintained at approximately 5×10^{-10} Torr. Methanol (Fisher Scientific, 99.9 %) was purified by several freeze-pump-thaw cycles before usage. All TPD/R experiments were performed with a heating rate of 1 K/sec. Methodology for formaldehyde TPR analysis and mass-fragment cracking ratio details can be found in Price et al.[61] Briefly, the formaldehyde signal is the excess signal between m/z = 29 contributions from methanol and formaldehyde as well as the cracking ratio of methanol to m/z = 29:31 = 1.02. The equation for the overall formaldehyde signal is

$$I_{\mathrm{Form}} = I_{29} - (1.02 \times I_{31}). \tag{7.1}$$

To calculate methane, the cracking ratio m/z = 15:31 was found in our system to be 0.63. Excess signal calculated as

$$I_{\mathrm{Meth}} = I_{15} - (0.63 \times I_{31}) \tag{7.2}$$

can then be assigned to methane desorption.

All UHV-STM experiments were carried out on a second TiO_2 (110) substrate (Princeton Scientific), polished on one side ($10 \times 2 \times 0.5$ mm^3) and mounted in a sample holder with a silicon slab for resistive heating. The STM substrate was prepared by the same

procedure used for the TPD substrate and yielded a O_{vac} density of approximately 4.4% ML (1 ML = 5.2×10^{14} cm^{-2} Ti atom density) as determined by direct counting over areas greater than 2000 nm^2. All STM experiments were performed in a separate STM chamber of the apparatus (base pressure below 2×10^{-10} torr), on an RHK STM100/AFM100 combination scan head, see elsewhere for more details see.[149] All micrographs were obtained with electrochemically etched W tips and cleaned by several cycles of electron-bombardment. Empty-state images were obtained at RT with biases between +1.4 V - 2.0 V, in constant current mode and processed with WSxM 5.0 (Nanotech) software.[150] The substrate was transferred to the surface-science chamber for direct methanol exposure and imaged immediately afterward.

7.3 Results and Discussion

Methanol TPD/R from VO/r-TiO_2 (110) - (1 × 1) surface following exposure to 100 L of methanol is shown in Fig 7.4(a). For comparison, methanol TPD/R from the o-TiO_2 (110) - (1 × 1) and r-TiO_2 (110) - (1 × 1) surfaces are shown in Fig 7.4(b - c). Methanol reactivity on the VO-decorated surface closely resembles the pre-oxidized surface in Fig 7.4(b) in three ways: (1) the R_1 desorption peak for methanol (black trace) is notably enhanced compared to TPD spectrum from the pristine surface in Fig 7.4(c), (2) the R_2 desorption peak is absent, (3) the classical disproportionation reaction ($D_{5c\text{-}Ti}$) share similar enhancement. A new desorption peak denoted D_{VO}, reveals an excess of m/z = 29:31 signal at 665 K, indicating formaldehyde production. No discernible water desorption peak was observed, as illustrated in Fig 7.5(a), suggesting the concomitant desorption of methanol and formaldehyde at D_{VO} is a disproportionation reaction. Fur-

thermore, the lack of water desorption with formaldehyde and methanol production also suggests that the D_{VO} desorption is a VO cluster-mediated disproportionation reaction. The absence of methanol recombination and desorption from O_{vac} sites is surprising and suggests that the adsorption of VO clusters on the surface of r-TiO_2 results in a slightly oxidized surface; presumably due to the transfer of electrons to adsorbed VO^+ clusters.

Further evidence VO clusters oxidized the surface is illustrated in the water TPR shown in Fig 7.5(a). The R_2 peak corresponding to OH_{br} recombination from O_{vac} sites appears as a minor shoulder to lower temperature desorption peaks. For reference, recombination from O_{vac} sites typically results in a large peak centered around 500 K in the water TPR spectrum of r-TiO_2 as depicted in Fig 7.5(c). This suggests that the VO/r-TiO_2 surface is more oxidized than the bare r-TiO_2 surface and OH_{br} have shifted to a lower binding energy. Furthermore, the water TPR from the methanol-covered VO/r-TiO_2 surface resembles that from the oxidized surface (o-TiO_2) shown in Fig 7.5(b) despite the fact that VO clusters do not directly fill O_{vac} sites. Both our methanol TPD spectrum and our water TPR on the VO-decorated surface are consistent with oxidation of of the surface. We attribute this oxidation to VO clusters scavenging electrons from O_{vac} sites.

Finally, the water TPR spectrum from the methanol-covered VO/r-TiO_2 surface shown in Fig 7.5(a), is similar to the water TPD spectrum reported by Tong et al.[178] In the TPD experiments from reference 171, surfaces were prepared by 2.0% ML deposition of mass-selected VO^+ clusters followed by 2.5 L of H_2O at 300 K. Integration of the subsequent water TPD spectrum there-in indicated two new desorption peaks: (1) at 390 K corresponding to molecular dimers and (2) a shoulder at 445 K corresponding

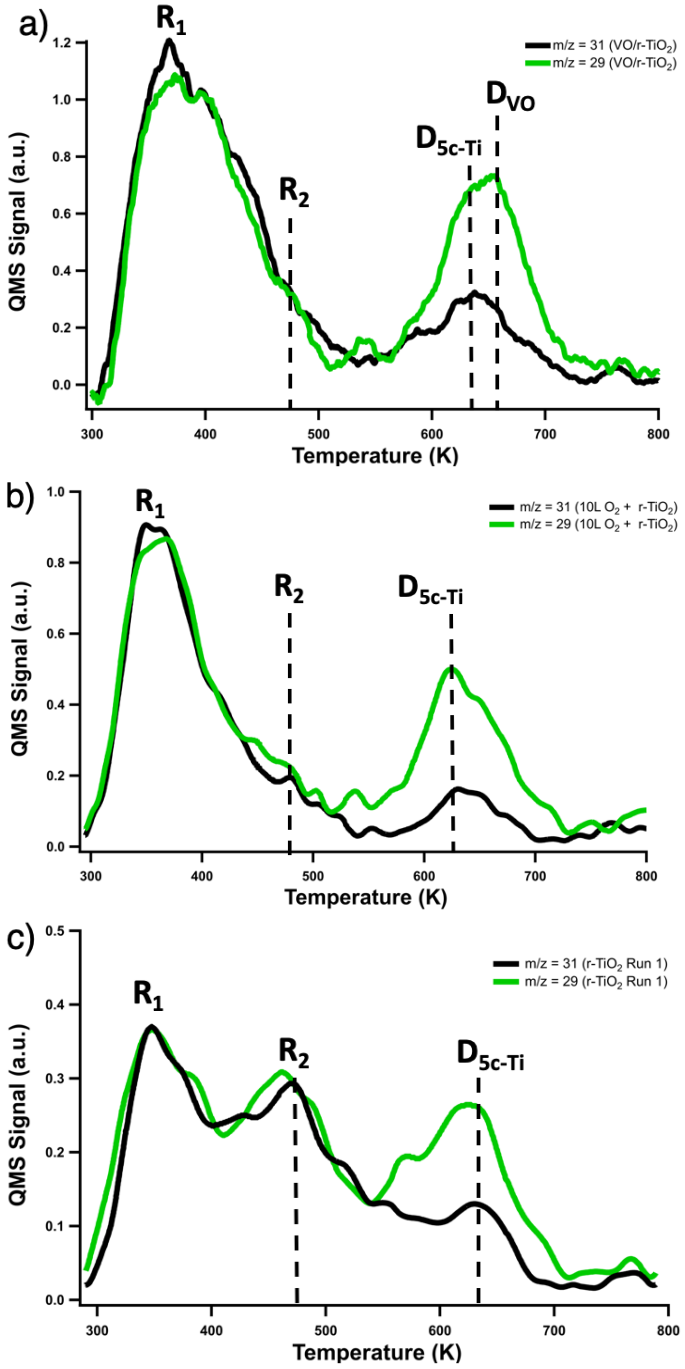

Figure 7.4: Comparative methanol TPD of (a) 7.0% ML $VO/r\text{-}TiO_2$ with (b) 10 L O_2 decorated surface and (c) bare reduced surface.

to molecular monomers bound to a VO cluster. The two peaks at 398 K and 447 K observed in our water TPR spectrum shown in Fig 7.5(a) can therefore be attributed to molecular water from VO clusters. The similarity between our water TPR spectrum from the methanol-covered VO/r-TiO_2 surface and the water TPD spectrum from the water-covered VO/r-TiO_2 surface reported by Tong et al[178] suggests the formation and stabilization of molecular water from nearby OH_{br} sites is energetically favorable near room temperature. This result in conjunction with our finding that VO clusters oxidize the reduced substrate is interesting and somewhat unexpected. To further understand the structural basis for these novel findings, a series of variable-temperature UHV-STM experiments were conducted below.

The mechanism by which VO clusters oxidize the reduced surface was revealed by imaging the VO/r-TiO_2 surface along the thermal desorption pathway of methanol. Representative large scale micrographs depicted in Fig 7.6(a) show that exposure of 100 L of methanol results in the formation of 1D chain (red) features along the [001] crystallographic direction. The 1D features are very similar to those observed for a clean surface in chapter 6 (Fig 6.6), and therefore consist of both the molecular and dissociated forms of methanol. Fig 7.6(b) reveals a majority of methanol desorbed after the surface was flashed to 400 K, corresponding to the R_1 peak in our methanol TPD. Following a flash to 500 K in Fig 7.6(c), we observed an abundance of stranded Ti_{5c}-OCH_3 (red) features that likely correspond to the classical disproportionation reaction $D_{5c\text{-}Ti}$, in addition the (1×1) surface, consisting of Ti_{5c} troughs (blue) and protruding bridging oxygen rows (black) remained intact. As discussed in the previous chapter, following a flash above the disproportionation reaction temperature ($\sim$620 K), typically results in the formation

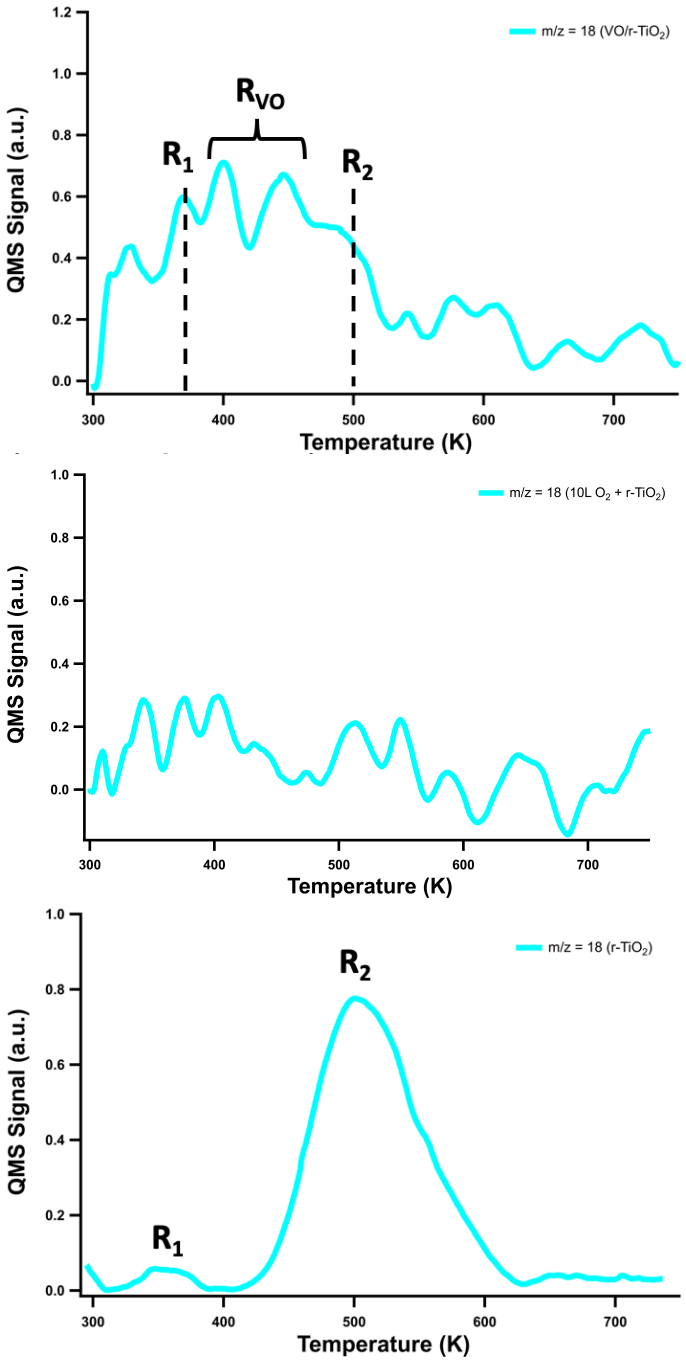

Figure 7.5: Comparative water TPR following methanol exposure of (a) 7% ML $VO/r\text{-}TiO_2$ with (b) 10 L O_2 decorated surface and (c) bare reduced surface.

of TiO_x islands, however no such features were observed on the VO/r-TiO_2 surface after an additional flash to 700 K.

Fig 7.6(d) illustrates a typical image of the surface following a flash to 700 K. The lack of TiO_x islands indicate no oxidation reaction between methoxides and near-surface Ti interstitials. In addition only minor amounts of O_{vac}-OCH_3 (red) and OH_{br} were observed in desorption process, suggesting O_{vac} defects were effectively oxidized, consistent with methanol TPD on VO/r-TiO_2. One way in which methoxides avoid oxidizing the surface is by the formation of VO-$(OCH_3)_n$ at the expense of methoxides binding to Ti interstitials, which ultimately leads to the formation of TiO_x islands. The emergence of various sizes of VO-$(OCH_3)_n$ (white circles) are readily visible through out the desorption process, as observed in Fig 7.6(b - d). Formation of well-defined, isolated VO-$(OCH_3)_n$ were observed following a flash to 500 K in Fig 7.6(c) and have a density of $\sim$1.5% ML, consistent with our calculated $\sim$2.0% ML VO deposition coverage. Following a flash to 700 K, the typical size of a VO-$(OCH_3)_n$ in Fig 7.6(d) appears to be much smaller than the VO-$(OCH_3)_n$ at 500 K, indicating a desorption event at VO sites. We therefore attribute the shrinking of the VO-$(OCH_3)_n$ size in STM to a VO-mediated methoxide disproportionation reaction, which forms to formaldehyde and methanol, consistent with our methanol TPR. Our results suggest the VO-$(OCH_3)_n$ at 500 K are the precursor intermediates to the VO-mediated methoxide disproportionation reaction. The identity and formation of these precursor intermediates will be discussed later.

To understand the anatomy of a typical VO-$(OCH_3)_n$, a set of magnified images from Fig 7.6(a - d) are shown in Fig 7.7(a - d). For clarity, a lattice grid overlays each image featuring nodes to denote Ti atoms and rectangles to denote the (1 $\times$ 1) unit cell. The

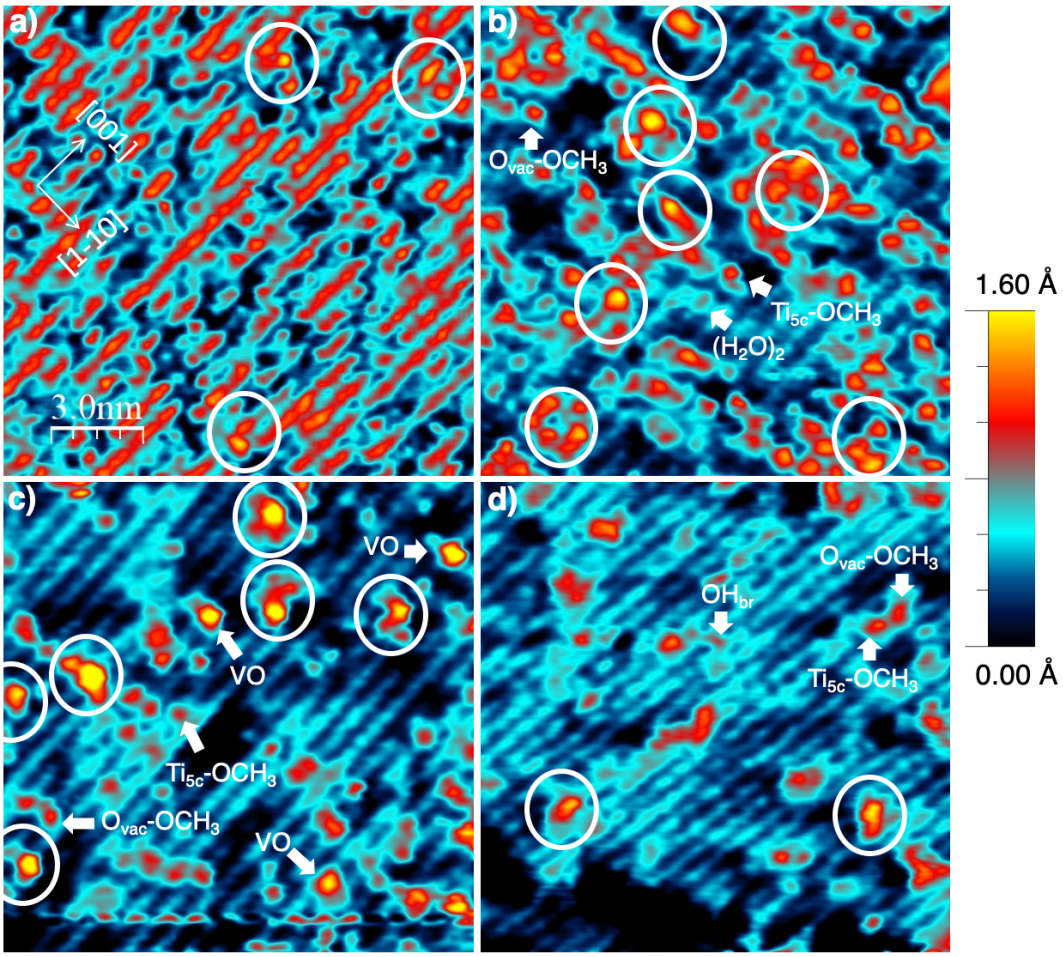

Figure 7.6: Selected room temperature STM images (150 × 150 $Å^2$) of VO/r-TiO_2 along the desorption pathway. (a) VO clusters deposited on r-TiO_2 following exposure to 100 L of methanol. (b) Flashed to 400 K, various sizes of large VO-$(OCH_3)_n$ (white circles) appear. (c) Flashed to 500 K, isolated methoxides and small VO-$(OCH_3)_n$ (white circles) appear. (d) Flashed to 700 K, VO-$(OCH_3)_n$ consisting of one to two methoxides remain.

formation of methanol 1D chains (red) adjacent to a VO cluster (yellow) is apparent in Fig 7.7(a). VO can be identified by the characteristic height and asymmetric adsorption over the 3-fold oxygen hollow site, in agreement with a previous STM investigation by Price et al.[179] Desorption of 1D chains following a flash to ∼400 K shown in Fig 7.7(b), reveal features consistent with the size and geometry of monomers and dimers of molecular water bound to Ti_{5c}, in agreement with previous STM experiments by Matthiesen et al.[180] Stabilization of molecular water on the surface at 400 K is expected as our water TPR contains various desorption peaks between 350 K to 500 K. Interestingly, formation of the VO-$(OCH_3)_n$ begins around 400 K; both methoxides (red) and molecular water (light red) are bound at sites adjacent to VO clusters along with nearby Ti_{5c}-OCH_3 (red) and O_{vac}-OCH_3 (red). Likely, these nearby Ti_{5c}-OCH_3 adsorbates contribute to the methanol TPD shoulder peak around ∼ 410 K depicted in Fig 7.4. A subsequent flash to ∼500 K in Fig 7.6(c) reveals the emergence of a well-defined isolated VO-$(OCH_3)_n$. The geometry of the feature suggests a VO-$(OCH_3)_4$ complex whereby each methoxide is bound to VO and a perimeter Ti_{5c} site. The proximity of the methoxides in the VO-$(OCH_3)_n$ likely correspond to the cluster-mediated D_{VO} reaction to formaldehyde and methanol previously observed in our methanol TPR. To confirm our assignment, a third flash to 700 K in Fig 7.7(d) reveals a complex consisting of one methoxide: VO-(OCH_3). As shown in the large scale image in Fig 7.6, VO-(OCH_3) is the most common complex. It should be noted that although various geometries of the VO-$(OCH_3)_n$s were observed at 500 K, they all share a common motif: one Ti_{5c}-OCH_3 sharing a O_{br} row with the asymmetrically bound VO cluster. In addition, these VO complexes typically range in composition between VO-$(OCH_3)_3$ and VO-$(OCH_3)_4$ based on their size. Nearly 33% of the VO clusters found at 500 K did not form complexes, although at higher temperatures

it is likely that isolated methoxides may diffuse and bind to a bare cluster.

To confirm the features shown here are not due to the formation of VO/TiO_x islands, the bare VO/r-TiO_2 surface was flashed to ∼400 K *in vacuo* and investigated by STM. Flashing to ∼400 K was justified based on the known diffusion activation barrier, E_d ∼ 1.0 eV, typically observed around 390 K.[172] A comparison of images of the surface before the flash, shown in Fig 7.8(a) and after the flash in Fig 7.8(b) reveal no difference in the VO features. Our control experiments thus show that VO clusters do not react with Ti interstitials.

From a thermodynamic perspective, the complexation of multiple methoxides to a single VO cluster may seem unfavorable as their configuration entropy will decrease! Nonetheless, magnified images in Fig 7.7(a) - (d) indicate multiple methoxides bind to a single VO cluster. By invoking the Langmuir adsorption model and the chemical potential, μ(T,θ_i), we can find a thermodynamic justification for the formation of VO-$(OCH_3)_n$. Here μ(T,θ_i), depends on temperature T and number of occupied sites θ_i of methoxide species i and is calculated via the following equation:

$$\mu_i(T,\theta_i) = \mu_i^0(T) + K_b T ln\frac{\theta_i}{\theta_{tot}} = E^{tot} + \Delta\mu_i(T) + K_b T ln\frac{\theta_i}{\theta_{tot}}. \quad (7.3)$$

The standard chemical potential, ${\mu_i}^0$(T), for species i is broken up into two terms: (1) E^{tot}, is a total energy term equal to the partition function of the species at T = 0 K and accounts for the zero-point energy, (2) $\Delta\mu_i$(T) is a thermal correction term. Both E^{tot} and $\Delta\mu_i$(T) can be routinely calculated by DFT methods.[181] For reference, the standard chemical potential ${\mu_i}^0$(T) = 0. Lattice models of a typical VO-$(OCH_3)_n$ are

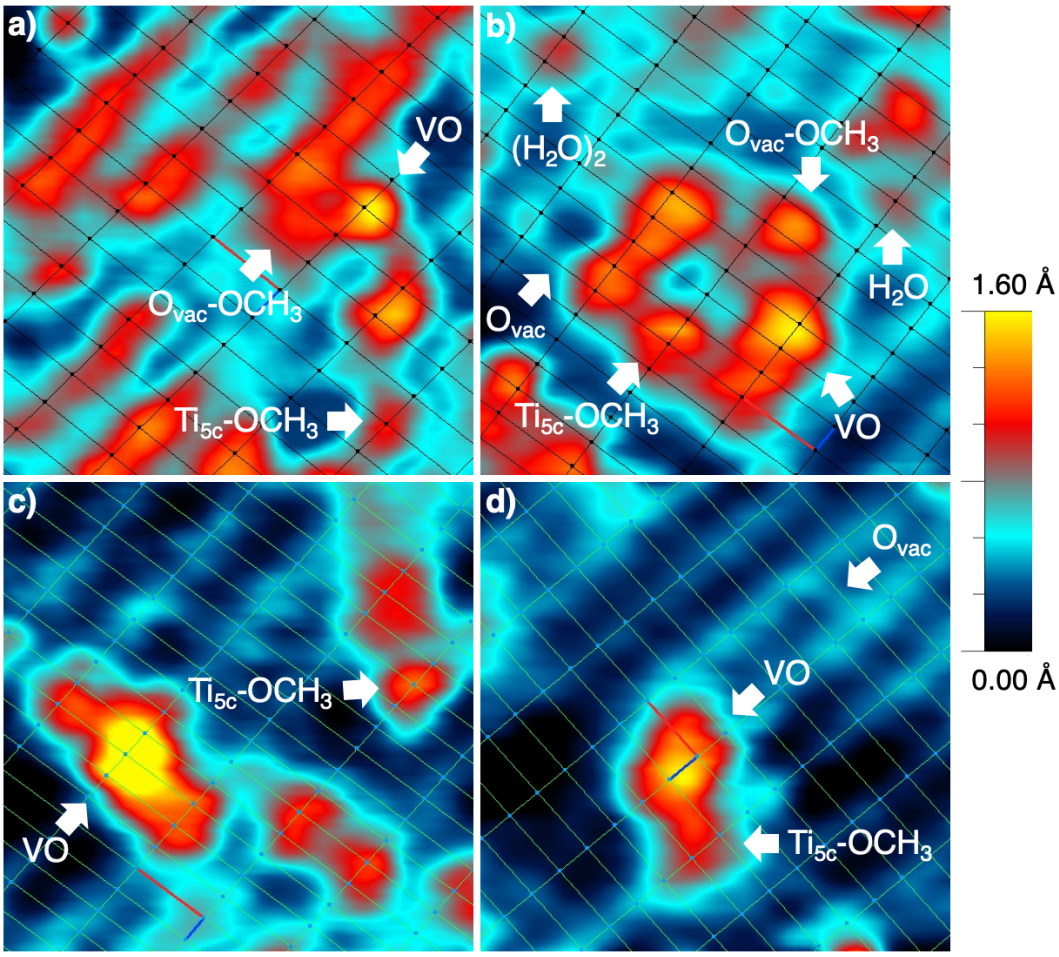

Figure 7.7: Magnified room temperature STM images (40 × 40 Å^2) of a single VO-$(OCH_3)_n$ complex and typical adsorbates along the desorption pathway. (a) VO cluster bound to a O_{vac}-OCH_3 adjacent to 1D methanol chains. (b) Flashed to 400 K, a typical VO-$(OCH_3)_2$. (c) Flashed to 500 K, isolated methoxides and small VO-$(OCH_3)_n$ (white circles) appear. (d) Flashed to 700 K, VO-$(OCH_3)_n$ consisting of one to two methoxides remain.

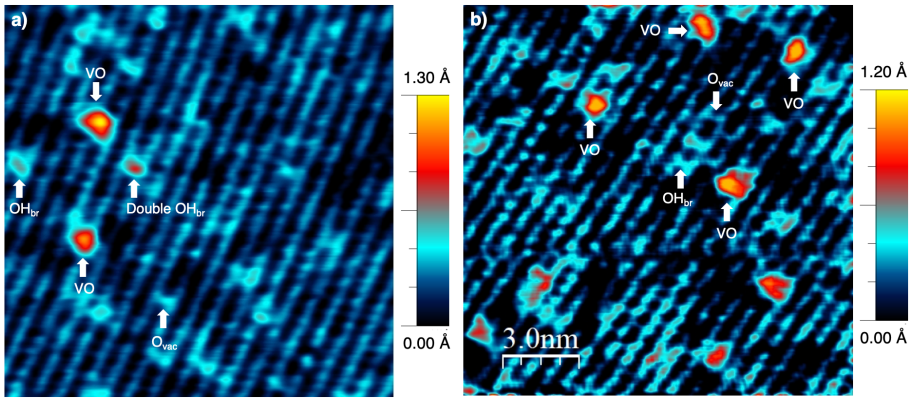

Figure 7.8: Room temperature images (150 × 150 Å^2) of the VO/r-TiO_2 surface before (a) and after (b) after flashing to 400 K. Typical O_{vac} and OH_{br} defects and VO clusters are labeled with white arrows.

based on their respective STM images illustrated in Fig 7.9(a - f) and used here-in for chemical potential calculations. All Ti_{5c} sites adjacent to the VO cluster in our model were assumed to have the same adsorption energy. For the bare VO cluster at T = 300 K, μ = 0 eV since all perimeter sites are free. At 500 K, the formation of the VO-$(OCH_3)_n$ precursor to the disproportionation reaction is thermodynamically downhill, with a μ(500 K) = -54.0 meV. Post-disproportionation reaction, the VO-$(OCH_3)_n$ retains one methoxide, yielding μ(700 K) = -159.2 meV. The difference in chemical potentials $\Delta\mu$ = -105.2 meV demonstrates the VO mediated methoxide disproportionation reaction to methanol and formaldehyde is exothermic. Despite the high desorption temperature of the reaction products, the net lowering of the chemical potential is associated with the property of a *good catalyst*.[181] Although the thermodynamics of the VO-clusters have been established, the exact mechanism detailing the formation of the complex is unknown; especially since the methyl groups associated with each methoxide would sterically hinder the binding adjacent adsorbates near the VO perimeter site. In fact, DFT calculations from Silber et al.[144] predict unfavorable adsorption of methanol on a Ti_{5c} directly

adjacent to Ti_{5c}-OCH_3.

In order to elucidate the formation kinetics of a VO-$(OCH_3)_n$, room temperature STM experiments were carried out following various methanol exposures (0.3 L, 0.6 L and 2.4 L) at room temperature. Before discussing our results, we need to consider the interaction of methanol on bare r-TiO_2 surfaces at room temperature. Previous STM experiments found that methanol at low exposures, prefer to fill O_{vac} sites resulting in O_{vac}-OCH_3 and OH_{br} species.[153, 182] DFT calculations confirmed these results by finding methanol dissociation at O_{vac} sites is energetically downhill compared to dissociation over Ti_{5c} sites. In the presence of $\sim$ 1.5% ML density of VO clusters however, exposure to 0.3 L of methanol results in the creation of stable Ti_{5c}-OCH_3 adsorbates. Moreover, VO clusters do not form complexes, indication of a high kinetic barrier. Representative images of the clean VO/r-TiO_2 surface before (a) and after (b) 0.3 L of methanol exposure shown in Fig 7.10 (a - b) illustrate the appearance of Ti_{5c}-OCH_3 (red) and the preservation of isolated VO clusters (yellow). The O_{vac} density is between 5 - 7 % ML. The assignment of Ti_{5c} features to Ti_{5c}-OCH_3 and not intact CH_3OH is justified by two findings: (1) the density of Ti_{5c}-OCH_3 and O_{vac}-OCH_3 (red) are nearly equal ($\sim$1.6% ML : $\sim$1.3% ML), and (2) The total density of methoxides is nearly equal to the density ($\sim$2.9% ML) of OH_{br} features (light red). How Ti_{5c}-OCH_3 adsorbates are created on VO/r-TiO_2 is not observed directly, but we can speculate on possible mechanisms.

One possible mechanism is spillover: methanol dissociates into Ti_{5c}-OCH_3 and OH_{ad} bound directly to a VO cluster and diffuses towards lower densities of methoxides and may fill O_{vac} defects. Given that the majority of VO clusters (yellow) on the surface do not form complexes at 0.3 L exposure, methanol spillover is a viable mechanism. A similar

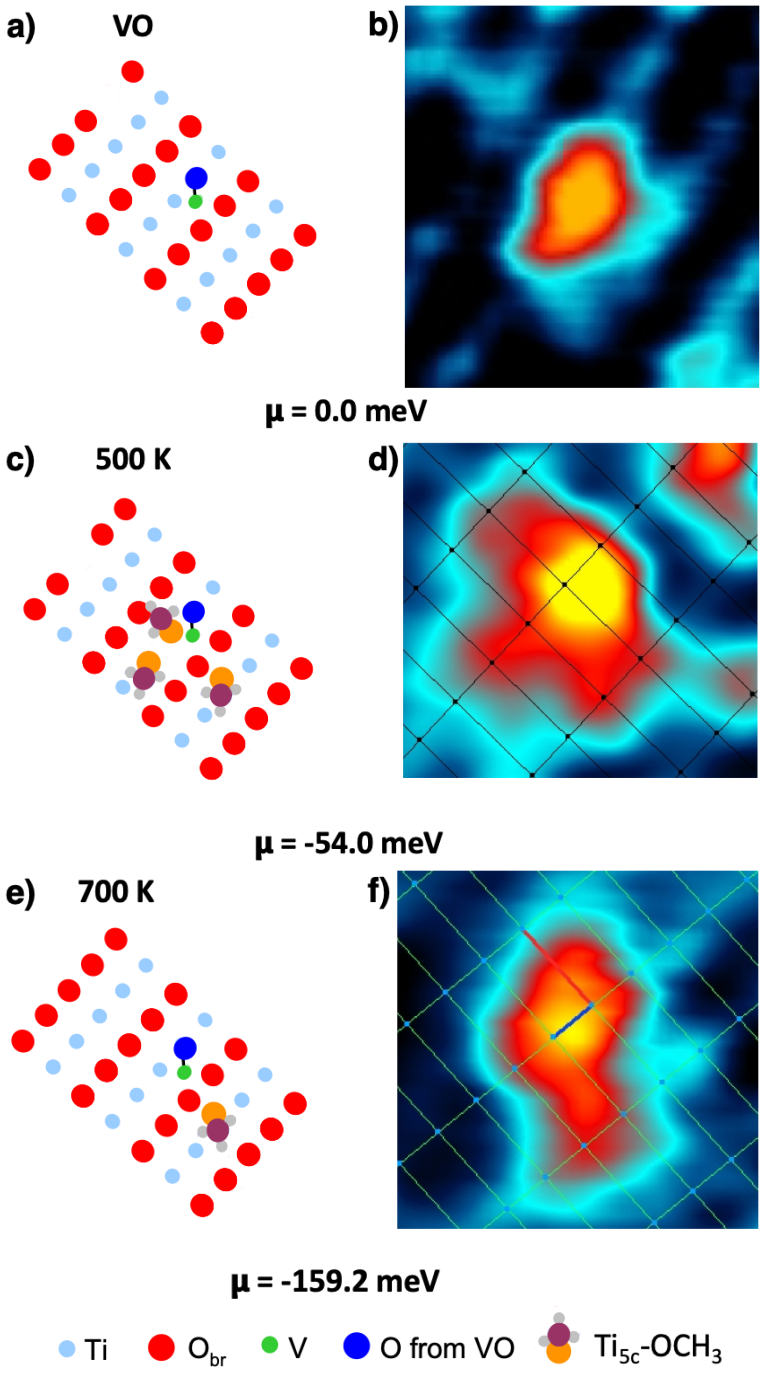

Figure 7.9: Models of various VO-$(OCH_3)_n$ complexes correlated with their STM images and respective chemical potentials. a - b) a VO cluster on the bare surface prior to methanol exposure. c - d) is a single VO-$(OCH_3)_4$ complex after flashing to 500 K: pre-methanol disproportionation reaction. e - f) is a single VO-$(OCH_3)_1$ complex after flashing to 700 K: post-methanol disproportionation reaction.

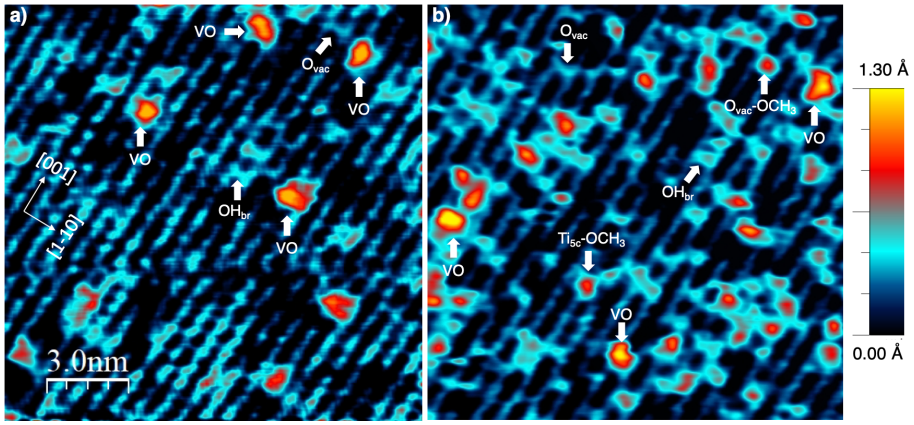

Figure 7.10: Room temperature images (150 × 150 $Å^2$) of two different areas on the VO/r-TiO_2 surface before (a) and after (b) exposure to 0.3 L of methanol at 300 K. (a) The O_{vac} density is between 5 - 7 % ML. (b) The image was taken 30 min after evacuation of methanol vapor from the STM chamber. Key adsorbate features are labeled with white arrows.

result was reported for small Pt clusters (∼1.6 nm) deposited on r-TiO_2, although OH_{br}'s were not directly observed by room temperature STM.[183] The authors in the report claimed that the asymmetry of Ti_{5c}-OCH_3 features suggested the presence of an adjacent hydroxyl. An alternative explanation is that the VO clusters may cause interfacial lattice strain on the support, resulting in a lower barrier for methanol dissociation at Ti_{5c} sites and thereby precluding any direct dissociation at VO sites. A previous STM investigation illustrates how underlying edge-dislocation defects in single crystal Ru (0001) indirectly lead to nearby dissociation of NO adsorbates.[184] Unlike our results however, the STM images reported in this study show a clear gradient of N adsorbate density around each defect. We plan to examine mechanisms for our system by DFT.

Further evidence VO clusters did not form complexes at 0.3 L of methanol was resolved by imaging the surface after flashing the substrate to 400 K: if methoxides did bind to VO clusters, the resulting VO-$(OCH_3)_n$ would be stable up to 700 K. Fig 7.11(a) reveals

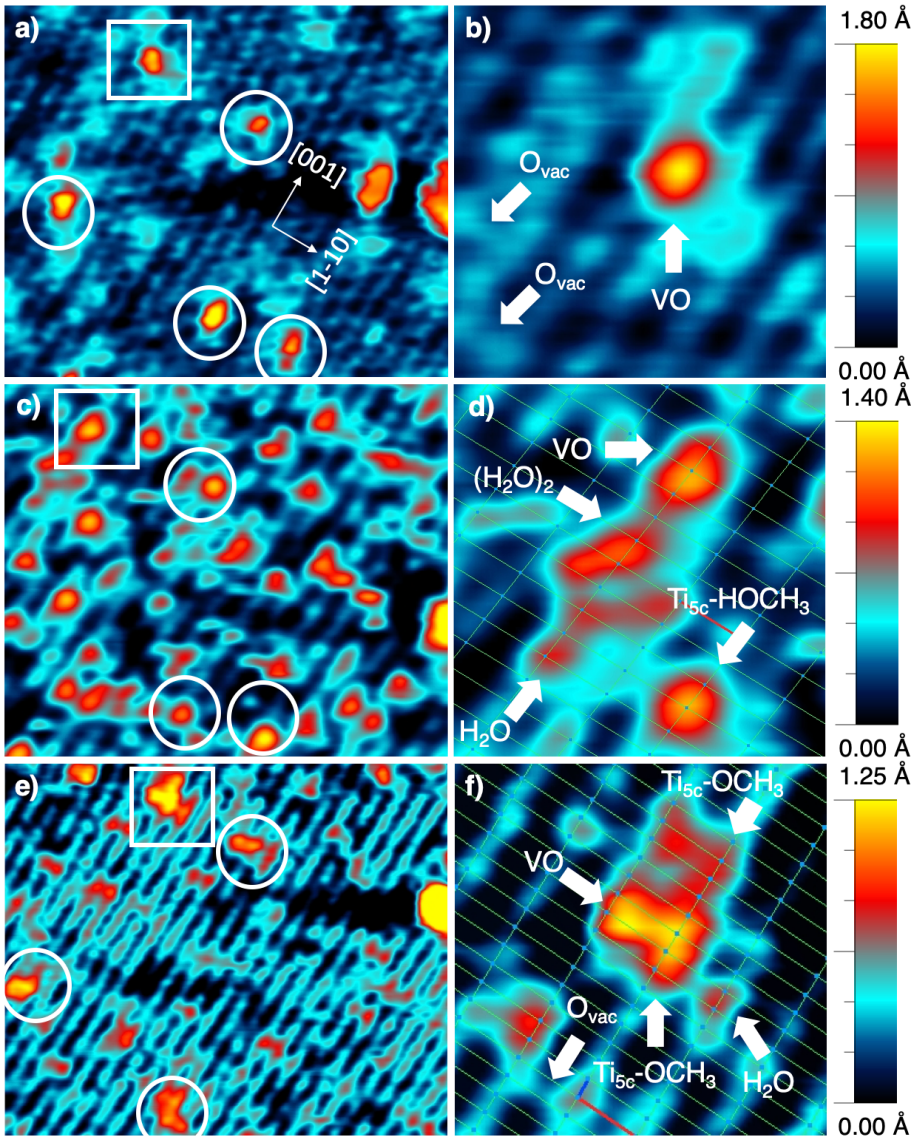

Figure 7.11: Large scale room temperature images (150 × 120 Å^2) of the same area on the VO/r-TiO_2 surface and their magnified images (50 × 50 Å^2) indicated by white boxes reveal the effects of multiple methanol exposures. VO clusters (yellow) are outlined in white circles. (a - b) is the surface after exposure to 0.3 L of methanol and flashed to 400 K. The image was recorded 45 mins after cooling the substrate back to room temperature. (c - d) image was taken 2 hours after exposure to 0.6 L of methanol. (e - f) Is taken 3.5 hours after exposure to an additional 1.8 L of methanol.

the recovery of several VO clusters (white circles) following the flash to 400 K. A typical VO cluster (white box) magnified for clarity in Fig 7.11(b) displays the characteristic asymmetric adsorption and physical appearances consistent with VO clusters on the bare r-TiO_2 surface shown previously in Fig 7.8(b). Defects like O_{vac}'s (light blue) were also observed, suggesting the surface was still reduced. After exposure to 0.6 L of methanol, an image of the same area shown in Fig 7.11(c) reveals VO clusters (white circles) remain isolated despite the increased density of adsorbates. Interestingly, compared to the surface following 0.3 L of methanol, the densities of both OH_{br} and O_{vac}-OCH_3 features at 0.6 L decreased to less than 1% ML. Instead, an abundance of Ti_{5c}-OCH_3 and intact species like Ti_{5c}-$HOCH_3$ and Ti bound water appeared. We will discuss the source of water later. The total coverage of adsorbates is estimated to be ∼7.6% ML. The magnified image in Fig 7.11(d) shows VO bound to a water dimer (bright red) and two water monomers (light red) formed along the [001] direction. For clarity, the (1 × 1) lattice is overlaid in the magnified image, whereby each node represents a Ti atom. It is clear that water monomers and dimers are discernible by their adsorption sites: the monomer directly over one node, and the dimer is centered between two nodes and appears enlongated along the [001] direction, consistent with previous STM experiments.[180] The stabilization of intact methanol at room temperature is surprising given that methanol typically desorbs around 295 K.[60] The confirmation of intact methanol and their effect on VO-$(OCH_3)_n$ation will be discussed later. The stabilization of water chain features on the VO-decorated surface is not surprising as Xiao et al.[178] had discovered previously, however, what is new is the *formation* of water from methanol dissociation at room temperature. Water formation and their effects on the surface chemistry will be discussed later.

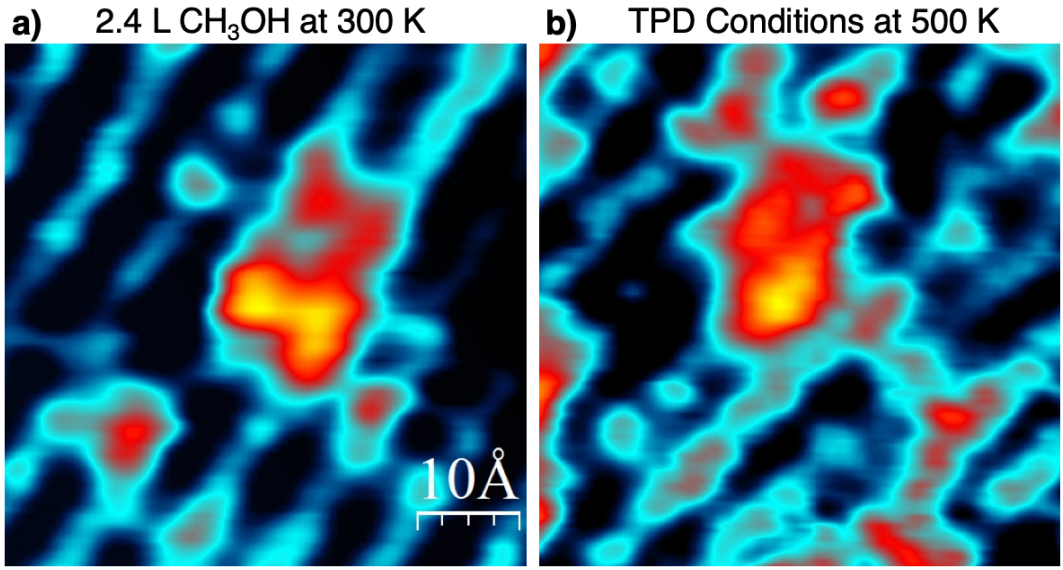

Figure 7.12: Representative room temperature images (80 × 80 Å^2) of a prototypical VO-$(OCH_3)_n$ prepared by (a) exposure to 2.4 L of methanol at room temperature with (b) a VO-$(OCH_3)_n$ prepared by TPD conditions: exposure to 100 L of methanol at room temperature and flashed to 500 K.

VO-$(OCH_3)_n$ formed at room temperature after a total methanol exposure of 2.4 L. The large scale image in Fig 7.11(e) depicts the same area of the surface following an additional exposure to 1.8 L of methanol. The same set of VO clusters (white circles) drastically grew in size following exposure, indicative of complexation with methoxides. Like the previous 0.6 L exposure, negligible amounts of OH_{br} and O_{vac}-OCH_3 were found on the surface. The VO-$(OCH_3)_n$ (white box) magnified in Fig 7.11(f) reveals multiple methoxides bound directly to the VO cluster. In addition, monomers and dimers of water were found at Ti_{5c} sites adjacent to VO-$(OCH_3)_n$. For clarity, the (1 × 1) lattice is overlaid in the magnified image, whereby each node denotes a Ti atom. The VO-$(OCH_3)_n$ formed here-in at room temperature appear to be similar to the VO-$(OCH_3)_n$ formed under TPD experimental conditions. A comparison of both complexes shown in Fig 7.12 illustrate their remarkable resemblance. Given their facile kinetics at room

temperature and their stability at 500 K, we conclude the formation of VO-$(OCH_3)_n$ is driven by thermodynamic forces. The low kinetic barrier of formation also indicates that very accurate adsorption energy profiles of the VO-$(OCH_3)_n$ can be calculated by DFT.

After establishing VO clusters bond with methoxides at room temperature, we now address their mechanism of formation. Here, we will explore how the interactions between VO clusters and O_{vac} defects stabilizes intact adsorbates and gives rise to VO-$(OCH_3)_n$. Our kinetic experiments shown in Fig 7.11(a - f) reveal that the formation of stable VO-$(OCH_3)_n$ coincide with the formation of water, Ti_{5c}-OCH_3 and intact Ti_{5c}-$HOCH_3$ species. Concomitantly, we observed negligible densities of both OH_{br} and O_{vac}-OCH_3 at these elevated exposures. This finding is counter-intuitive considering that after 0.3 L exposure, Fig 7.10(a - b) shows methanol readily dissociated into OH_{br} and O_{vac}-OCH_3 at O_{vac} defects. We reason that the preference for Ti_{5c} bound species over vacancy bound species occurs when the density of adsorbates approaches the density of O_{vac}'s. Following 0.6 L of methanol, the total density of adsorbates $\sim$7.6% ML (excluding VO clusters) in Fig 7.11(c - d), surpasses the density of O_{vac}'s $\sim$ 5 - 7 % ML. This kinetic effect is consistent with previous STM experiments that reported the formation and diffusion of Ti_{5c}-$HOCH_3$ on bare r-TiO_2 at 235 K following excess methanol exposure at room temperature.[182] Still, the observation of intact methanol on the VO-decorated surface at room temperature is unusual. On the bare surface, intact methanol diffuses too fast at room temperature to be imaged by STM.[153] Therefore we propose VO indirectly stabilizes the adsorption of the Ti_{5c}-$HOCH_3$ species, as depicted in Fig 7.11(c - d). This is similar stabilization to Ti_{5c}-$(H_2O)_n$ by VO clusters, n = 1, 2, 3, ...

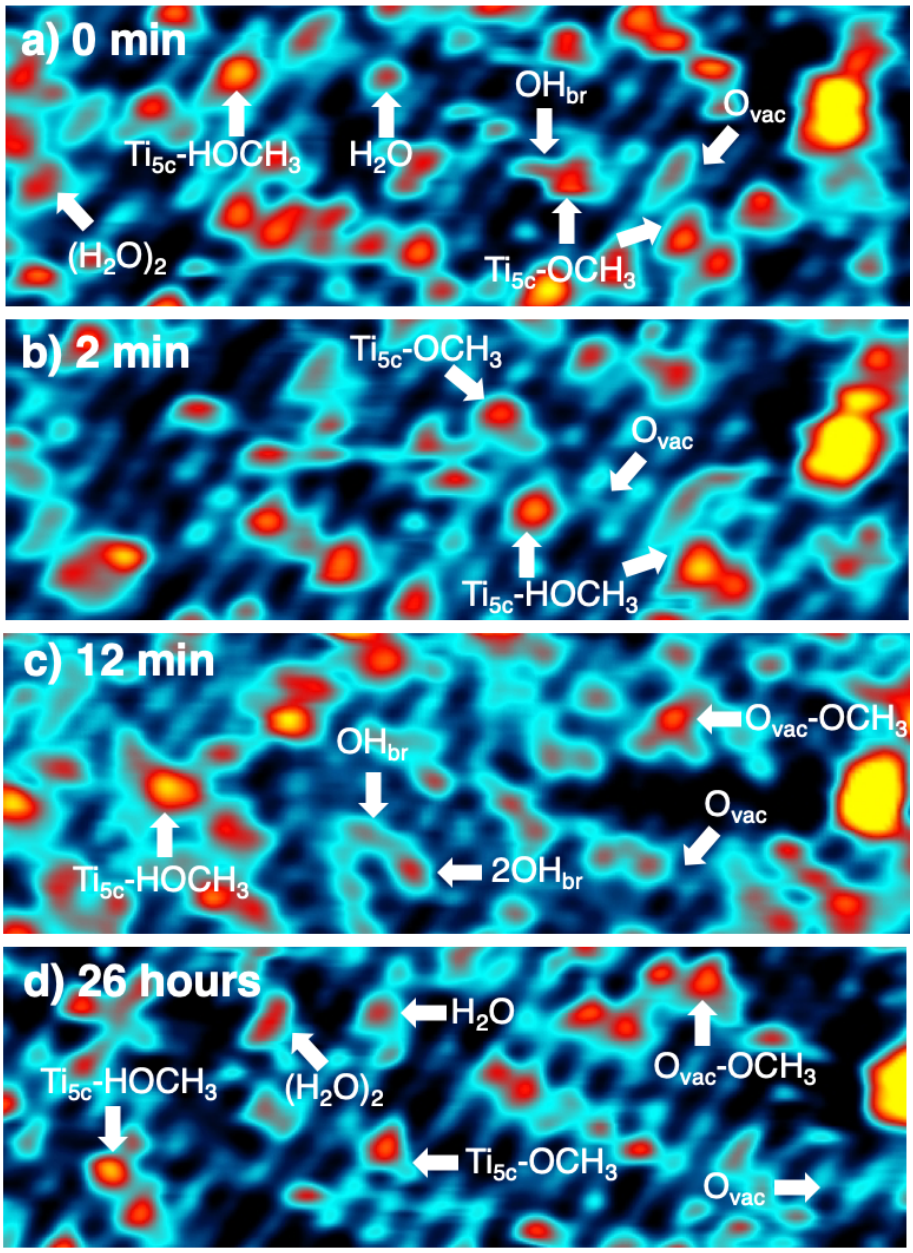

Figure 7.13: Time-Lapsed room temperature images (175 × 50 Å^2) of the same region on the VO/r-TiO_2 surface. Note that no VO clusters are present in this image. (a) the surface following 0.3 L exposure to methanol and flashed to 400 K. (b) the same area immediately following 0.6 L methanol exposure at t = 0 min. (c) At t = 2 min. (d) At t = 26 hours.

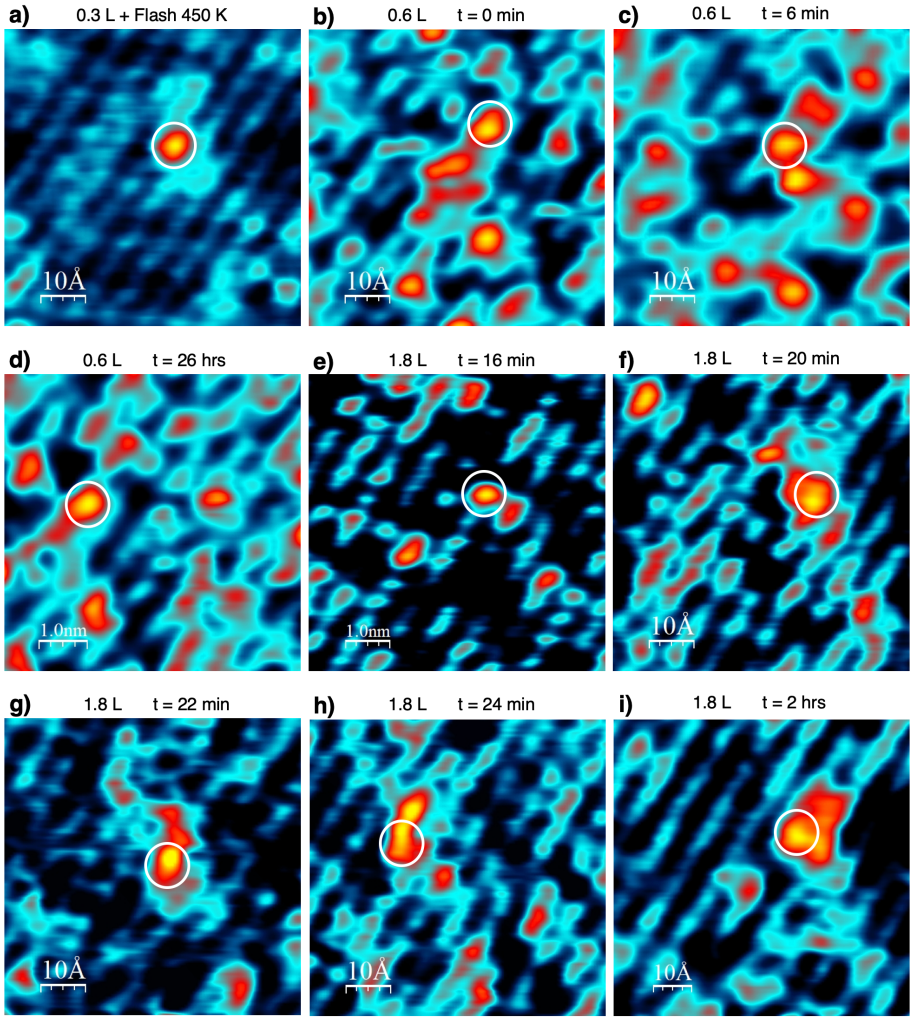

Figure 7.14: Room temperature images (70×70 Å^2) captures the evolution of a single VO cluster (white circle) into a VO-$(OCH_3)_n$ at additional exposures denoted above. Each time stamp denotes the time taken since the first image immediately following an exposure of methanol.

A consequence of VO's ability to stabilize water and methanol on Ti_{5c} sites is the onset of diffusion and reversible dissociation events at O_{vac} defects at elevated methanol exposures. This remarkable reversibility in dissociation at room temperature is illustrated in Fig 7.13(a - d) by a series of time-lapsed images of the same region following 0.6 L of methanol. In Fig 7.13(a - b), the recombination of Ti_{5c}-$HOCH_3$ was directly captured in the sequential images from t = 0 min to t = 2 min. The mechanism proceeds by Ti_{5c}-OCH_3 hopping across the OH_{br} site to form Ti_{5c}-$HOCH_3$ in the adjacent Ti trough. The same feature at t = 12 min diffuses out of sight. Many O_{vac} defects visible through out the sequence of images were reversibly filled and vacated by hydroxyls and methoxides. The sequence of micrographs from t = 12 min to t = 26 hours in Fig 7.13(c - d) demonstrates the recovery of O_{vac} sites following hydroxyl formation. Water monomers and dimers were also observed on the surface and can be seen diffusing in and out of sight. The facile recombination barrier for methanol and water at O_{vac} is also consistent with our attenuation of the R_2 peaks in our water TPR and methanol TPD spectra. This mechanism is also confirmed by the negligible vacancy bound adsorbates in our variable-temperature STM experiments. The instability associated with OH_{br} and O_{vac}-OCH_3 species therefore suggests that VO clusters getter excess electrons from O_{vac} defects. In effect, the surface has been oxidized despite the fact that VO clusters do not adsorb at O_{vac} defects and do not dissociate.

With knowledge of the adsorbates that form under elevated exposures and their diffusion properties we can deduce the orientation of VO clusters and their preferential adsorbate binding sites during complexation *in situ*. Interestingly, the formation of VO-$(OCH_3)_n$ation is also very dynamic despite the fact methoxide complexation is exothermic

at room temperature. In Fig 7.14 (a - i) we tracked the formation of one VO-$(OCH_3)_n$ over 27 hours and over various methanol exposures. Starting with the recovery of an intact VO cluster, we exposed the surface to 0.6 L and imaged immediately after methanol was evacuated from the chamber. The VO cluster was seen oscillating between VO-H_2O and VO-CH_3OH complexes with monomers and dimers of water, as well as methanol, previously identified by the lattice grid in Fig 7.11(d). This dance between VO and the different adsorbates is illustrated in Fig 7.14(b - d). Surprisingly, both water and methanol were not found to bind simultaneously to VO; this may reflect a constraint in the electronic structure or steric hinderance of the system. This trade off between the different adsorbates occurs frequently and at the same orientation relative to VO, indicating there is a large preference for water to share the same Ti trough as VO and for methanol to adsorb in the adjacent Ti trough closest to the V atom. The preference for water to bind to VO along the same Ti trough was observed previously by Xiao et al.[178]. DFT calculations from the same authors suggests VO-H_2O complex is mediated by a hydrogen bond between water and the O atom from the VO cluster. The adsorption preference for methanol and whether the species is dissociated however is still ambiguous. To confirm methanol's adsorption preferences, we exposed the surface to an additional 1.8 L of methanol and imaged immediately after methanol evacuation.

As previously shown in Fig 7.11(e - f), exposure to an additional 1.8 L of methanol forms stable VO-$(OCH_3)_n$, but their final structure and geometry were inaccessible by STM. By tracking the formation of VO-$(OCH_3)_n$ formation *in-situ* we can infer the structure of the final VO-$(OCH_3)_n$. Time-lapsed images of methanol complexation with VO are shown in Fig 7.14(e - i). After 16 min, a methoxide appeared adjacent to the

VO cluster. The methoxide was identified by adsorption site on a lattice grid not shown here. The same feature remained stable in subsequent images, indicating the presence of methoxide. In Fig 7.14(f) intact methanol, identified by height diffuses up the [001] direction and anchors to the left side of the VO cluster. The adsorbate appeared to have dissociated into a methoxide based on the apparent height changes. Concomitantly, a second methanol appeared in the adjacent Ti trough and a second methoxide appeared on the right side of the complex. The subsequent images in Fig 7.14(g - i) reveal the VO-$(OCH_3)_n$ undergoes a series of configurations before reaching a stable state. The VO-$(OCH_3)_n$ in Fig 7.14(i) does not change structure after an additional 45 min of imaging. The final state of the complex is likely made up of several Ti_{5c}-OCH_3. The orientation of the complex indicates that the Ti trough right of the VO complex is most stable and likely due to a bond formed with the V atom. The preference for adsorption is also consistent with methanol adsorption at the same Ti site at 0.6 L.

7.4 Conclusion

We have deposited mass-selected VO^+ clusters on the reduced r-TiO_2 (110) - (1 $\times$ 1) surface and carried out methanol TPD/R and UHV-STM experiments. Our TPD/R results show VO scavenges electrons from the titania support as evident by the absence of methanol and water recombination from bridging oxygen vacancy defects. In addition to the classical methoxide disproportionation reaction, methanol TPR also reveal a VO-mediated high temperature disproportionation reaction to methanol and formaldehyde. In this respect, methanol chemistry on the VO-decorated surface appears to be similar to the oxygen-decorated surface (o-TiO_2). Room temperature STM experiments following

flashes to various temperatures along the methanol desorption pathway on the VO/r-TiO_2 surface confirm a precursor intermediate state consisting of several methoxides bound to VO to form a VO-$(OCH_3)_n$. In addition we confirm the surface was effectively oxidized in two ways: (1) nearly negligible densities of vacancy-bound adsorbates were observed above 500 K and (2) no TiO_x islands following high temperature methoxide disproportionation were observed.

We also resolved the structure and formation of the precursor VO-$(OCH_3)_n$. STM experiments on VO/r-TiO_2 exposed to various amounts of methanol show the formation barrier for the VO-$(OCH_3)_n$ is facile at room temperature. Our time-lapsed images at elevated methanol exposures reveal the recombination barrier of vacancy-bound hydroxyls and methoxides are facile, indicating vacancy defects were oxidized. In addition, VO indirectly stabilizes both molecular water and methanol on the Ti_{5c} row at room temperature. As a result, methanol and water diffuse around the surface until a stable VO-$(OCH_3)_n$ is formed. We also observe methanol preferentially dissociates at Ti_{5c} proximal to the V atom. The drive for several methoxides to complex with VO is likely due to the desire for V to be in a higher oxidation state. Our results suggest electron-donating point defects, Ti interstitials and bridging oxygen vacancies, are oxidized by the presence of VO despite the fact VO does not dissociate nor fill a vacancy defect. Methoxide disproportionation reactions were also observed in our previous work on mass-selected V_2O_6 and V_3O_9 clusters under UHV conditions[62]. It is therefore likely that the cluster-mediated methoxide disproportionation reaction is a general consequence of supported vanadia catalyst. Oddly, our findings are very similar to methanol TPD and STM results of platinum clusters deposited on rutile TiO_2.[185, 183]

Chapter 8

Conclusion & Outlook

The unique combination of a home-built Smalley-type cluster source with TPD/R and UHV-STM capabilities provides us with unprecedented molecular detail into the inner workings of the oxidative dehydrogenation (ODH) reaction on a mixed-metal oxide model catalyst. In short, we have identified the active sites and elementary mechanisms associated with methanol ODH on the bare rutile support and investigated how this system is perturbed by the deposition of mass-selected VO^+ clusters. Our conclusions discussed below are particularly novel as many of the questions resolved here-in would not be possible without our ability to deposit mass-selected metal-oxide clusters of well-defined stoichiometry and the employ of high-resolution UHV-STM. For example, ensemble-characterization techniques like He^+ ion scattering and grazing-incidence X-ray scattering, commonly used by our colleagues, Prof. Anderson (University of Utah) and Dr. Vajda (Argonne National Laboratory), would have difficulty elucidating the non-periodic structure of VO-$(OCH_3)_n$, the presence of TiO_x islands and resolving the intricacies associated with adsorbate dynamics.

8.1 Summary of CH_3OH Reactivity on TiO_2

Previous investigations by ensemble based techniques had found both the deoxygenation of methanol into methane, and the disproportionation of methanol into formaldehyde, to be highly dependent on the oxidation state of the titania substrate.[60, 162] Despite this work, no fundamental insight into the substrate active sites associated with methanol reactivity have been reported. Here we reveal with a combination of temperature programmed desorption and reaction (TPD/R) and variable temperature UHV-STM, that Ti interstitials implicated in the bulk reduction of the substrate, are reactive sites in the production of formaldehyde and methane via a new disproportionation reaction between methoxides. This new disproportionation reaction occurs between two methoxides; one bound at a Ti interstitial and one isolated on the five-coordinated titanium (Ti_{5c}) row. The reaction produces methane and formaldehyde, and leaves behind an oxygen adatom (O_{ad}) bound to the Ti interstitial. After the disproportionation reaction, new TiO_x islands were observed by STM, indicating sub-surface Ti interstitials were oxidized by methanol. TPR results revealed that surfaces depleted of Ti interstitials by annealing in O_2 were the least active for methane production. While reduced surfaces free of surface oxygen vacancies were the most reactive, suggesting that methanol reactivity occurs via a Ti interstitial pathway. Our results resolve fundamental questions regarding Ti interstitials in methanol reactivity, and suggest that the role of Ti interstitials must be considered in studies of catalysis and photocatalysis on titania. Additionally our results add to the growing body of evidence that suggest Ti interstitials contribute excess electrons in rutile TiO_2.

8.2 Future Experiments on CH_3OH Reactivity on TiO_2

Although we have established Ti interstitials are active sites for methanol reactivity, the proposed reaction mechanisms are questionable given that we also see by STM, vacancy bound methoxides (O_{vac}-OCH_3) at high temperatures. The formation of methanol and formaldehyde at high temperature was proposed by Henderson et al.[60] to be due to Ti_{5c} bound methoxides (Ti_{5c}-OCH_3), however none of our current TPD/R and STM can confirm this assignment. One way to confirm Henderson's assignment would be to perform methanol TPD/R above the recombination temperature ($\sim$480 K) of O_{vac}-OCH_3 and OH_{br}, assuming the sticking probability of methanol is high enough. If Henderson's assignment is correct, we should still see this disproportionation reaction. This experiment will also confirm or rule out whether methane is created by our new proposed disproportionation mechanism or between OH_{br} and one Ti_{5c}-OCH_3. Lastly, the use of CD_3OH in similar methanol TPD/R experiments may also help confirm our proposed reaction mechanisms.

8.3 Summary on CH_3OH Reactivity on VO/TiO_2

The extent of methanol ODH on supported vanadia catalysts has been shown to correlate monotonically with substrate reducibility, however the nature in which support defects contribute to catalytic synergy is unknown[13]. While many surface science groups have established that the electronic structure of the support is indeed altered by the presence of vanadium and vanadium oxide, exactly how these alterations affect the re-

active sites and their surface chemistry remains unknown. Here-in we have demonstrated that the Ti interstitial-mediated reaction pathway in methanol disproportionation is perturbed by the deposition of VO^+ clusters. Our TPD/R and UHV-STM results indicate VO clusters oxidize the R_2 methanol recombination peak and provide a new disproportionation reaction pathway, in which multiple methoxides form VO-$(OCH_3)_n$- a precursor intermediate. To understand how VO-$(OCH_3)_n$ arise we imaged their formation under different methanol exposures. We find VO clusters indirectly stabilize the adsorption of isolated Ti_{5c}-OCH_3: a feature that is not found on the bare reduced surface.[153] At increased adsorbate densities, VO indirectly stabilizes intact water and methanol. As a result, VO clusters destabilize those species that are bound at O_{vac} defects and ensure recombination and diffusion of adsorbates. Our STM experiments indicate that excess electrons associated O_{vac} defects are gettered by VO clusters. Coupled with our lack of TiO_x islands observed under variable temperature experiments, we conclude VO oxidizes both the electron donating defects: O_{vac} and Ti interstitials. In conclusion, methanol reactivity on the VO/r-TiO_2 closely resembles the oxidized surface (o-TiO_2), despite the fact that VO adsorbs intact at the upper three-fold hollow site.[179] Platinum clusters have also been shown to oxidize the r-TiO_2 support and stabilize Ti_{5c}-OCH_3 at room temperature.[185, 183] It is therefore likely that ODH reactions on supported vanadia and supported platinum share some common traits and mechanisms.

8.4 Future Experiments on CH_3OH Reactivity on VO/TiO_2

A key experiment missing from our results is methane desorption. The detection of methane in this system would offer insight into whether VO directly interacts with sub-surface Ti interstitialst. If no methane is detected, it is likely VO has completely quenched the reactivity of Ti interstitials by oxidation. On the other hand, methane detection would indicate VO clusters are becoming partially charged. Indeed, our results do indicate VO clusters act as electron scavengers. As a result, VO clusters may be mediating a disproportionation reaction to formaldehyde and methane. The product of which would produce a VO_2 or VO and oxygen adatom.

The remarkable ability of VO^+ clusters to stabilize Ti_{5c}-OCH_3 highly suggests that VO/r-TiO_2 could be an excellent photocatalyst. It is well known among the surface science community that Ti_{5c}-OCH_3 and not intact methanol is the active species in photocatalytic experiments on rutile TiO_2 (110).[117, 118, 151, 163] Theorists have reasoned that the Ti_{5c}-OCH_3 HOMO lies near the top of the valence-band and interacts with the electron-hole pair upon photo-adsorption to produce formaldehyde and an adjacent OH_{br}.[186] I therefore propose, installing a fiber-optic system in the UHV chamber to deliver the requisite 365 nm wavelength of light and carrying out methanol TPD/R experiments on the VO-decorated surface following UV light irradiation. Our beetle-head scanner from RHK also gives us the ability to scan in-situ while the surface is irradiated with UV light. These kinds of STM and TPD/R experiments coupled with our Smalley-type cluster source could offer completely new insight into how isolated stoichiometrically

well-defined metal and metal-oxide clusters modify the electronic structure and reactivity of a photocatalyst- a feat no other group has attempted.

Given that VO^+ clusters render O_{vac} defects unfavorable for dissociation, we propose exploring how ethanol may interact with this system. Unlike methanol, the dissociation of ethanol at O_{vac} defects was concluded by STM and TPD/R to be more stable than Ti_{5c} bound ethoxides at high temperatures.[177, 165] Following an anneal to 480 K, no Ti_{5c} bound ethoxides were found. In addition, ethanol is well known to undergo dehydration into ethylene and water at these O_{vac} defect sites.[175, 176] We propose conducting ethanol TPD/R experiments on the VO-decorated surface to explore whether this reaction in quenched or re-routed to a VO-mediated pathway.

Lastly, the ability of VO^+ clusters to scavenge electrons from electron donating defects in rutile TiO_2 (110) begs the question: how would VO modify the chemistry on anatase TiO_2? Anatase is extremely interesting for a myriad of reasons: (1) the anatase polymorph is the most industrially relevant substrate given their common synthesis methods[14] and (2) the excess electrons in reduced anatase are characterized by free carrier dynamics.[137] For comparison, excess electrons in rutile localize as polarons. The difference in electronic properties between both polymorphs would present an excellent system to investigate how electrons in the lattice directly interact with VO^+ clusters. Due to their free carrier dynamics, anatase is considered to be the better substrate for photocatalysis.[187] We propose conducting photocatalytic experiments with methanol on the VO-decorated anatase (101) surface in a similar manner discussed above. Single crystals of anatase (101) can be prepared in a similar manner to rutile substrate, see references there-in.[137]

8.5 Summary on Imaging Wet Electron States in CH_3OH

By sheer serendipity, we have discovered that the so-called wet electron state could be directly visualized by UHV-STM. The wet electron state is defined as the partial hydration/solvation of interfacial excess electrons in protic solvents, and is absolutely fundamental to photocatalysis and electrocatalysis. Wet electron states in a saturated layer of methanol adsorbed on TiO_2, appear resonantly at 2.3 $\pm$0.1 electron volts above the Fermi energy level, and coincide with solvent reorientation and delocalization of unoccupied surface states.[188, 139, 141] We employed room temperature constant-current scanning tunneling microscopy (STM) to directly visualize the spatial distribution of unoccupied states in a saturated layer of methanol on rutile TiO_2 (110) - (1 $\times$ 1) as a function of the scan bias. Our measurements below 2.00 V, reveal unoccupied states localize on methyl groups, appearing as well-ordered 1D structures. Micrographs recorded in the wet electron state regime reveal delocalization between methyl groups and the substrate, resulting in the appearance of quasi-disordered clusters dispersed heterogeneously through out the surface. Our results provide the first time wet electron states have been directly imaged, and should further stimulate research into understanding interfacial electron transport.

8.6 Future Experiments on Wet Electron States in CH_3OH

Our STM experiments on the wet electron state do not address the exact location of the solvated electrons in the methanol over-layer. To correlate their location, we can conduct constant-current imaging under negative biases and conduct I-V spectroscopy at every pixel on the rastor scan to obtain a spatial map of their filled and unfilled states.[79] This can be achieved by conducting scanning tunneling spectroscopy (dI/dV) with a lock-in amplifier. In addition to methanol, water is also known to have a wet electron state centered around 2.5 eV.[188] Performing similar experiments on monolayer water around 2.5 volts should achieve the same results obtained for methanol. However to image monolayer water, we must cool the sample to less than their monolayer desorption peak $\sim$ 270 K. Imaging in our system at colder temperatures however is not ideal, as the liquid nitrogen refrigerator introduces too much noise to obtain sufficient resolution. Suspending the refrigerator from springs bolted to the ceiling has been discussed.

Bibliography

[1] H. A. Wittcoff, B. G. Reuben, and J. S. Plotkin, *Industrial Organic Chemicals*. John Wiley Sons, Inc., second ed., 2004.

[2] E. W. McFarland and H. Metiu, *Catalysis by doped oxides*, *Chemical Reviews* **113** (2013), no. 6 4391–4427.

[3] "America's new energy future: The uncoventional oil gas revolution and the us economy."

[4] M. Bhasin, J. McCain, B. Vora, T. Imai, and P. Pujadó, *Dehydrogenation and oxydehydrogenation of paraffins to olefins*, *Applied Catalysis A: General* **221** (2001), no. 1 397 – 419.

[5] "Uop oleflex process for light olefin production."

[6] J. J. H. Sattler, J. Ruiz-Martinez, E. Santillan-Jimenez, and B. M. Weckhuysen, *Catalytic dehydrogenation of light alkanes on metals and metal oxides*, *Chemical Reviews* **114** (2014) 10613–10653.

[7] B. Ajayi, B. R. Jermy, K. Ogunronbi, B. Abussaud, and S. Al-Khattaf, *n-butane dehydrogenation over mono and bimetallic mcm-41 catalysts under oxygen free atmosphere*, *Catalysis Today* **204** (2013) 189 – 196.

[8] F. Cavani, N. Ballarini, and A. Cericola, *Oxidative dehydrogenation of ethane and propane: How far from commercial implementation?*, *Catalysis Today* **127** (2007), no. 1 113 – 131.

[9] D. J. Stacchiola, S. D. Senanayake, P. Liu, and J. A. Rodriguez, *Fundamental studies of well-defined surfaces of mixed-metal oxides: Special properties of mox/tio2(110) M = V, Ru, Ce, or W*, *Chemical Reviews* **113** (2013), no. 6 4373–4390.

[10] M. B. Gawande, R. K. Pandey, and R. V. Jayaram, *Role of mixed metal oxides in catalysis science: versatile applications in organic synthesis*, *Catalysis Science and Technology* **2** (2012) 1113–1125.

[11] K. Weissermel and H. J. Arpe, *Industrial organic chemicals- important raw materials and intermediates*, *Verlag Chemie* (1978) 335–339.

[12] B. M. Weckhuysen and D. E. Keller, *Chemistry, spectroscopy and the role of supported vanadium oxides in heterogeneous catalysis*, *Catalysis Today* **78** (2003), no. 1 25 – 46.

[13] I. E. Wachs, *Recent conceptual advances in the catalysis science of mixed metal oxide catalytic materials*, *Catalysis Today* **100** (2005), no. 1 79 – 94.

[14] F. Roozeboom, P. D. Cordingley, and P. J. Gellings, *Vanadium oxide monolayer catalysts: The vapor-phase oxidation of methanol*, *Journal of Catalysis* **68** (1981), no. 2 464 – 472.

[15] M. Chaar, D. Patel, M. Kung, and H. Kung, *Selective oxidative dehydrogenation of butane over vmgo catalysts*, *Journal of Catalysis* **105** (1987), no. 2 483 – 498.

[16] I. E. Wachs, *Catalysis science of supported vanadium oxide catalysts*, *Dalton Trans.* **42** (2013) 11762–11769.

[17] I. Muylaert and P. Van Der Voort, *Supported vanadium oxide in heterogeneous catalysis: elucidating the structure–activity relationship with spectroscopy*, *Phys. Chem. Chem. Phys.* **11** (2009) 2826–2832.

[18] G. Deo, I. E. Wachs, and J. Haber, *Supported vanadium oxide catalysts: Molecular structural characterization and reactivity properties*, *Critical Review Surface Chemistry* **4** (1994) 141–187.

[19] G. Centi, *Nature of active layer in vanadium oxide supported on titanium oxide and control of its reactivity in the selective oxidation and ammoxidation of alkylaromatics*, *Applied Catalysis A: General* **147** (1996), no. 2 267 – 298.

[20] G. Bond, *Preparation and properties of vanadia/titania monolayer catalysts*, *Applied Catalysis A: General* **157** (1997), no. 1 91 – 103.

[21] A. Khodakov, B. Olthof, A. T. Bell, and E. Iglesia, *Structure and catalytic properties of supported vanadium oxides: Support effects on oxidative dehydrogenation reactions*, *Journal of Catalysis* **181** (1999), no. 2 205 – 216.

[22] K. Chen, A. Khodakov, J. Yang, A. T. Bell, and E. Iglesia, *Isotopic tracer and kinetic studies of oxidative dehydrogenation pathways on vanadium oxide catalysts*, *Journal of Catalysis* **186** (1999), no. 2 325 – 333.

[23] M. D. Argyle, K. Chen, A. T. Bell, and E. Iglesia, *Ethane oxidative dehydrogenation pathways on vanadium oxide catalysts*, *Journal of Physical Chemistry B* **106** (2002), no. 21 5421–5427.

[24] P. Mars and D. van Krevelen, *Oxidations carried out by means of vanadium oxide catalysts*, *Chemical Engineering Science* **3** (1954) 41 – 59.

[25] H. Tian, E. I. Ross, and I. E. Wachs, *Quantitative determination of the speciation of surface vanadium oxides and their catalytic activity*, *Journal of Physical Chemistry B* **110** (2006), no. 19 9593–9600.

[26] T. Kim and I. E. Wachs, *Ch3oh oxidation over well-defined supported v2o5/al2o3 catalysts: Influence of vanadium oxide loading and surface vanadium–oxygen functionalities*, *Journal of Catalysis* **255** (2008), no. 2 197 – 205.

[27] J. Z. Hu, S. Xu, W. Li, M. Y. Hu, X. Deng, D. A. Dixon, M. Vasiliu, R. Cracium, Y. Wang, X. Bao, and C. H. F. Peden, *Investigation of the structure and active sites of tio2 nanorod supported vox catalysts by high-field and fast-spinning* ^{51}v *mas nmr*, *ACS Catalysis* **5** (2015) 3945–3952.

[28] K. Routray, L. E. Briand, and I. E. Wachs, *Is there a relationship between the mo bond length (strength) of bulk mixed metal oxides and their catalytic activity?*, *Journal of Catalysis* **256** (2008), no. 1 145 – 153.

[29] N. Magg, B. Immaraporn, J. B. Giorgi, T. Schroeder, M. Bäumer, J. Döbler, Z. Wu, E. Kondratenko, M. Cherian, M. Baerns, P. C. Stair, J. Sauer, and H.-J. Freund, *Vibrational spectra of alumina- and silica-supported vanadia revisited: An experimental and theoretical model catalyst study*, *Journal of Catalysis* **226** (2004), no. 1 88 – 100.

[30] X. Rozanska, R. Fortrie, and J. Sauer, *Oxidative dehydrogenation of propane by monomeric vanadium oxide sites on silica support*, *Journal of Physical Chemistry C* **111** (2007) 6041–6050.

[31] H. Y. Kim, H. M. Lee, and H. Metiu, *Oxidative dehydrogenation of methanol to formaldehyde by vanadium oxide cluster supported on rutile tio2 (110): Which oxygen is involved?*, *Journal of Physical Chemistry C* **114** (2010), no. 32 13736–13738.

[32] B. Beck, M. Harth, N. G. Hamilton, C. Carrero, J. J. Uhlrich, A. Trunschke, S. Shaikhutdinov, H. Schubert, H.-J. Freund, R. Schlögl, J. Sauer, and R. Schomäcker, *Partial oxidation of ethanol on vanadia catalysts on supporting oxides with different redox properties compared to propane*, *Journal of Catalysis* **296** (2012) 120 – 131.

[33] L. J. Burcham and I. E. Wachs, *The origin of the support effect in supported metal oxide catalysts: in situ infrared and kinetic studies during methanol oxidation*, *Catalysis Today* **49** (1999), no. 4 467 – 484.

[34] M. Ruitenbeek, A. van Dillen, F. de Groot, I. Wachs, J. Geus, and D. Koningsberger, *The structure of vanadium oxide species on γ-alumina; an in situ x-ray absorption study during catalytic oxidation*, *Topics in Catalysis* **10** (2000), no. 3 241–254.

[35] L. J. Burcham, G. Deo, X. Gao, and I. E. Wachs, *In situ ir, raman, and uv-vis drs spectroscopy of supported vanadium oxide catalysts during methanol oxidation*, *Topics in Catalysis* **11** (2000), no. 1 85–100.

[36] X. Gao, J.-M. Jehng, and I. E. Wachs, *In situ uv–vis–nir diffuse reflectance and raman spectroscopic studies of propane oxidation over zro2-supported vanadium oxide catalysts*, *Journal of Catalysis* **209** (2002), no. 1 43–50.

[37] J. L. Bronkema and A. T. Bell, *Mechanistic studies of methanol oxidation to formaldehde on isolated vanadate sites supported on high surface area zirconia*, *Journal of Physical Chemistry C* **112** (2008), no. 16 6404–64012.

[38] V. Shapovalov and H. Metiu, *Vox (x = 1-4) submonolayers supported on rutile tio2 (110) and ceo2 (111) surface: The structure, the charge of the atoms, the xps spectrum, and the equilibrium composition in the presence of oxygen.*, *Journal of Physical Chemistry C* **111** (2007) 14179–14188.

[39] H. Raebiger, S. Lany, and A. Zunger, *Charge self-regulation upon changing the oxidation state of transition metals in insulators*, *Nature* **453** (2008) 763–766.

[40] A. C. Papageorgiou, N. S. Beglitis, C. L. Pang, G. Teobaldi, G. Cabailh, Q. Chen, A. J. Fisher, W. A. Hofer, and G. Thornton, *Electron traps and their effect on the surface chemistry of tio2(110)*, *Proceedings of the National Academy of Sciences* **107** (02, 2010) 2391–2396.

[41] H. Y. Kim, H. M. Lee, R. G. S. Pala, V. Shapovalov, and H. Metiu, *Co oxidation by rutile tio_2 (110) doped with v, w, cr, mo, and mn*, *Journal of Physical Chemistry C* **112** (2008), no. 32 12398–12408.

[42] A. Goodrow and A. T. Bell, *A theoretical investigation of the selective oxidation of methanol to formaldehyde on isolated vanadate species supported on titania*, *Journal of Physical Chemistry C* **112** (2008), no. 34 13204–13214.

[43] T. Kropp, J. Paier, and J. Sauer, *Support effect in oxide catalysis: Methanol oxieation on vanadia/ceria*, *Journal of the American Chemical Society* **136** (2014), no. 41 14616–14625.

[44] Y. Cao, S. Chen, Y. Li, Y. Gao, D. Yang, Y. R. Shen, and W.-T. Liu, *Evolution of anatase surface active sites probed by in situ sum-frequency phonon spectroscopy*, *Science Advances* **2** (2016), no. 9.

[45] M. Setvín, U. Aschauer, P. Scheiber, Y.-F. Li, W. Hou, M. Schmid, A. Selloni, and U. Diebold, *Reaction of o₂ with subsurface oxygen vacancies on tio₂ anatase (101)*, *Science* **341** (2013), no. 6149.

[46] D. Yun, Y. Wang, and J. Herrera, *Ethanol partial oxidation over vo_x/tio_2 catalysts: The role of titania surface oxygen on vanadia reoxidation in the mars-van krevelen mechanism*, *ACS Catalysis* **8** (2018), no. 5 4681–4693.

[47] H. Abbott, A. Uhl, M. Baron, Y. Lei, R. Meyer, D. Stacchiola, O. Bondarchuk, S. Shaikhutdinov, and H. Freund, *Relating methanol oxidation to the structure of ceria-supported vanadia monolayer catalysts*, *Journal of Catalysis* **272** (2010), no. 1 82–91.

[48] M. V. Ganduglia-Pirovano, C. Popa, J. Sauer, H. Abbott, A. Uhl, M. Baron, D. Stacchiola, O. Bondarchuk, S. Shaikhutdinov, and H. Freund, *Role of ceria in oxidatie dehydrogenation on supported vanadia catalysts*, *Journal of the American Chemical Society* **132** (2010) 2345–2349.

[49] J. L. Bronkema, D. C. Leo, and A. T. Bell, *Mechanistic studies of methanol oxidation to formaldehyde on isolated vanadate sites supported on high surface area anatase*, *Journal of Physical Chemistry C* **111** (2007), no. 39 14530–14540.

[50] U. Diebold, *The surface science of titanium dioxide*, *Surface Science Reports* **48** (2003), no. 5 53 – 229.

[51] G. Deo, A. M. Turek, I. E. Wachs, T. Machej, J. Haber, N. Das, H. Eckert, and A. M. Hirt, *Physical and chemical characterization of surface vanadium oxide supported on titania: influence of the titania phase (anatase, rutile, brookite and b)*, *Applied Catalysis A: General* **91** (1992), no. 1 27–42.

[52] G. Wong, D. Kragten, and J. Vohs, *Temperature-programmed desorption study of the oxidation of methanol to formaldehyde on tio2(110)-supported vanadia monolayers*, *Surface Science* **452** (2000), no. 1 293–297.

[53] G. S. Wong, D. D. Kragten, and J. M. Vohs, *The oxidation of methanol to formaldehyde on tio2(110)-supported vanadia films*, *The Journal of Physical Chemistry B* **105** (2001), no. 7 1366–1373.

[54] G. Wong, M. Concepcion, and J. Vohs, *Reactivity of monolayer v2o5 films on tio2(110) produced via the oxidation of vapor-deposited vanadium*, *Surface Science* **526** (2003), no. 3 211 – 218.

[55] Q. Wang and R. J. Madix, *Preparation and reactions of v2o5 supported on tio2(110)*, *Surface Science* **474** (2001), no. 1 213–216.

[56] Q. Wang and R. J. Madix, *Partial oxidation of methanol to formaldehyde on a model supported monolayer vanadia catalyst: vanadia on tio2(110)*, *Surface Science* **496** (2002), no. 1 51–63.

[57] J. Biener, M. Bäumer, J. Wang, and R. J. Madix, *Electronic structure and growth of vanadium on tio2(110)*, *Surface Science* **450** (2000), no. 1 12 – 26.

[58] L. Artiglia, S. Agnoli, A. Vittadini, A. Verdini, A. Cossaro, L. Floreano, and G. Granozzi, *Atomic structure and special reactivity toward methanol oxidation of vanadia nanoclusters on tio$_2$ (110)*, *Journal of the American Chemical Society* **135** (2013) 17331–17338.

[59] S. Agnoli, C. Castellarin-Cudia, M. Sambi, S. Surnev, M. Ramsey, G. Granozzi, and F. Netzer, *Vanadium on tio2(110): Adsorption site and sub-surface migration*, *Surface Science* **546** (2003), no. 2 117 – 126.

[60] M. A. Henderson, S. Otero-Tapia, and M. E. Castro, *The chemistry of methanol on the tio2(110) surface: the influence of vacancies and coadsorbed species*, *Faraday Discuss.* **114** (1999) 313–329.

[61] S. P. Price, X. Tong, C. Ridge, H. L. Neilson, J. W. Buffon, J. Robins, H. Metiu, M. T. Bowers, and S. K. Buratto, *Catalytic oxidation of methanol to formaldehyde by mass-selected vanadium oxide clusters supported on a tio2(110) surface*, *The Journal of Physical Chemistry A* **118** (2014), no. 37 8309–8313.

[62] H. L. Neilsen, *The Reactivity and Structure of Size-Selected VxOy Clusters on TiO2 (110) - (1 X 1) Surface of Variable Oxidation State*. PhD thesis, University of California Santa Barbara, Santa Barbara, 2015.

[63] Z. Zhang and V. E. Henrich, *Electronic interactions in the vanadium/tio2(110) and vanadia/tio2(110) model catalyst systems*, *Surface Science* **277** (1992), no. 3 263 – 272.

[64] S. Lee, G. W. Zajac, and D. W. Goodman, *A study of the electronic structure and reactivity of v/tio2(110) with metastable impact electron spectroscopy (mies) and ultraviolet photoelectron spectroscopy (ups)*, *Topics in Catalysis* **38** (Jul, 2006) 127–132.

[65] D. P. Woodruff and T. A. Delchar, *Modern Techniques of Surface Science*. Cambridge University Press, New York, 1986.

[66] J. F. Ready, *Effects of High-Power Laser Radiation*. Academic Press, 1971.

[67] J. T. Yardley, *Introduction to Molecular Energy Transfer*. Academic Press, 1980.

[68] M. A. Duncan, *Invited review article: Laser vaporization cluster sources*, *Review of Scientific Instruments* **83** (2012), no. 4 041101.

[69] R. E. Smalley, *Laser studies of metal cluster beams*, *Laser Chemistry* **2** (1983), no. 3-4 167–184.

[70] M. D. Spain. E. M. Morse, *Bond strengths of transition-metal dimers: Tiv, v2, tico, and vni*, *Journal of Physical Chemistry* **96** (1992) 2479–2486.

[71] N. Aristov and P. B. Armentrout, *Bond energy-bond order relations*, *Journal of the American Chemical Society* **106** (1984), no. 14 4065–4066.

[72] E. Miliordos and A. Mavridis, *Electronic structure of vanadium oxide. neutral and charge species, vo*, *Journal of Physical Chemistry A* **111** (2007) 1953–1965.

[73] T. C. Jackson, T. J. Carlin, and B. S. Freiser, *Gas-phase reactions of v and vo with hydrocarbons using fourier transform mass spectrometry*, *Journal of the American Chemical Society* **108** (1985) 1120–1126.

[74] D. J. Griffiths, *Introduction to Electrodynamics*. Prentice-Hall, Inc., Upper Saddle River, NJ, 1999.

[75] P. J. Estrup, E. F. Greene, M. J. Cardillo, and J. C. Tully, *Influence of surface phase transitions on desorption kinetics: The compensation effect*, *The Journal of Physical Chemistry* **90** (1986), no. 17 4099–4104.

[76] J. Bardeen, *Tunnelling from a many-particle point of view*, *Physical Review Letters* **6** (1961), no. 57.

[77] D. R. Tersoff, J. Hamann, *Theory and application for the scanning tunneling microscope*, *Physical Review Letters* **50** (1983), no. 1998.

[78] J. Tersoff and D. R. Hamann, *Theory of the scanning tunneling microscope*, *Phys. Rev. B* **31** (1985), no. 2.

[79] C. J. Chen, *Introduction to Scanning Tunneling Microscopy*. Oxford University Press, 1993.

[80] R. C. Bell, K. A. Zemski, H. T. Deng, and A. W. Castleman, *Reactivity and collision-induced dissociation of vanadium oxide cluster cations*, *Journal of Physical Chemistry A* **102** (1998), no. 10 1733–1742.

[81] S. E. Kooi and A. W. Castleman, *Photofragmentation of vanadium oxide cations*, *Journal of Physical Chemistry A* **103** (1999), no. 29 5671–5674.

[82] J. J. Yeh and I. Lindau, *Atomic subshell photoionization cross sections and asymmetry paramters*, *Atomic Data and Nuclear Data Tables* **32** (1985) 1–55.

[83] C. Bai, *Scanning Tunneling Microscopy and Spectroscopy*. Springer, New York, 1992.

[84] J. P. Ibe, P. P. Bey, S. L. Brandow, R. A. Brizzolara, N. A. Burnham, D. P. DiLella, K. P. Lee, C. R. K. Marrian, and R. J. Colton, *On the electrochemical etching of tips for scanning tunneling microscopy*, *Journal of Vacuum Science & Technology A* **8** (1990), no. 4 3570–3575.

[85] C. L. Pang, R. Lindsay, and G. Thornton, *Structure of clean and adsorbate-covered single-crystal rutile tio2 surfaces*, *Chemical Reviews* **113** (2013), no. 6 3887–3948.

[86] Z. Dohnálek, I. Lyubinetsky, and R. Rousseau, *Thermally-driven processes on rutile tio2(110)-(11): A direct view at the atomic scale*, *Progress in Surface Science* **85** (2010), no. 5 161 – 205.

[87] A. Fujishima and K. Honda, *Electrochemical photolysis of water at a semiconductor electrode*, *Nature* **238** (1972), no. 37-38.

[88] T. Kawai and T. Sakata, *Photocatalytic hydrogen production from liquid methanol and water*, *J. Chem. Soc., Chem. Commun.* (1980) 694–695.

[89] C. Xu, W. Yang, Q. Guo, D. Dai, M. Chen, and X. Yang, *Molecular hydrogen formation from photocatalysis of methanol on tio2(110)*, *Journal of the American Chemical Society* **135** (2013), no. 28 10206–10209.

[90] Q. Guo, C. Xu, Z. Ren, W. Yang, Z. Ma, D. Dai, H. Fan, T. K. Minton, and X. Yang, *Stepwise photocatalytic dissociation of methanol and water on tio2 (110)*, *Journal of the American Chemical Society* **134** (2012) 13366–13373.

[91] K. R. Phillips, S. C. Jensen, M. Baron, S.-C. Li, and C. M. Friend, *Sequential photo-oxidation of methanol to methyl formate on tio2(110)*, *Journal of the American Chemical Society* **135** (2013), no. 2 574–577.

[92] C. McCullagh, J. M. C. Robertson, D. W. Bahnemann, and P. K. J. Robertson, *The application of tio2 photocatalysis for disinfection of water contaminated with pathogenic micro-organisms: a review*, *Research on Chemical Intermediates* **33** (2007), no. 3 359–375.

[93] G. E. Samsonov, *The Oxide Handbook*. IFI/Plenum Press, New York, 1982.

[94] E. Yagi, R. R. Hasiguti, and M. Aono, *Electronic conduction above 4 k of slightly reduced oxygen-deficient rutile* tio_{2-x}, *Phys. Rev. B* **54** (1996) 7945–7956.

[95] M. Li, W. Hebenstreit, L. Gross, U. Diebold, M. Henderson, D. Jennison, P. Schultz, and M. Sears, *Oxygen-induced restructuring of the tio2(110) surface: a comprehensive study*, *Surface Science* **437** (1999), no. 1 173 – 190.

[96] M. A. Henderson, *Mechanism for the bulk-assisted reoxidation of ion sputtered tio2 surfaces: diffusion of oxygen to the surface or titanium to the bulk?*, *Surface Science* **343** (1995), no. 1 L1156 – L1160.

[97] M. A. Henderson, *A surface perspective on self-diffusion in rutile tio2*, *Surface Science* **419** (1999), no. 2 174 – 187.

[98] K. T. Park, M. H. Pan, V. Meunier, and E. W. Plummer, *Surface reconstructions of* $\mathrm{tio}_2(110)$ *driven by suboxides*, *Phys. Rev. Lett.* **96** (2006).

[99] J. Sasaki, N. L. Peterson, and K. Hoshino, *Trace impurity diffusion in single-crystal rutile tio2*, *Journal of Physics and Chemistry of Solids* **46** (1985), no. 11 1267–1283.

[100] H. B. Huntington and G. A. Sullivan, *Interstitial diffusion mechanism in rutile*, *Physical Review Letters* **14** (1965), no. 6 177–178.

[101] S. Wendt, P. T. Sprunger, E. Lira, G. K. H. Madsen, Z. Li, J. Ø. Hansen, J. Matthiesen, A. Blekinge-Rasmussen, E. Lægsgaard, B. Hammer, and F. Besenbacher, *The role of interstitial sites in the ti3d defect state in the band gap of titania*, *Science* **320** (2008), no. 5884 1755–1759.

[102] P. W. Tasker, *The stability of ionic crystal surfaces*, *Journal of Physics C: Solid State Physics* **12** (1979), no. 22 4977–4984.

[103] J. P. LaFemina, *Total energy computations of oxide surface reconstructions*, *Critical Review Surface Chemistry* **3** (1994) 297–386.

[104] M. E. Arroyo-de Dompablo, A. Morales-García, and M. Taravillo, *Dft+u calculations of crystal lattice, electronic structure, and phase stability under pressure of tio2 polymorphs*, *The Journal of Chemical Physics* **135** (2011), no. 5.

[105] R. A. Bennett, S. Poulston, P. Stone, and M. Bowker, *Stm and leed observations of the surface structure of* $tio_2(110)$ *following crystallographic shear plane formation*, *Phys. Rev. B* **59** (1999) 10341–0346.

[106] I. M. Brookes, C. A. Muryn, and G. Thornton, *Imaging water dissociation on tio2 (110)*, *Physical Review Letters* **87** (2001), no. 26.

[107] S. Wendt, J. Matthiesen, R. Schaub, E. K. Vestergaard, E. Lægsgaard, F. Besenbacher, and B. Hammer, *Formation and splitting of paired hydroxyl groups on reduced* $tio_2(110)$, *Physical Review Letters* **96** (2006), no. 4.

[108] M. A. Henderson, *An hreels and tpd study of water on tio2(110): the extent of molecular versus dissociative adsorption*, *Surface Science* **355** (1996), no. 1 151 – 166.

[109] N. Osterloh, D. Silber, F. Traeger, and C. Wöll, *Water adsorption on r-tio2(110): Presence of a well-defined (1×1)-structure as evidenced by he-atom scattering*, *physica status solidi (b)* **250** (2013), no. 6 1235–1241.

[110] J. Lee, D. C. Sorescu, X. Deng, and K. D. Jordan, *Water chain formation on* tio_2 *(110)*, *Journal of Physical Chemistry Letters* **4** (2013), no. 1 53–57.

[111] M. B. Hugenschmidt, L. Gamble, and C. T. Campbell, *The interaction of h2o with a tio2(110) surface*, *Surface Science* **302** (1994), no. 3 329 – 340.

[112] P. Scheiber, A. Riss, M. Schmid, P. Varga, and U. Diebold, *Observation and destruction of an elusive adsorbate with stm: O2/tio2 (110)*, *Physical Review Letters* **105** (2010).

[113] E. Lira, J. Ø. Hansen, P. Huo, R. Bechstein, P. Galliker, E. Lægsgaard, B. Hammer, S. Wendt, and F. Besenbacher, *Dissociative and molecular oxygen chemisorption channels on reduced rutile tio2(110): An stm and tpd study*, *Surface Science* **604** (2010), no. 21 1945 – 1960.

[114] S. Tan, J. Yongfei, Y. Zhao, A. Zhao, B. Wang, J. Yang, and J. G. Hou, *Molecular oxygen adsorption behaviors on the rutile tio2 (110) 1x1 surface: An in situ study with low-temperature scanning tunneling microscopy*, *Journal of the American Chemical Society* **133** (2011) 2002–2009.

[115] Y. Du, Z. Dohnálek, and I. Lyubinetsky, *Transient mobility of oxygen adatoms upon o2 dissociation on reduced tio2(110)*, *The Journal of Physical Chemistry C* **112** (2008), no. 7 2649–2653, [https://doi.org/10.1021/jp077677u].

[116] Y. Du, N. A. Deskins, Z. Zhang, Z. Dohnalek, M. Dupuis, and I. Lyubinetsky, *Two pathways for water interaction with oxygen adatoms on tio2 (110)*, *Physical Review Letters* **102** (2009).

[117] M. Shen and M. A. Henderson, *Identification of the active species in photochemical hole scavenging reactions of methanol on tio2*, *The Journal of Physical Chemistry Letters* **2** (2011), no. 21 2707–2710.

[118] M. Shen, D. P. Acharya, Z. Dohnálek, and M. A. Henderson, *Importance of diffusion in methanol photochemistry on tio2(110)*, *The Journal of Physical Chemistry C* **116** (2012), no. 48 25465–25469.

[119] Y. Du, N. A. Deskins, Z. Zhang, Z. Dohnalek, M. Dupuis, and I. Lyubinetsky, *Formation of o adatom pairs and charge transfer upon o2 dissociation on reduced tio2(110)*, *Phys. Chem. Chem. Phys.* **12** (2010) 6337–6344.

[120] S. Wendt, R. Schaub, J. Matthiesen, E. Vestergaard, E. Wahlström, M. Rasmussen, P. Thostrup, L. Molina, E. Lægsgaard, I. Stensgaard, B. Hammer, and F. Besenbacher, *Oxygen vacancies on tio2(110) and their interaction with h2o and o2: A combined high-resolution stm and dft study*, *Surface Science* **598** (2005), no. 1 226 – 245.

[121] R. Deskins, N. A. Rouseesau, , and M. Dupuis, *Localized electronic states from the surface hydroxyls and polarons in tio2 (110)*, *Journal of Physical Chemistry C* **113** (2009) 14583–14586.

[122] V. E. Henrich, G. Dresselhaus, and H. J. Zeiger, *Observation of two-dimensional phases associated with defect states on the surface of tio_2*, *Phys. Rev. Lett.* **36** (1976) 1335–1339.

[123] N. G. Petrik, Z. Zhang, Y. Du, Z. Dohnalek, I. Lyubinetsky, and G. A. Kimmel, *Chemical reactivity of reduced tio2 (110): The dominant role of surface defects in oxygen chemisorption*, *Journal of Physical Chemistry C* **113** (2009) 12407–12411.

[124] Z. Zhang, Y. Du, N. G. Petrik, G. A. Kimmel, I. Lyubinetsky, and Z. Dohnálek, *Water as a catalyst: Imaging reactions of o2 with partially and fully hydroxylated tio2(110) surfaces*, *The Journal of Physical Chemistry C* **113** (2009), no. 5 1908–1916.

[125] Y. Du, N. A. Deskins, Z. Zhang, Z. Dohnalek, M. Dupuis, and I. Lyubinetsky, *Imaging consecutive steps of o2 reaction with hydroxylated tio2 (110): Idenfitication of ho2 and terminal oh intermediates*, *Journal of Physical Chemistry C* **113** (2009), no. 2 666–671.

[126] M. A. Henderson, *The interaction of water with solid surfaces: fundamental aspects revisited*, *Surface Science Reports* **46** (2002), no. 1 1 – 308.

[127] A. Tilocca, C. Di Valentin, and A. Selloni, *O2 interaction and reactivity on a model hydroxylated rutile(110) surface*, *The Journal of Physical Chemistry B* **109** (2005), no. 44 20963–20967.

[128] J. Ø. Hansen, J. Matthiesen, E. Lira, L. Lammich, and S. Wendt, *A new recipe for preparing oxidized tio2(1 1 0) surfaces: An stm study*, *Surface Science* **666** (2017) 113 – 122.

[129] P. Stone, R. A. Bennett, and M. Bowker, *Reactive re-oxidation of reduced tio 2 (110) surfaces demonstrated by high temperature stm movies*, *New Journal of Physics* **1** (1999), no. 1 8.

[130] L. Benz, J. Haubrich, R. G. Quiller, S. C. Jensen, and C. M. Friend, *Mcmurry chemistry on tio2(110): Reductive cc coupling of benzaldehyde driven by titanium interstitials*, *Journal of the American Chemical Society* **131** (2009), no. 41 15026–15031.

[131] L. Benz, J. Haubrich, S. C. Jensen, and C. M. Friend, *Molecular imaging of reductive coupling reactions: Interstitial-mediated coupling of benzaldehyde on reduced tio2(110)*, *ACS Nano* **5** (2011), no. 2 834–843.

[132] L. Chen, R. S. Smith, B. D. Kay, and Z. Dohnalek, *Direct deoxygenation of phenylmethanol to methylbenzene and benzyl radicals on rutile tio2(110)*, *ACS Catalysis* **7** (2017), no. 3 2002–2006.

[133] C. M. Yim, C. L. Pang, and G. Thornton, *Oxygen vacancy origin of the surface band-gap state of* $\mathrm{tio_2}(110)$, *Physical Review Letters* **104** (2010).

[134] P. Krüger, S. Bourgeois, B. Domenichini, H. Magnan, D. Chandesris, P. Le Fèvre, A. M. Flank, J. Jupille, L. Floreano, A. Cossaro, A. Verdini, and A. Morgante,

Defect states at the $tio_2(110)$ *surface probed by resonant photoelectron diffraction*, *Phys. Rev. Lett.* **100** (Feb, 2008) 055501.

[135] P. Kruger, J. Jupille, S. Bourgeois, B. Domenichini, A. Verdini, L. Floreano, and A. Morgant, *Intrinsic nature of the excess electron distribution at the tio2 (110) surface*, *Physical Review Letters* **108** (2012).

[136] T. Minato, Y. Sainoo, K. Y., Y. K. Kato, A. Ken-ichi, M. Kawai, J. Zhao, H. Petek, T. Huang, W. He, B. Wang, Z. Wang, Y. Zhao, J. Yang, and J. G. Hou, *The electronic structure of oxygen atom vacancy and hydroxyl impurity defects on titanium dioxide (110) surface*, *Journal of Chemical Physics* **130** (2009).

[137] M. Setvin, C. Franchini, X. Hao, M. Schmid, A. Janotti, M. Kaltak, C. G. Van de Walle, G. Kresse, and U. Diebold, *Direct view at excess electrons in* tio_2 *rutile and anatase*, *Phys. Rev. Lett.* **113** (Aug, 2014) 086402.

[138] K. Mitsuhara, H. Okumura, A. Visikovskiy, M. Takizawa, and Y. Kido, *Reaction of co with o adatoms on rutile tio2 (110) surfaces*, *Chemical Physics Letters* **513** (2011) 84–87.

[139] K. Onda, B. Li, J. Zhao, and H. Petek, *The electronic structure of methanol covered tio2(110) surfaces*, *Surface Science* **593** (2005), no. 1 32 – 37.

[140] B. Li, J. Zhao, K. Onda, K. D. Jordan, J. Yang, and H. Petek, *Ultrafast interfacial proton-coupled electron transfer*, *Science* **311** (2006), no. 5766 1436–1440.

[141] J. Zhao, J. Yang, and H. Petek, *Theoretical study of the molecular and electronic structure of methanol on a* $tio_2(110)$ *surface*, *Phys. Rev. B* **80** (Dec, 2009) 235416.

[142] H. Petek and J. Zhao, *Ultrafast interfacial proton-coupled electron transfer*, *Chemical Reviews* **110** (2010), no. 12 7082–7099.

[143] S. Liu, A.-a. Liu, B. Wen, R. Zhang, C. Zhou, L.-M. Liu, and Z. Ren, *Coverage dependence of methanol dissociation on tio2(110)*, *The Journal of Physical Chemistry Letters* **6** (2015), no. 16 3327–3334.

[144] D. Silber, P. M. Kowalski, F. Traeger, M. Buchholz, F. Bebensee, B. Meyer, and C. Wöll, *Adsorbate-induced lifting of substrate relaxation is a general mechanism governing titania surface chemistry*, *Nature Communications* **7** (09, 2016) 12888 EP –.

[145] C. M. Yim, J. Chen, Y. Zhang, B.-J. Shaw, C. L. Pang, D. C. Grinter, H. Bluhm, M. Salmeron, C. A. Muryn, A. Michaelides, and G. Thornton, *Visualization of*

water-induced surface segregation of polarons on rutile tio2(110), *The Journal of Physical Chemistry Letters* **9** (2018), no. 17 4865–4871.

[146] A. Migani, D. J. Mowbray, A. Iacomino, J. Zhao, H. Petek, and A. Rubio, *Level alignment of a prototypical photocatalytic system: Methanol on tio2(110)*, *Journal of the American Chemical Society* **135** (2013), no. 31 11429–11432.

[147] A. Migani, D. J. Mowbray, J. Zhao, H. Petek, and A. Rubio, *Quasiparticle level alignment for photocatalytic interfaces*, *Journal of Chemical Theory and Computation* **10** (2014), no. 5 2103–2113.

[148] R. Feenstra, J. A. Stroscio, and A. Fein, *Tunneling spectroscopy of the si(111)2 1 surface*, *Surface Science* **181** (1987), no. 1 295 – 306.

[149] P. Kemper, A. Kolmakov, X. Tong, Y. Lilach, L. Benz, M. Manard, H. Metiu, S. K. Buratto, and M. T. Bowers, *Formation, deposition and examination of size selected metal clusters on semiconductor surfaces: An experimental setup*, *International Journal of Mass Spectrometry* **254** (2006), no. 3 202 – 209.

[150] I. Horcas, R. Fernández, J. M. Gómez-Rodríguez, J. Colchero, J. Gómez-Herrero, and A. M. Baro, *Wsxm: A software for scanning probe microscopy and a tool for nanotechnology*, *Review of Scientific Instruments* **78** (2007), no. 1 013705.

[151] D. Wei, X. Jin, C. Huang, D. Dai, Z. Ma, W.-X. Li, and X. Yang, *Direct imaging single methanol molecule photocatalysis on titania*, *The Journal of Physical Chemistry C* **119** (2015), no. 31 17748–17754.

[152] J. C. Robins, X. Tong, H. L. Neilson, J. W. Buffon, H. Metiu, M. T. Bowers, and S. K. Buratto, *On the role of ti interstitials in methanol reactivity on tio2*, *Manuscript in Preparation* (2018).

[153] Z. Zhang, O. Bondarchuk, J. M. White, B. D. Kay, and Z. Dohnálek, *Imaging adsorbate oh bond cleavage: methanol on tio2(110)*, *Journal of the American Chemical Society* **128** (2006), no. 13 4198–4199.

[154] M. Chander, Y. Z. Li, J. C. Patrin, and J. H. Weaver, *Si(100)-(21) surface defects and dissociative and nondissociative adsorption of* h_2o *studied with scanning tunneling microscopy*, *Phys. Rev. B* **48** (Jul, 1993) 2493–2499.

[155] N. N. Lichtin and M. Avudaithai, *Tio2-photocatalyzed oxidative degradation of ch3cn, ch3oh, c2hcl3, and ch2cl2 supplied as vapors and in aqueous solution under similar conditions*, *Environmental Science & Technology* **30** (1996), no. 6 2014–2020.

[156] D. S. Muggli, M. J. Odland, and L. R. Schmidt, *Effect of trichloroethylene on the photocatalytic oxidation of methanol on tio2*, *Journal of Catalysis* **203** (2001), no. 1 51 – 63.

[157] I. Mora-Seró, T. L. Villarreal, J. Bisquert, Á. Pitarch, R. Gómez, and P. Salvador, *Photoelectrochemical behavior of nanostructured tio2 thin-film electrodes in contact with aqueous electrolytes containing dissolved pollutants: a model for distinguishing between direct and indirect interfacial hole transfer from photocurrent measurements*, *The Journal of Physical Chemistry B* **109** (2005), no. 8 3371–3380.

[158] L. S. Al-Mazroai, M. Bowker, P. Davies, A. Dickinson, J. Greaves, D. James, and L. Millard, *The photocatalytic reforming of methanol*, *Catalysis Today* **122** (2007), no. 1 46 – 50. Materials, Applications and Processes in Photocatalysis.

[159] G. L. Chiarello, M. H. Aguirre, and E. Selli, *Hydrogen production by photocatalytic steam reforming of methanol on noble metal-modified tio2*, *Journal of Catalysis* **273** (2010), no. 2 182 – 190.

[160] S. V. Awate, S. S. Deshpande, K. Rakesh, P. Dhanasekaran, and N. M. Gupta, *Role of micro-structure and interfacial properties in the higher photocatalytic activity of tio2-supported nanogold for methanol-assisted visible-light-induced splitting of water*, *Phys. Chem. Chem. Phys.* **13** (2011) 11329–11339.

[161] M. A. Henderson and I. Lyubinetsky, *Molecular-level insights into photocatalysis from scanning probe microscopy studies on tio2(110)*, *Chemical Reviews* **113** (2013), no. 6 4428–4455.

[162] E. Farfan-Arribas and R. J. Madix, *Different binding sites for methanol dehydrogenation and deoxygenation on stoichiometric and defective tio2(110) surfaces*, *Surface Science* **544** (2003), no. 2 241 – 260.

[163] M. Shen and M. A. Henderson, *Role of water in methanol photochemistry on rutile tio2(110)*, *The Journal of Physical Chemistry C* **116** (2012), no. 35 18788–18795.

[164] K. Onda, B. Li, and H. Petek, *Two-photon photoemission spectroscopy of* $\mathrm{Tio_2}(110)$ *surfaces modified by defects and* $\mathrm{o_2}$ *or* $\mathrm{h_2O}$ *adsorbates*, *Phys. Rev. B* **70** (Jul, 2004) 045415.

[165] U. Martinez, J. O. Hansen, E. Lira, H. H. Kristoffersen, P. Huo, R. Bechstein, E. Lægsgaard, F. Besenbacher, B. Hammer, and S. Wendt, *Reduced step edges on rutile* $\mathrm{tio_2}(110)$ *as competing defects to oxygen vacancies on the terraces and reactive sites for ethanol dissociation*, *Phys. Rev. Lett.* **109** (Oct, 2012) 155501.

[166] R. Zehr and M. Henderson, *Influence of o2-induced surface roughening on the chemistry of water on tio2(110)*, *Surface Science* **602** (2008), no. 8 1507 – 1516.

[167] Z. Li, R. S. Smith, B. D. Kay, and Z. Dohnálek, *Determination of absolute coverages for small aliphatic alcohols on tio2(110)*, *The Journal of Physical Chemistry C* **115** (2011), no. 45 22534–22539.

[168] D. Wei, X. Jin, C. Huang, D. Dai, Z. Ma, W.-X. Li, and X. Yang, *Direct imaging single methanol molecule photocatalysis on titania*, *The Journal of Physical Chemistry C* **119** (2015), no. 31 17748–17754.

[169] H. Feng, S. Tan, H. Tang, Q. Zheng, Y. Shi, X. Cui, X. Shao, A. Zhao, J. Zhao, and B. Wang, *Temperature- and coverage-dependent kinetics of photocatalytic reaction of methanol on tio2 (110)-(1 1) surface*, *The Journal of Physical Chemistry C* **120** (2016), no. 10 5503–5514.

[170] U. Martinez, L. B. Vilhelmsen, H. H. Kristoffersen, J. Stausholm-Møller, and B. Hammer, *Steps on rutile tio_2(110): Active sites for water and methanol dissociation*, *Phys. Rev. B* **84** (Nov, 2011) 205434.

[171] L.-Q. Wang, K. F. Ferris, J. P. Winokur, A. N. Shultz, D. R. Baer, and M. H. Engelhard, *Interactions of methanol with stoichiometric and defective tio2(110) and (100) surfaces*, *Journal of Vacuum Science & Technology A: Vacuum, Surfaces, and Films* **16** (1998), no. 5 3034–3040.

[172] Z. Zhang, J. Lee, J. T. Yates, R. Bechstein, E. Lira, J. Ø. Hansen, S. Wendt, and F. Besenbacher, *Unraveling the diffusion of bulk ti interstitials in rutile tio2(110) by monitoring their reaction with o adatoms*, *The Journal of Physical Chemistry C* **114** (2010), no. 7 3059–3062.

[173] P. Redhead, *Thermal desorption of gases*, *Vacuum* **12** (1962), no. 4 203 – 211.

[174] A. S. Crampton, L. Cai, N. Janvelyan, X. Zheng, and C. M. Friend, *Methanol photo-oxidation on rutile tio2 nanowires: Probing reaction pathways on complex materials*, *The Journal of Physical Chemistry C* **121** (2017), no. 18 9910–9919.

[175] L. Gamble, L. S. Jung, and C. T. Campbell, *Decomposition and protonation of surface ethoxys on tio2(110)*, *Surface Science* **348** (1996), no. 1 1 – 16.

[176] Y. K. Kim, B. D. Kay, J. M. White, and Z. Dohnálek, *Alcohol chemistry on rutile tio2(110): the influence of alkyl substituents on reactivity and selectivity*, *The Journal of Physical Chemistry C* **111** (2007), no. 49 18236–18242.

[177] J. O. Hansen, P. Huo, U. Martinez, E. Lira, Y. Y. Wei, R. Streber, E. Lægsgaard, B. Hammer, S. Wendt, and F. Besenbacher, *Direct evidence for ethanol dissociation on rutile* $tio_2(110)$, *Phys. Rev. Lett.* **107** (Sep, 2011) 136102.

[178] X. Tong, S. P. Price, J. C. Robins, C. Ridge, H. Y. Kim, P. Kemp, H. Metiu, M. T. Bowers, and S. K. Buratto, *Vo-stabilized h2o adsorption on a tio2(110) surface at room temperature*, *Manuscript in Preparation*.

[179] S. P. Price, X. Tong, C. Ridge, V. Shapovalov, Z. Hu, P. Kemper, H. Metiu, M. T. Bowers, and S. K. Buratto, *Stm characterization of size-selected v1, v2, vo, and vo2 clusters on a tio2(110)-(11) surface at room temperature*, *Surface Science* **605** (2011), no. 9 972 – 976.

[180] J. Matthiesen, J. O. Hansen, S. Wendt, E. Lira, R. Schaub, E. Lægsgaard, F. Besenbacher, and B. Hammer, *Formation and diffusion of water dimers on rutile* $tio_2(110)$, *Phys. Rev. Lett.* **102** (2009).

[181] J. Cheng and P. Hu, *Theory of the kinetics of chemical potentials in heterogeneous catalysis*, *Angewandte Chemie International Edition* **50** (2011), no. 33 7650–7654.

[182] Q. Zheng, S. Tan, H. Feng, X. Cui, J. Zhao, and B. Wang, *Dynamic equilibrium of reversible reactions and migration of hydrogen atoms mediated by diffusive methanol on rutile tio2 (110)-(1 1) surface*, *The Journal of Physical Chemistry C* **120** (2016), no. 14 7728–7735.

[183] S. Takakusagi, K.-i. Fukui, R. Tero, K. Asakura, and Y. Iwasawa, *First direct visualization of spillover species emitted from pt nanoparticles*, *Langmuir* **26** (2010), no. 21 16392–16396.

[184] J. Wintterlin, T. Zambelli, J. Trost, J. Greeley, and M. Mavrikakis, *Atomic-scale evidence for an enhanced catalytic reactivity of stretched surfaces*, *Angewandte Chemie International Edition* **42** (2003), no. 25 2850–2853.

[185] Q. Hao, ZhiqiangWang, T. Wang, Z. Ren, C. Zhou, and X. Yang, *Role of pt loading in the photocatalytic chemistry of methanol on rutile tio2(110)*, *ACS Catalysis* **9** (2019), no. 1 286–294.

[186] M. A. Henderson, *A surface science perspective on tio2 photocatalysis*, *Surface Science Reports* **66** (2011), no. 6 185 – 297.

[187] X. Chen and S. S. Mao, *Titanium dioxide nanomaterials: Synthesis, properties, modifications, and applications*, *Chemical Reviews* **107** (2007), no. 7 2891–2959.

[188] K. Onda, B. Li, J. Zhao, K. D. Jordan, J. Yang, and H. Petek, *Wet electrons at the h2o/tio2(110) surface*, *Science* **308** (2005), no. 5725 1154–1158.